Fall 2014

Aircraft-based measurements for the identification and quantification of sources and sinks in the carbon cycle

Dana R Caulton
Purdue University

Graduate School Form 30
(Revised 08/14)

PURDUE UNIVERSITY
GRADUATE SCHOOL
Thesis/Dissertation Acceptance

This is to certify that the thesis/dissertation prepared

By Dana R. Caulton

Entitled
AIRCRAFT-BASED MEASUREMENTS FOR THE IDENTIFICATION AND QUANTIFICATION OF SOURCES AND SINKS IN THE CARBON CYCLE

For the degree of Doctor of Philosophy

Is approved by the final examining committee:

Paul B. Shepson

Qianlai Zhuang

Dor Ben-Amotz

Garth J. Simpson

To the best of my knowledge and as understood by the student in the Thesis/Dissertation Agreement, Publication Delay, and Certification/Disclaimer (Graduate School Form 32), this thesis/dissertation adheres to the provisions of Purdue University's "Policy on Integrity in Research" and the use of copyrighted material.

Paul B. Shepson

Approved by Major Professor(s): _____

_____

Approved by: R. E. Wild 12/05/2014

Head of the Department Graduate Program Date

AIRCRAFT-BASED MEASUREMENTS FOR THE IDENTIFICATION AND QUANTIFICATION OF SOURCES AND SINKS IN THE CARBON CYCLE

A Dissertation

Submitted to the Faculty

of

Purdue University

by

Dana R. Caulton

In Partial Fulfillment of the

Requirements of the Degree

of

Doctor of Philosophy

December 2014

Purdue University

West Lafayette, Indiana

ACKNOWLEDGEMENTS

I would like to thank my parents John and Lorraine Caulton, for their support and encouragement. I would also like to thank my advisor, Paul Shepson, for the amazing opportunities he provided and the mentorship he has given. I'd like to thank the current and past Shepson group members for their support and camaraderie. I would like to thank Brian Stirm and the Purdue Department of Aviation Technology, and the members of the Jonathan Amy Facility for Chemical Instrumentation, for their help and support, without which this research would not be possible.

TABLE OF CONTENTS

Page

Page

LIST OF TABLES

Table Page

LIST OF FIGURES

Figure Page

Figure Page

Figure Page

Figure Page

Figure Page

Figure Page

Figure Page

ABSTRACT

Caulton, Dana R. Ph. D., Purdue University, December 2014. Aircraft-Based Measurements for the Identification and Quantification of Sources and Sinks in the Carbon Cycle. Major Professor: Paul B. Shepson.

Improved quantification of carbon-cycle sources and sinks is an important requirement for determining mitigation strategies and modeling future climate interactions. Analytically robust measurements require high-precision instrumentation and thoughtful experimental design to produce rigorous and reproducible results despite complex and quickly changing meteorological and environmental conditions. Here, an aircraft platform equipped with a high-precision cavity ring-down spectrometer for CO_2, CH_4 and H_2O quantification was used to acquire data from previously un-sampled sources. The aircraft mass-balance technique was used to quantify CH_4 emissions from natural gas well pads in the drilling stage, which were 2-3 orders of magnitude higher than previous estimates of emissions from this stage. In addition, the first in-situ flare emission data was collected for natural gas flares in North Dakota, Pennsylvania and Texas. Flare efficiency was high for most flares, higher than assumed efficiency. However, a few flares sampled with lower efficiencies closer to the assumed flare efficiency suggest the need for characterization of operational conditions specific to operators and basins. Finally, eddy-covariance CO_2 and heat fluxes were measured over

three east-coast forests at sites close to and far from surface eddy-covariance towers. Tower data is often used in models to represent a larger heterogeneous region. Aircraft and tower CO_2 and sensible heat flux agreed well, indicating that for these sites, tower data is a good approximation of the larger region, though significant variability was observed. Aircraft latent heat fluxes were routinely much larger that tower fluxes, most likely due to the influence of advection which is measured by the aircraft eddy-covariance technique, but not by towers.

CHAPTER 1. INTRODUCTION

1.1 Atmospheric Structure

The atmosphere acts as a unique bridge between all life on earth where emissions from, and deposition to, the surface profoundly affect the atmosphere's composition. Increased understanding of atmospheric dynamics has led to interest in using the geological records of the earth's atmosphere to peer into the past and use this knowledge to help predict and understand the future evolution of the atmosphere and its impact on life (Otto-Bliesner et al., 2006; Dakos et al., 2008, Hansen et al., 2008). Understanding the structure and transport mechanisms of the atmosphere is therefore critical for meaningful interpretation of atmospheric data or experimental design. The atmosphere is divided into several layers based largely on temperature changes associated with each layer. These layers, from the earth's surface to the top of the atmosphere, are the troposphere, stratosphere, mesosphere, thermosphere and ionosphere. The troposphere is the only layer in direct contact with the earth and is most heavily impacted by surface activity. The troposphere can be further divided into different layers and, being heavily influenced by the surface, exhibits a strong diurnal cycle as depicted in Figure 1.1.

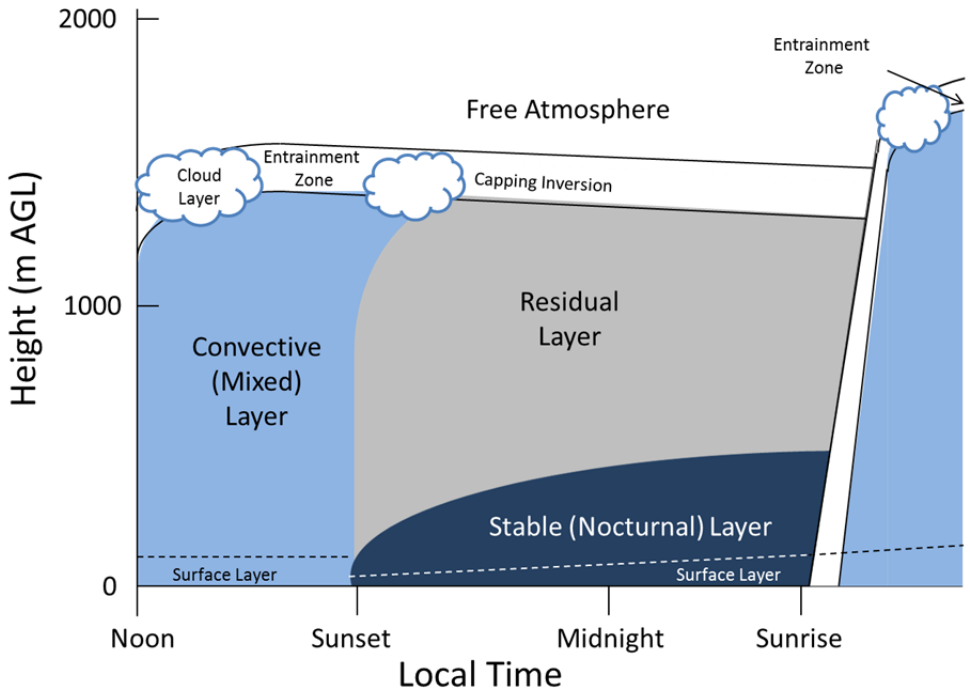

Figure 1.1 The idealized structure of the troposphere as affected by the diurnal cycle. Height is represented as meters above ground level (m AGL). Figure adapted from Stull (1988).

In the daytime these layers are the surface layer, convective or mixed layer (also called the convective boundary layer or CBL), the entrainment zone and the free atmosphere (also called the free troposphere). During the night these layers are the surface layer, stable (or nocturnal) boundary layer (SBL or NBL), residual layer, capping inversion and free atmosphere. In both cases the free atmosphere is separated by an entrainment zone, where a temperature inversion effectively caps the lower troposphere prohibiting efficacious transport. This temperature inversion is created by the condensation of water from the gas phase to the liquid phase. As water condenses it releases heat warming the air parcel. Warm (less dense) air above colder (more dense) air

is very stable and will not readily mix. In addition, the lowest 10% (~50-200m) of the atmosphere is called the surface layer and is most strongly affected by surface roughness, which, along with the horizontal wind, creates mechanical turbulence (Stull, 1988).

1.2 Boundary Layer Conditions

Boundary layer characteristics are largely determined by the type of convection or mixing that occurs, of which there are two main types. Buoyancy driven turbulence is typical during daytime and is caused by incoming radiation that warms surface air parcels causing them to expand, thus become less dense, and rise, creating vertical motion. As the net vertical motion of air must be zero, this vertical motion creates eddies, circular motions of air as air rises and displaces more dense air parcels downward. Vertical eddies also cause the boundary layer to grow as air rises above the entrainment zone and free tropospheric air mixes downward. A second type of turbulence is mechanical turbulence, which is produced from flow over a rough surface. This type of turbulence is generated primarily in the horizontal direction and typically affects only the lowest portion of the boundary layer. This type of turbulence is usually dominant at night where there are no buoyant air parcels to produce vertical turbulence. However, under certain daytime conditions that resist buoyancy-driven turbulence, such as continuous cloud cover or high pressure systems, mechanical turbulence can become relatively important. In addition, areas with particularly rough surfaces will be more impacted by this type of turbulence (i.e. mountainous regions, built-up urban centers, etc.).Typical daytime CBL heights can be 1000-2000 m above ground level (AGL) with nighttime SBL heights of 100-500 m AGL.

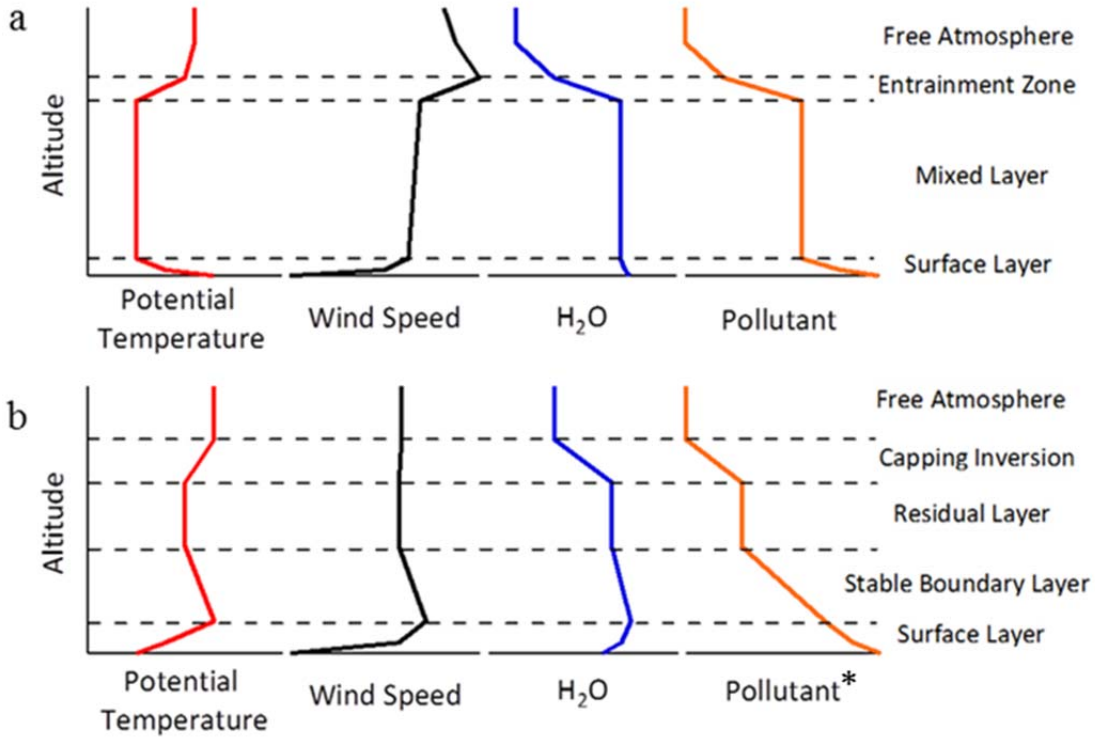

Figure 1.2 Idealized mean boundary layer profiles of selected variables for (a) the convective boundary layer and (b) the stable boundary layer. *Pollutant species may have variable profiles in the SBL and may even separate by density and become stratified, therefore a sample profile (not a universal profile) is shown. Figure adapted from Stull (1988).

The presence of turbulence greatly affects the transport of variables such as heat, water vapor and emitted pollutants. Figure 1.2 shows the profiles of selected variables for both the daytime and nighttime boundary layer. Measured profiles can be used to identify characteristics and sub-layers of an unknown boundary layer. The potential temperature profile, which is temperature corrected for the work of expansion or compression caused by pressure changes, can be used to identify areas that are strongly

convective, neutral or stable. The equation for potential temperature is shown in Equation 1.1.

$$\theta = T \times \left(\frac{1000}{P}\right)^{R/C_p} \quad 1.1$$

Here, θ is potential temperature, T is temperature (K), P is pressure (mbar), R is the gas constant (287.04 J K^{-1} kg^{-1}) and C_p is the specific heat capacity of air at constant pressure (1004.67 J K^{-1} kg^{-1}). Profiles that show decreasing potential temperature with altitude represent conditions that are unstable and promote mixing while an increasing potential temperature profile denotes stable conditions with poor mixing (Stull, 1988). A profile that is unchanging with altitude may denote a neutral boundary layer or a convective boundary layer (Stull, 1988). At night, because as a black body radiator the ground cools faster than the air above it, a temperature inversion develops which causes stable conditions (Stull, 1988).

The definition of a boundary layer dates back to the seminal work by Dr. Ludwig Prandtl in 1904 (Tulapurkara, 2005). Theories of turbulence structure began to be investigated in earnest in the 1920s (Tulapurkara, 2005). The first measurements occurred over ideal (i.e. flat and homogeneous) surfaces in the 50s with a key study conducted in Kansas in 1968 by the Air Force Cambridge Research Laboratories that revealed the expected vertical profiles of variables of interest (e.g. potential temperature, water, trace gases, etc.) and also provided information about the drivers of transport, mean wind and turbulence, the results of which are reported in a multitude of influential papers on these subjects (Kaimal, 1969; Businger et al., 1971; Wyngaard et al., 1971a; Wyngaard et al., 1971b; Wyngaard and Cote, 1971; Wyngaard and Cote, 1972; Kaimal et

al., 1972; Kaimal and Wyngaard, 1990). With the incorporation of advanced statistical analysis, decomposing a time series of wind speed data by Fourier transform (FT) into a frequency spectrum has been used to provide information about sources of turbulence. For instance, an FT of long-term high frequency wind speed data shows a peak around the 4d mark showing wind speed is affected by synoptic conditions, the passage of high or low pressure systems and cold fronts (Stull, 1988). The 1-day peak represents the diurnal cycle impact on the winds. Additionally, there will be a peak around 1min that follows an expected decay curve. This peak is caused by thermal production of turbulence that creates big eddies first, which decay into smaller and smaller eddies until the energy is dissipated as heat, a process represented by a predictable inertial sub-range decay curve (Stull, 1988). A generalized power spectrum for horizontal wind is shown in Figure 1.3.

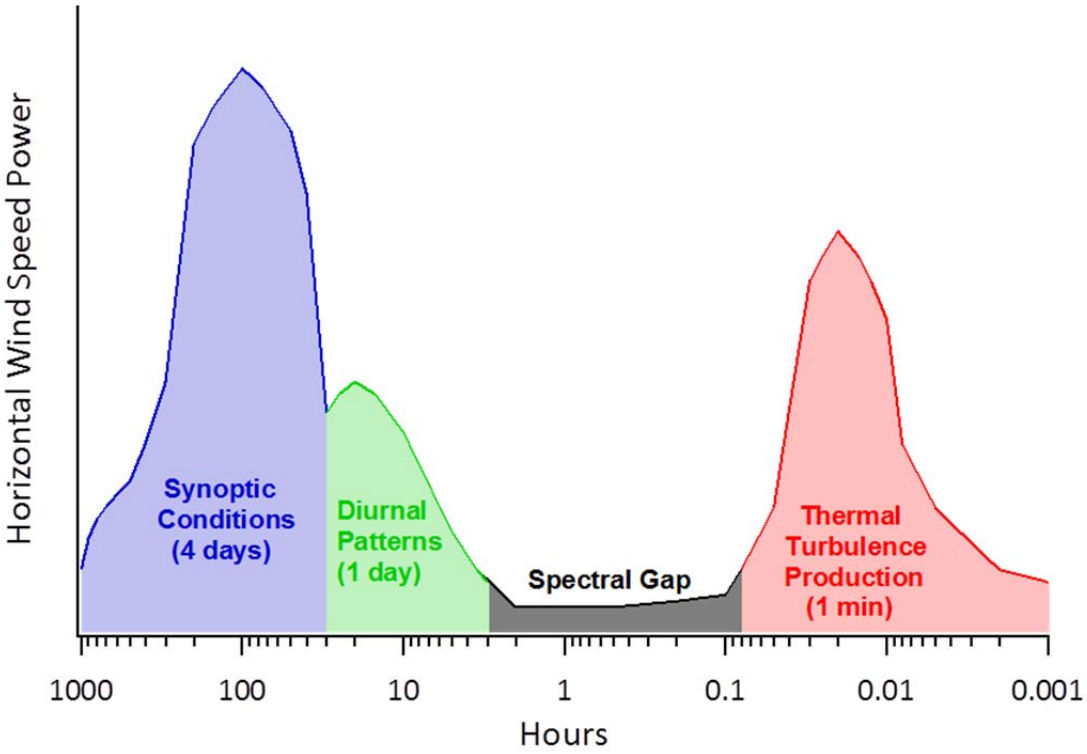

Figure 1.3 The power spectrum of horizontal wind showing distinct regions of production as well as the spectral gap, where no significant production mechanisms are present. Figure adapted from Van der Hoven (1957).

This type of analysis is also useful for determining characteristics of boundary layers as spectra should follow expected shapes (Stull, 1988). The presence of unusual peaks in the power spectra may indicate the presence of other influences that can affect the boundary layer, such as gravity waves or upslope or downslope flows caused by the warming or cooling of air close to the surface of a hill (Horst and Doran, 1986; Lee et al., 1997; McNaughton and Laubach, 2000). Furthermore, spectral analysis can be used to identify limitations in instrumentation or interpretation of measurements. As turbulence decays to thermal energy, eddies are produced that have smaller and smaller frequencies

requiring very high resolution measurements which may be difficult or impossible to obtain with certain instruments (Stull, 1988). Conversely, low frequency eddies may be difficult to accurately quantify due to the low frequency of such measurements which make satisfying statistical criteria difficult (Lenschow et al., 1994).

1.3 Surface-Atmosphere Interactions

Boundary layer conditions are important for many reasons. They can be used to predict daily weather, cloud cover, rain or potentially dangerous weather conditions, e.g. severe turbulence. Boundary layer models can be used to predict the transport and dispersion of hazardous particles, or other species of interest such as greenhouse gases (GHGs) that are emitted from the surface. The interactions of the atmosphere and the surface are of particular importance as either can be a source of heat, water or other scalars (such as CO_2) to the other. Correctly modeling surface-atmosphere interactions conditions is largely based on elements of fluid physics as the atmosphere can be thought of as a fluid with interfaces (i.e. boundary layers), the properties of which affect the interactions.

The basic governing principles of the boundary layer are the conservation of mass, momentum and moisture and the equation of state of the atmosphere, the ideal gas law (Stull, 1988). These principles are combined and multiple approximations are made to simplify the equation. The conservation equation is first defined, for momentum, heat or mass. For instance, the conservation of a scalar (C) can be expressed as:

$$\frac{\partial C}{\partial t} + M_j \frac{\partial C}{\partial x_j} = \frac{\nu \partial^2 C}{\partial x_j^2} + S_c \qquad 1.2$$

I II III IV

The total wind (M) is usually broken into three wind vectors, (U, V, and W) which are denoted by the subscripts on M where j can range from 1 to 3. U is the northerly wind component, V is the easterly wind component and W is the vertical wind component. A geographic coordinate system is also applied as denoted by the subscript j on x which can also range from 1 to 3. Here x is the east direction, y is the north direction and z is the vertical direction. In addition, ν is the molecular diffusivity. In this equation term I corresponds to inertia (also called storage), term II indicates C advection by the wind, term III is the influence of viscous stress (the tendency of moving particles to drag nearby particles) and term IV is a source or emission/deposition flux term.

In order to fully investigate different types of surface-atmosphere interactions some mathematical convention must be applied. Instantaneous wind can be broken into the mean and turbulent part of the wind, called the Reynold's decomposition:

$$M = \bar{M} + m' \qquad 1.3$$

Here M is the true wind speed, $\bar{M}$ is the mean wind and m' in the turbulent wind component (i.e. the deviation from the mean). These conventions provide the distinction between mean and turbulent transport of an air parcel (Stull, 1988).

In order to take advantage of the Reynold's decomposition a total conservation equation is expanded to separate the mean and turbulent wind components and the whole equation is averaged. Because the average of m' must equal zero this removes some

terms. In addition the average vertical wind (W) must be zero. For example, a simplified expression for the conservation of mass of a scalar in the atmosphere is (Stull, 1988):

$$\underset{\text{I}}{\frac{\partial \bar{c}}{\partial t}} + \underset{\text{II}}{\bar{M}_j \frac{\partial \bar{c}}{\partial x_j}} = \underset{\text{IV}}{-S_c} - \underset{\text{V}}{\frac{\partial (\overline{m_j' c'})}{\partial x_j}} \qquad 1.4$$

Here all the terms have the same meaning as before with the addition of term V, the turbulent flux divergence of C. Term III has been neglected because the magnitude of this term is much smaller than the other terms.

If stationarity is assumed, i.e. that turbulence statistics are not changing in time, the advection term can be removed. Storage is also typically assumed to be negligible. In a homogeneous environment advection will be negligible and U and V component terms will drop out. In this environment the change in concentration of a species with low chemical reactivity is approximated by the vertical turbulent flux. Vertical turbulent flux is a measure of the transport of a species by vertical eddies. Positive fluxes denote sources and negative fluxes indicate a sink for a specific species. In the surface layer this flux is constant to within 10% (Stull, 1988). Above the surface layer fluxes are expected to linearly decrease to the boundary layer, a process known as flux divergence, driven by the decrease of turbulent energy with height. To practically measure vertical turbulent flux (F_c), measurement periods of half an hour to an hour are typically used with the following equation called the eddy-covariance equation (Baldocchi et al., 1988):

$$F_c = \overline{w'c'} = \frac{1}{T} \sum w'c' \, \Delta t \qquad 1.5$$

Here T is the total averaging time, w' and c' are the deviations of vertical wind and the scalar from the mean during the averaging interval and Δt is the time between measurements. As shown in Figure 1.4 the correlation between positive vertical wind

peaks and positive potential temperature and H_2O peaks shows an expected positive H_2O flux. Likewise the anti-correlation between vertical wind and CO_2 suggest a downward flux of CO_2.

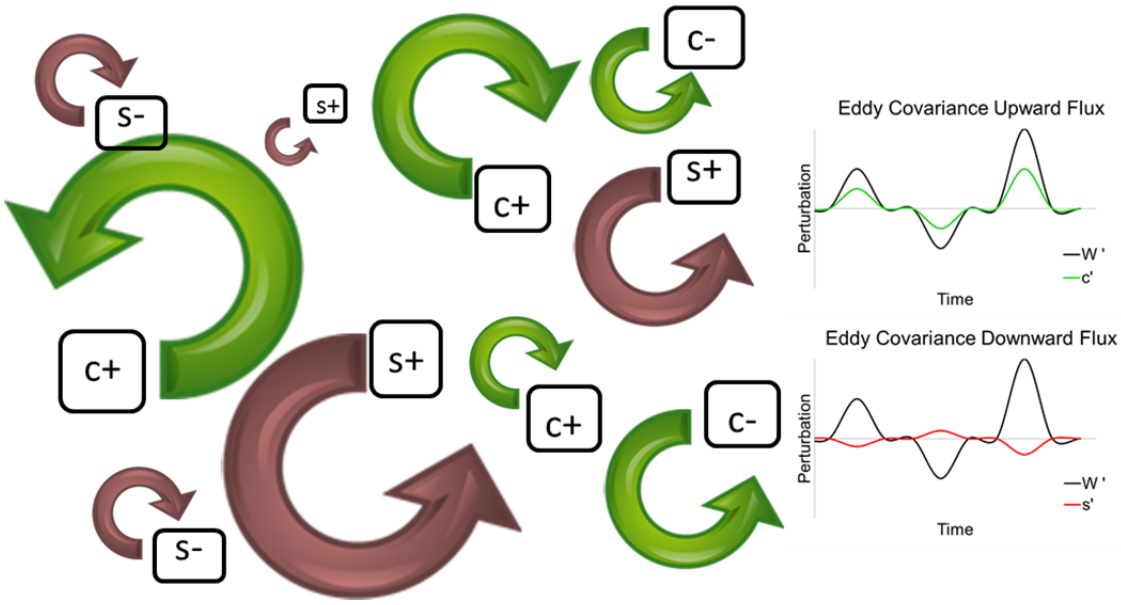

Figure 1.4 Theoretic mechanism of eddy-covariance flux. Eddies move positive and negative (relative to the mean) air parcels up and down. Positively correlated eddies produce upward (positive) fluxes and negatively correlated eddies produce downward (negative) fluxes.

For aircraft measurements, turbulent flux is averaged over distance instead of time, meaning the ground speed (S) must also be incorporated into the equation as presented below to take into account ground speed variations that affect the aircrafts ability to equally sample positive (updraft) and negative (downdraft) eddies (Crawford et al., 1993):

$$F_c = \frac{1}{\bar{S}T}\sum(w'c')S_i\,\Delta t \qquad 1.6$$

Turbulent flux measurements using the eddy covariance technique require fast sensors (often ≥10 Hz measurement frequency) and have been implemented since the 1960s for momentum and heat flux. The first report of eddy covariance flux measurements of CO_2 came from Desjardins and Lemon (1974) over a corn field in New York. The full potential of the eddy covariance technique to be used to generate long-term monitoring of annual net ecosystem exchange (NEE) of carbon was realized in the 1980s with the first long-term station in Harvard forest, MA in 1990, and subsequent tower sites across the U.S. and the globe (Baldocchi et al., 1988; Wofsy et al., 1993; Baldocchi et al., 2001). Recently there has been work by the National Ecological Observatory Network to maintain long-term tower sites measuring turbulent fluxes in representative biomes across North America (~13 permanent tower sites) (Keller et al., 2008). The long-term data, shown in Figure 1.5, proves invaluable for earth system modeling, but the small spatial scale accessed by towers makes it challenging to use this data to scale up to the global level. The advent of aircraft platforms equipped with eddy covariance systems to measure CO_2 flux has allowed fluxes to be measured over larger spatial areas, but due to operating costs and larger time input, they cannot contribute continuous measurements like towers and instead provide complementary 'snapshots' of carbon exchange in forests and other sites (e.g. wetland, oceans), rather than annual NEE estimates (Desjardins et al., 1989; Desjardins, et al., 1995; Desjardins, et al., 1997; Dobosy, et al., 1997; Gioli et al., 2004; Gioli et al., 2006; Miglietta et al., 2007; Kirby et al., 2008; Hutjes et al., 2010; Maselli et al., 2010; Vellinga et al., 2010; Metzger et al., 2012; Metzger et al., 2013; Vellinga et al., 2013).

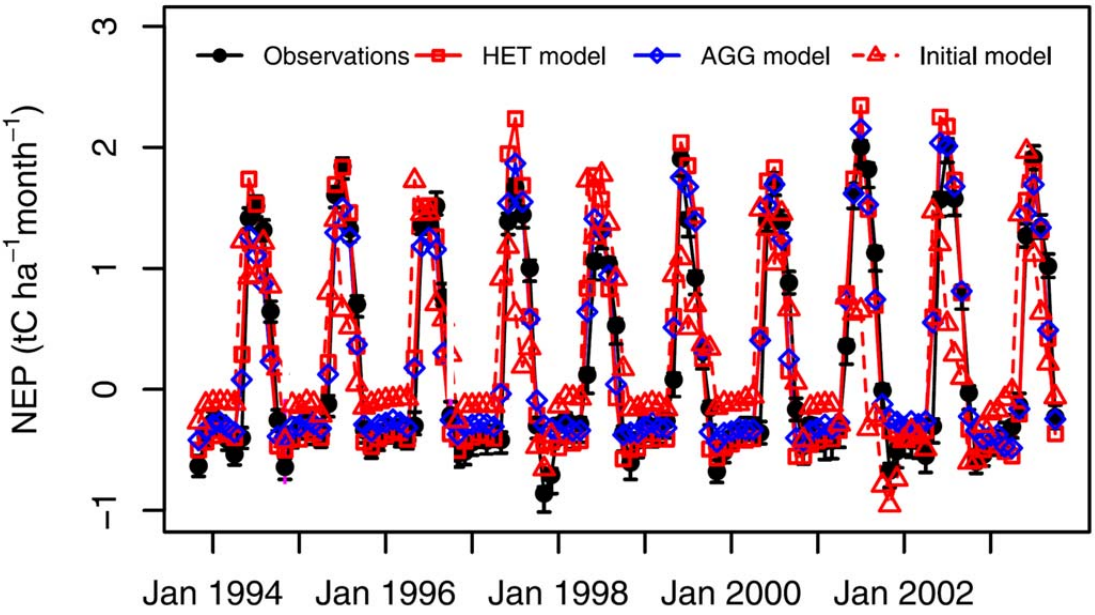

Figure 1.5 Long-term CO_2 fluxes from a site in Harvard Forest, MA, and several different model fit attempts (from Medvigy et al., 2009).

Additionally, advection measurement techniques using aircraft have been used since the 1990s (Trainer et al., 1995; Mays et al., 2009; Turnbull et al., 2011). This technique allows the flux from a surface source (e.g. a city) to be isolated and has been updated with more precise instrumentation as well as better data analysis protocols as described in Cambaliza, et al. (2014). The method relies on application equation 1.7.

$$F_c = \int_0^{z_i} \int_{-x}^{x} \Delta[c]_{ij} \times M_{\perp_{ij}} \, dxdz \qquad 1.7$$

Here z_i is the boundary layer depth, x and –x are the horizontal extent of a measurement transect and $M_\perp$ is the perpendicular wind speed at each measurement point denoted by the subscripts ij. Essentially, concentration measurements downwind of a source are isolated by subtracting a background concentration, obtained from the upwind air

concentration. The plume is multiplied by the perpendicular wind speed and the observations are summed across the width of the plume and over the depth of the boundary layer. This provides an emission flux across the vertical plane estimate. Figure 1.6 shows a block diagram of the mass-balance method.

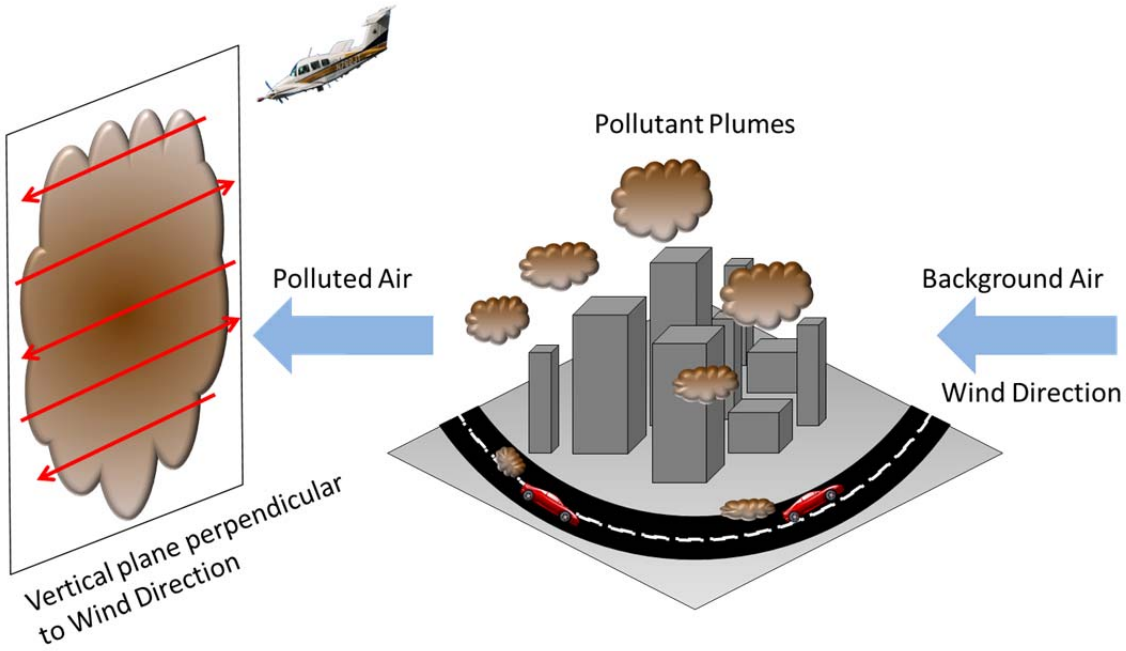

Figure 1.6 Block diagram of the mass-balance approach showing background air picking up pollutant plumes over a city and an aircraft raster the source plume downwind of the city perpendicular to the mean wind direction.

1.4 The Carbon Cycle

Gases in the atmosphere have diverse effects on the human experience. Some gases like ozone remove UV radiation in the stratosphere, but in the troposphere undergo

reactions causing photochemical smog, which includes ozone and reactive nitrogen oxides, which can cause respiratory problems and is responsible for the death of 10s of thousands of people in the U.S. every year (Bell et al., 2005; Fann et al., 2012). One important contribution of some gases is the greenhouse effect (Arrnehius, 1896). Greenhouse gases (GHGs) absorb in the infrared (IR) region but do not absorb in the ultra violet or visible (UV-Vis) region of the electromagnetic spectrum. This allows GHGs to transmit the radiation from the sun in the UV-Vis region but absorb and re-emit the radiation emitted by the earth in the IR region, depicted in Figure 1.7. This causes a net warming effect without which the earth would have an average surface temperature of 255 K, well below the freezing temperature of water (273 K) (Hartman, 1994). Instead, because of the greenhouse effect, the average temperature of the Earth's surfaces was, before human impacts, 288 K, or 33 K warmer (Hartman, 1994).

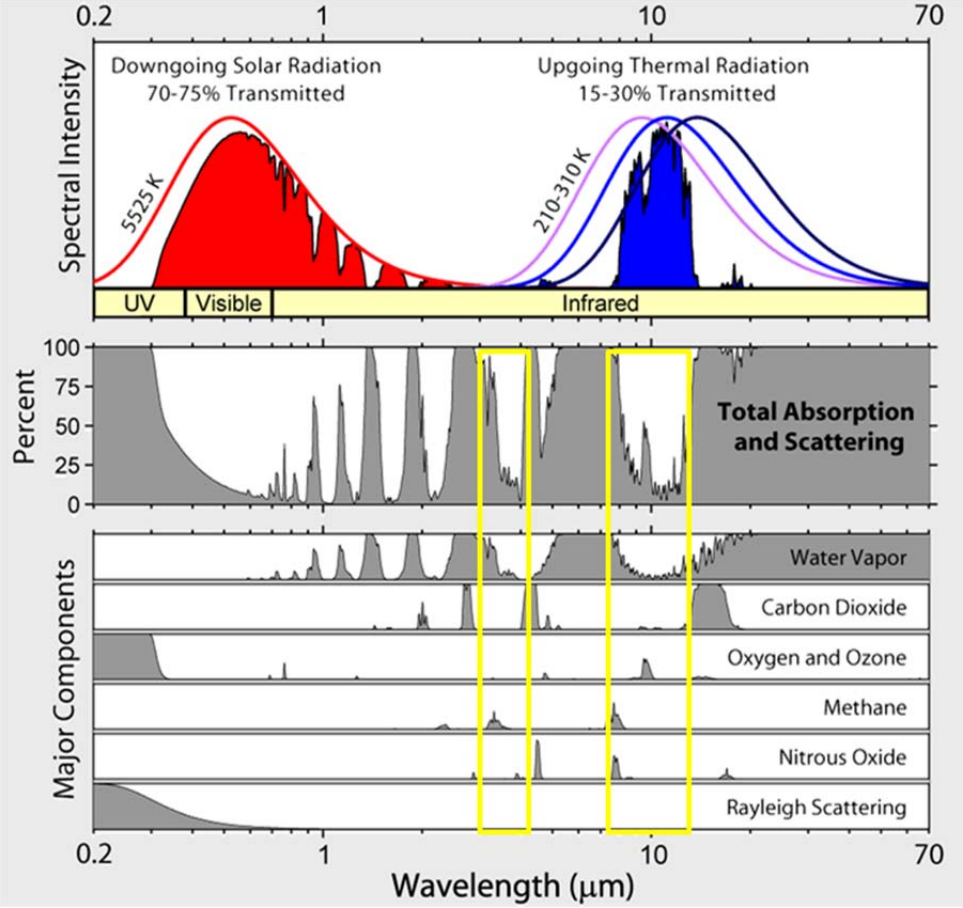

Figure 1.7. Radiation transmitted and absorbed by the total atmosphere and various gases. Also shown are two important atmospheric windows in yellow boxes. Figure from Global Warming Art (www.globalwarmingart.com/wiki/File:Atmospheric_Transmission_png).

The most important GHGs in the atmosphere are water and carbon dioxide due to their abundance and radiation absorption spectrums. Both of these species absorb strongly and broadly in the infrared region, as shown in Figure 1.7, prohibiting heat from leaving the atmosphere. Also noticeable are the 'atmospheric windows' where these particular species and the total atmosphere do not absorb IR radiation. These areas are important because many other trace GHGs absorb in these windows, increasing the absorption and retention of heat by the atmosphere. Trace gasses that absorb in the same

region as CO_2 and H_2O will not contribute significantly to global warming because the atmosphere already absorbs strongly at these wavelengths. Other lower abundance gases like methane, nitrous oxide and sulfur hexafluoride also contribute even though they exist in much lower abundance because they have a much greater global warming potential (GWP) than carbon dioxide and absorb radiation inside the atmospheric windows (Wuebbles et al., 1999). GWP is defined as the amount of radiation absorbed by a mass of a specific species divided by the amount of radiation absorbed by the same mass of CO_2 (Jain et al., 2000; IPCC, 2013). Table 1.1 shows relevant gas abundances, lifetimes and GWPs.

Table 1.1 Abundance of Selected Greenhouse Gases in the Atmosphere

Gas (Formula)	Abundance (%)	GWP (100 yr)	Lifetime (years)
Water (H_2O)	1-5	--	~0.025 [a]
Carbon Dioxide (CO_2)	3.91 E-2 [b]	1	Variable [c]
Methane (CH_4) (fossil CH_4)	1.803 E-4 [b]	28-34 [d] (30-36) [e]	12.4 [d]
Nitrous Oxide (N_2O)	3.24 E-5 [b]	265-298 [d]	121 [d]
CFC-12 (CCl_2F_2)	5.28 E-8 [b]	10200 [f]	100 [f]
CFC-11 (CCl_3F)	2.38 E-8 [b]	4660-5350 [d]	45 [d]
HCFC-22 ($CHClF_2$)	2.13 E-8 [b]	1760 [f]	11.9 [f]
Tetrachloromethane (CCl_4)	8.58 E-9 [b]	1730 [f]	26 [f]
Tetrafluormethane (CF_4)	7.9 E-9 [b]	6630-7350 [d]	50000 [d]
CFC-113 (CCl_2FCClF_2)	7.43 E-9 [b]	5820 [f]	85 [f]
HFC-134a (CH_2FCF_3)	6.27 E-9 [b]	1300-1550 [d]	13.4 [d]
Sulfur Hexafluoride (SF_6)	7.28 E-10 [b]	23,500 [c]	3,200 [f]

[a] Hartman, 1998.
[b] IPCC, 2013 Table 8.2 abundances for 2011. Compositions are reported as fraction of dry air, expect for H_2O.
[c] See Joos et al. (2013).
[d] IPCC, 2013 Table 8.7. The reported range reflects warming with and without climate feedback.
[e] GWP for fossil CH4, See note in IPCC, 2013 Table 8.7.
[f] IPCC, 2013 Table 8.A.1.

As carbon dioxide has increased from the pre-industrial level of 280 ppm to the current level of 400 ppm due mostly to emissions from human activities, the enhanced greenhouse effect has become problematic causing the global average temperature to increase 0.85° C with the potential to increase much more (Tans and Bakwind, 1995; Rosenzweig et al., 2008; IPCC, 2013). Figure 1.8 shows the increase levels of CO_2 over the last ~11,000 years as well as the temperature anomaly (i.e. the deviation from the 1961-1990 average temperature). Carbon dioxide is the main GHG of interest for mitigation and regulation due to its long lifetime, abundance and its continued emission by human activities and importance to atmospheric warming. Svante Arrhenius published the first hypothesis of CO_2 induced warming in 1896 and posited the first greenhouse law: "*if the quantity of carbonic acid* [CO_2] *increases in geometric progression, the augmentation of the temperature will increase nearly in arithmetic progression"* (Arrhenius, 1896). Carbon dioxide is still the most important contributor to global warming as shown in Figure 1.9, which depicts the total radiative forcing, i.e. heat added to the atmosphere, from various sources. It is noteworthy that the uncertainty on the total radiative forcing does not overlap with zero.

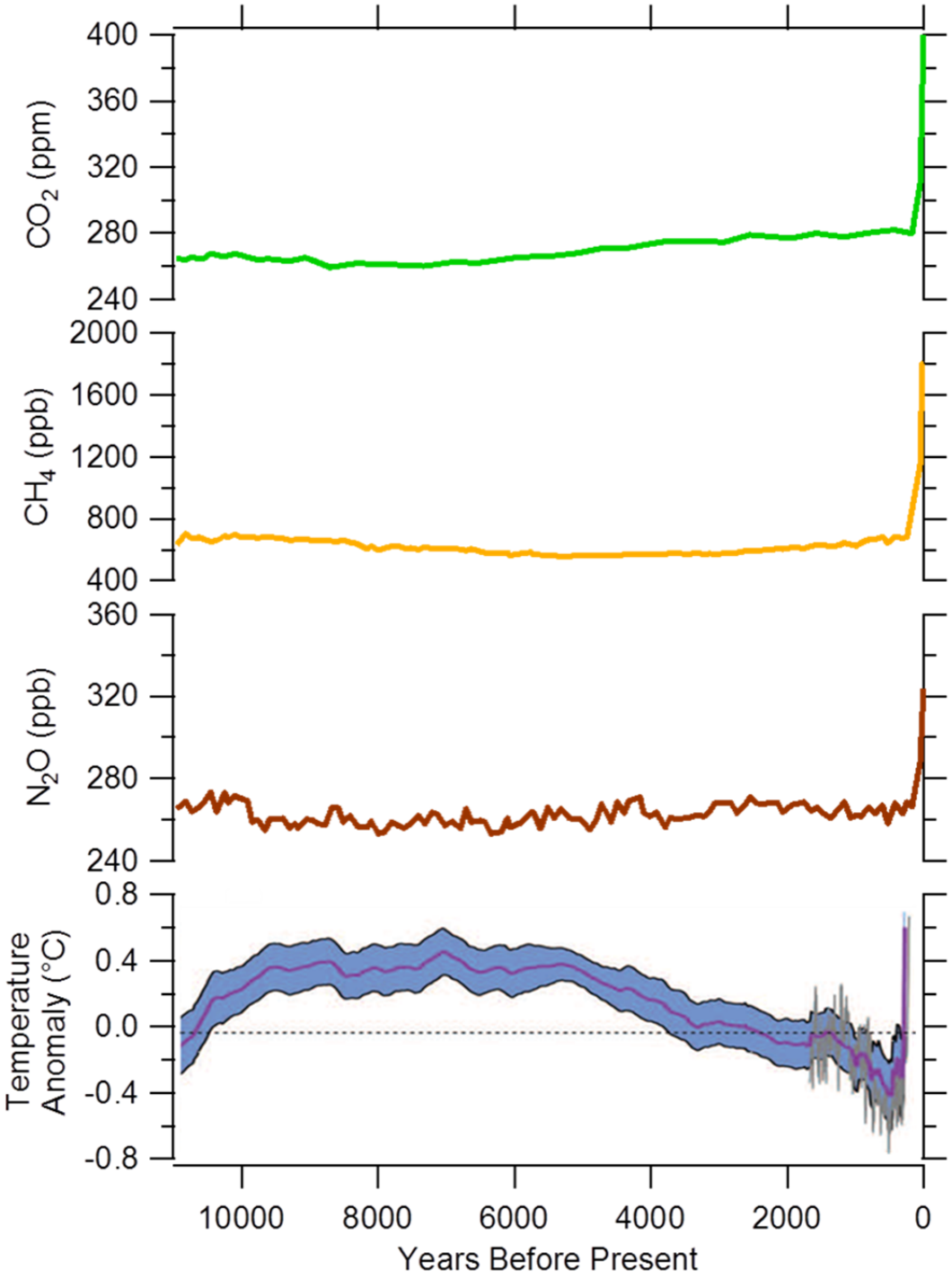

Figure 1.8. Ice core data for the last ~11 000 years showing CO_2, CH_4, N_2O and temperature anomaly. Data is presented as years before present (yr BP). Data from Fluckinger et al. (2002) and IPCC, 2013.

Other GHGs shown in Table 1 may either be removed faster through reactions with other species or be present and emitted at such low quantities as to make regulation potentially unfavorable, though as shown is Figure 1.8, these species have also increased in the atmosphere recently. However, short-lived GHGs such as methane and black carbon are getting more attention as their mitigation would show climate benefits much sooner (Shindell et al., 2012). Water vapor in the atmosphere has a short lifetime, on the order of a week, and though it is responsible for much of Earth's greenhouse effect, it is treated as a feedback of other climate forcing. Humans are not emitting H_2O in a significant way. As temperature increases more water can be added to the air, but as temperature decreases the reverse situation is true.

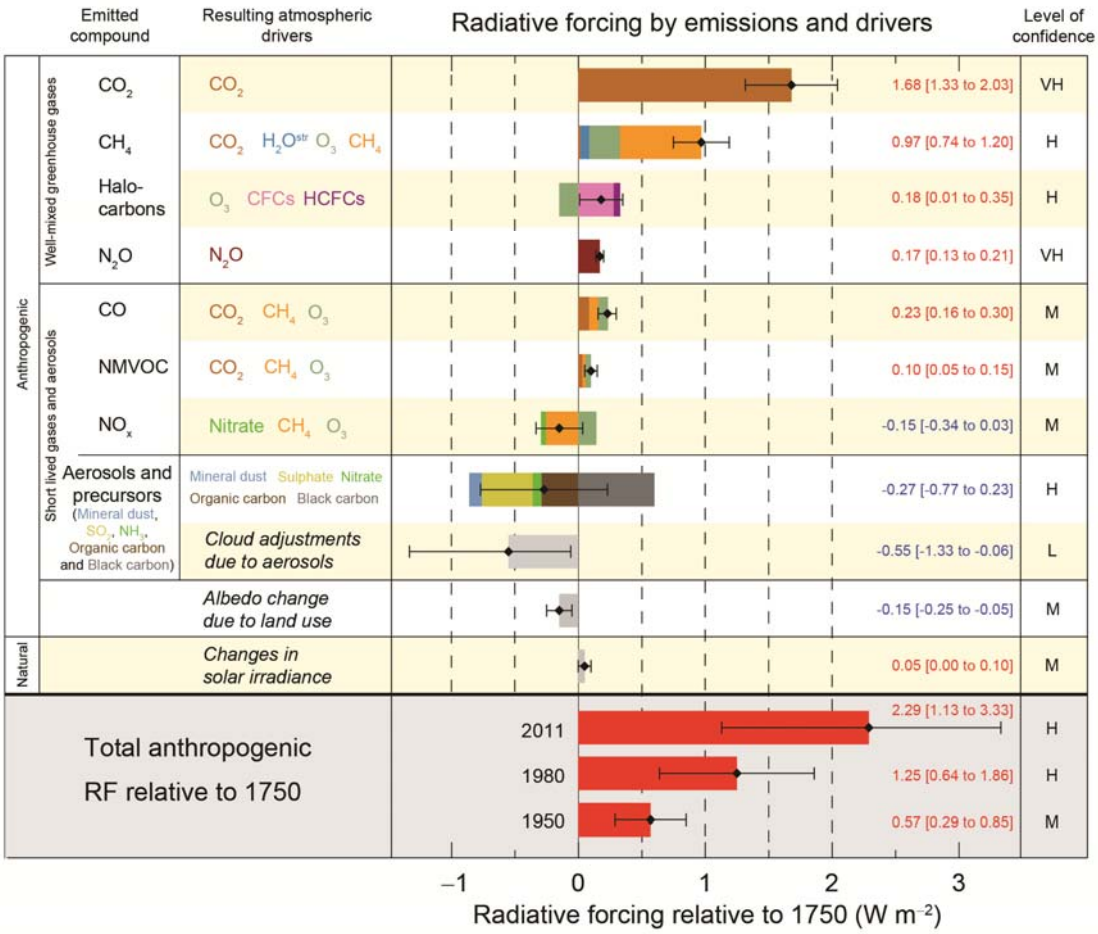

Figure 1.9. Radiative forcing of various components. Figure from the IPCC 2013 report.

Carbon dioxide has a variable lifetime in the atmosphere due to its removal mechanisms (Eby et al., 2009; Joos et al., 2013). While other gases will react until they are deposited out of the atmosphere, carbon dioxide's environmental lifetime is dictated by the carbon cycle, shown in Figure 1.10. Carbon dioxide is emitted into the atmosphere by fossil fuel combustion, respiration from vegetation, decay of organic matter, the ocean and volcanoes. Carbon dioxide is then absorbed by vegetation, the ocean and a small portion dissolves in rain water and is rained out. Many of these fluxes are assumed to be in balance, i.e. the ocean emits and then absorbs the same amount of CO_2 and mature

forests uptake the same amount of CO_2 during the growing season that they emit later through respiration and decomposition. However, in the ocean CO_2 dissolved to form carbonic acid, shown in Figure 1.11, which is used in photosynthesis by ocean life. Decaying phytoplankton sink to the ocean floor as sediment (Smetacek, 1999). This removal of CO_2 allows the ocean to be a net sink of carbon, and accounts for the very long environmental lifetime (~3000 yrs) (Eby et al.,2009). Vegetation that is re-growing, such as areas of former cropland that are now reforesting in the Northeast and Midwest United States, is also a net sink of carbon. Areas of regrowth may occur due to decreased timber demand or land-use change, such as the shift of agriculture land from the Northeast to the Midwest plains (Caspersen et al., 2000; Parks et al., 2000). Additionally, carbon fertilization experiments such as those done in Duke Forest, NC have shown that increased CO_2 levels can increase uptake even in mature forest stands leading them to be a net sink of carbon (Herrick et al., 1999; Luo et al., 2001; Oren et al., 2001; Hamilton et al., 2002; Schafer et al., 2003; Schlesinger et al., 2006; McCarthy et al., 2007). Nitrogen availability is an additional constraint on forest CO_2 uptake, which is affected by anthropogenic activities (Magnani et al., 2007). The combined effect of the ocean and vegetation sink has removed about half of the anthropogenically emitted CO_2, even as annual anthropogenic emission rates have increased by about 0.1 Pg C per year (Ballantyne et al., 2012).

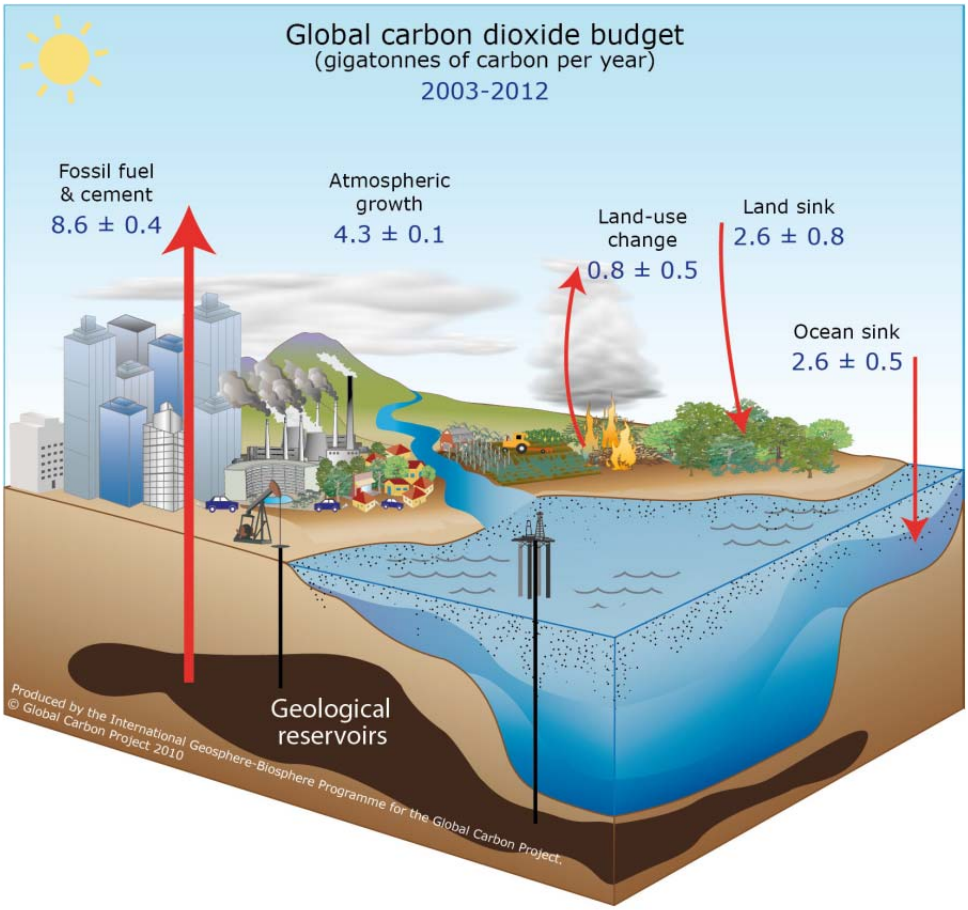

Figure 1.10. The carbon cycle. Figure from Le Quéré et al., (2014).

a $CO_2 + H_2O \rightleftharpoons H_2CO_3$

b $H_2CO_3 + H_2O \rightleftharpoons H_3O^+ + HCO_3^-$

c $HCO_3^- + H_2O \rightleftharpoons H_3O^+ + CO_3^{2-}$

Figure 1.11 Reaction scheme of CO_2 dissolving into water.

Shown in Figure 1.10 is the release of carbon from geological reservoirs and the main component of anthropogenic carbon emissions. Fossil fuel combustion releases carbon into the atmosphere that was previously stored in the earth. This carbon was initially part of the biogenic carbon cycle millions of years ago. The majority of fossil fuel carbon molecules were part of the biogenic cycle during the Carboniferous Period of the Paleozoic Era (~360-286 B.C.E) (Berner, 2003). During this period there were large prehistoric forests and swamps. Decaying organic matter from these areas sank to the bottom of swaps and oceans and formed peat, partially oxidized organic material (Berner, 2003). Cellulose is preferentially decomposed by microorganisms while complex biopolymers, such as lignin, the main component of cell walls, remain (Hatcher and Clifford, 1997). As sediment deposits over the peat, water becomes forced out. This caused a reducing environment where carbon underwent reactions to produce kerogen at pressures and temperatures that do not permit pyrolysis (below 100 bar and 50 °C) (Schobert, 2013). An example chemical scheme of a lignin monomer reduction to kerogen is presented in Figure 1.12.

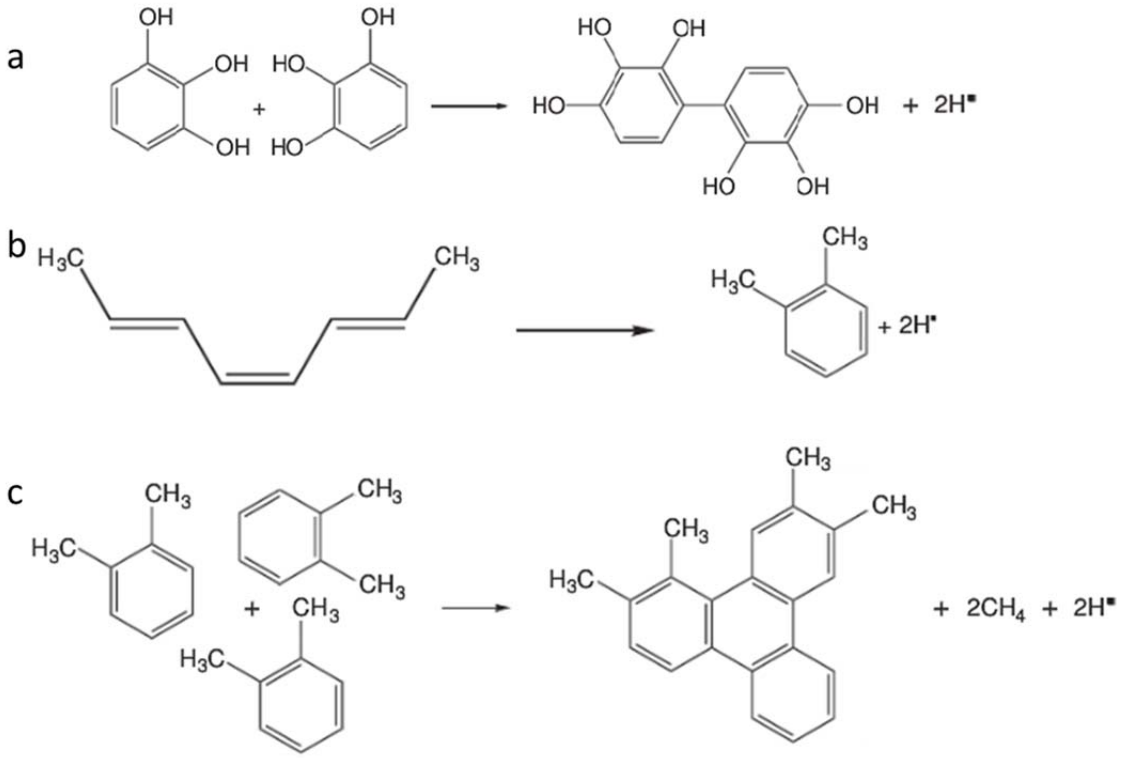

Figure 1.12 Initial reactions of lignin monomers to form kerogen including (a) self-condensation, (b) ring formation and (c) aromatization (Schobert, 2013).

This material, shown in Figure 1.13, can then undergo natural pyrolysis to form coal, petroleum and natural gas. However, kerogen itself may be targeted by fossil fuel production activities as low levels of heat (50 -150 °C) can produce oil that can be recovered. Catagenesis, a type of pyrolysis, occurs above 60 °C where thermal decomposition drives radical reactions that produce smaller hydrocarbon segments while preserving the aromatic structures typical of coal deposits (Retcofsky, 1977). Catagenesis differs from traditional definitions of pyrolysis, reactions at temperatures >350 °C in the absence of oxygen, because catagenesis occurs over long time scales where reactions can occur at lower temperatures (Schobert, 2013). Because kerogen from lignin is naturally C

rich (H/C ratio <1) it promotes coal formation. Coal is formed when temperature and pressure cause carbon bonds to form and dehydroxylation to occur, gradually decreasing the H/C ratio (Hatcher and Clifford, 1997). Temperature increases 10-30 °C/km below the surface due to heat produced from radioactive decay of ^{40}K, ^{232}Th, ^{235}U, and ^{238}U (Schobert, 2013).

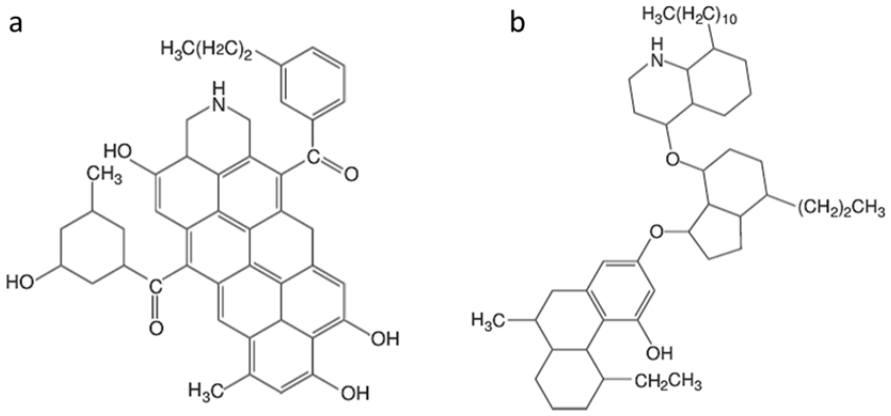

Figure 1.13 Typical chemical structure of kerogen formed from (a) C-rich lignin and (b) H-rich algal biopolymers (from Schobert, 2013).

Biopolymers from algal and plankton deposits are naturally H-rich with a H/C ration of ~1.7 and promote oil and natural gas formation (Schobert, 2013). Additionally, these deposits typically form deeper than coal deposits where pressure and temperature are higher. Temperatures of 60-170 °C degrees produce oil, while temperatures of 170-225 °C produce natural gas (Schobert, 2013). Typically pyrolysis, also called thermal cracking, starts with large molecules (16-40 carbons) and initial radicals are formed. Radicals will continue to combine and break apart until termination reactions (the reaction of two radicals) occur or until the smallest unit (CH_4) is made. Figure 1.14

shows typical radical (a) initiation, (b) propagation and (c) termination reaction. Because oil and natural gas are mobile and are formed under high pressure, they can migrate into surrounding rock. However, the surrounding rock must be porous, such as shale for the liquids and gases to move. Eventually the migration is stopped by a layer of impermeable rock. The natural undulation of impermeable rock traps liquids and gases in anticlines (Schobert, 2013).

a $C_{30}H_{62} + \text{heat} \rightarrow \bullet C_{29}H_{59} + \bullet CH_3$

b $R{-}CH_2{-}CH_2{-}CH{=}CH_2 + R' \rightarrow R{-}CH_2{-}CH\bullet{-}CH{=}CH_2 + R'H$

c $2R{-}CH_2{-}CH_2{-}CH_2\bullet \rightarrow R{-}CH_2{-}CH_2{-}CH_3 + R{-}CH_2{-}CH{=}CH_2$
$C_7H_{16} \rightarrow 4CH_4 + 3C$
$C_7H_{16} + 12H \rightarrow 7CH_4$

Figure 1.14 Typical radical (a) initiation, (b) propagation (c) termination for thermal cracking to produce oil and natural gas (from Schobert, 2013).

In addition to this thermogenic production of fossil fuels, methane can be produced biogenically by bacteria (Schobert, 2013). In particular, methanogenic bacteria in shallow organic rich (coal) sediments can produce methane when exposed to water. This is the source of coal-bed methane. Because bacteria produce only methane, coal-bed methane tends to be a very pure methane source (Schobert, 2013). Figure 1.15 shows a schematic of the location of the fossil fuels.

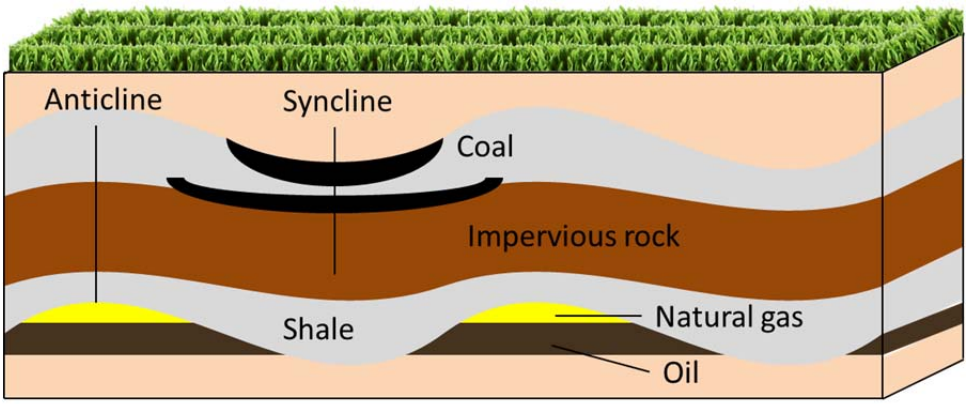

Figure 1.15 Location of fossil fuel deposits.

The ability of the biosphere and hydrosphere to absorb anthropogenic emissions has greatly reduced the climate impact of anthropogenic activities. Between 2003 and 2012, an average of about 8.6 Pg of carbon (PgC) was released each year from fossil fuel activities and about 0.8 PgC was also emitted from deforestation activities and land use change. About 55% of these emissions were removed from the atmosphere (Le Quéré et al., 2013; Ballantyne et al., 2012). The oceans uptake about 2.6 Pg C with the biosphere absorbing another 2.6 Pg C (Le Quéré et al., 2013). As shown in Figure 1.16, it is clearly known that total emissions are greater than uptake causing CO_2 to build up in the atmosphere, with an atmospheric accumulation rate of 4.3 Pg C per year (Keeling et al., 1976).

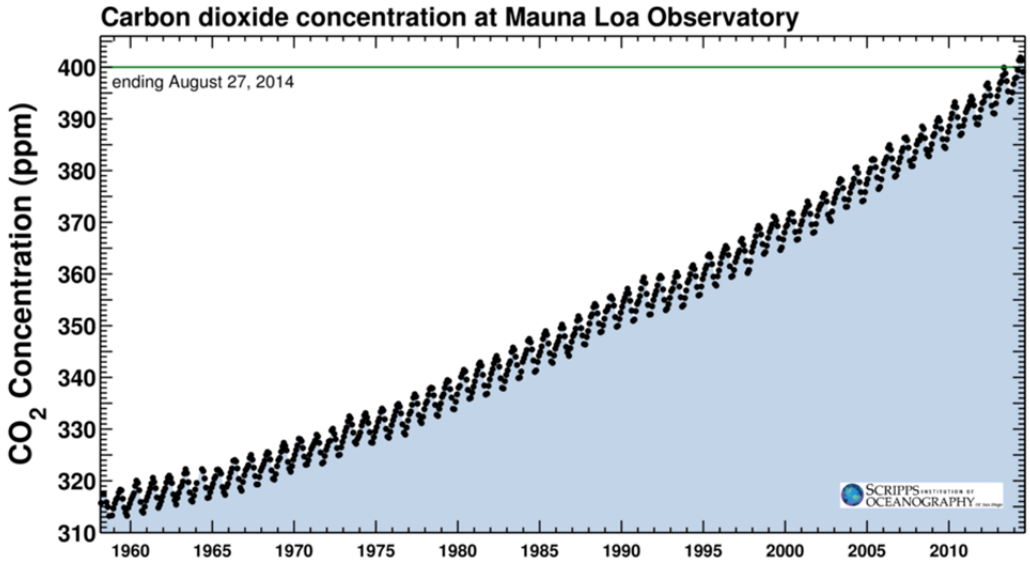

Figure 1.16 The atmospheric CO_2 record at Mauna Loa Observatory showing a steady increase. Figure from C. D. Keeling scripps.ucsd.edu/programs/keelingcurve/.

The magnitudes of the most current carbon cycle sinks and emissions are summarized in Table 1.2 and show an increase relative to the numbers for the 2003-2012 average reported in Figure 1.10 for all sectors except the land sink. However, the percent of carbon removed from the atmosphere by biological processes has remained relatively constant (Ballantyne et al., 2012; Le Quéré et al., 2014). The consistency of this sink in the presence of increasing anthropogenic emissions suggests that these mechanisms represent negative feedbacks to carbon emissions where increased atmospheric CO_2 concentration causes increased CO_2 biogenic and hydrologic uptake. The mechanisms that cause the negative feedbacks likely have physical limitations meaning they cannot sustain their level of carbon removal indefinitely and there is some evidence to suggest these limits are already being reached (Raupach et al., 2013). For instance, as the ocean absorbs more CO_2 they become more acidic as shown in Figure 1.11. Acidic ocean

conditions could kill organism that would normally fix dissolved CO_2 into other forms or start to dissolve carbon sediment (Feely et al., 2009). This would diminish the capacity of the ocean to uptake an increasing rate of CO_2 input. Likewise, CO_2 fertilization of vegetation will likely increase carbon uptake only while photosynthesis is limited by carbon availability, though there are other complex interactions, including nitrogen availability, that would affect when this limit is reached (Sage et al., 2008). In plants CO_2 is fixed by the enzyme RuBisCO. RuBisCO will increase its reaction rate with increasing CO_2 concentration until it reaches its maximum reaction rate (V_{max}), after which the photosynthetic reaction becomes independent of CO_2 concentration and becomes dependent on other factors, such as light availability for electron transport (Sage et al., 2008). There has been increasing interest in determining the nature of these significant carbon sinks and what their limitations may be.

Table 1.2 Magnitude and uncertainty of important emissions and sinks in the carbon cycle as of 2012 from Le Quéré et al., 2014.

Source	Magnitude (Pg C)	Standard deviation
Fossil Fuel/Cement Emissions	9.7	0.05
Land Use Change	1.0	0.05
Total Anthropogenic	**10.7**	0.10
Land Uptake	- 2.7	0.9
Ocean Uptake	-2.9	0.5
Atmospheric Accumulation	**5.1**	0.2

One example of this investigation is the use of modelling to determine the location of the carbon sinks. Inverse modeling of CO_2 transport, from what were primarily ground observations, was used to determine where the biosphere and

hydrosphere were absorbing the emitted CO_2. Inverse modeling uses traditional forward models of the state of the atmosphere and projects them back in time to discern where the observations come from based on initial guesses or 'priors' (Jacob, 2007). The large South American tropical rainforest was suspected to be the source of much of the biosphere CO_2 uptake, however, early model results concluded that the strongest CO_2 sink must be in the Northern hemisphere (Tans et al., 1990; Fan et al., 1998; Ciais et al., 2000; Peylin et al., 2002; Gurney et al., 2002; Gurney et al., 2004). Much work has been done to quantify carbon fluxes in northern forests to see if observed fluxes would match the model outputs (Friedlingstein et al., 1995; Myneni et al., 1997; Schimel et al., 2000; Pacala et al., 2001; Barford et al., 2001, Peters et al. 2007). However, after analyzing aircraft data to characterize the vertical structure of CO_2 in the atmosphere, it was revealed that original models did not have correct vertical mixing rates and a corrected model instead predicted a large tropical land sink (Stephens et al., 2007; Parazoo et al. 2014). While tropical forests are indeed the largest forest gross CO_2 sink, due to lack of observational data, the influence of rapid land use change in the Amazon and biomass burning, it is unclear whether the area is a net CO_2 sink or source (Grace et al., 2014; Pan et al., 2014). Northern Hemisphere boreal and temperate forests uptake about 1.2 Pg C per year, or nearly half of the forest total. (Pan et al., 2014).

Global earth system models have since been used to predict climatic changes. However, intercomparison of these models has shown wide variability in their outputs with a significant portion caused by differences in their carbon cycle assumptions (Friedlingstein et al., 2006; Knutti and Sedlacek, 2013; Friedlingstein et al., 2014). In an effort to more accurately understand and model the biosphere, more specific carbon cycle

models have been developed that include detailed variables such as soil type, soil moisture and plant functional type. Models may attempt to replicate biogeochemical interactions of these variables or relate input variables in empirical relationships that do not have any inherent physical basis. Often models will use elements of both these approaches due to lack of available data for physical processes, or ease of computation using empirical relationships. Many initial models simulated forest activity as a whole neglecting possible heterogeneity in the forest in so called 'big-leaf' models, which focused primarily on photosynthesis and drivers at the leaf scale including CO_2 concentration, available soil moisture and specific leaf traits for different plant types (Moorcroft, 2006). Increasingly, models have been updated to include in-situ data, particularly flux data from tower sites to test and optimize their performance (Raupach et al., 2005). One of the most sophisticated recent models is the Ecosystem Demography model, which simulates individual plant level fluxes and can incorporate in situ measurements of carbon fluxes, plant species heterogeneity as well as satellite data (Medvigy et al., 2009). Though there has been huge progress made in model complexity and computational efficiency, models continue to suffer from the lack of data for pertinent ecosystem drivers and often use in situ data at very small spatial scales (1m-1km) to represent much bigger regions.

1.5 Anthropogenic and Biogenic Greenhouse Gas Emissions

Anthropogenic CO_2 emissions have increased from fossil fuel use and land use change practices, such as deforestation, that promote carbon emission (Friedlingstein, 2010). As of 2012, the global carbon emissions from these sources equals around 9.7 Pg

C with the fossil fuel portion continuing to grow while the land use change component has remained constant since 2000 (Le Quéré et al., 2014). The U.S. emitted 1.5 Pg C in 2012, roughly 15% of the global emissions while accounting for only 4.5% of the global population (EIA, 2013b). U.S. emissions had been fairly steady, but dropped slightly in 2008 due to the global economic recession and have since slightly decreased due to reduced CO_2 emissions from coal energy production and more efficient vehicles and energy generators (EIA, 2014). The majority of these emissions come from electricity generation and transportation (EIA, 2013b). As discussed in the previous section, natural sinks remove roughly half of the anthropogenic CO_2 emissions. The net effect of the anthropogenic emissions has raised the global CO_2 concentration from the pre-industrial revolution (~1750) concentration of ~280 ppm to the current level of 400 ppm (IPCC, 2013).

In the U.S., CO_2 emissions from transportation are expected to decline as consumers keep their cars longer and regulations for emissions and fuel efficiency become stricter or new regulations are introduced (EIA, 2014). In addition, electrical generation is expected to continue its current trend to produce less CO_2 per kWh due to increased use of renewable energy and natural gas power plants (EIA, 2014). Recent low natural gas prices, shown in Figure 1.17, contributes to an increasing share of natural gas-based electricity generation (EIA, 2014). More carbon-efficient energy generation coupled with slowly increasing energy demand in the U.S. should cause U.S. CO_2 emissions from energy sectors to remain constant at their current levels or potentially decrease (EIA, 2014). In the U.S., oil and natural gas production will increasingly depend on extraction from tight and shale formations (EIA, 2014). Globally, energy demand is

increasing in developing countries such as India and China (EIA, 2013a). These countries also have access to less efficient energy producing technology, largely coal-fired power plants, leading to large increases in global CO_2 emissions from energy production. Coal is expected to be the fastest growing source of fossil fuel globally, though natural gas from shale and tight formations in China and Canada will also grow (EIA, 2013a). Global CO_2 emissions from the transportation sector are also expected to increase due to increasing use by developing countries (EIA, 2013a).

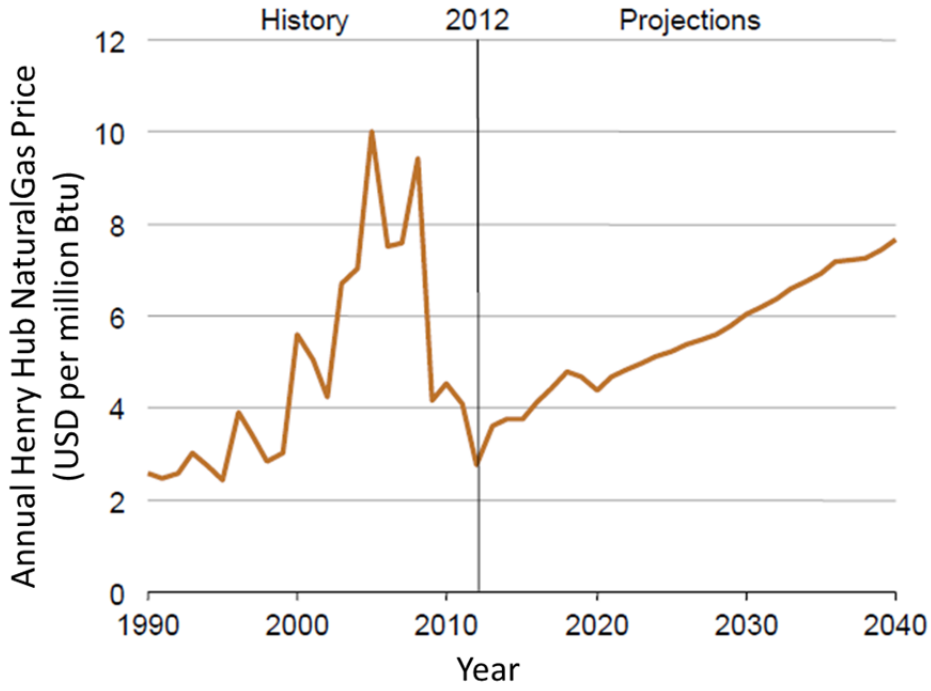

Figure 1.17. U.S. Natural Gas prices at the Henry Hub. Figure from EIA 2014.

The U.S. emits about 27 Tg CH_4 annually (EPA, 2013). Using the global warming potential range in Table 1.1 this equates to about 760-920 Tg CO_2 equivalent (or 210-250 Tg C) of methane annually. Globally, around 333 Tg of CH_4 from anthropogenic sources

are emitted annually, with about 29% of these emissions coming from fossil fuels (Kirschke et al., 2013). Of the U.S. methane emissions, the single largest source (7 Tg CH_4) comes from enteric fermentation, the digestive process of some animal ruminants that produce methane (EPA, 2013). For the energy sectors, 6 Tg CH_4 come from natural gas systems, 2.5 Tg CH_4 from coal mining and petroleum systems contribute 1.5 Tg CH_4 (EPA, 2013). Combined, energy sector emissions account for 37% of the U.S. annual methane emissions (EPA, 2013). Other important U.S. methane sources are landfills, contributing 5 Tg CH_4, and manure management of livestock, contributing 2.5 Tg CH_4. Increasing energy demand will increase anthropogenic CH_4 emissions in the U.S. and globally particularly due to the increased use of natural gas (EPA, 2013).

The global methane budget is also affected by natural sources and sinks. Globally about 218-347 Tg CH_4 are emitted each year from natural sources, with wetlands contributing the majority of these emissions (Kirschke et al., 2013). The predominant sink of methane is the reaction with the hydroxyl radical, which removes 528 Tg CH_4 annually, with the total methane sink expected to be 540-632 Tg CH_4 per year, roughly equivalent to the source strength (Kirschke et al., 2013). Thus nearly all of the emitted CH_4 is removed, with an imbalance of around 27 Tg CH_4 per year that remains in the atmosphere (Kirschke et al., 2013). The imbalance explains the increasing atmospheric CH_4 concentrations from ~720 ppb in 1750 to the current level of ~1800 ppb, though the yearly imbalance changes and causes periods of faster and slower CH_4 accumulation (IPCC, 2013).

Unlike the negative feedbacks to increasing CO_2 emissions previously described, CH_4 emissions may have positive feedbacks to climate change. The largest natural source

is wetlands, and rising temperatures may uncover wetlands and soil in high northern latitude regions that usually remain frozen, or increase wetland CH_4 production (O'Connor et al., 2010). This area is already assumed to have released 3.7 Pg C since 1970 into the atmosphere in the form of both CH_4 and CO_2, due to the thaw of soils that allow organic compounds to decompose (Hayes et al., 2014). In addition, there is an estimated reservoir of ~1360 Pg CH_4 in the top 3m of the Artic that is currently trapped due to the permafrost, a subsurface region of the Artic that remains frozen through the entire year and an additional ~2100 Pg CH_4 locked in methane hydrates in the arctic seabed (O'Connor et al., 2010; Isaksen et al., 2011). Recently, large methane emissions ranging from 2 mg CH_4 d^{-1} m^{-2} to 14 mg CH_4 d^{-1} m^{-2} from areas in the Arctic Ocean have been reported (Shakhova et al., 2010; Kort et al., 2012).

1.6 Research Objectives

The research described in this thesis will address the challenges to accurately quantify and fully apply uncertainty analysis to GHG fluxes, specifically CO_2 and CH_4, from anthropogenic and biogenic arenas. An aircraft platform was used to investigate and quantify fluxes from and to the surface, some of which had not been previously sampled in situ. The aircraft platform enables valuable access to individual sites that would be difficult to access from the ground and the ability to investigate large areas at scales that are difficult to obtain using ground or satellite instrumentation. Specifically, CH_4 emissions from a Pennsylvania shale gas field, as well as emissions from individual or grouped shale gas well pads, were quantified and compared to estimated emission rates from bottom-up estimates. Additionally, the efficiency of flaring of associated natural gas

on oil well pads in North Dakota was investigated by measuring emission factors for CH_4 from associated gas flares. Finally, fluxes of CO_2 and heat were measured via the eddy covariance method over three east coast forest sites: Harvard Forest, MA; Howland Forest, ME; and Duke Forest, NC. This work was part of a NASA-funded effort to understand the impact of soil moisture on carbon fluxes to improve model estimates of carbon exchange in North America. The robustness of the meteorological techniques used are evaluated and the magnitude and relative importance of the quantified GHG fluxes are discussed. Potential improvements in data acquisition and data analysis will be discussed in the conclusions.

CHAPTER 2. METHANE EMISSION FLUXES FROM SHALE GAS PRODUCTION IN PENNSYLVANIA

2.1 Motivation for Research

The advent of horizontal drilling combined with hydraulic fracturing has allowed unprecedented access to fossil fuel reservoirs in unconventional geographic formations, as shown in Figure 2.1. Hydraulic fracturing or 'fracking' is the process by which high pressure fluid (water mixed with chemicals and sand) is used to extract fossil fuels from shale and other porous rock formations. The fracking process begins with a traditional vertical well-bore drilled many 1000s of feet deep (Crawford, 2013). Once the shale formation is reached the well bore is turned horizontally and follows the shallow shale seam for up to a few miles. Explosive changed are set off in the shale (Crawford, 2013). Then high pressure fluid is pushed well-bores so that fissures are formed perpendicular to the well-bore (Crawford, 2013). The sand, called a proppant, in the fracking fluid keeps the fissures open after the water returns up the well-bore in a process called flowback (Crawford, 2013). The natural gas trapped in impermeable rock formation can then diffuse into the openings and up the well-bore (Crawford, 2013). Natural gas production from shale rock formation has increased natural gas production in the U.S., leading to a natural gas 'boom' with shale natural gas production expected to account for about half of all U.S. produced natural gas by 2040 (EIA, 2014). Currently the U.S. is the only country to employ wide-scale production of shale derived natural gas, but many countries

contain significant shale natural gas resources that could be tapped in the future (EIA, 2013a).

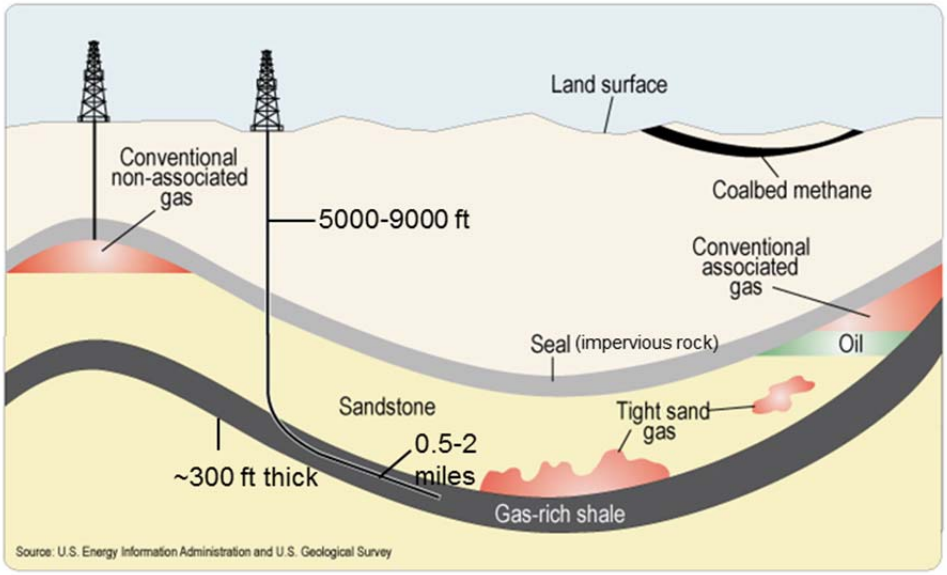

Figure 2.1 Geological formations that contain natural gas (Figure from USGS, 2002).

'Fracking' was first pioneered in the 1860s in Pennsylvania to extract valuable fossil fuels more easily (MacRae, 2012). Original methods used an explosive detonated at the base of the well shaft. Non-explosive fracking methods were developed in the 1930s and hydraulic fracturing was commercially used by 1949 (MacRae, 2012). Early hydraulic fracturing also directed pressure only to the base of a vertical well shaft and used about 750 gallons of fluid and 400 lbs. of sand (MacRae, 2012). Current fracking practices were used beginning in the 1980s and by about 2003 this practice had widespread use across shale fields in many states (Crawford, 2013). Because the well shafts being drilled are much longer due to horizontally following the shale seams for up

to 2 miles, current fracking practices use around 8 million gallons of water and 35 to 160 tons of sand (MacRae, 2012).

The full natural gas lifecycle process starts with production of natural gas from wells on well pads. Well pads can host multiple wells and may have additional equipment for flaring or compressing on them. From individual well pads raw gas will be separated to produce and store heavier hydrocarbons and more pure natural gas (EIA, 2008). Excess natural gas that cannot be stored will be flares (EIA, 2008). Natural gas is usually transported via long interstate pipelines (EIA, 2008). The gas will then go to a gas processing plat for further refinements and storage (EIA, 2008). Compressor stations will be used to compress gas for transport to direct consumers or natural gas companies (EIA, 2008). The lifecycle of natural gas is shown in Figure 2.2. Step 1 and 2 are known as production, steps 3-6 as transmission and steps 7-8 as distribution.

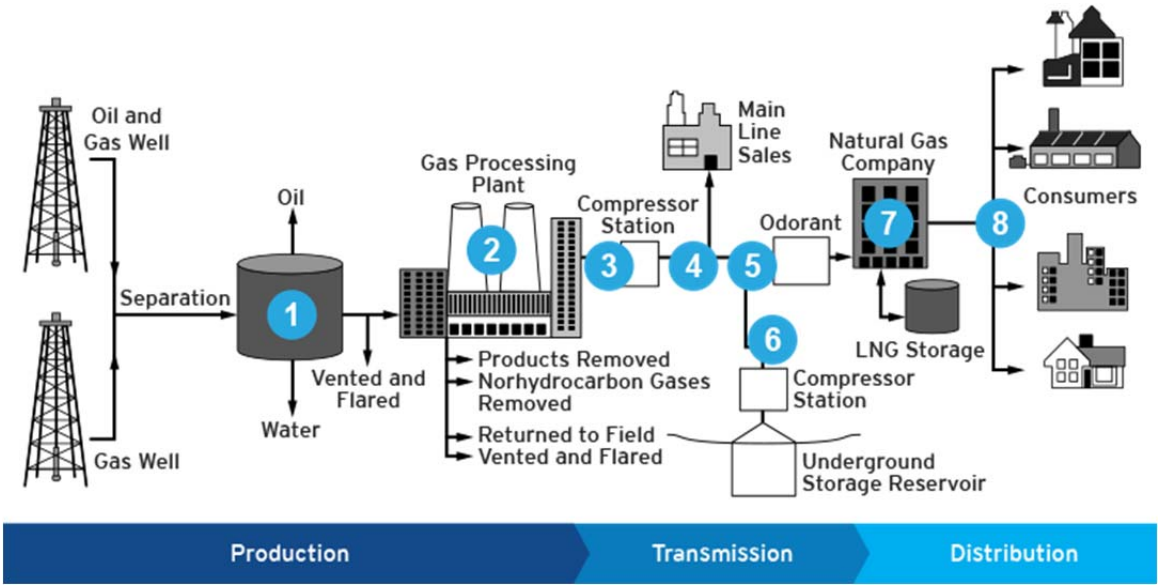

Figure 2.2 The natural gas production cycle (from www2.dteenergy.com/wps/wcm/connect/5c7b1f11-f813-4937-be53-b900bf0957c2/naturalgas_processing_delivery.png?MOD=AJPERES&CACHEID=5c7b1f11-f813-4937-be53-b900bf0957c2).

As natural gas becomes an abundant and inexpensive source of energy, companies have taken advantage of this resource and natural gas power plants and generating capacity have risen and are expected to rise as shown in Figure 2.3 (EIA, 2014a). One touted advantage of natural gas power plants is their lower direct CO_2 emission per unit energy production compared to coal power plants due to the lower carbon intensity of methane for electricity generation (Stephenson et al., 2012). Natural gas emits about ~180 g CO_2 per kWh while coal emits ~330 g CO_2 per kWh (EIA, 2014a). Recent regulations by the EPA to cut CO_2 emissions from coal-fire power plants allow the use of renewable-energy and natural gas power plants as alternatives to implementing carbon capture storage (CCS) technology at existing coal power plants, which will likely drive a

further increase in natural gas power plants in many areas (Clark and Herzog et al., 2014; Office of the Federal Registrar, 2014). As our energy generating economy relies more on natural gas there has been growing interest in discovering the total GHG 'footprint' of natural gas production to identify what changes in total GHG emissions may occur (Howarth et al., 2011; Hultman et al., 2011; Jiang et al., 2011; Stephenson et al., 2011; NETL, 2011; Venkatesh et al., 2011; Burnham et al., 2012; Weber and Clavin 2012). Despite the lower direct CO_2 emission per unit energy produced by natural gas power plants, significant amounts of methane, the main component of natural gas with a GWP of 36-38 times higher than CO_2, may be released during production, processing and transportation of natural gas (IPCC, 2013). If the amount of CH_4 leaked is significant it may present equivalent GHG emissions, or even a total GHG emission increase, relative to 'normal' coal energy production GHG emissions. According to Alvarez et al. (2012) the tradeoff point occurs at a nominal natural gas leak rate of 3.2% of a natural gas wells lifetime production, e.g. if natural gas wells emits more than 3.2% of its natural gas production over its production lifetime, the total GHG emission from natural gas energy production will be greater than the GHG emissions from coal energy production on a time horizon of 100 years.

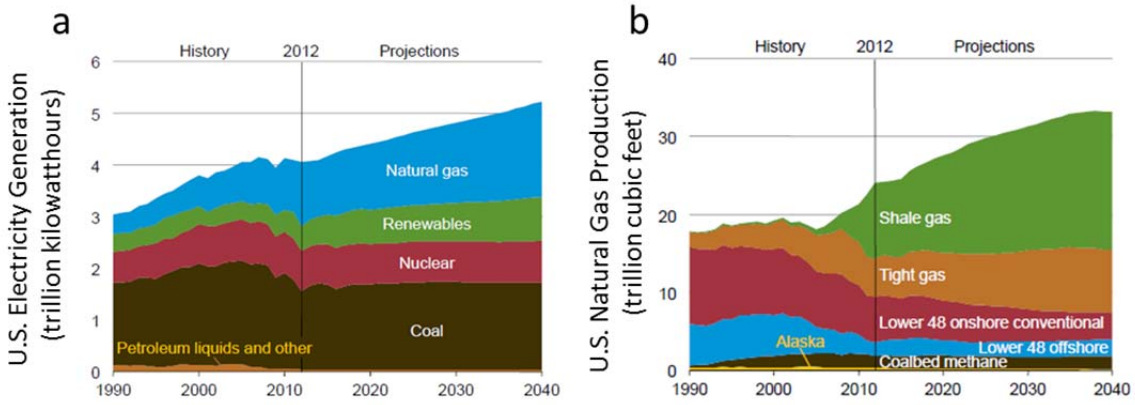

Figure 2.3 (a) U.S. electricity generation by fuel type and (b) U.S. production of natural gas (EIA, 2014a).

The large number of natural gas wells (~480,000 in the U.S. in 2012) drilled by a number of different operators and the range of components that can leak makes leaks difficult to identify and quantify (EIA, 2014c). Many current studies have used bottom-up emission factors (EF), the ratio of an emission of a pollutant to a source emission, typically from non-peer-reviewed data sources such as government or industry organizations that measure emissions from individual sources. The individual sources are identified, summed up and multiplied by their EFs to produce a total emission rate. Lifecycle estimates based primarily on government and industry supplied data have resulted in a wide array of total CO_2 equivalent emissions for natural gas electricity generation that are both greater and smaller than emissions from coal electricity generation (Howarth et al., 2011; Hultman et al., 2011; Jiang et al., 2011; Stephenson et al., 2011; NETL, 2011; Venkatesh et al., 2011; Burnham et al., 2012; Weber and Clavin 2012). The spread in the emissions is driven in large part by the uncertainty in so called 'fugitive emissions' or venting of natural gas directly to the atmosphere (often

unintended). The EPA 2010 greenhouse gas inventory estimates this rate as 2% of gross production. A recent bottom-up study that used emission rates calculated from natural gas sites to which the investigators were given access suggested a substantially lower leak rate of 1% (Allen et al., 2013). However, recent inverse modelling attempts to constrain fugitive leak rates using observed CH_4 and hydrocarbon data combined with transport data suggests the possibility of higher leak rates up to 5% of gross natural gas production (Miller et al., 2013; Schwietzke et al., 2014). As Miller et al. (2013) show, some regions can be larger contributors to the leak rate than others. The distribution of shale formations across the U.S. is shown in Figure 2.4. Different shale plays can have substantially different geology and topography that may affect both emission rates and potential mitigation strategies for those regions.

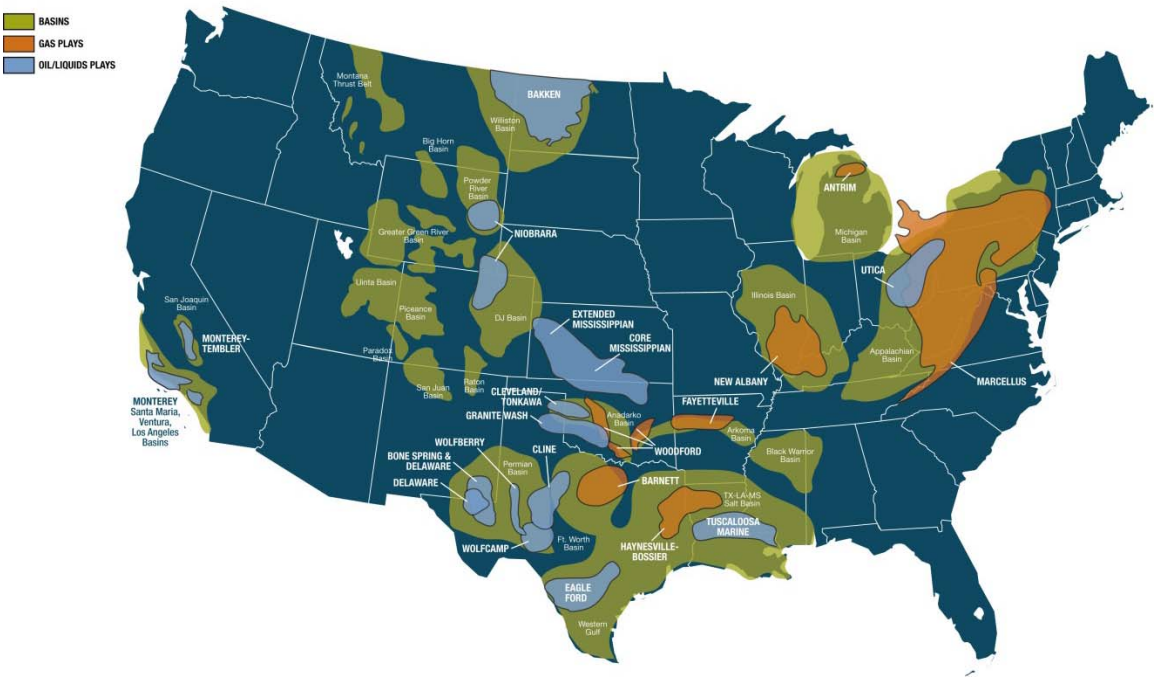

Figure 2.4 Major shale basins in the U.S (from pacwestcp.com/2012/07/pacwest-publishes-updated-shaleunconventional-play-maps/).

Bottom-up inventories are crucial because they simulate our current understanding of emissions sources, are temporally and spatially explicit and can be used by other modeling systems (such as inverse modelling). However, it is a recognizable challenge that bottom-up inventories may underestimate emissions as it is difficult to accurately assess and quantify the numerous emission sources. Top-down measurements, measurements that require no knowledge of specific source strengths or distribution, are a necessary compliment to bottom-up measurements as they provide real observational data that must reflect the actual emissions. Due to cost and time restrictions, top-down measurements tend to be snapshots of specific regions in space and time and may not provide much spatially explicit data as to the specific sources of measured emissions. In the past years many top-down studies using tower and aircraft data have produced a leak rate estimate of 2.3-17% from the Uintah, Los Angeles and Denver-Julesburg (abbreviation DJ) basins shown in Figure 2.4(Petron et al., 2012, Karion et al., 2013, Peischl et al., 2013, Petron et al., 2014). Some of these studies focus on the same geographic area where results are expected to be consistent and can thus be directly compared (e.g. Petron et al., 2012 and Petron et al., 2014). However, other study sites are separated by hundreds of miles and should be compared with caution.

2.2 Instrumentation

2.2.1 Wind and Turbulence Measurements

All instrumentation is located on-board the Airborne Laboratory for Atmospheric Research (ALAR), a modified Beechcraft Duchess twin-engine aircraft, shown in Figure

2.5. The Best Air Turbulence (BAT) Probe is a nine pressure port probe located at the nose of ALAR, also shown in Figure 2.5. The pressure data from the probe, along with the temperature data, recorded by a microbead thermistor, aircraft attitude and airspeed information can be used to calculate 3-D wind vectors that are recorded at 50Hz. An on board Global Position System (GPS) records latitude, longitude and altitude data at 50 Hz. The GPS, combined with an inertial navigation system, provides rates of rotation along with the pitch, roll and yaw of the aircraft. These are used along with the BAT probe data for wind vector calculation.

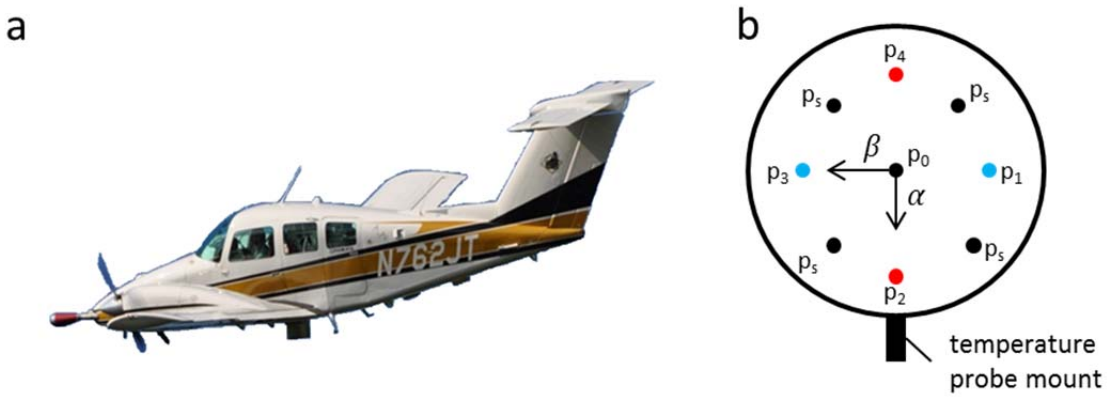

Figure 2.5 (a) Purdue's Airborne Laboratory for Atmospheric Research (ALAR). (b) A frontal view of the BAT probe showing the location of the pressure ports and temperature probe.

The BAT Probe is based on the design reported in Crawford and Dobosy (1992) and has been extensively calibrated using aircraft maneuvering and wind-tunnel tests as reported in Garman et al. (2006, 2008), and corrected for lift-induced upwash generated during flight. To calculate wind vectors, the nine pressure ports shown in Figure 2.5 (b)

are connected to 4 differential pressure sensors that record the differential pressure in the x (p_s to p_0), y (p_1 to p_3) and z (p_2 to p_4) directions as well as the static (ambient) air pressure p_s. In addition, the attack angle (α) and sideslip angle (β) are shown in figure 2.5 (b) and are used in the wind calculations. This raw data is combined with aircraft attitude and velocity data to compute wind vectors as per the equations described in Garman et al. (2008). Horizontal wind speeds are reported with a precision of ~0.4 m/s and vertical wind speeds are reported with a precision of 0.06 m/s. Wind direction precision is dependent on wind speed. However, a precision of ~1° is typical.

2.2.2 Cavity Ring-Down Spectrometer

To quantify CO_2, CH_4 and H_2O at 0.5Hz a Picarro high-precision Cavity Ring-Down Spectrometer (CRDS) is also installed on ALAR. The CRDS samples ambient air from a manifold with twin inlet ports located directly behind the BAT probe. Air is pulled through the manifold at ~1500 L/min by a commercial blower yielding a residence time ~0.1s in the manifold. The CRDS is attached to its own pump to pull sample air through the instrument at ~0.45 L/min. The CRDS houses two tunable diode lasers that emit light at 1603 nm (CO_2 absorption feature) and 1651 nm (CH_4 and H_2O absorption feature). Wavelengths are maintained to ± 10 MHz by a patented wavelength monitor system (Crosson, 2006). This system uses dual wavelength monitors so wavelength stabilization takes ~100 μs compared to previous systems that took ~100 ms. This addition allows for high-frequency data acquisition, which has been a shortcoming of other CRDS instrumentation designs (Fidric et al., 2003).

Gas flows through a 35 cm^3 cavity maintained at 140 Torr and 45° C while the lasers inject light pulses into the cavity through a partially reflecting mirror. The light reflects between two high-reflectivity mirrors enabling a long (~10 km) path length and the light is monitored by a photo-detector to detect the laser intensity decay constant or 'ring-down'. One key advantage of the CRDS technique is the measurement of ring-downs that are time dependent. This means that the measurement is entirely independent from the laser light intensity, a source of variability in other spectroscopic techniques (Berden et al., 2000). The acquisition rate of the ring-downs is 100 Hz. The data are averaged over 2s to produce the reported, high-precision data. The instrument can also be set to a fast-flux mode where data are averaged to produce 10Hz data. The detection of H_2O also allows CO_2 and CH_4 dry air mole fractions to be reported, which is done using instrument software. A block diagram of the CRDS from Crosson (2008) is shown in Figure 2.6. The residence time through the instrument is ~6 s. The response time is 2 s.

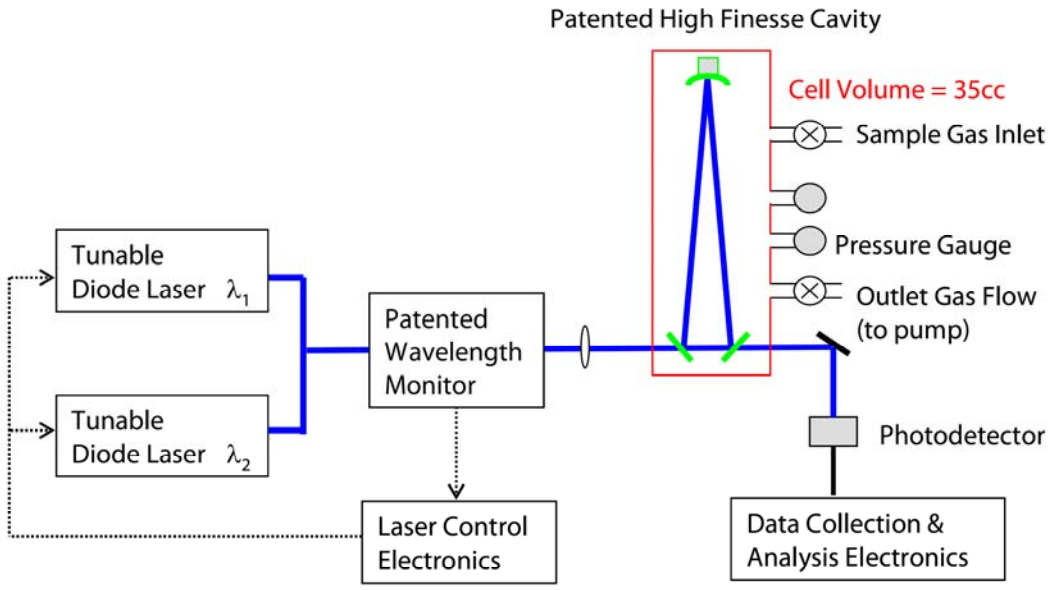

Figure 2.6 A block diagram of the Picarro CRDS. Diagram from Crosson, 2008.

As with all spectroscopic techniques, the measurement approach is derived from Beer's law, shown in Equation 2.1.

$$\frac{I}{I_0} = e^{-\sigma \cdot N \cdot L} \qquad 2.1$$

Here, I is the light intensity after it has exited a sample, I_0 is the initial light intensity, σ is the absorption cross section, N is the number density of the sample and L is the path length. The absorption cross section is specific for each molecule at each wavelength. As described in Section 1.4, each molecule has a different absorption spectrum which contributes to the total absorption spectrum of Earth's atmosphere. Absorption coefficients are determined by individual molecule size and electronic nature. Ideally spectroscopic techniques will take advantage of wavelengths that are specific to the absorption features of one molecule (Skoog et al., 1994). An additional consideration is

the effect of pressure-broadening on absorption features. Molecule collisions can cause line broadening that deviates from the expected Lorentzian line shape and thus give inaccurate results (Skoog et al., 1994). This can be counteracted by maintaining a constant pressure and temperature, as is done in the CRDS. To obtain a concentration measurement, first the decay rate of the laser intensity is monitored (Fidric et al., 2003). The decay is assumed to be exponential and the ring-down decay constant can be extracted according to Equation 2.2.

$$\frac{I}{I_0} = e^{-t/\tau} \tag{2.2}$$

Here, I is the laser intensity at time t, I_0 is the initial intensity and τ is the ring-down decay constant. The ring-down decay constant is specific to each wavelength and specific to individual cavity properties, including mirror reflectivity. The equation for τ is presented in Equation 2.3.

$$\tau = \left(\frac{1_{cav}}{c}\right) \cdot (L_{opt} + \sigma \cdot N \cdot 1_{samp})^{-1} \tag{2.3}$$

Here, 1_{cav} is the optical length of the cavity, c is the speed of light, L_{opt} is the optical loss of the empty cavity, σ is the absorption cross section at a specific wavelength, N is the sample number density and 1_{samp} is the physical length. Using the obtained ring-down constant, N can be calculated and converted into the sample concentration using the volume, pressure and temperature of the cavity.

To calibrate the CRDS, three on-board gas standards are introduced via a rotary valve system to ensure easy and efficient sampling as shown in Figure 2.7. The standards are prepared by the NOAA Earth System Resource Laboratory (ESRL). The standards contain CH_4 concentrations of 1803.05 ± 0.40, 2222.2 ± 0.3 and 2599.5 ± 1.2 ppb and

CO_2 concentrations of 378.491 ± 0.013, 408.826 ± 0.021 and 438.288 ± 0.019 ppm, respectively. Calibration plots for the whole experiment (6/18/12-6/21/12) are presented in Figure 2.8, which shows the excellent linearity and stability of the instrument as reported in Chen et al. (2010). Also shown in Figure 2.8 is the long-term stability of the slope and intercepts over a two year period. The in-flight precision (1 σ) for CO_2 and CH_4 is 0.07 ppm and 1 ppb, respectively, calculated from 30 second averages of standard gas sampling. These correspond to a relative precision (1 σ) for ambient measurements of 0.02% and 0.06% for ambient CO_2 and CH_4 concentrations of 400 ppm and 1800 ppb, respectively.

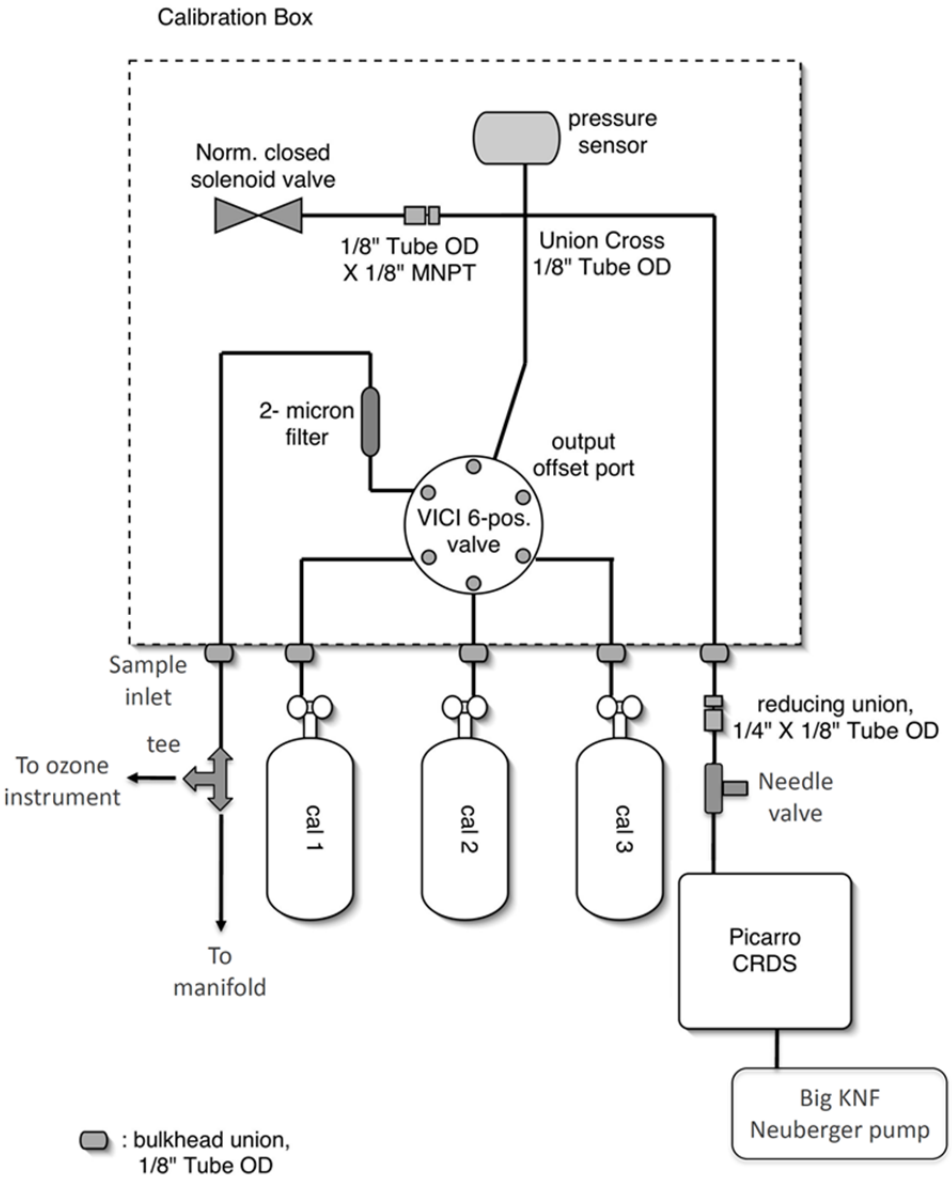

Figure 2.7 On board calibration set up for the CRDS.

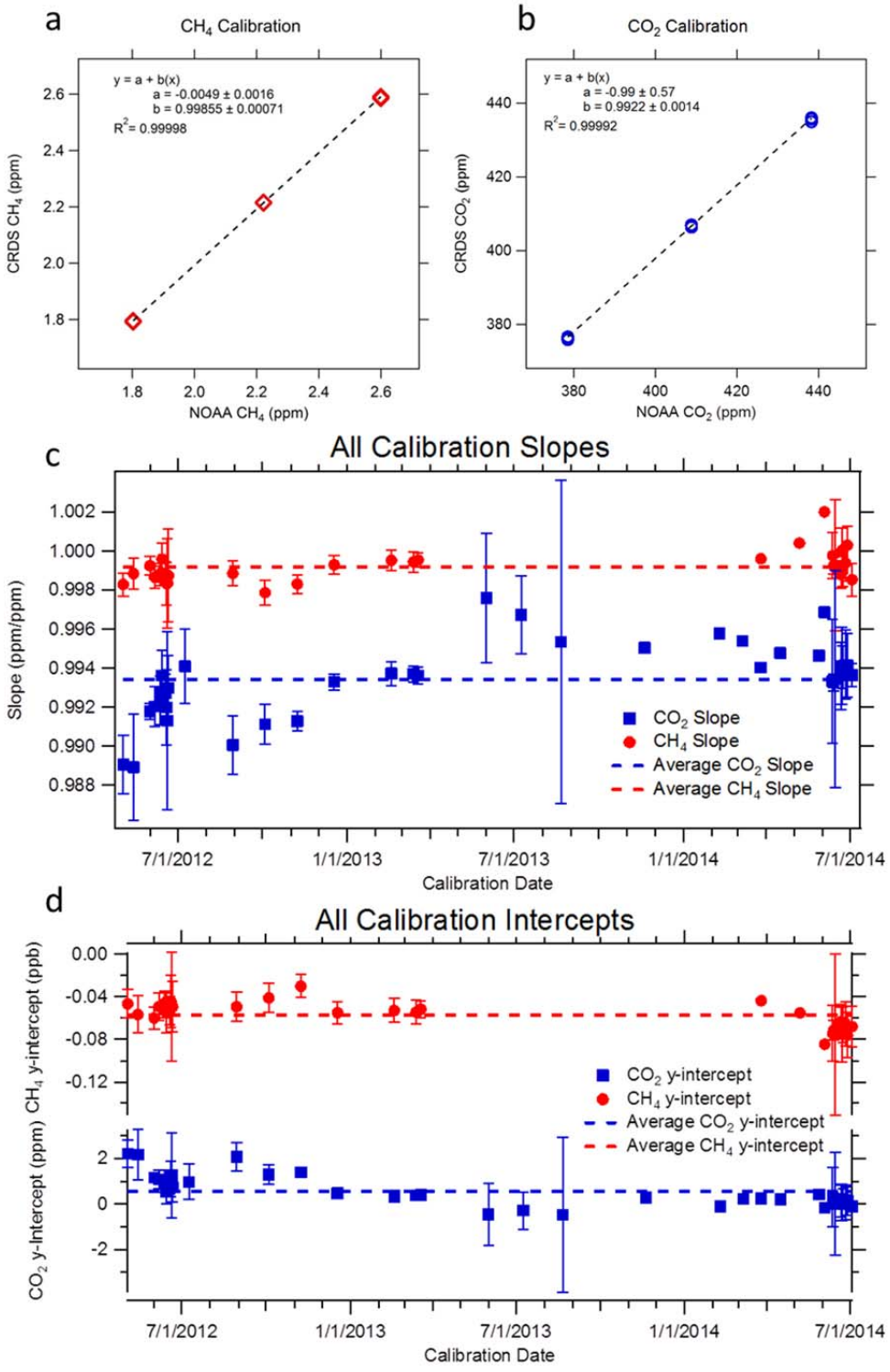

Figure 2.8 Calibration plot for (a) CH_4 and (b) CO_2 showing 45 calibration points collected over the course of the experiment (6/18/12-6/21/12). Long-stability plots of (c) the y-intercept and (d) the slope for CH_4 and CO_2 are also shown.

2.2.3 Whole Air Sampling

Also on board ALAR is a NOAA programmable flask package (PFP) for whole air sampling, shown in Figure 2.9. The PFP contains 12 700 mL glass canisters connected by two ports to a local stainless steel manifold that is connected to ALAR's sampling manifold. When activated, the PFP flushes air through the manifold and canister. Once sampling is initiated, one valve on the canister is closed and the canister is filled to 2.7 atm pressure after which the other valve is closed. The PFP is then sent to the NOAA/ESRL campus for determination of up to 55 trace gases and isotope species. Samples for methane determination are separated with a gas chromatograph with a flame-ionization detector, which reports CH_4 values with a precision of 1.2 ppb. Hydrocarbons are determined using a gas chromatograph mass spectrometer. Before injection, 200 ml aliquots are pre-concentrated using a cryogenic trap, followed by desorption of the analyte hydrocarbons at 140° C. Uncertainties for hydrocarbons concentrations are less than 5%.

Figure 2.9 NOAA PFP showing 12 glass canisters.

2.3 Flight Design

2.3.1 Site Description

This work was conducted over southwest Pennsylvania between 6/18/2012 and 6/21/2012 and primarily included Washington and Greene Counties. This area is largely rural forest and farming land, but these counties have some of the highest well densities in the state. Three flight designs were flown: investigative (I), mass-balance (MB) and regional flux (RF). Investigative flights were flown to identify possible wells of interest, mass-balance flights were used to sample downwind of identified point source(s) and regional flux flights were flown over a large region to calculate an area flux. Table 2.1 identifies types of selected flights and meteorological conditions during those flights. Additional investigative flights were flown north of Washington, PA that did not reveal any consistently emitting point sources that could be sampled using the mass-balance

approach, though this area also had high well density. One compressor station was observed releasing intermittent plumes of CH_4 up to 45 ppm, but this source did not emit a consistent plume necessary for mass-balance sampling.

Table 2.1. Meteorological conditions and time duration of each aircraft flight experiment.

Flight Type*	Flight #	Start Time (EDT)	Duration	Wind Speed (m/s)	Wind Direction
RF	1	10:00	96 min	3.0	276
RF	2	8:55	89 min	3.7	270
MB	1	11:55	30 min	3.1	236
MB	2	15:15	56 min	3.3	239
MB	3	16:00	60 min	5.5	252
MB	4	14:05	73 min	4.7	226
I	1	12:25	5 min	3.0	258
I	2	15:22	6 min	4.7	227
I	3	9:14	15 min	4.2	257

* Flights are classified into three flight types, Regional Flux (RF), Mass Balance (MB) and Investigative (I). Investigative flights were short and occurred between and during the longer RF and MB flights. Flights are identified by their flight type and flight number (e.g. RF-1, MB-3, etc.).

2.3.2 Regional Flux Flight

On two mornings (6/20/12 and 6/21/12) a wide spread CH_4 enhancement was observed south of Washington, PA. The extent of this enhancement was mapped by flying transects at ~ 250 m AGL through the plume until we detected roughly background CH_4 levels (~1.9 ppm). Figure 2.10 shows the observed CH_4 concentrations for flight RF-1 and RF-2. In addition, we performed several short vertical profiles to ascertain the boundary layer depth. As flights were flown in the morning, observed boundary layer depths were low.

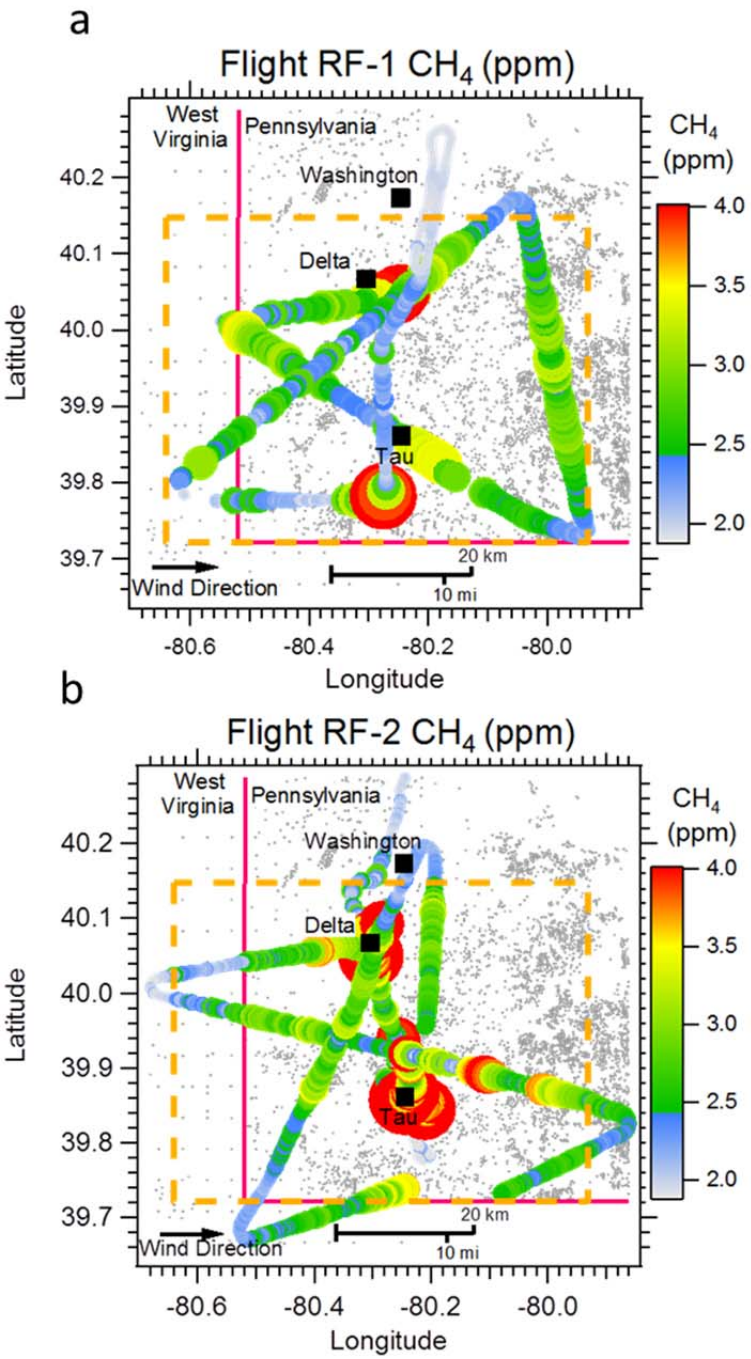

Figure 2.10 Raw transect data for (a) RF-1 and (b) RF-2 collected at ~250 m AGL. The orange box corresponds to the original sampling area (OSA).

The observed wide-spread high concentration levels likely occurred as a result of a stable nocturnal boundary layer, which trapped surface emissions near their source allowing CH_4 to accumulate. Low wind speed, and minimal turbulence keep the emissions from being dispersed, particularly in the vertical direction.

2.3.3 Mass-Balance

Mass-balance flights were flown as described in Mays et al. (2009) and Cambaliza et al. (2014). Briefly, horizontal transects are flown downwind of a source, perpendicular to the prevailing wind direction, at several heights up to the top of the boundary layer or, in this case, up to the height at which the plume was no longer observed. The observation of plumes that did not extend to the top of the boundary layer is attributed to the short downwind distance the sources were sampled (1-5 km), which was necessary to isolate sources in a region with dense potential sources. There was thus not sufficient time for complete vertical mixing. The horizontal transects are projected on to an imaginary plane and interpolated using a kriging method to extract a 2-D matrix of concentration values. The CH_4 background is then calculated from the edges of the matrix, where no upwind sources are present, and subtracted from the matrix to produce a ΔCH_4 matrix. The ΔCH_4 values are multiplied by the perpendicular wind speed and integrated over the width of the plume and height of the plume or boundary layer.

Two areas of interest were identified from investigative flights where circles were flown around potential sources. Sources were identified by observing CH_4 enhancements only on the downwind side of a potential source, as shown in Figure 2.11. Two such identified sources were designated ‘Delta’ and ‘Tau.’ In addition, a coal mine was

detected near Tau. The area around Delta was sampled three times with Delta isolated during flight MB-2. The area around Tau was sampled once during MB-4. Raw transect data is presented in Figure 2.12 for flights MB-1 through MB-4.

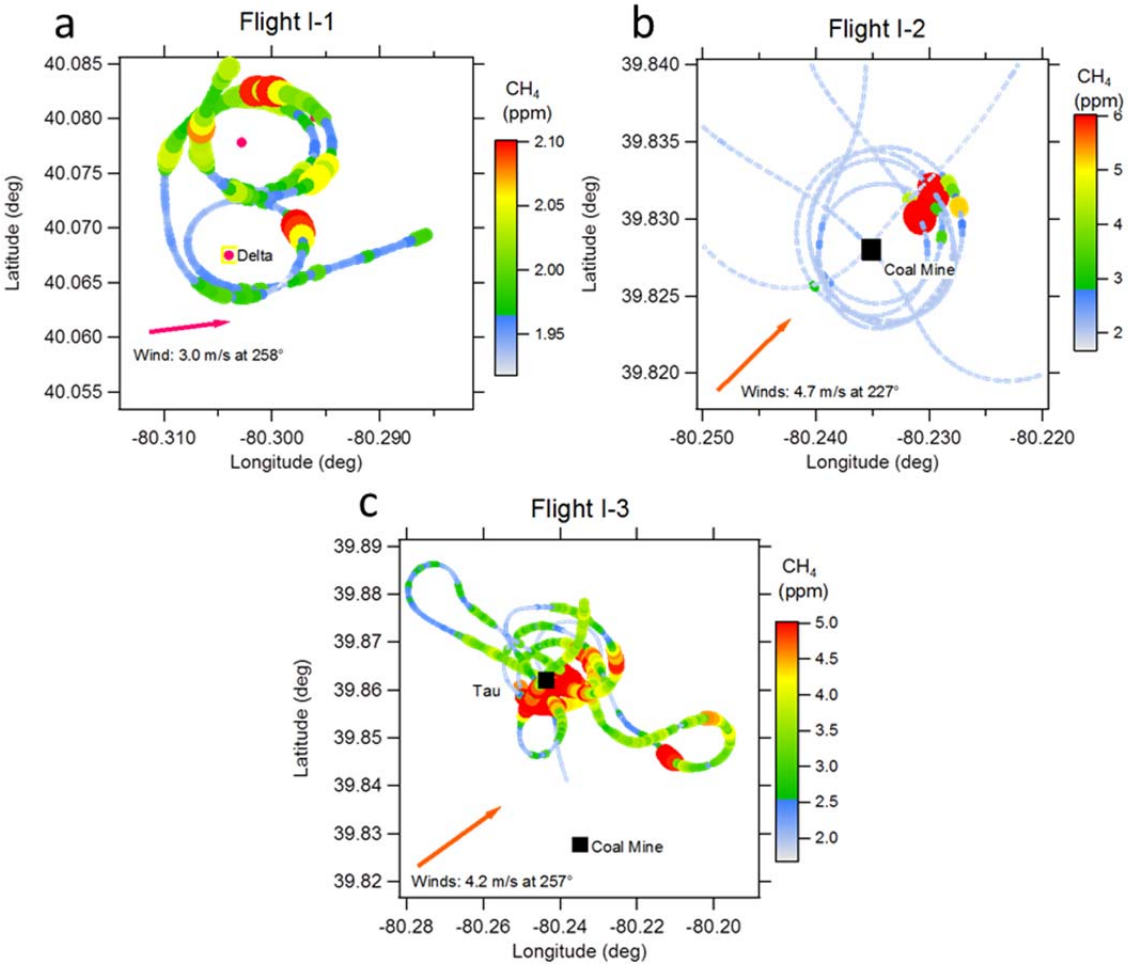

Figure 2.11 Investigative flights (a) near well pad Delta showing a distinct strongCH_4 plume downwind of Delta and an additional weak plume downwind of a nearby well-pad, (b) near a coal mine and (c) near Tau showing the same coal mine.

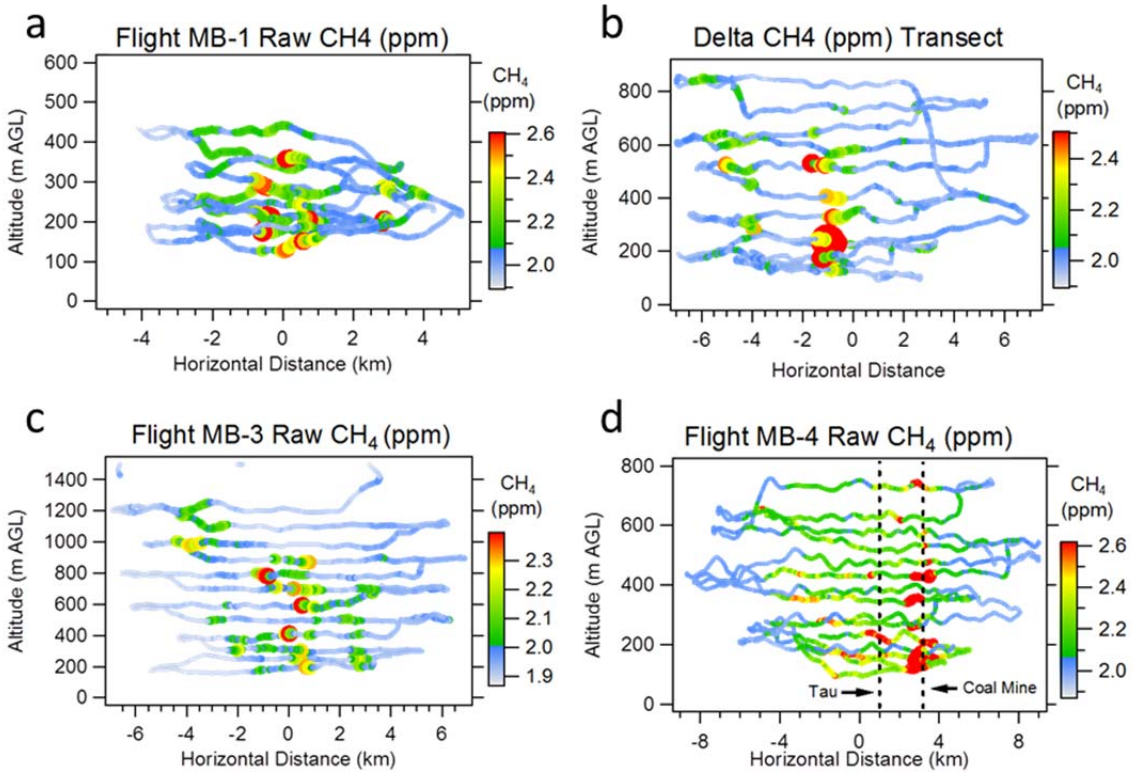

Figure 2.12 Raw CH_4 transect data for (a) MB-1, (b) MB-2, (c) MB-3 and (d) MB-4. The location of Delta in MB-2 is shown as a dashed line. The location of Tau and a nearby coal mine are shown in MB-4.

2.4 Data Analysis and Results

2.4.1 Kriging, Interpolation and Calculation of the Regional Flux Emissions

To calculate a flux from RF-1 and RF-2 a box encompassing the original sampling area (OSA) was identified and is shown as a dashed orange box in Figure 2.10. The height of the box was determined from the boundary layer depth from the earliest collected vertical profile during each flight. This corresponded to a BL depth of 370 m for RF-1 and 560 m for RF-2. A sample vertical profile for RF-1 is shown in Figure 2.13.

RF data collected at 250 m AGL was kriged using EasryKrig 3.0 (Chu, 2004). The kriging program interpolates between data points according the resolutions set by the user. In this case kriging resolution was 250 m. The kriging interpolation method computes a variogram between observation points to which the interpolation algorithm is fit. As part of the output the routine also produces error/quality control criteria (called Q1 and Q2), which must be lie within a range of accepted values. The interpolation parameters are changed until Q1 and Q2 lie within the acceptable regions.

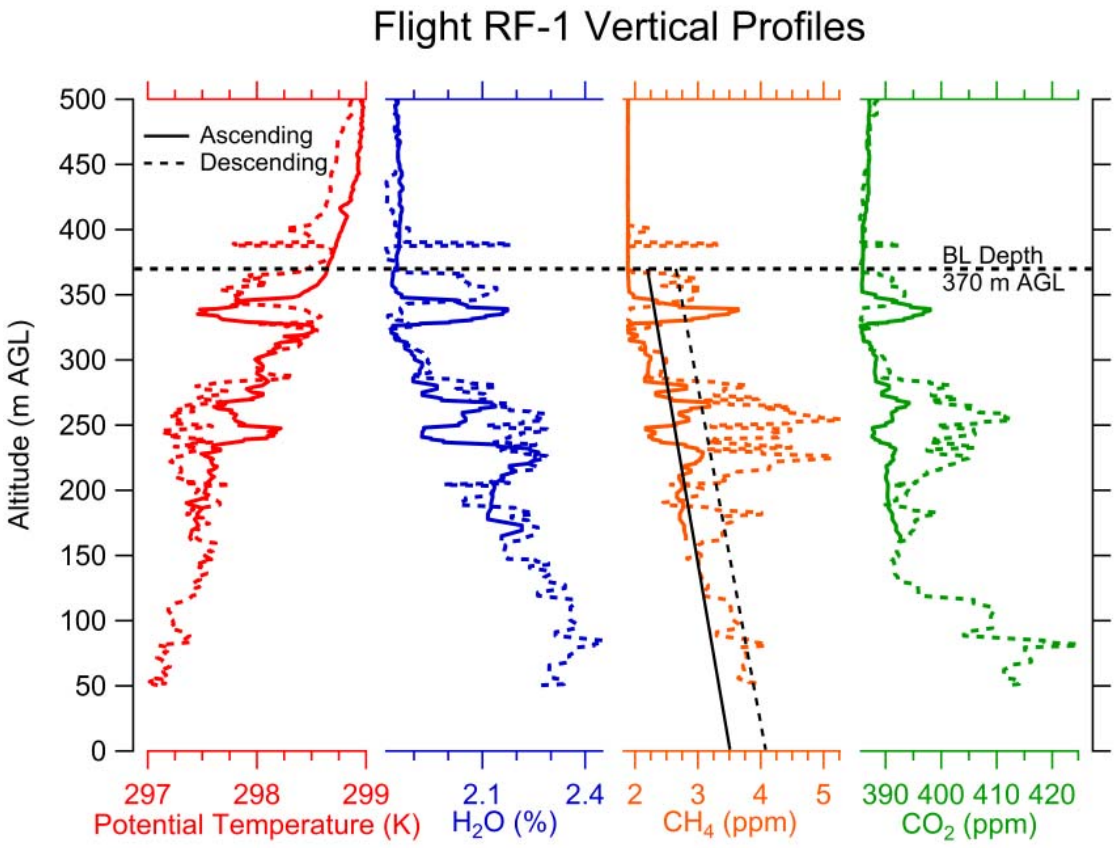

Figure 2.13 A vertical profile of potential temperature, H_2O, CH_4 and CO_2 during RF-1showing a clear boundary layer at ~370 m AGL.

As shown in Figure 2.13 the CH_4 profile was approximately linearly decreasing to the BL depth where background concentrations were observed. To obtain a 3-D matrix of data, the 2-D output from the kriging program was linearly interpolated to the ground and boundary layer depth. This was done by assuming a linear profile and a value of 1.9 ppm at the boundary layer height. The results of the kriging output at 250 m AGL and linear extrapolation to ground level for both days are shown in Figure 2.14. To ensure that the linear approximation was a viable approach the actual vertical profiles for CH_4 were fit with a linear fit and the results from integrating under both the observation and the linear approximation (shown in Figure 2.13) were compared. The integrations results differed by less than 7% in both cases indicating the linear approximation is appropriate.

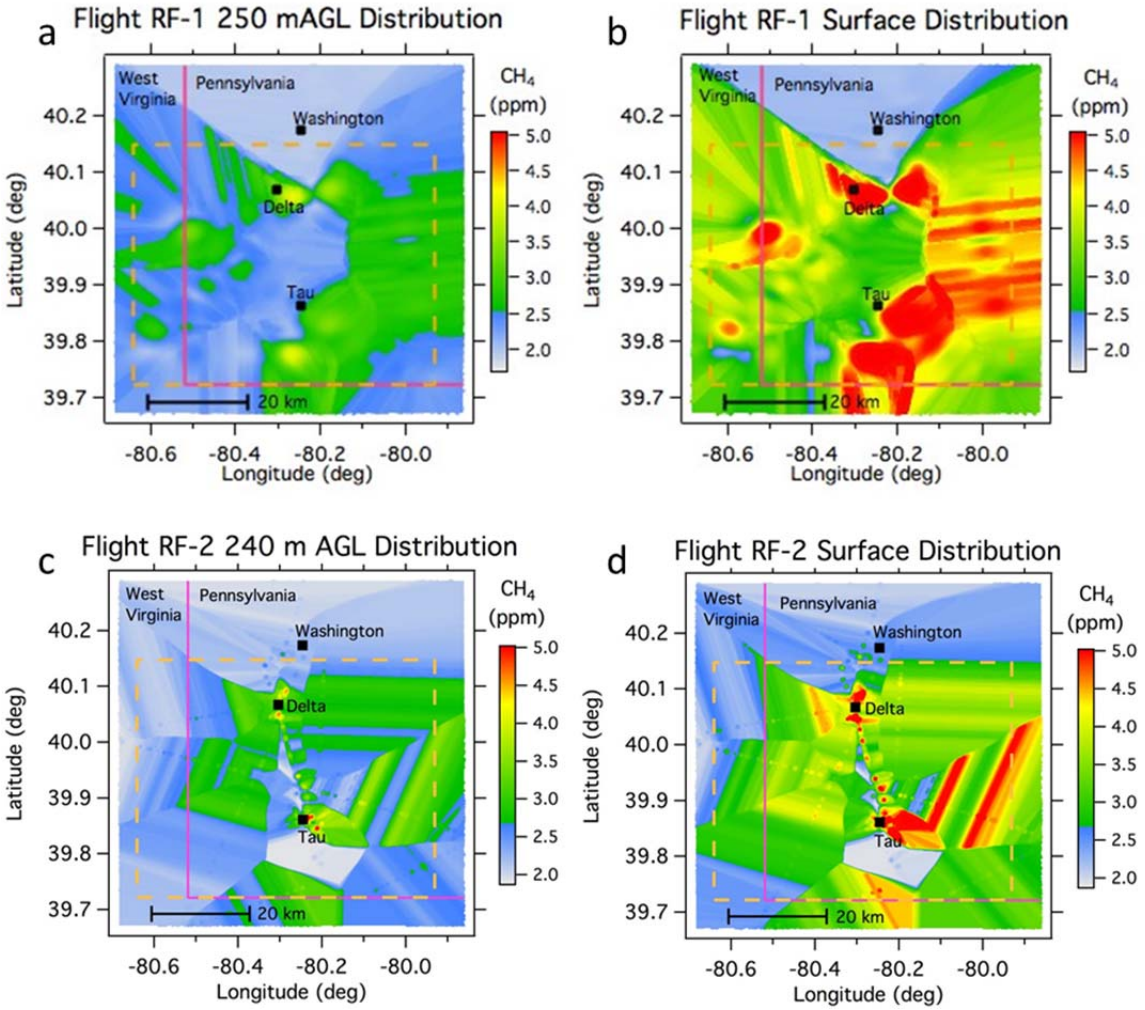

Figure 2.14 Flight RF-1 kriged output of CH_4 values at the flight level (240-250 m AGL) for (a) RF-1 and (c) RF-2 and the linearly interpolated values to the surface for (b) RF-1 and (d) RF-2.

To calculate a flux from the produced matrix Equation 2.4 was used. The background concentration was subtracted and the enhancement (Δc) was integrated in three dimensions to the height of the BL depth above the OSA. The enhancement was then divided by a chosen time-scale (T). The presence of an early morning enhancement is due to the buildup of emissions into a stable nighttime boundary layer where

turbulence and wind speed is low. Two time-scales were used as extremes for the physical limitations for the duration of the accumulation event. The minimum time-scale, 6 hours on RF-1 and 5 hours for RF-2, is equal to the time for wind to flush the box. The maximum time-scale, 18 hours, corresponds approximately to the time between collapse of the boundary layer the night before and the measurement time. The flux was then divided by the area (A) of the OSA, 2844 km^2, to obtain a flux per unit area. The flux equation is presented in Equation 2.4.

$$F_c = \frac{\int_0^z \int_{-y}^{y} \int_{-x}^{x} \Delta[c]_{ijk}\ dxdydz}{T \times A} \qquad 2.4$$

Uncertainty in the regional flux calculations was assessed by changing the time-scale and examining the effect of different interpolation schemes and background concentrations. In addition to the elaborate kriging and linear interpolation, a simpler method using an average linear profile across the entire OSA was used to calculate enhancement. Enhancements differed by ~30% using this method. A minimum background (1.9 ppm CH_4) was obtained from the residual layer and a maximum background (2 ppm CH_4) was obtained from the upwind (SW) sections of the RF data. The CH_4 enhancements differed by ~20% using this method. The combined uncertainty estimate, ± 75%, is dominated by the time-scale uncertainty, the most uncertain parameter, but the other variables do contribute noticeably to the uncertainty range. The average range of the top-down flux after including the uncertainty analysis is 2.0-14.0 g CH_4 s^{-1} km^{-2}.

As stated earlier, top-down measurements are an important compliment to bottom-up inventories because they can be used to independently evaluate the accuracy

of the bottom-up inventory, which represents the current state of knowledge for a specific process. For evaluation, a bottom up-inventory in the OSA was conducted using Howarth et al. (2011) and NETL (2011) emission factors for fossil-fuel emissions. Default gas compositions were assumed (API, 2009). The majority of the bottom-up inventory emissions for the three different scenarios were provided by Cornell. In addition, the emissions from animal feeding operations (AFOs) were included by using animal counts and emission factors for enteric fermentation and manure management (Jorgensen et al., 2007; Hong et al., 2011). Finally, EPA reports of significant CH_4 emitters were used to include relevant point sources (EPA, 2010a). Because the top-down estimated emissions may include the influence of upwind sources, or the effect of dilution from cleaner upwind air, a bottom-up inventory was also compiled for the area corresponding to an18-hour back trajectory (to correspond with the longest time-scale possible for accumulation to occur), shown in Figure 2.15. This area is named the upwind accumulation area (UAA) and covered 14,597 km^2. Full results of the bottom up inventory are shown in Table 2.2.

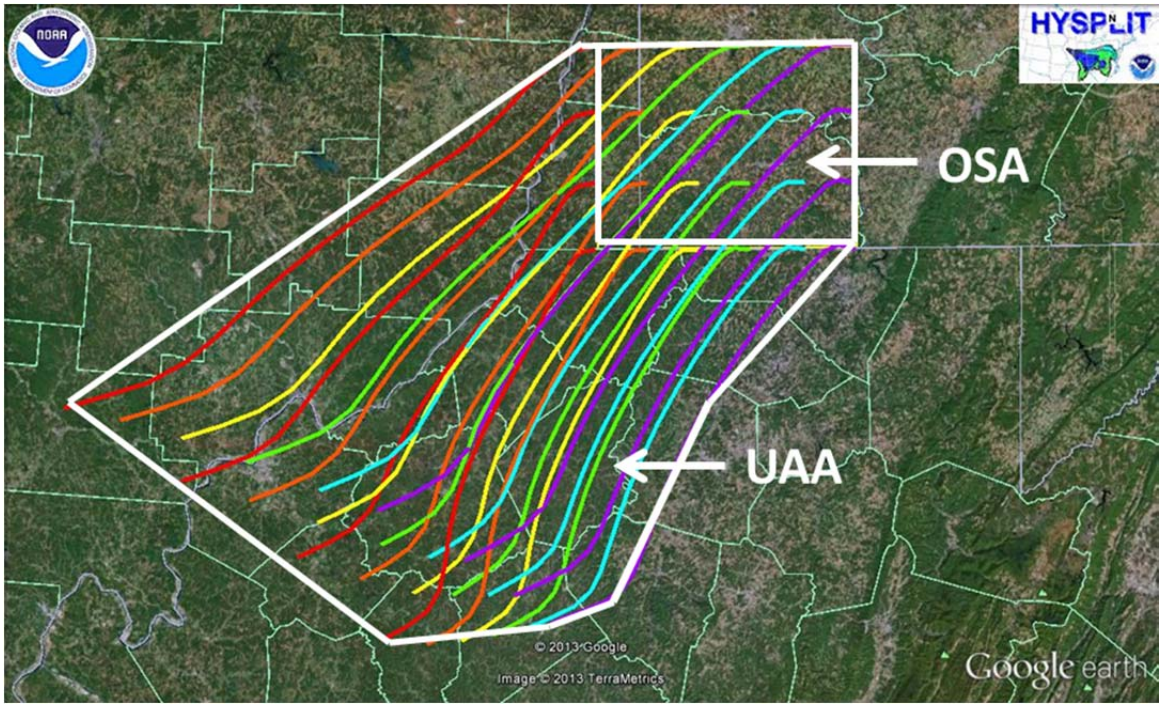

Figure 2.15 An 18 hour isobaric back trajectory computed by HYSPLIT at 50m AGL for 6/20/12 showing the OSA outlined with a white rectangle and the UAA outlined with a white polygon. The UAA region includes the OSA.

Table 2.2 Total expected emissions from all sources and percent contribution to the total emission for the OSA and the UAA using Howarth et al. (2011) emission factors and for the OSA using NETL (2011) emission factors.

Area	Source	Expected Emissions (g CH_4 s^{-1} km^{-2})	Contribution (%)
	Natural Gas	0.85 (low) – 2.23 (high)	21.9– 42.0
	Oil	0	0
	Coal	2.96	55.7 – 76.3
OSA	Flowback	0.05 – 0.10	1.3 – 1.9
(Howarth	AFO	0.015	0.3 – 0.4
EF's)	Other	0	0
	Total (Avg)	**3.88 – 5.31** (4.60)	
	Natural Gas	0.76 (low) – 1.70 (high)	42.0 – 61.6
	Oil	0	0
	Coal	1.01	36.6 – 55.8
UAA	Flowback	0.01 – 0.02	0.6 – 0.7
(Howarth	AFO	0.015	0.5 – 0.8
EF's)	Other	0.019	0.7 – 1.0
	Total (Avg)	**1.81 – 2.76** (2.29)	
	Natural Gas	1.41	31.4 – 31.8
	Oil	0	0
	Coal	2.96	65.9 – 66.7
OSA	Flowback	0.05 – 0.10	1.1 – 2.3
(NETL	AFO	0.015	0.3
EF's)	Other	0	0
	Total (Avg)	**4.42 – 4.49** (4.46)	

AFO emissions were estimated using county level animal counts for every county the OSA or UAA even partially touched (Hong et al. 2011). Due to privacy laws, individual AFO emissions are not available and so could not be screened for the AFOs that were actually covered by either the OSA or UAA. It is assumed that AFOs are evenly distributed throughout the county. The emissions, derived using emission factors from Jorgensen (2007) and Zhou et al. (2007), were then divided by the total area of all the counties used and scaled to emissions representing the OSA and UAA using their respective actual areas. Point source data was extracted from the Greenhouse Gas

Reporting Program (EPA 2010) to identify 3 and 29 potential CH4 sources in the OSA and UAA, respectively. Of these, 2 and 5 sources in the OSA and UAA, respectively, overlapped with our analysis of methane emissions from energy production and were excluded. The remaining 1 source in the OSA contributed a negligible amount of methane. In the UAA the remaining 24 sources include a landfill, which produces 85% of the CH_4 emission from this subset of emission sources, various production facilities, power plants and incineration plants. The combined emissions for the UAA are equal to 0.019 g CH_4 s^{-1} km^{-2}. In addition, these counties were searched for flowback events, which can contribute large emissions, using data from FracFocus.org (http://www.fracfocusdata.org/DisclosureSearch/MapSearch.aspx). Only one well was potentially in flowback during the time of sampling.

2.4.2 Calculation of Mass-Balance Emissions

Interpolated outputs of the raw transect data (shown in Figure 2.12) are presented in Figure 2.16. Mass-balance flux estimates are calculated according to the following equation:

$$F_c = \int_0^{z_i} \int_{-x}^{x} \Delta[c]_{ij} \times M_{\perp_{ij}} \, dxdz \qquad 2.5$$

Where z_i is the boundary layer depth, x and –x are the horizontal extent of a measurement transect from an arbitrary middle point and $M_\perp$ is the perpendicular wind speed at each measurement point denoted by the subscripts ij.

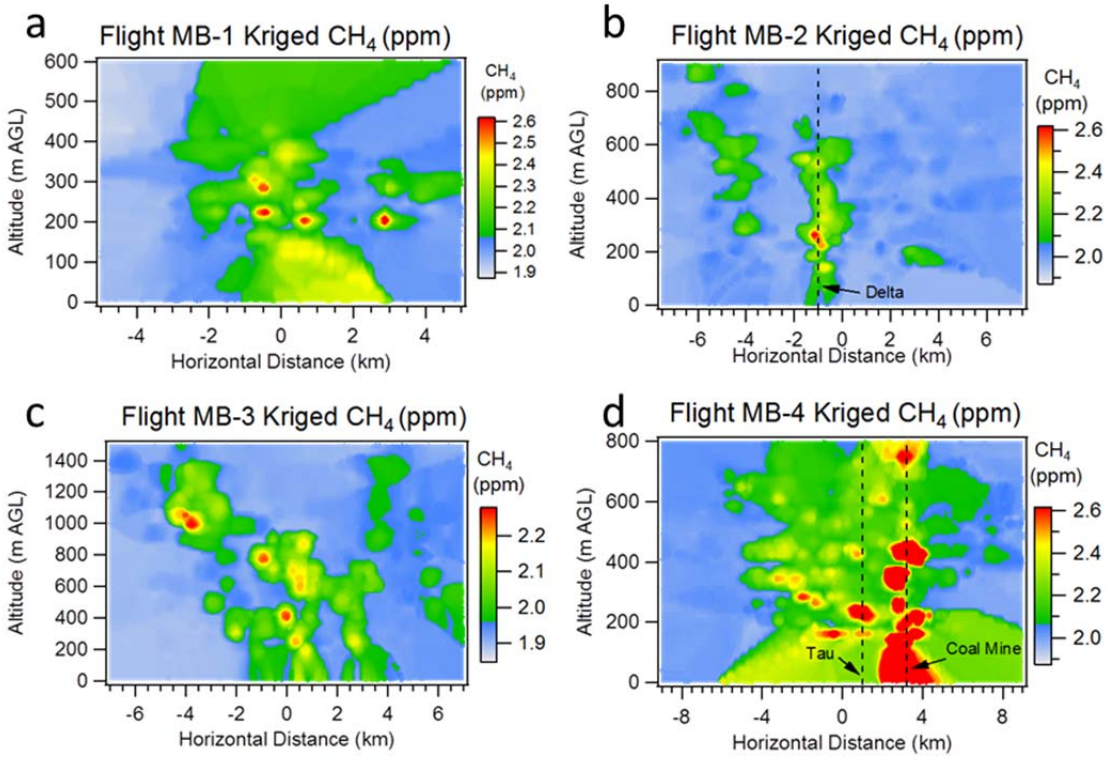

Figure 2.16 Kriged CH_4 outputs for (a) MB-1, (b) MB-2, (c) MB-3 and (d) MB-4 of the raw CH_4 transect data shown in Figure 2.12.

Fluxes were calculated for each mass-balance flight. Source attribution for each flight was done by investigating the possible contributing sources using well inventories and the investigative flights. Inventory data shows locations of well pads and how many wells are permitted for that pad. For MB-4, the area flux had a dense upwind area of many well pads, including numerous coal-bed methane well pads, which made specific attribution impossible. In addition, during MB-4 a large signal from a nearby coal mine is prominent in the data. Table 2.2 summarizes the mass-balance results and source attribution.

Table 2.3 Results from 4 mass balance experiments and the number of pads and wells contributing to the flux. Flights 1-3 were conducted near pad Delta and Flight 4 near pad Tau. Flux per pad and per well is obtained by dividing the total flux by either the total number of pads or total number of wells.

Flight	Flight MB-1	Flight MB-2*	Flight MB-3	Flight MB-4	Average ± σ
Total Flux (gCH_4/s)	380	248	1880	1490	--
Total Pads Contributing	2	1	7	--	--
Flux (gCH_4/s) per Pad	190	248	269	--	236 ± 41
Total Permitted Wells	15	8	41	--	--
Flux (gCH_4/s) per well	25	31	46	--	34 ± 11

*isolated pad Delta

Investigation of on-site equipment identified from aerial photos taken during the study suggests that all the well pads sampled were in the drilling stage. Figure 2.17a shows typical drilling-stage equipment, the most prominent of which is the drill-rig, a vertical structure that is easily identified from the air. Publicly available data from the Pennsylvania Department of Environmental Protection confirmed that the sampled wells were drilling and had not reached total vertical depth (PADEP 2012). The estimated emission per well, 34 g CH_4/s, is 2-3 orders of magnitude higher than EPA estimated emissions per well for drilling emissions, obtained by dividing the EPA estimated total emissions per well by a range encompassing the typical well drilling duration (2 weeks) and the minimum well drilling duration that can be confirmed at this site (2 days) (EPA, 2012a). There are several possible causes of this anomalously high emission. Nearby abandon old wells may be venting. Abandoned wells are not always documented so this

is impossible to verify. Another possibility is the occurrence of ‘gas-kicks’, where a region of the well-bore enters an unexpectedly high-pressure rock formation that causes the high-pressure gas to be emitted out of the well-bore (ASME 2005). Gas-kicks can be dangerous and generally assumed to be short-lived incidents (ASME 2005). A more reasonable hypothesis is the use of under-balanced drilling, where the well-bore is intentionally kept at lower pressure than the surrounding rock formation so that higher pressure gas and fluid from the surrounding rock enters up and out of the well-bore, for recovery (ASME 2005). This hypothesis is supported by the presence of an unlit stack visibly venting at well pad Delta (shown in Figure 2.17 a) and by the lack of mud-pits at any of the observed sites (Figure 2.17 a-c). Conversely to under-balanced drilling, over-balanced drilling is a technique where the well-bore is kept at higher pressure than surrounding rock-formations by using ‘mud’ during the drilling process, an example of which is shown in Figure 2.17 d.

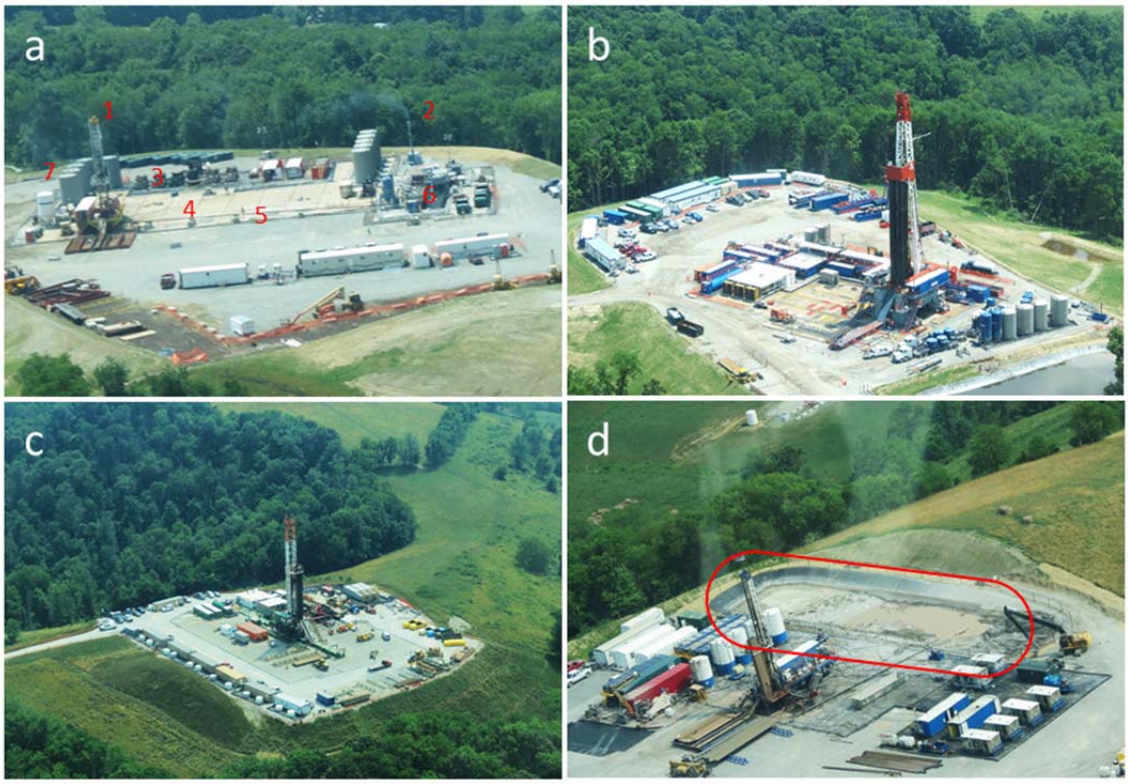

Figure 2.17 (a) Well-pad Delta showing (1) a drill rig, (2) an unlit, venting stack, (3) air compressors, (4) main high-pressure air line, (5) flow line, (6) separator unit and (7) water tanks. (b) Well-pad Epsilon showing a prominent drill rig. (c) Well-pad Tau showing a prominent drill rig. (d) A well-pad near tau showing a drill rig and mud-pit (circled in red) expected during over-balanced drilling.

2.4.3 Flask Analysis

During RF-2 a NOAA PFP was used to collect 12 flask samples. Two of these samples were collected above the boundary layer in the residual layer or free troposphere. These flasks were analyzed for GHG and hydrocarbon composition. The remaining 10 flasks collected in the boundary layer were used to calculate hydrocarbon ratios. First, the lowest concentration flask was subtracted from the other nine flasks, then the remaining background subtracted flask data were plotted so the ratio was the slope generated from a linear least-squares fit. Ratios investigated included C_3H_8 / CH_4 (C3/C1), n-C_4H_{10} / CH_4

(nC4/C1), n-C_4H_{10} / C_3H_8 (nC4/C3) and n-C_5H_{12} / C_3H_8 (nC5/C3). Figure 2.18 shows the regression analysis for these ratios, all ratios are in ppb/ppb. Results of the hydrocarbon regressions and typical ratios for this region are shown in Table 2.4. The collected flask data show nC4/C3 and nC5/C3 ratios similar to typical Marcellus shale gas, but much lower C3/C1 and nC4/C1 ratios. This indicates that the region is being diluted with an essentially pure CH_4 sources and is consistent with the hypothesis of significant emissions from coal bed methane, which is ~98% CH_4 and contains trace amounts of higher hydrocarbons (Kotarba, 2001).

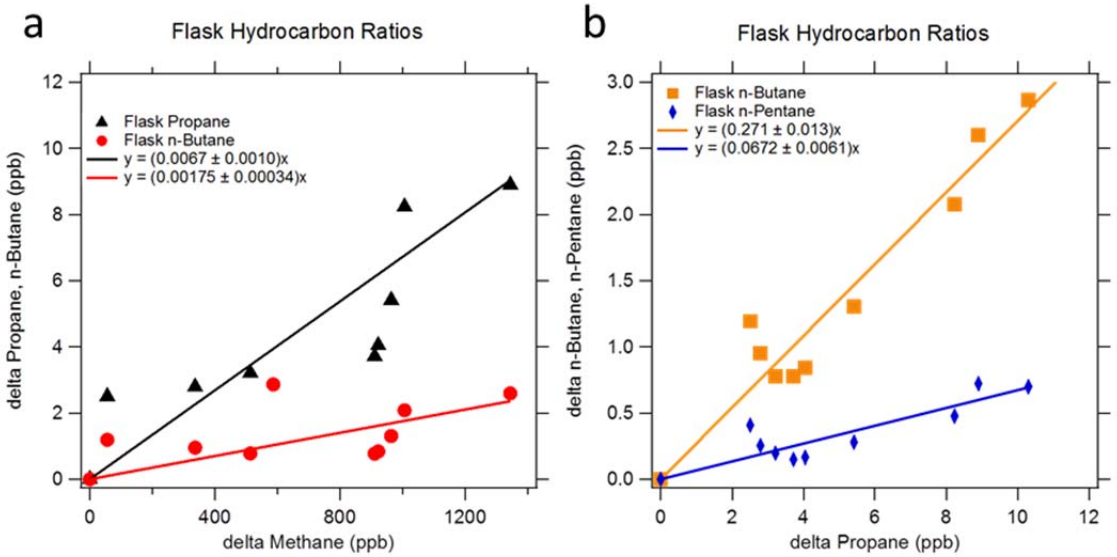

Figure 2.18 Flask hydrocarbon ratios of (a) C3/C1 and nC4/C1 and (b) nC4/C3 and nC5/C3.

Table 2.4 Hydrocarbon ratios for RF-1 and typical shale gas in this region.

Study	Ratio (ppb/ppb)			
	C3/C1	nC4/C1	nC4/C3	nC5/C3
RF-1	0.007 ± 0.001	0.0018 ± 0.0003	0.27 ± 0.01	0.079 ± 0.006
Osborne and McIntosh, 2010; Braziel, 2011	~0.05	~0.01	~0.24	~ 0.09

2.5 Discussion and Conclusions

This work demonstrated the ability of the aircraft mass-balance approach to identify and quantify the emission of point sources. Importantly, the well pads quantified were identified as in the drilling phase, a pre-production stage not previously associated with significant methane emissions. The hypothesis for these emissions is the use of underbalanced drilling, suggested from aerial picture of equipment of the pads, combined with the presence of shallow coal seams prevalent in this region that produce coal-bed methane. Our flask analysis supports the presence of a pure CH_4 source in this region, potentially from coal-bed methane which is low in hydrocarbons, with the observation of C3/C1 and nC4/C1 ratios that were anomalously low. This work highlights the potential for some sites to be 'super-emitter,' sources that emit an outsized portion of the total regional emission based on their prevalence. The high-emitting well pads in the drilling phase sampled here, which represent 1% of the wells in the OSA, emitted at a rate 2-3 orders of magnitude higher than EPA estimates, yet emitted 4-30% of the observed regional flux. Brandt et al. (2014) studied data from multiple field studies and observed a skewed distribution of sources where, in some cases, most of the emissions came from

low-frequency super-emitters. This work theorizes the possibility of drilling to be another source with a skewed distribution and highlights the difficulties in traditional bottom-up techniques in capturing a true regional or national scale emissions estimate.

Table 2.5. Natural gas portion of the top-down flux as a percentage of the unassociated natural gas production rate.

Parameter	18-h Estimate		5 to 6-h Estimate	
	Low	High	Low	High
Top-Down Flux (g $CH_4 s^{-1} km^{-2}$)	2.0	4.2	6.6	14.0
CH_4 from Nat. Gas (%)	22	62	22	62
Nat. Gas Prod. Rate (g $CH_4 s^{-1} km^{-2}$)	15.9		50.1	
Nat. Gas Flux/ Prod. Rate (%)	2.8	16.4	2.9	17.3

In addition, ALAR was used to observe and quantify a large region of CH_4 enhancement in southwest Pennsylvania. Using a bottom up-inventory provided by Cornell University, the top-down natural gas fraction of the observed flux was estimated by assuming the fractional distribution of sources of the top-down and bottom-up estimates were the same. The bottom-up inventory produced a range of 30-60% of the observed top-down flux expected to come from natural gas production activities. This fraction of the observed top-down flux divided by the gross natural gas production rate associated with each time scale leads to a leak rate equal to 3-17%o f production in this area, as shown in Table 2.5. This is within the range of results from other top-down estimates across the U.S., 2.3-17%, and previous observational studies indicating that high leak rates are a national problem (Katzenstein et al., 2005, Petron et al., 2012, Karion et al., 2013, Peischl et al., 2013, Petron et al., 2014). Further research including long-term observations is needed to definitively identify the true leak rate, but further

studies should also aim to identify large emission sources to generate potential emission reduction targets. In its current production process and use, natural gas may not provide any GHG reduction (Davis and Shearer, 2014; McJeon et al., 2014). Additionally, natural gas production can cause air and water quality issues that should be studied (Osborne et al. 2011; Moore, et al., 2014).

CHAPTER 3. EMISSION FACTORS AND EFFICIENCY OF ASSOCIATED GAS FLARES IN NORTH DAKOTA

3.1 Motivation for Research

In addition to allowing access to natural gas locked in shale formations like the Marcellus region, the advent of hydraulic fracturing and horizontal drilling have allowed extraction of oil from oil shale and 'tight' or low porosity formations such as the Bakken Formation in North Dakota. As fossil fuels are often co-located it is not uncommon to produce significant amount of natural gas at oil production sites. Flaring safely removes the unwanted natural gas and converts the more potent GHG CH_4 and other pollutants into CO_2, but also produces reactive nitrogen species NO and NO_2 (together called NO_x).The rapid proliferation of oil wells in the Bakken has outpaced the construction of natural gas pipelines and ancillary systems to contain and transport the associated natural gas produced from oil wells and, combined with the low economic incentive to sell the associated natural gas, has led to an increase in flaring (EPA, 2012). Currently, about one third of the natural gas produced in North Dakota is reported as vented or flared (EIA, 2014). As shown in Figure 3.1 the reported amount of natural gas vented or flared in North Dakota had been steady for several years, but has increased by a factor of 30 since 2004 and is partly responsible for the factor of 2 increase in total U.S. venting and flaring between 2004 and 2012 (EIA, 2014). Flaring is also a large source of CO_2 and black

carbon worldwide with 250 million tons CO_2 and 228 thousand tons black carbon attributed to global flaring annually (Stohl et al., 2013; Olivier et al., 2013).

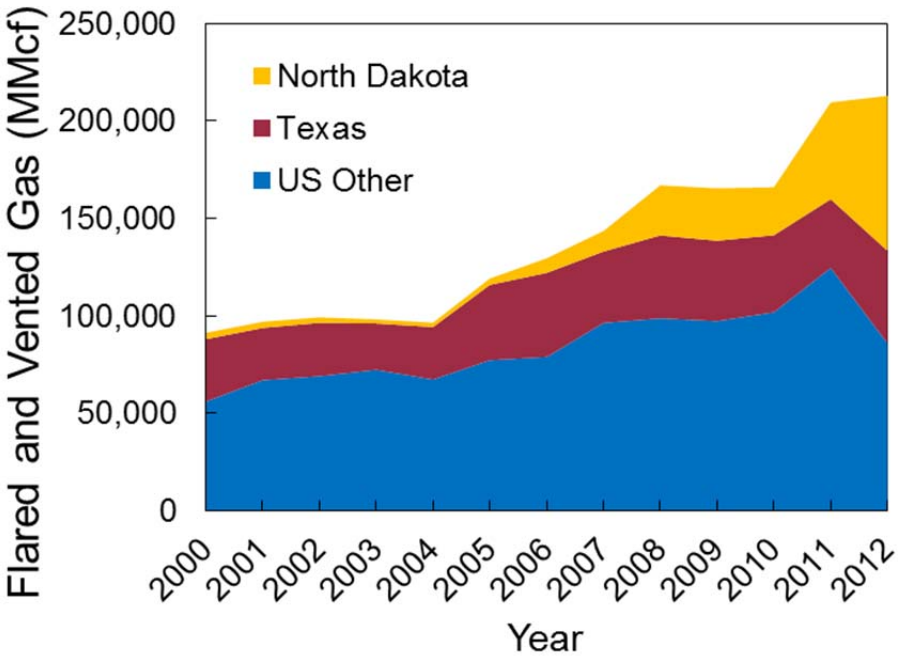

Figure 3.1 Total flared and vented gas in the U.S. and select states. Data from the EIA 2014.

Given the large and increasing quantity of flaring currently occurring in the U.S. and North Dakota specifically, the quantification of emissions from flaring is essential. The magnitude of CH_4 emissions is of particular consequence for natural gas flares due to the higher GWP of CH_4. Flaring is generally assumed to have a CH_4 destruction removal efficiency (DRE) value of 98%, according to a 1996 EPA/Gas Research Institute (GRI) study. This number is supposed to account for incomplete combustion and intermittency (periods when the flame goes out). Included in the EPA/GRI report is a review of earlier

studies, however only two of these used natural gas and these two actually used processed natural gas. No available studies have used a fuel representative of raw natural gas, which may have significantly different hydrocarbon ratios than processed natural gas.

Previous peer-reviewed studies designed to investigate flare efficiency have generally used scaled-down constructions of flares, for use in a laboratory, and predict very high (>98%) efficiency (Johnson and Kostiuk, 2000; Kostiuk et al., 2000). Actual on-site flaring techniques may differ significantly from downscaled simulation. One technical report from two on-site flare samples in Canada reported efficiencies as low as 66-84% despite their own small and full-size laboratory tests that returned very high efficiencies (98-99%) (ECCP, 1996). More recent work to understand flare efficiency, combustion products and particulate matter emission, has been performed at a test facility using an industrial flare, which typically uses significant amounts of propylene and steam-assist technology (Johnson et al., 2011; Torres et al., 2012a; Torres et al., 2012b; Knighton et al., 2012) . On-site natural gas flares at oil wells are often temporary, simple and may not be subject to emissions reporting. Steam-assisted technology is usually used on flares at chemical plants and refineries while operators with field natural gas flares may choose to use air-assisted flares to ensure a smokeless flare (Akeredolu and Sonibare, 2004). A typical flare set-up with an optional steam assist nozzle is shown in Figure 3.2. Briefly, fuel gas is let into a flare stack. As the gas travels through the stack it passes through seals designed to prevent flame ignition beyond the flare tip as well as a baffle (or gas barrier) to remove liquids which could quench the flame, which will be collected in a canister called a knock-out drum and drained (Akeredolu and

Sonibare, 2004). A pilot burner is used to ensure the flare stays lit (Akeredolu and Sonibare, 2004). Air-assisted flares contain a fan at the bottom of the stack and a slotted exit near the flare tip to mix air more efficiently ensuring there is enough oxygen to promote complete combustion (Akeredolu and Sonibare, 2004). Steam-assisted flares contain a ring of steam nozzels near the flare tip to spray a fine mist of water into the flame. Once in the flame, the water breaks down into H and OH radicals which help oxidize the hydrocarbons in the gas (Akeredolu and Sonibare, 2004).

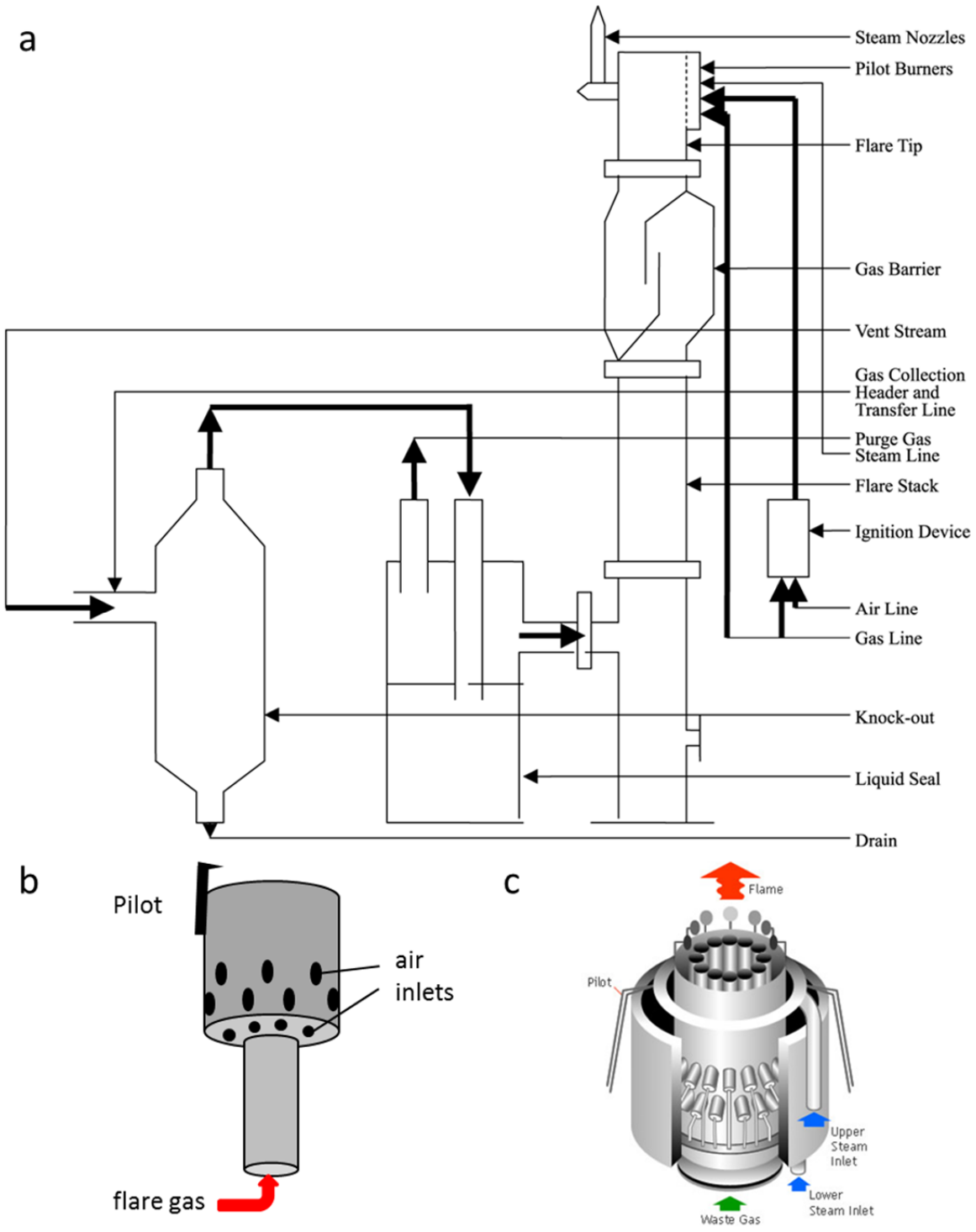

Figure 3.2 (a) A typical flare set up (from Akeredolu and Sonibare, 2004). Also shown are (b) an air-assist flare burner nozzle and (c) a steam-assists burner nozzle (from www.tlv.com/global/TI/steam-theory/principal-applications-for-steam.html).

In May and June of 2012 the first in-situ flare data was collected using ALAR. Ten flares were sampled in the Bakken Formation of North Dakota and an additional flare was sampled in the Marcellus Shale of Pennsylvania. In October, 2013 2 flares were sampled in the Eagle Ford shale of Texas and will also be discussed. Flare data was analyzed to produce emission factors for CH_4 as well as CH_4 destruction efficiency. In addition, the effect of a range of crosswinds was examined.

3.2 Experiment Design

3.2.1 Site Description

This work was primarily conducted in the Williston basin of the Bakken Formation in western North Dakota with an additional flare sampled in the Marcellus Shale formation in southwestern Pennsylvania. Ten flares in North Dakota were visually identified and sampled on 5/14/12 and 6/12/12-6/14/12 with the flare in Pennsylvania sampled on 6/18/12. Figure 3.3 shows the oil fields, active wells and flares sampled in North Dakota. Table 3.1 gives the detailed location and sampling dates for each flare in North Dakota and Pennsylvania.

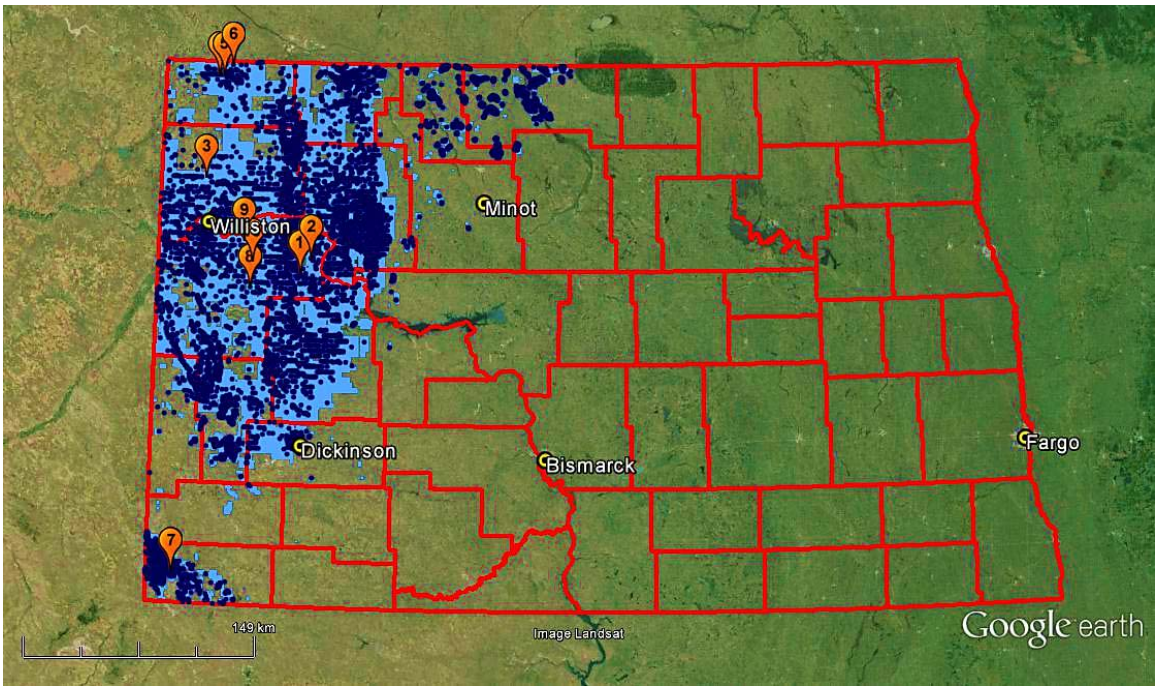

Figure 3.3 Location of oil fields (light blue), active wells (dark blue) and flares sampled (numbered balloons) in North Dakota.

Flares were identified and sampled randomly on the basis of their visibility in an attempt to sample multiple operators and common flare configurations used on-site. This sampling approach may be biased toward the largest, and potentially most efficient, flares as large flares were the most easily identified. Flaring was prevalent across the entire Bakken Formation with flare configurations ranging from very small stacks burning in small dugout pits, which were only successfully sampled once, to flares with stacks several meters high. Example flare set ups are shown in Figure 3.4. At the time of this work we identified only one large flare in southwest Pennsylvania, though recent EPA regulations have been enacted that will prevent direct venting, thus likely increase the prevalence of flaring in Pennsylvania, at least temporarily (PADEP, 2014). Additional EPA regulations require better infrastructure for gas transportation which may reduce the

prevalence of flaring overall (PADEP, 2014). Elevated flare stack heights typically range from 9-30 m above ground level (AGL) and aerial photographs and observations suggest that in this region elevated flares were ~9 m AGL (Akeredolu and Sonibare, 2004). Flame heights varied between sites and meteorological conditions, though at all sites flares were constantly lit and never sputtered or showed periods of intermittency.

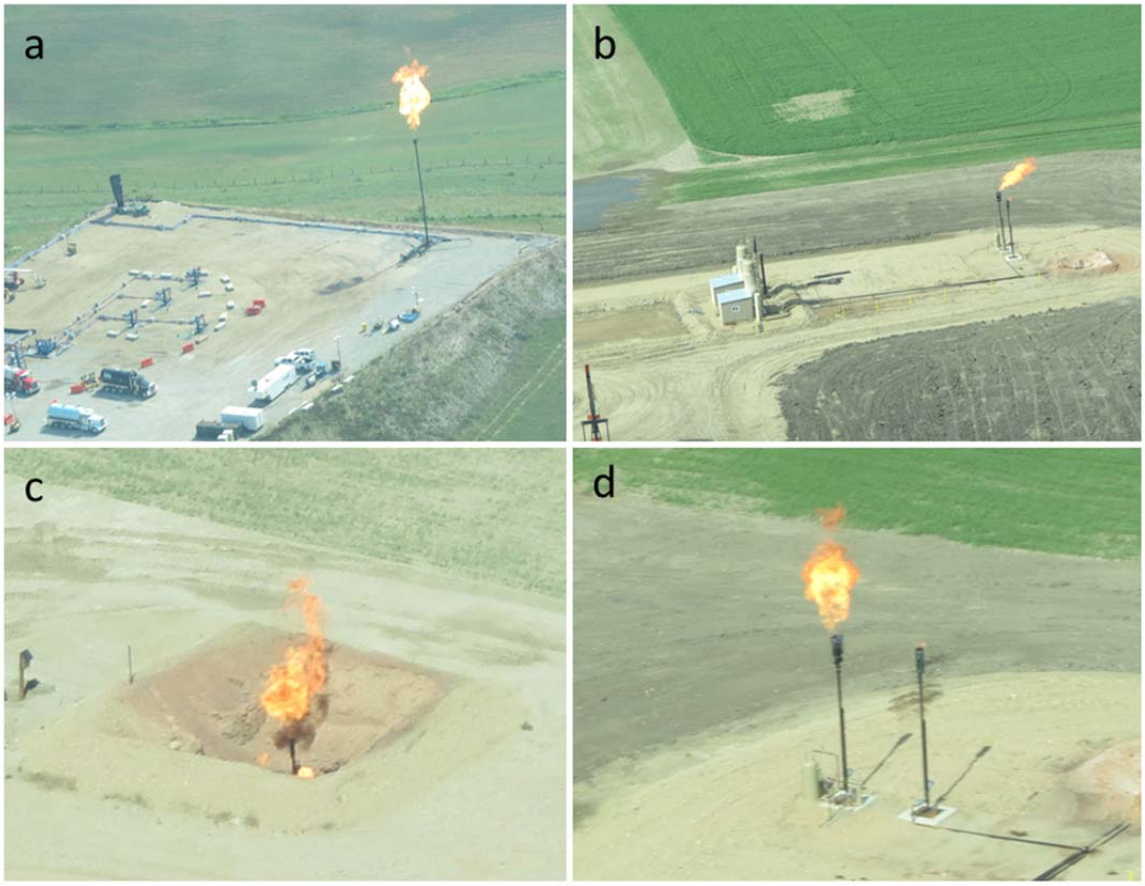

Fiugre 3.4 Typical flares in (a) Pennsylvania and (b) North Dakota. Also shown are a close up (c) a ground pit flare and (d) a more typical flare with a nearby flare with a much smaller flame.

Table 3.1 Flare locations and sample dates.

Flare	Sample Date(s)	Latitude	Longitude	State
1	5/14/2012	47.819	-102.835	ND
2a	5/14/2012	47.905	-102.763	ND
2b	6/14/2012	47.907	-102.747	ND
3a	6/12/2012	48.341	-103.663	ND
3b	6/14/2012	48.341	-103.663	ND
4	6/12/2012	48.923	-103.591	ND
5a	6/12/2012	48.924	-103.549	ND
5b	6/14/2012	48.924	-103.549	ND
6	6/12/2012	48.980	-103.476	ND
7	6/13/2012	46.122	-103.835	ND
8	6/13/2012	47.733	-103.254	ND
9	6/13/2012	47.993	-103.318	ND
10	6/13/2012	47.876	-103.242	ND
11a	6/18/2012	40.285	-80.431	PA
11b	6/18/2012	40.285	-80.431	PA

3.2.2 Instrumentation and Flight Design

The instrumentation used is described in Chapter 2.2.2 and consists of a 0.5 Hz $CO_2/CH_4/H_2O$ high-precision Picarro CRDS, 50 Hz BAT probe reporting wind and other meteorological data and 50 Hz GPS data. All instrumentation is aboard ALAR. A calibration plot for the CRDS for the duration of the experiment (5/14/12- 6/14/12 is presented in Figure 3.5. Measurement uncertainties for CO_2 and CH_4 are ±0.07 ppm and ±1 ppb, respectively

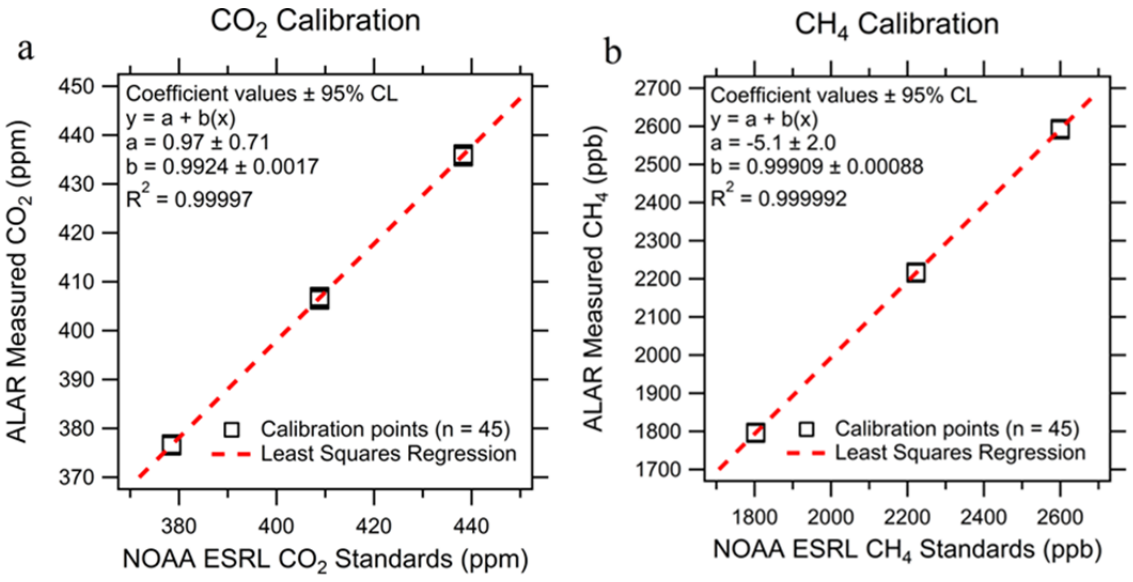

Figure 3.5 A composite (a) CO_2 and (b) CH_4 calibration plot for the CRDS for the duration of this experiment (5/14/2012-6/14/2012). Coefficient values are shown +/- the 95% confidence level.

Flare plumes were sampled by flying directly into the flare plume from the downwind side. Sampling was completed by passing directly over the flare to maximize data collection in the flare plume. A sample flight path is shown in Figure 3.6 for flare 2a. Previous investigation of flare plume structure has been examined at laboratory scale and a distinct combustion (buoyant) and uncombusted fuel (non-buoyant) plume has been observed at local scales (Kostiuk et al., 2000; Gollahalli et al., 1995). However, in a convective boundary layer buoyant and non-buoyant plumes emitted near the surface have similar dispersion rates and atmospheric turbulence should quickly mix heat and pollutants (Nieuwstadt and de Valk, 1987; Stull 1988). Thus it is assumed that at the sampling height distance from the flare the CO_2 and CH_4 plumes will be correlated and well-mixed. Thus, the unburned CH_4 can be obtained from a regression of background subtracted CH_4 vs CO_2.

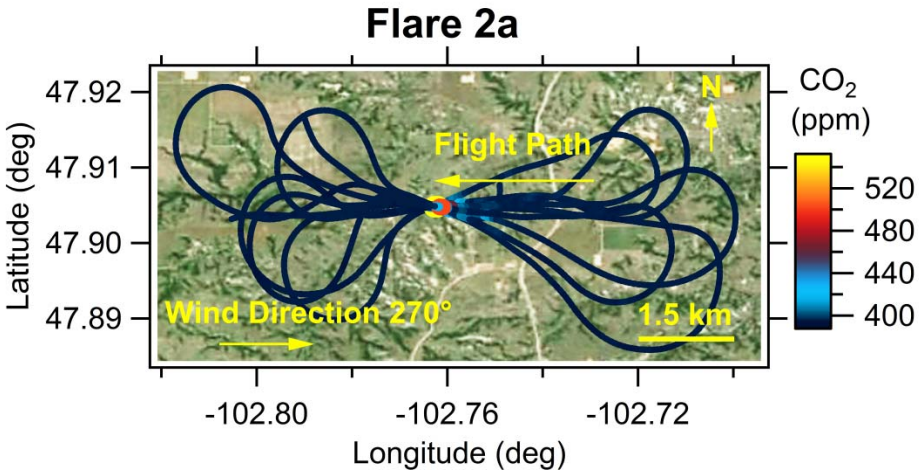

Figure 3.6 Example flight path colored by observed CO_2 for Flare 2a, shown in Figure 3.3.

3.2.3 Flare Plume Isolation

An example data series for a single flare, Flare 2a, is shown in Figure 3.7. Flare plume data was identified by isolating CO_2 peaks greater than 7 σ above the background concentration. Background concentration and standard deviations were calculated from regions where no CO_2 and CH_4 peaks were present. However, as some flare sites were far from the initial background sampling area, the local background changes slightly. At these sites the local background was determined by calculating the mean excluding outliers (flare plumes). The standard deviation was assumed to be the same as the original background area. Mean background concentrations were then subtracted from the flare sampling CO_2 and CH_4 time series to produce ΔCO_2 and ΔCH_4 time series. Background concentrations ranged from 385.37-393.25 ppm and 1874.4-1919.8 ppb for CO_2 and CH_4, respectively. The 7 σ threshold was used to exclude weak CO_2 plumes from other sources, such as diesel engines on the well pads. In addition, only flare data points within

4 seconds of the maximum CO_2 peak were used to exclude contamination from other nearby CH_4 sources. The background CO_2 standard deviation ranged from 0.27-0.44 ppm in North Dakota and was 0.61 ppm in Pennsylvania. The CH_4 standard deviation ranged from 1.1-3.6 ppb.

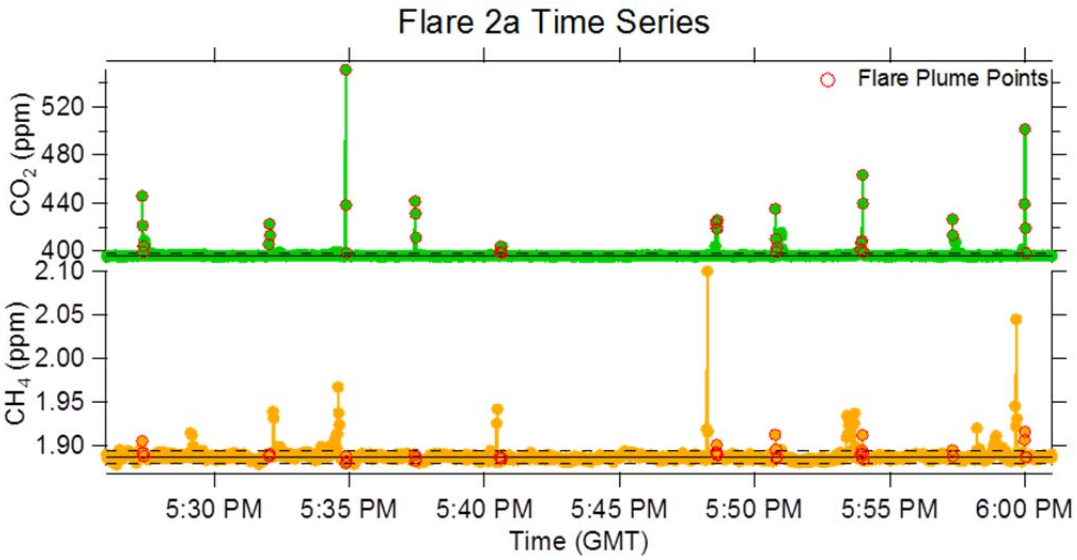

Figure 3.7 An example time series of data collected for Flare 2a shown in Figure 3.3.

3.3 Data Analysis and Results

3.3.1 Calculation of Flare Emission Factors for CH_4

Flare emission factors (EFs) were calculated three ways. A simple regression of ΔCO_2 vs ΔCH_4 for all corresponding plume points from a single flare was performed for each flare. In addition, regression of integrated flare was also made for the integrated ΔCO_2 vs ΔCH_4 for each flare pass for all corresponding plume peaks with at least three

points. In both cases regressions were forced through zero and the slope is then equal to the EF for each flare. Plots for the simple regression approach are shown in Figure 3.8. The data shown represent 4-14 flare passes. Simple regression results are reported in Table 3.2 and integration regression results are reported in Table 3.3. The integration regression was performed to assess the assumption of a well-mixed plume with correlated CO_2 and CH_4 concentrations. If plumes are more heterogeneous than expected, this may cause increased random scatter in the data. The effect of random scatter can be mitigated by sufficient repeated sampling, however, an alternate approach to reduce scatter would be to integrate peaks. Due to the time resolution of the instrumentation used and the time in the plume (<10 s), only 3-4 points were generally isolated by the plume criteria for each flare pass. Thus integration is not ideal for these types of non-fully resolved peaks. Nevertheless, integration was performed using a canned integration tool with a trapezoidal fit, a built in function of the IgorPro by Wavemetrics ® analysis package.

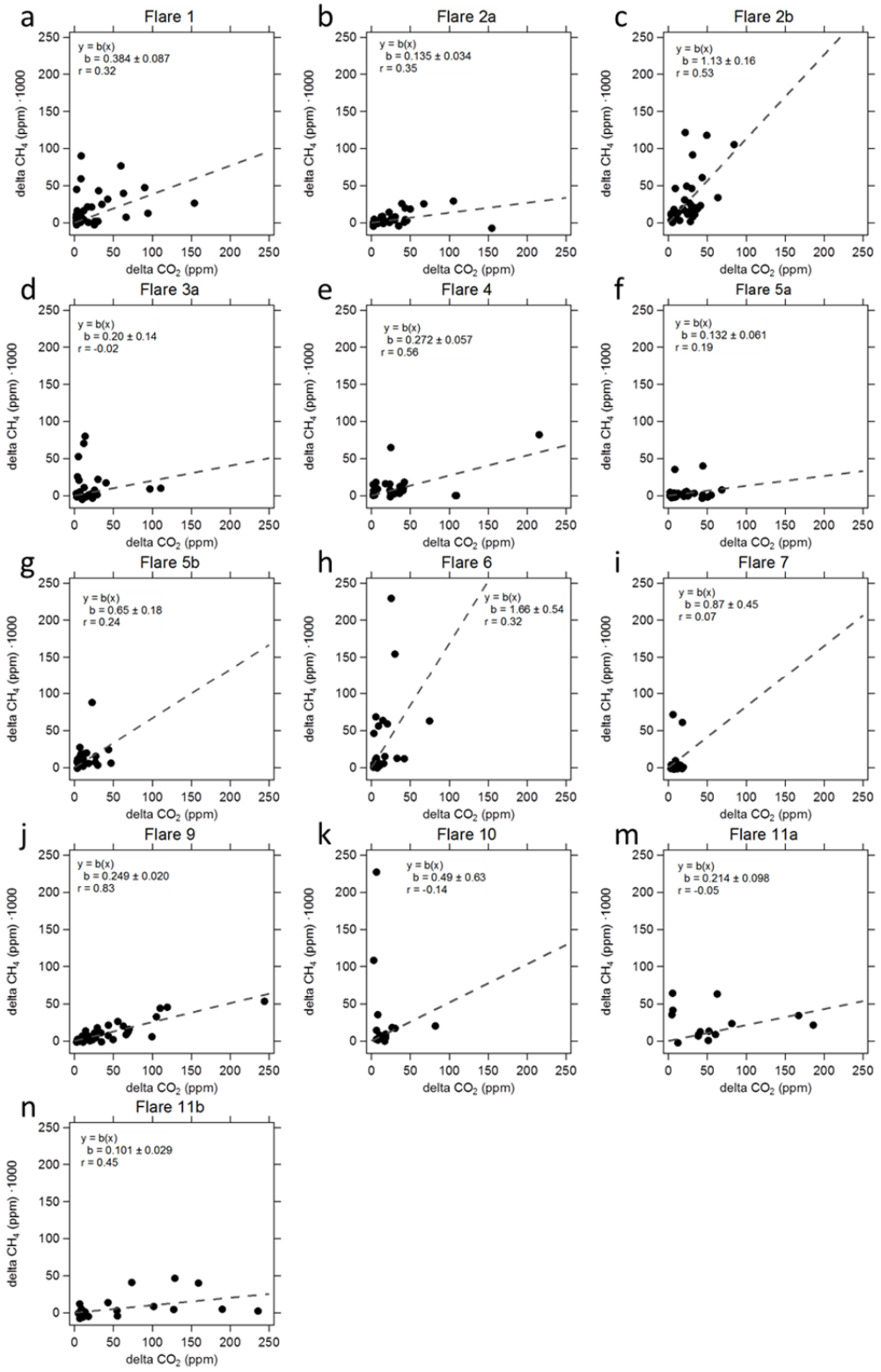

Figure 3.8 (a)-(n) Simple regression plots for all flares sampled. One sigma error of the slope and Person's correlation coefficient are reported.

Table 3.2 Simple regression results for each flare. The EF is equal to the slope. Also reported are the 1σ error of the slope and the Pearson correlation coefficient for each flare.

Flare	Points	Slope (ppm/ppm) ·1000	1σ Error of Slope	r
1	46	0.38	0.087	0.32
2a	37	0.135	0.034	0.35
2b	33	1.13	0.16	0.53
3a	29	0.20	0.14	-0.02
4	26	0.272	0.057	0.56
5a	35	0.132	0.061	0.19
5b	28	0.65	0.18	0.24
6	20	1.66	0.54	0.32
7	20	0.87	0.45	0.07
9	33	0.249	0.020	0.83
10	14	0.49	0.63	-0.14
11a	13	0.214	0.098	-0.05
11b	21	0.101	0.029	0.45
Average ± σ		0.50 ± 0.47		
Median		0.272		

Table 3.3. Regression results from integrated peaks for each flare. The EF is equal to the slope. Also reported are the 1σ error of the slope and the Pearson correlation coefficient for each flare. Points represent the number of plume transects with at least 3 points in the plume.

Flare	Points	Slope (ppm/ppm) ·1000	1σ Error of Slope	r
1	9	0.57	0.11	0.76
2a	9	0.177	0.054	0.59
2b	7	1.24	0.13	0.86
3a	7	0.32	0.32	-0.10
4	4	0.265	0.044	0.82
5a	8	0.187	0.083	0.61
5b	6	0.74	0.28	-0.19
6	5	2.19	0.43	0.89
7	3	0.79	0.42	-0.98
9	8	0.265	0.035	0.86
10	4	1.1	1.1	0.00
11a	4	0.33	0.15	0.12
11b	5	0.105	0.044	0.25
Average ± σ		0.64 ± 0.59		
Median		0.33		

In addition, an aggregate approach was performed by combining data from all flares and directly calculating the EF as the ratio of ΔCH_4 (in ppm) to ΔCO_2 (in ppm) for all matched data points (n = 355). During this analysis, several of the matched points produced negative EFs, which are not possible. This is assumed to be the result of small negative ΔCH_4 values that occur when the ΔCH_4 concentration is within the variability of the background concentration. The matched data points were screened for instances where the ΔCH_4 value was within $\pm 3\sigma$ of zero (a standard background criteria). Of the 355 data points from the entire data set, only 168 of these passed the 3σ CH_4 criteria. After isolating these points the effective limit of quantification (LOQ) for EFs was determined from the smallest quantifiable EF left. This value, 9.0×10^{-5}, was used for the points where the EF was not determinable. Thus 53% of the data is reported as the LOQ. The aggregated EF analysis is presented as an Ogive plot in Figure 3.9. Ogive plots present data (in this case EF) versus the cumulative probability where each data point has the probability 1/(n+1). This approach is similar to a cumulative histogram. However, an Ogive plot does not depend on classes like histograms, which may not preserve as much information as to the density of observations, particularly when data spans several orders of magnitude.

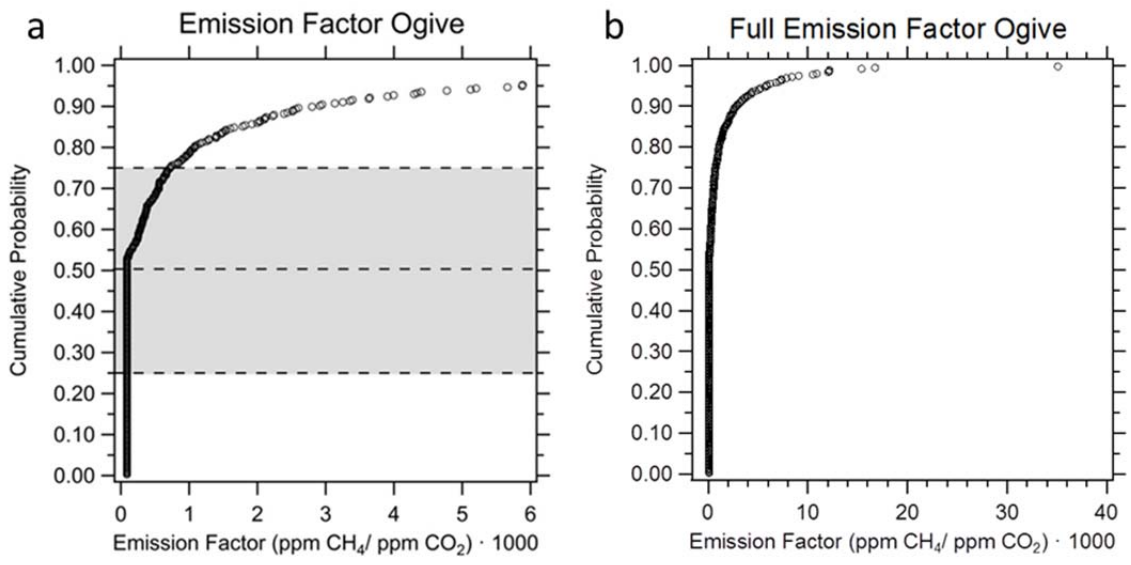

Figure 3.9 (a) The EF ogive up to 95% cumulative probability. The shaded area represents the 25-75% quartiles. (b) The full EF ogive plot.

3.3.2 Calculation of Flare Efficiency

Previous literature has traditionally used either combustion efficiency (CE) or destruction removal efficiency (DRE) in regards to flare efficiency (EPA, 1996; Johnson and Kostiuk, 2000; Kostiuk et al., 2000; Johnson et al., 2011; Torres et al., 2012a; Torres et al., 2012b; Knighton et al., 2012). CE is defined as the efficiency with which a flare completely converts the carbon in the fuel gas to CO_2. DRE is a measure of how efficiently a flare removes a certain species (such as CH_4) regardless of the combustion product. As complete information as to the composition of the fuel gas and combustion products are not available, calculation of DRE can be made by adopting with a few assumptions. First, it is assumed that CH_4 combusts completely to produce CO_2 and that CO and other combustion product production is negligible. Secondly, it is assumed that the original amount of CH_4 in the flare fuel gas is equal to the observed unburnt CH_4

plume plus some fraction of the observed CO_2 plume. The fraction of CO_2 from CH_4 combustion is derived from some commonly assumed natural gas composition scenarios (60, 80 and 100% CH_4) in recent literature (Howarth et al., 2011; Hultman et al., 2011; Jiang et al., 2011; Stephenson et al., 2011; NETL, 2011; Venkatesh et al., 2011; Burnham et al., 2012; Weber and Clavin 2012). The other major flare gas constituents (C_2H_6, C_3H_8, C_4H_{10} and C_5H_{12}) are distributed according to Rojey et al. (1997). Table 3.4 shows the three scenarios, the flare gas mol % distribution of each species, and the carbon mol % of each species.

Table 3.4 Assumed composition of flare gas for DRE calculations. Estimates for associated gas composition come from Rojey et al. (1997).

Scenario	Species	Flare Gas Mol (%)	Carbon Mol (%)
High CH_4	CH_4	100	100
	C_2H_6	0	0
	C_3H_8	0	0
	C_4H_{10}	0	0
	C_5H_{12}	0	0
Avg. CH_4	CH_4	80	58.4
	C_2H_6	10	14.6
	C_3H_8	5	10.9
	C_4H_{10}	3	8.8
	C_5H_{12}	2	7.3
Low CH_4	CH_4	60	35.1
	C_2H_6	20	23.4
	C_3H_8	12	21.0
	C_4H_{10}	5	11.7
	C_5H_{12}	3	8.8

After these assumptions have been applied the DRE can be calculated via equation 3.1:

$$DRE(\%) = (1 - \frac{\mu CH_4}{((X)\cdot \mu CO_2)+\mu CH_4}) \cdot 100 \quad 3.1$$

Where μCH_4 and μCO_2 are molar ratios and X is the fractional carbon composition attributed to CH_4 in the pre-ignited flare gas from Table 3.4. The DRE results calculated under each scenario for individual flare EFs from the simple regression are presented in Table 3.5. The Ogive plots for the aggregate analysis for each scenario are shown in Figure 3.10. The highest quantifiable DREs for each the 100, 80 and 60% CH_4 scenarios are 99.99%, 99.98% and 99.97%, respectively. Table 3.6 reports pertinent statistics for the aggregate EF and DRE results.

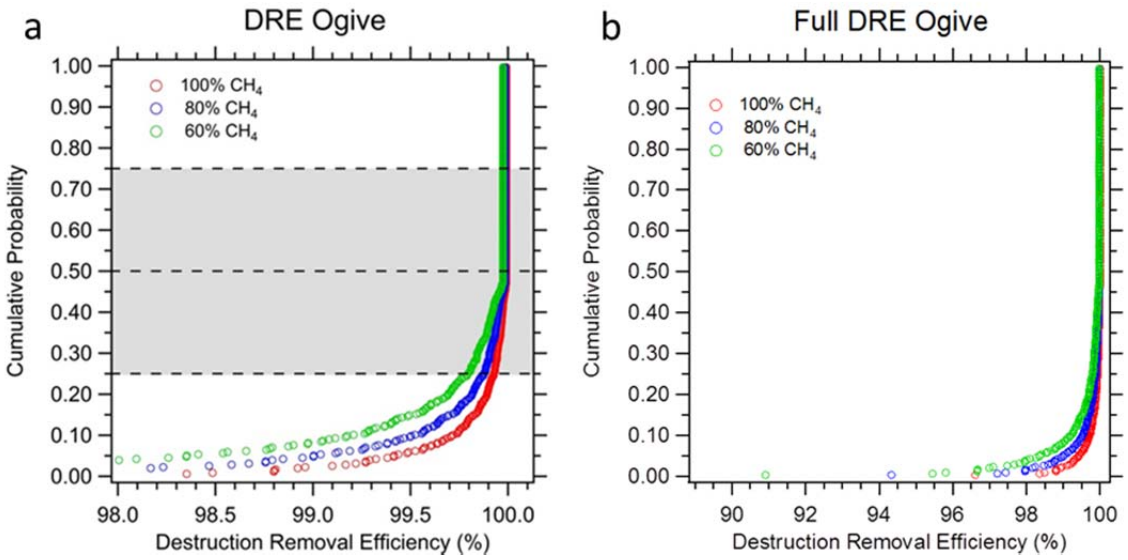

Figure 3.10 (a) The DRE ogives showing DREs greater than 98% efficient. The shaded area represents the 25-75% quartiles. (b) The full DRE ogives.

Table 3.5 Emission factors (ppm CH_4 /ppm CO_2) ·1000 and CH_4 destruction removal efficiency (DRE) calculated for each flare. No flare peaks were identified during analysis of Flare 8 and the second sampling of Flare 3.

Flare	Flight Passes	Emission Factor (ppm/ppm)·1000	DRE (100% CH_4)	DRE (80% CH_4)	DRE (60% CH_4)	Wind Speed (m/s)
1	14	0.38	99.962	99.935	99.892	4.8
2a	10	0.135	99.987	99.977	99.962	4.8
2b	7	1.13	99.887	99.807	99.679	14.7
3a	7	0.20	99.980	99.966	99.943	7.0
4	7	0.272	99.973	99.953	99.923	9.7
5a	10	0.132	99.987	99.977	99.962	8.6
5b	8	0.65	99.935	99.889	99.825	14.7
6	6	1.66	99.834	99.717	99.529	7.8
7	8	0.87	99.913	99.851	99.753	7.9
9	9	0.249	99.975	99.957	99.929	9.1
10	4	0.49	99.951	99.916	99.861	10.2
11a	4	0.214	99.979	99.963	99.939	5.6
11b	5	0.101	99.990	99.983	99.971	5.9
Average ± σ		0.50 ± 0.47	99.950 ± 0.047	99. 915± 0.080	99.86 ± 0.13	
Median		0.272	99.973	99.953	99.923	

Table 3.6 EF and DRE statistics including the median, min, max, mean and 25% and 75% quartile values. Also shown is the limit of quantification (LOQ) for the EF and the corresponding highest quantifiable DRE for each scenario.

Statistics		EF ppm/ppm	Statistics	DRE 100 % CH_4	DRE 80% CH_4	DRE 60% CH_4
Quartiles	Min	$<9.0 \times 10^{-5}$	Max	>99.99	>99.98	>99.97
	25%	$<9.0 \times 10^{-5}$	75%	>99.99	>99.98	>99.97
	Med	$<9.0 \times 10^{-5}$	Med	>99.99	>99.98	>99.97
	75%	7.1×10^{-4}	25%	99.93	99.88	99.80
	Max	3.5×10^{-2}	Min	96.61	94.33	90.91
	Mean	1.11×10^{-3}	Mean	99.89	99.81	99.69
	LOQ	9.0×10^{-5}	LOQ	99.99	99.98	99.97

3.3.3 Analysis of Wind Speed Effects on Efficiency

As part of the meteorological data collected, wind speeds were measured during each flight. In laboratory studies it has been observed that crosswind (wind perpendicular to the flare stack) speed can have a significant negative impact on flare efficiency and high crosswinds (15 m/s) decreased efficiency by up to 10% (Johnson and Kostiuk, 2000; Kostiuk et al., 2000). Simple regression data was used for the wind speed analysis as a directly corresponding average wind speed was calculated for each flare. A plot of wind speed and regression EF as well as the corresponding regression is shown in Figure 3.11. An exponential function was assumed because previous laboratory work suggests the relationship between wind speed and efficiency is not linear and appears to be exponential (Johnson and Kostiuk, 2000). The plots shows a low correlation coefficient of 0.09 and large scatter in the data that is likely unrelated to wind speeds.

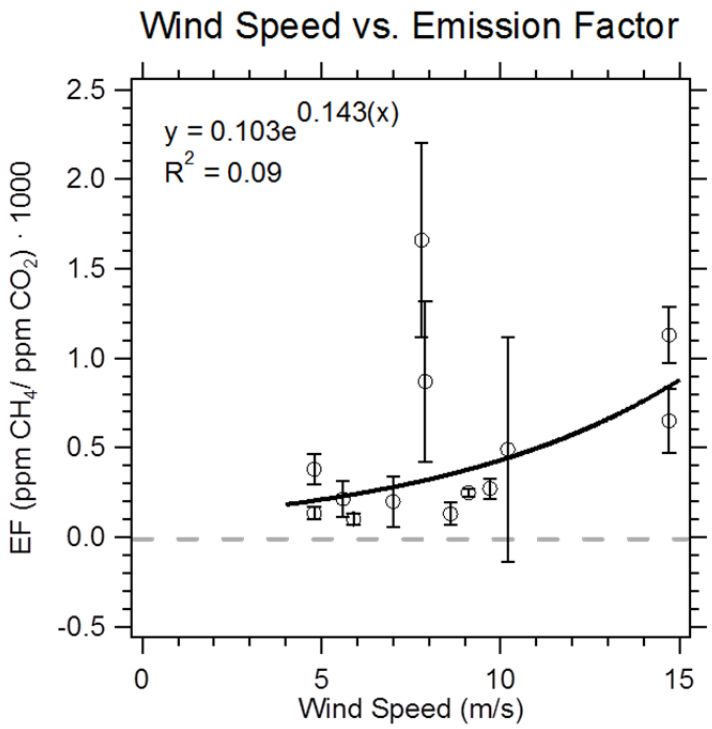

Figure 3.11 EF regression values for each flare plotted against crosswind speed. Error bars represent the 1σ error of the slope.

3.3.4 Flaring from other Shale Fields

As of 2012, the latest year with complete production data, flaring and venting in North Dakota accounted for about 37% of total U.S. flaring and venting and represented the state with the largest flaring and venting amount (EIA, 2014). However, other states, which may have different flaring practices or geology that affect flaring, also contribute to U.S. flaring. As of 2012, Texas was the state with the second largest flaring and venting amount, accounting for 22% of the total U.S. flaring and venting (EIA, 2014). In June of 2014 two flares located at (28.991°, -97.724°) and (29.076°, -97.699°) in the Texas Eagle Ford Shale were identified and successfully sampled as previously described

in this work, however, a limited number of sampling passes were performed for each flare. The flares were observed to have very small flames that often sputtered and went out. Due to the limited number of passes for each flare, EFs and DRE were calculated according to the aggregate analysis approach described in section 3.3.1. The results are shown in Figure 3.12. Statistics for the aggregate analysis are recorded in Table 3.7.

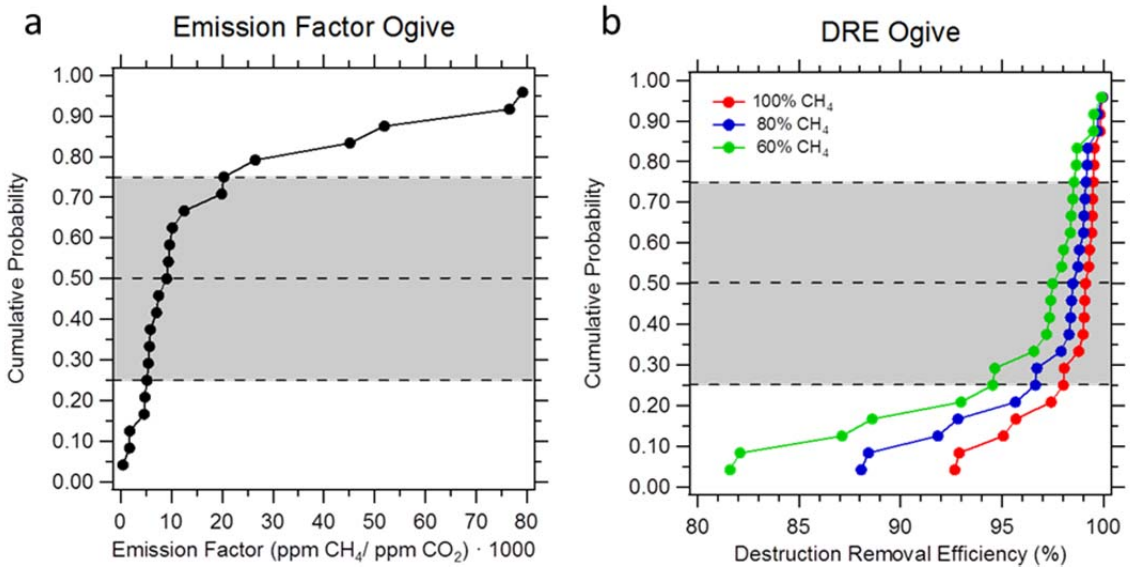

Figure 3.12 (a) The EF Ogive for the Texas flares. (b) The DRE Ogive for the Texas flares. In both graphs the shaded area represents the 25-75% quartile region.

Table 3.7 EF and DRE statistics including the median, min, max, mean and 25% and 75% quartile values for the Texas flares.

Statistics		EF ppm/ppm	Statistics	DRE 100 % CH_4	DRE 80% CH_4	DRE 60% CH_4
Quartiles	Min	4.0×10^{-4}	Max	99.9	99.9	99.9
	25%	5.3×10^{-3}	75%	99.5	99.1	98.5
	Med	9.0×10^{-3}	Med	99.1	98.5	97.5
	75%	2.0×10^{-2}	25%	98.0	96.7	94.6
	Max	7.9×10^{-2}	Min	92.7	88.1	81.6
	Mean	1.8×10^{-2}	Mean	98.3	97.1	95.4
	Std	2.3×10^{-2}	Std	2.1	3.5	5.4

3.4 Discussion and Conclusions

The EF results between the simple regression, integration regression, and aggregate analysis are consistent. The 25-75% EF quartile range for these analysis are 2.0×10^{-4} to 6.5×10^{-4} ppm/ppm, 3.3×10^{-4} to 7.9×10^{-4} ppm/ppm and 9.0×10^{-5} to 7.1×10^{-4} ppm/ppm, respectively. The consistency of these results suggests that any of these approaches will give accurate results. However, the calculated Pearson's product-moment for the integration regression analysis often shows higher values indicating better correlation between the data. This suggests that plume inhomogeneity is a source of random error. When multiple passes are available for integration the integration approach may reduce the scatter in the regression. However, the integration regression also generally had higher standard error on the slope (EF) as a result of the reduced data quantity from integration. The simple regression and aggregate analysis approaches have the advantage of preserving more observations in the event where data quantity is limited.

In all cases the reported EFs are very low. Median and 25-75% quartile values are used as best estimates for the EF values because the mean is often equal or greater than the 75% quartile value. Unlike the median, the mean can be greatly impacted by the low frequency high EFs we observed. These few very high EFs are likely caused by the inhomogeneity in the flare plume and/or the influence of other nearby CH_4 sources like venting operations on the well pad that could not be distinguished from the flare signal. The 25-75% quartile values from all analyses span less than a factor of 8 indicating that flare EFs did not very greatly over different sites and sampling days. The correspond DREs for all scenarios are also very high with 25% quartile values of 99.93%, 99.88% and 99.80% for the 100, 80 and 60% CH_4 scenarios, respectively. These results indicate that the sampled flares are extremely efficient in removing CH_4 and that the default 98% flare efficiency is overly conservative for these flares. It is important to note that these flares were constantly lit and never sputtered. The original 98% efficiency number also accounts for flame intermittency and venting when the flare is out (DRE = 0). It is therefore possible that flares under different conditions (e.g. the flares observed in Texas) that produce sputtering flames may be better represented by the 98% efficiency number. Limited observations from small, sputtering flare in Texas suggest the 98% efficiency may be appropriate for these types of flares, where the observed 25-75% quartile DREs were 98.0-99.5%, 96.7-99.1% and 94.6-98.5% for the 100, 80 and 60% CH_4 scenarios, respectively.

The wind speed analysis revealed a minimal negative effect caused by high wind speeds. Between the lowest (~5 m/s) and highest (~15 m/s) observed wind speeds the projected EF increases by less than a factor of 3. Overall the wind speed was not

observed to significantly impact the flare efficiency with no DRE value lower than 99.68% for the flares sampled under high wind speeds in all composition scenarios. In addition, the exponential fit, the fit that most closely resembles the expected relationship from previous work (Johnson and Kostiuk, 2000; Kostiuk et al., 2000), provides a coefficient of determination (R^2) value of 0.09 indicating that wind speed only marginally explains any observed variability in the flare EFs. The discrepancy between previous lab studies and these results may be explained by the configuration and operation of the flares sampled. Previous studies suggest that high gas exit velocities and large inside stack diameters correspond to lower sensitivity to crosswind speed (Johnson and Kostiuk, 2000; Kostiuk et al., 2000). Data related to actual flare construction and operation or the nature of any assist technology is not publicly available, however, it is possible that these variables mitigate any adverse effects of increased crosswind speed and are more important contributors to flare to flare EF variability.

In the course of sampling flare plumes over the Bakken Formation, CH_4 plumes uncorrelated to CO_2 plumes, and thus flares, were observed. As shown in Figure 3.13 these CH_4 plumes were often much larger than the flare CH_4 plumes. These non-flare plumes were typically sampled at altitudes 2-3 times higher than the flare plumes and were observed at higher altitudes and greater distances from potential sources indicating that these signals originated from substantially larger CH_4 sources than flares. The areas of the Bakken Formation sampled were generally undeveloped or cropland and noticeably strewn with oil well pads. This land use distribution means that common methane sources such as landfills, wetlands, dairy farms, waste water treatment plants and civic natural gas distribution infrastructure were scarce, and thus these plumes most

likely correspond to the extensive oil production activities in the area such as intentional venting or unintentional fugitive leaks and venting. In one case the source was identified as a dairy farm by circling the potential source and observing a CH_4 plume only downwind of the source. More field work is needed to identify these sources and understand how and why the emissions occur.

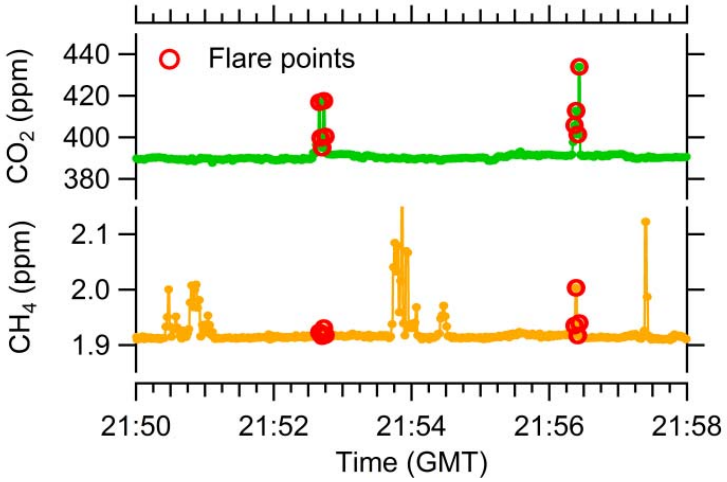

Figure 3.13 Time series of CO_2 and CH_4 for Flare 6, shown in Figure 3.3, showing flare signals circled in red. Several large CH_4 peaks are uncorrelated with flare signals.

Overall, existing shale gas flares can be very efficient in removing CH_4 such that, if the CH_4 would otherwise be vented, may have an advantageous short-term climate impact. Crosswind was not observed to be a significant contributor to decreased flare efficiency or flare to flare variability. Though all the analysis strategies used in this work were shown to produce similar results, some strategies may be more applicable for certain data measurement limitations. Future EF studies may be able to use high-frequency instruments to enable robust integration regressions and reduce the potential

for scatter in the regression techniques if a sufficient number of plumes are sampled. Additionally, small data sets where multiple passes are not available may benefit from the aggregate analysis approach to preserve data points, while still providing robust EFs. While CH_4 EFs are shown to be extremely low for all sampled flares in North Dakota and Pennsylvania it is important to note that flares used in different configurations that promote sputtering, such as those observed in Texas, may produce significantly different EFs. More work is needed to accurately assess emission factors and efficiencies of flares in different regions that may have different operators and different regulations. Nevertheless, in all sampled flares the CH_4 EFs are generally low and the impact of other compounds emitted from flaring, such as particulate matter, NO_x, black carbon or incomplete combustion products may have a more significant climate and air quality effect (Villasenor et al., 2003; Dung et al., 2008; Orimoogunje et al., 2010). These effects have not been extensively studied in the U.S., but should be pursued, particularly as flaring becomes more prevalent in the U.S (Villasenor et al., 2003; Dung et al., 2008; Orimoogunje et al., 2010). Recent tests of an industrial flare suggest flaring may increase NO_x emissions under low flow conditions using steam or air assist technology that allows too much air to mix into the flare (Torres et al., 2012a; Torres et al., 2012b; Torres et al., 2012c). However, recently NO_x emissions have been decreasing in the U.S. (Reuter et al., 2014). As NO_x and VOC emissions are important for ozone formation, regionally elevated NO_x levels may present local air quality problems despite nationally decreasing NO_x emissions (Ryerson et al., 2003; Kim et al., 2011; Oltmans et al., 2014).

CHAPTER 4. HEAT AND CO_2 FLUXES FROM THREE EAST COAST FOREST SITES

4.1 Motivation for Research

Real-time observations of ecosystem heat and CO_2 exchange are important for both understanding ecosystem interactions and variability and constraining models that aim to simulate the net ecosystem exchange (NEE) of CO_2 across large areas, e.g. continents (Hollinger et al., 2004; Maselli et al., 2010; Drohan et al., 2012; Fu et al., 2014;). However, long-term monitoring is typically conducted at tower sites, at which measurements of fluxes can be conducted from an upwind source area, or footprint, of only a few km^2. Tower sites are often chosen because they are accessible and cover simple topography and homogeneous landcover type to enable testing of our understanding of individual ecosystems through modeling. However, they may not be representative of the larger region they are being used by models to constrain, which may span ~10,000 km^2. Studies that focus on the representativeness of tower sites largely focus on landcover type and normalized difference vegetation index (NDVI), which is a measure of the extent and location of photosynthetically active vegetation types (Kustas et al., 2006; Barcza et al., 2009; Chen et al., 2012). Many other parameters may be important contributors to regionally heterogeneous surface fluxes including topography, soil type, temperature, precipitation and soil moisture (Urbanski et al., 2007; Medvigy et

al., 2010). Root zone soil moisture (RZSM), for instance, is expected to account for up to 80% of the interannual variability in NEE fluxes in boreal forests (Griffis et al., 2004; Krishnan et al., 2006; Seneviratne et al., 2010).RZSM has been defined or estimated differently in different studies based on data availability. In this analysis, RZSM is defined as the soil moisture content below the surface soil or the soil moisture content below 10 cm to a depth of 100 cm. There is urgent need for large scale data for important parameters, including large scale NEE fluxes for model comparison. To accomplish this, remote sensing and aircraft platforms are necessary.

Aircraft platforms have been used to measure surface fluxes since the late 1980s and can access and sample a much larger area than most tower measurements (Desjardins et al., 1989; Desjardins, et al., 1995; Desjardins, et al., 1997; Dobosy, et al., 1997; Gioli et al., 2004; Gioli et al., 2006; Miglietta et al., 2007; Kirby et al., 2008; Hutjes et al., 2010; Maselli et al., 2010; Vellinga et al., 2010; Metzger et al., 2012; Metzger et al., 2013; Vellinga et al., 2013). The extent of the footprints of aircraft measurements is dependent on the altitude and length of the sampling transect and thus may change significantly depending on the experimental design. Typical aircraft measurement footprints can range from 10-100 km^2. Additionally, as aircraft are highly mobile, they can sample areas far from towers and other monitoring sites including areas with high topographic variation that are not ideal for tower monitoring. However, aircraft data are typically not able to be collected over long time periods due to financial, technical, logistical and weather constraints. While aircraft platforms cannot provide necessary long-term monitoring, they can be used to supplement tower data and aid in model evaluation of regional scale models.

Measurements of parameters vital to models such as landcover and NDVI can be made with radar and satellite data. Landcover, which is a measure of the surface land type (e.g. deciduous forest, wetland, urban, etc.) is made using a combination of remotely sensed data including surface reflectance, surface temperature and surface texture (Friedl et al., 2002; Justice et al., 2002). A key parameter used in landcover determination is absorption at photosynthetically active wavelengths (Friedl et al., 2002; Justice et al., 2002). This is also a key determiner of NDVI. The Soil Moisture Active Passive (SMAP) satellite and the Soil Moisture Ocean Salinity (SMOS) satellites collect surface soil moisture data (typically up to a depth of ~5 cm) using L-band synthetic aperture radars (SAR) (Kerr et al., 2001; Entakhabi et al., 2010). Both satellites provide complete global soil moisture data every 3 days, though SMOS (operated by the European Space Agency) provides data at 50 km resolution and SMAP (operated by NASA/JPL) at 3 km resolution (Kerr et al., 2001; Entakhabi et al., 2010). L-band SARs use microwave radiation at wavelengths of about 23 cm, which can penetrate vegetation and cloud cover and soil up to ~5 cm (Ulaby et al., 1996; Moghaddam et al., 2000; Reigber and Moreira 2000). P-band SARs use microwave radiation at lower frequency (wavelength of around 68 cm), which can return information about soil moisture up to 1.2 m in depth and can is less affected by dense vegetation cover (Ulaby et al., 1996; Moghaddam et al., 2000; Reigber and Moreira 2000). Currently, P-band SAR has not been deployed on satellites for long-term monitoring.

In this study, an instrumented aircraft was flown over three east-coast forest sites, shown in Figure 4.1, to collect CO_2 and heat fluxes at sites over large study regions (~10,000km^2) including sites far from ground towers. The goal of this study is to

determine typical uncertainties for aircraft flux measurements as well as analyze the drivers of the observed variability. In addition, the Airborne Microwave Observatory for Subsurface and Subcanopy (AirMOSS) campaign was ongoing and coincident soil moisture detected by a P-band SAR onboard a NASA G-III jet was available for some flights. Finally, the aircraft data will be compared to tower data in an effort to evaluate the quality of the aircraft data and to evaluate tower representativeness of the broader regions they typically represent for modelling use.

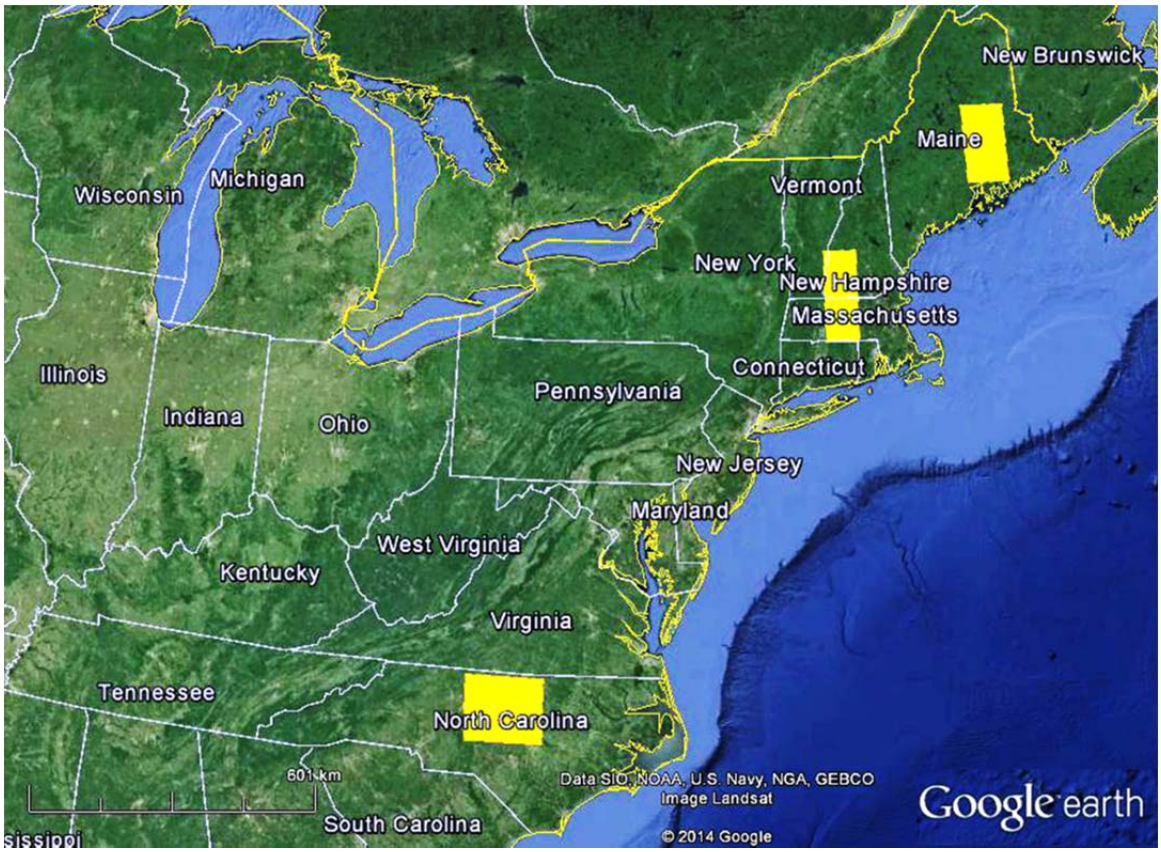

Figure 4.1 Forest sites sampled highlighted in yellow.

4.2 Experiment Design

4.2.1 Site Description

Measurements were conducted in July 2012 and May-August 2013 over Harvard Forest, Massachusetts, Howland Forest, Maine and Duke Forest, North Carolina. A summary of the flight experiments is shown in table 4.1. Harvard Forest is a ~80 year old temperate forest. The primary landcover is deciduous or mixed (deciduous and evergreen) forest with the dominant tree species being red oak, red maple, red and white pine, yellow and white birch, beech, ash, sugar maple and hemlock (Wofsy et al, 1993). The area is hilly and sparsely populated. The average canopy height is 23 m. An eddy covariance tower at this site is located at 42.5378°, -72.1715° and has been operational since 1990 (Wofsy et al, 1993). Flux and meteorological measurements at the tower are made half-hourly at 30m (Goulden et al., 1996). Howland Forest is a ~110 year old temperate forest that is primarily evergreen and mixed forest. The dominant tree species are red spruce, eastern hemlock, balsam fir, white pine, northern white cedar, red maple and paper birch. The area is flat and very sparely populated. The canopy height is 20 m. A tower measuring hourly fluxes and meteorology is located at 45.2041°, -68.7402° and has been operational since 1996 (Hollinger et al., 1999). Duke Forest is a temperate ~90 year old mixed forest. Dominant tree species include mockernut hickory, pignut hickory, tuliptree, sweetgum, white oak, red maple, loblolly pine, swamp chestnut oak, willow oak, American hornbeam, hophornbeam, winged elm, flowering dogwood, eastern redbud, and eastern redcedar (Herrick et al., 1999). The average canopy height is 19 m. A tower measuring hourly fluxes and meteorology is located at 35.9782°, -79.0942° and has

been non-continuously operational since 1998. The area is generally flat with prevalent crop and grazing land and large urban centers (Raleigh, Durham and Greensboro). Pertinent instrumentation at all sites consists of a LI-COR CO_2/H_2O infrared gas analyzer, an Applied Technologies sonic anemometer, and a Radiation and Energy Balance Systems Net Radiometer. The landcover distributions for the 3 forest sites are shown in Figure 4.2, with pie charts of the total landcover distribution at each site shown in Figure 4.3. The landcover distributions around the tower sites is shown in Figure 4.4and shown predominantly deciduous forest at Harvard and evergreen forest in Howland and Duke. Harvard and Howland Forests experience predominantly southwest and northwest winds, while Duke Forest experiences predominantly southwest winds.

Table 4.1 Summary of flight experiments.

Flight Date	Site	Time (EDT)	Wind Dir.	Wind Speed (m/s)	Soil Moisture Data	Main Landcover Type
7/7/2012	Harvard	12:04	294	6.54	N	Deciduous
7/7/2012	Harvard	13:35	294	7.19	N	Deciduous
7/8/2012	Harvard	12:07	307	4.67	N	Deciduous
7/8/2012	Harvard	13:01	284	5.71	N	Deciduous
7/8/2012	Harvard	15:34	308	6.93	N	Evergreen
7/9/2012	Harvard	13:20	325	5.86	N	Deciduous
7/9/2012	Harvard	16:01	310	6.03	N	Deciduous
7/10/2012	Howland	14:07	275	6.17	N	Evergreen
7/10/2012	Howland	15:05	278	7.15	N	N/A*
7/11/2012	Howland	13:14	268	4.96	N	Evergreen
5/30/2013	Harvard	13:45	276	8.18	Y	Deciduous
5/30/2013	Harvard	15:52	279	8.44	Y	Evergreen
5/31/2013	Harvard	12:06	262	6.46	N	N/A*
5/31/2013	Harvard	13:09	229	5.40	N	Deciduous
6/1/2013	Howland	12:57	227	7.72	N	Evergreen
6/1/2013	Howland	14:08	231	7.29	N	Evergreen
6/2/2013	Howland	12:19	175	5.66	Y	Evergreen
6/2/2013	Howland	13:35	171	7.01	Y	N/A*
6/4/2013	Duke	1237	47	4.18	Y	Deciduous
6/4/2013	Duke	14:01	74	4.33	Y	Cropland
7/7/2013	Duke	16:53	204	6.66	N	Deciduous
7/8/2013	Duke	12:41	249	2.63	N	Deciduous
7/8/2013	Duke	14:30	246	3.09	N	Deciduous
7/9/2013	Duke	12:39	200	3.78	Y	Deciduous
7/9/2013	Duke	14:37	183	4.28	Y	Deciduous
7/10/2013	Duke	12:57	214	6.78	N	Deciduous
7/10/2013	Duke	15:12	201	5.56	N	Cropland
8/19/2013	Howland	12:47	289	8.22	Y	Mixed Forest
8/19/2013	Howland	14:17	276	6.57	Y	Evergreen
8/20/2013	Howland	12:28	235	3.11	N	Evergreen
8/21/2013	Harvard	12:05	269	3.70	N	Deciduous
8/21/2013	Harvard	13:36	260	4.21	N	N/A*
8/22/2013	Harvard	12:20	224	5.08	Y	Evergreen
8/22/2013	Harvard	13:58	221	4.98	Y	Mixed Forest
8/23/2013	Duke	14:21	307	4.10	N	Deciduous
8/24/2013	Duke	12:20	39	6.13	Y	Deciduous
8/24/2013	Duke	14:07	46	6.84	N	Deciduous

*These sites had no majority landcover type. See Figure 4.16.

.

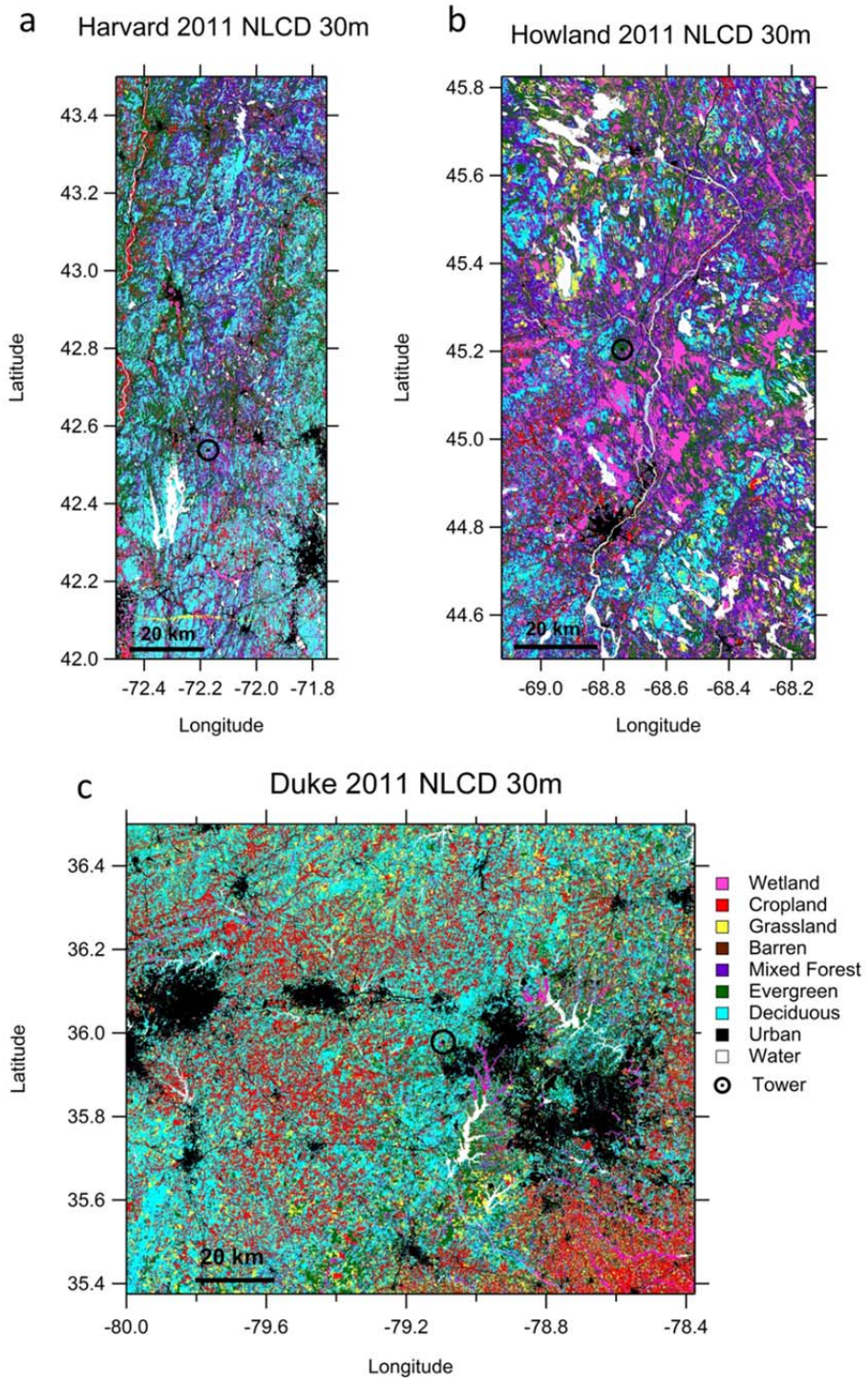

Figure 4.2 Landcover maps using 2011 national landcover database (NLCD) 30m resolution data for (a) Harvard, (b) Howland and (c) Duke Forests.

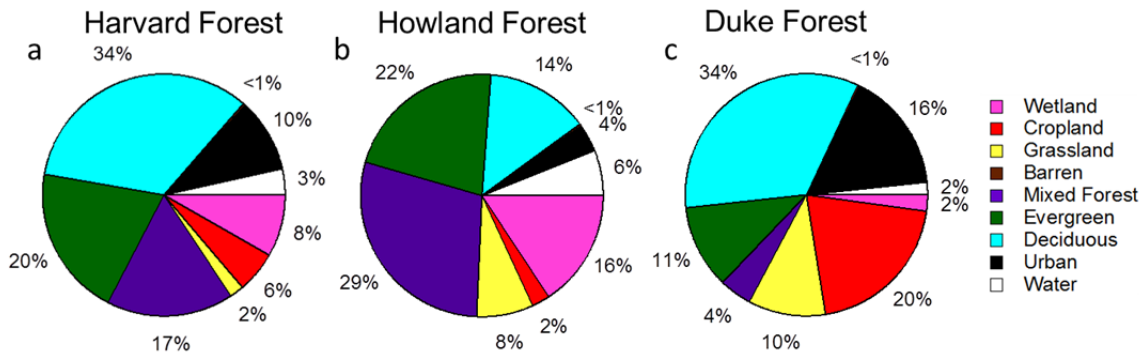

Figure 4.3 Pie charts of landcover distribution over the whole study are of (a) Harvard Forest, (b) Howland Forest and (c) Duke Forest.

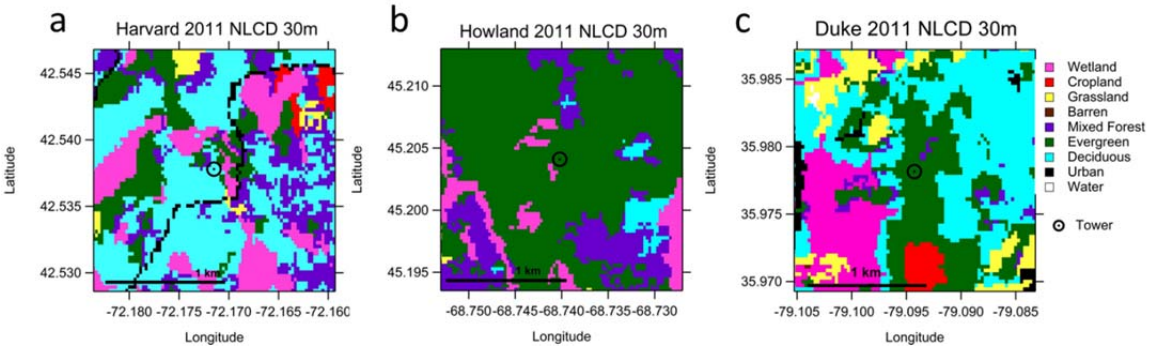

Figure 4.4 Location of tower sites on landcover maps for (a) Harvard, (b) Howland and (c) Duke Forests. Plots show a 4 km^2 region centered on the tower.

4.2.2 Instrumentation and Flight Design

Data was collected using ALAR equipped with instrumentation as described in Chapter 2. However, for eddy covariance measurements the CRDS was switched to flux mode, which allows for 10 Hz CO_2 and H_2O data collection. In this mode precision is calculated as 0.3 ppm for CO_2 and reported as 30 ppm for H_2O. While the CRDS collects

data at this frequency, a KNF vacuum pump pulls air through the CRDS at ~3 L min^{-1} giving an the actual response time of ~3 Hz, determined by response time tests. Due to inadequate pressure in the sampling line, calibrations must be made on the ground instead of in the air. Typically, one calibration is made using the previously described standards prior to each flight.

Sampling transects were chosen to isolate areas of relatively homogeneous landcover. Transect lengths were designed to encompass the entire spectrum of eddies that may contribute to flux and thus were between 15-20 km. Previous work indicates that the minimum distance that can be covered and still sample all important eddies is ~4 km (Desjardins et al., 1989; Lenschow et al., 1994; LeMone et al., 2003). Figure 4.5 shows an ogive plot of the CO_2 and vertical wind covariance that is used to derive the minimum flight distance. As a stringent cutoff, 99.9% of the contributing eddies occur at lengths less than or equal to10 km (10^{-4} m^{-1}). To ensure representative sampling of larger eddies, this minimum distance was doubled to produce the 20 km ideal transect length used in the flight design. The effect of using a less stringent transect length criteria will be examined. For example, approximately 99% of the eddies occur at length less than or equal to 5 km (2×10^{-4} m^{-1}). Reducing transect length requirements may allow for faster experiment completion and isolation of small homogeneous surface features.

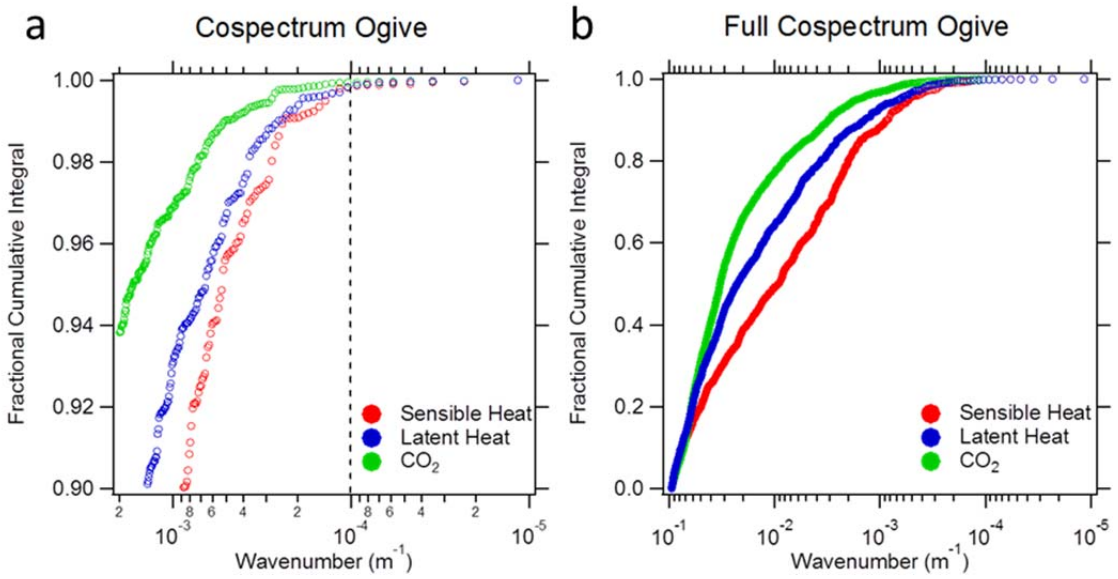

Figure 4.5 (a) Typical ogive plot for vertical wind covariance with potential temperature (red), H_2O (blue) and CO_2 (green) showing that >99% of the flux is carried by eddies smaller than 10 km. (b) Shows the full cospectrum ogive.

Flight experiments were designed to account for vertical flux divergence and minimize random sampling error (Stull, 1988). Typically, three low altitudes were chosen over a specified transect and each altitude was sampled three (non-sequential) times. Transect passes were flown at low air speeds (~55 m/s) and took less than 10 minutes each with a whole experiment completed in about 90 minutes. Data were collected between 11 AM and 4 PM in an attempt to sample large flux signals that did not change greatly over time, e.g. due to changes in boundary layer structure and photosynthetic activity. At least one vertical profile was collected during every experiment to determine boundary layer depth.

Once fluxes were calculated for each transect, results from similar heights were averaged and then a linear regression was used to extrapolate to surface level flux.

Extrapolation is necessary due to the flux divergence in the atmosphere above the surface layer as discussed in Chapter 1 (Stull, 1988). Additionally, Desjardins et al. (1989) observed significant flux divergence even in the surface layer. Fluxes are expected to linearly decrease up to the top of the boundary layer, therefore fluxes measured at individual sampling heights cannot be directly compared to tower or other surface data (Stull, 1988). Figure 4.6 shows an example extrapolation for all three fluxes. Tower data is typically calculated to half-hour or hour increments and must be linearly interpolated to compare to aircraft fluxes made between tower observations.

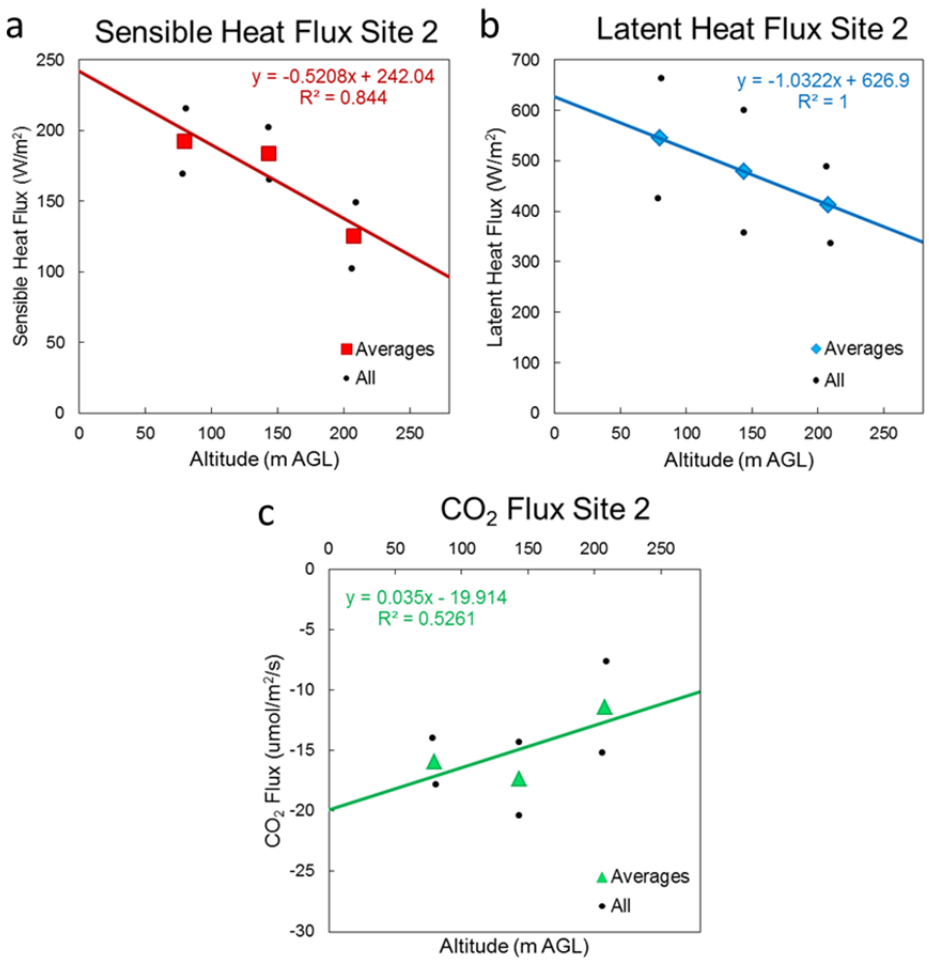

Figure 4.6 Linear extrapolation to the surface for (a) sensible heat, (b) latent heat and (c) CO_2 flux. The large colored points denote averaged fluxes, while the small black dots show individual observations.

4.3 Flux Calculations

As described in the introduction, turbulent flux measurements are made using the eddy covariance method, where high frequency vertical wind and trace gas data are used according to equation 4.1.

$$F_c = \frac{1}{\bar{S}T}\sum(w'c')S_i\,\Delta t \qquad 4.1$$

Here, S is the groundspeed of the aircraft (m/s), T is the duration of the measurements (s), Δt is the time between measurements (s), w is vertical wind (m/s) and c is a scalar on interest. The prime denotes the values used are perturbations from the average over the measurement timeframe. The effect of using both aircraft groundspeed and time is to produce a spatial average, rather than a time average produced by flux towers. A time series of raw data collected at ~180 m AGL used to calculate flux is shown in Figure 4.7. As shown in the figure upward eddies (positive vertical wind perturbations) are depleted in CO_2 and enriched in H_2O due to the surface forest sink and source, respectively.

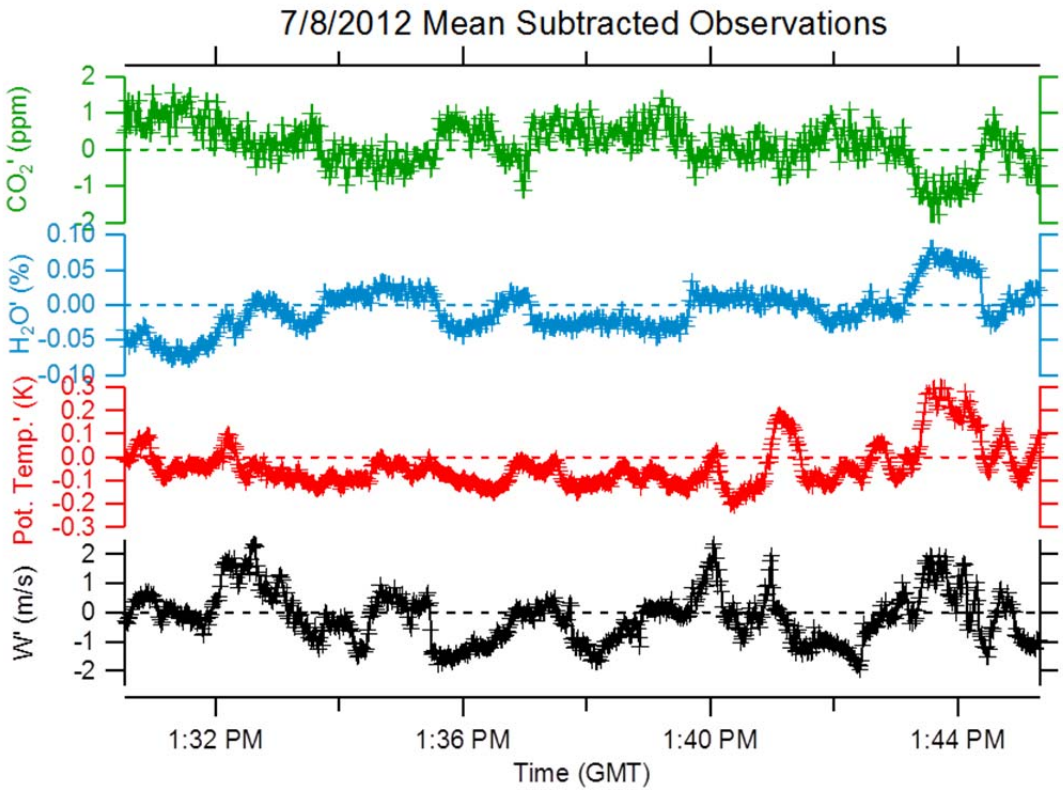

Figure 4.7 Mean-subtracted observations of CO_2, H_2O, Potential Temperature and Vertical wind over a forest site on 7/8/2012.

Prior to calculating fluxes a lag adjustment is made. Due to the delay between the measurement of air speed at the BAT probe and measurement of gas concentration in the CRDS, there is not synchronous correlation between the two measurements, in the absence of time scale adjustment. To realign the data, a covariance calculation between vertical wind and either CO_2 or H_2O is made for the data. The covariance program adds a lag to the CO_2 and H_2O data, effectively shifting it along the vertical wind speed time series. The output consists of a covariance value at each lag increment. The optimum lag is determined to be where CO_2 shows maximum negative correlation and H_2O shows maximum positive correlation with vertical wind. Lags were calculated for each experiment and did not drift significantly from day to day. Though H_2O and CO_2 have been observed to have different lags in certain experimental set-ups, no significant difference in lag was observed in this configuration. This is most likely due to the short manifold and low resonance time in the manifold (~0.1s). Data was visually inspected for potential spikes (outlier points caused by electronic or other noise), which were rare, and a de-spiking protocol was used only if a potential spike was suspected. After analysis no parameters were identified to contain real spikes, defined as points 10σ above the mean, at any time during flux transects.

Fluxes for sensible heat (H), latent heat (LE) and CO_2 were calculated according to equation 4.1 using dry air mixing ratios directly recorded by the CRDS. Sensible heat flux is the vertical transport of heat stored in the atmosphere and uses potential temperature as the generic scalar ‘c’ in equation 4.1. Latent heat flux is the vertical transport of potential heat stored in the evaporated water of the atmosphere and uses H_2O as ‘c’ in equation 4.1. Finally, CO_2 flux is the vertical transport of CO_2 and uses CO_2 as

'c' in equation 4.1. In all cases positive fluxes indicate a net upward transport or source and negative fluxes indicate a net downward transport or sink. The use of dry air mixing ratios allows corrections for density fluctuation caused by changes in temperature and water, known as the Webb-Pearman-Leuning (WPL) correction, to be neglected (Webb et al., 1980). Fluxes are then converted to standard units (Wm^{-2} and $\mu mol\ m^{-2}s^{-1}$) using average air density and the heat capacity of air.

4.3.1 Corrections

Typically, eddy-covariance measurements require multiple corrections to be made including wind corrections, density fluctuation corrections, sampling-line corrections and spectral corrections (Burba, 2005). Eddy covariance measurements require very accurate vertical wind measurements. At tower sites, which use stationary wind measurement equipment, vertical wind accuracy may be affected by tilted equipment and surface up-slope or down-slope flows (Horst et al., 1986; Frank et al., 2013). Slight tilting of the instrumentation can cause some of the horizontal wind to be recorded as vertical wind. Particularly at night and in early morning, up slope and down slope 'drainage' flows can cause the mean horizontal wind direction to deviate from being completely horizontal and also cause overestimation of the vertical wind component (Horst et al., 1986). Advancements have been made to account for errors in tower measurements (Wilczak et al., 2001). However, the aircraft BAT probe data processing already measures the angle at which wind data is collected and corrects the data. The BAT probe has been extensively calibrated and corrections have been made for lift-induced upwash, which would otherwise affect the vertical wind measurements (Garman et al., 2006, Garman et

al., 2008). Additionally, the aircraft should be far enough from the surface that local flow distortions do not affect the measured wind data. Therefore, no additional wind corrections were made. As stated previously, WPL corrections were neglected by using the dry air mixing ratios directly recorded by the CRDS. Sampling line corrections may be needed for sites with long sampling lines, particularly for H_2O, where long sampling lines dampen fluctuations and allow mixing in the tube (Burba, 2005). Due to the short nature of the sampling manifold, ~3m, and short resonance time (~0.1s), it is assumed that no sampling line corrections are needed.

Of the corrections mentioned, the only one identified as applicable was the spectral correction. Due to sampling frequency limitations, it is impossible to sample the full range of eddies contributing to the flux, particularly in the high-frequency range (Moore, 1986; Burba, 2005). As high frequency eddies are the result of the turbulent energy cascade, they follow a predictable decay curve in the inertial subrange (Stull, 1988). This area typically encompasses eddies smaller than ~100 m (Stull, 1988). This curve can be modelled and applied to the observed turbulence cospectrum of vertical wind and any desired parameter to correct for the flux carried by the eddies not sampled. The spectral correction procedure used was developed by Stefan Metzger and is described in Metzger et al. (2013). The procedure uses the Massman (2000) model to predict the cospectrum shape. The integration of the observations compared to the model can then be used to determine the flux underestimation. Median spectral corrections for CO_2, sensible and latent heat flux were 20%, 21% and 20%, respectively. Due to the influence of the surface limiting the size of eddies physically possible, lower altitudes are

expected to have higher spectral corrections. Figure 4.8 shows the smoothed vertical correction as a function of scaled height (observation altitude/CBL depth).

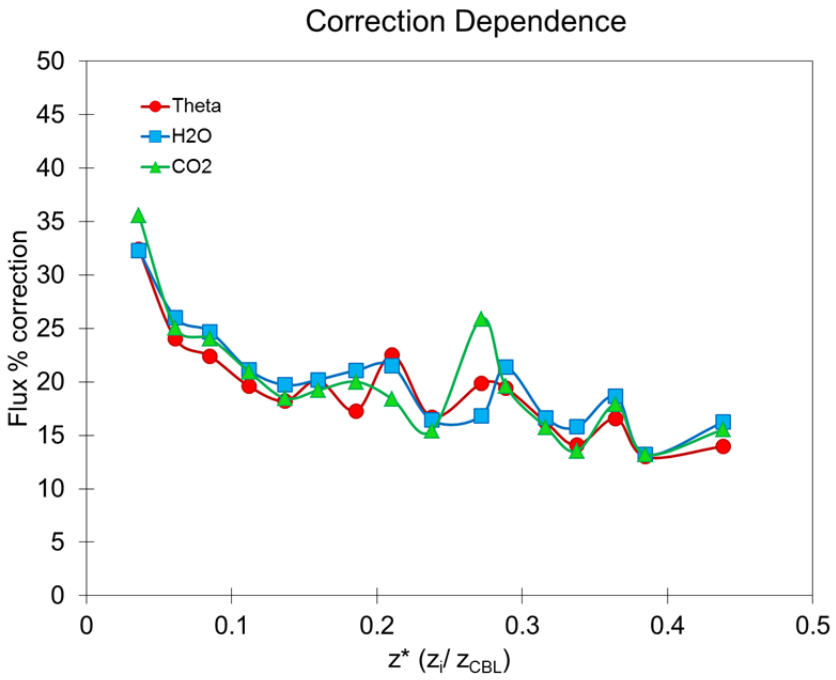

Figure 4.8 Smoothed plot of flux % correction vs. scaled altitude ($z_*=z_i/z_{CBL}$).

As part of the quality control process, data points were flagged if the magnitude of the spectral correction was larger than 50%. This value was chosen because it corresponds to the average spectral correction (33%) + 3σ of the spectral corrections at the lowest altitude (6%). In addition, data were flagged for transects with a friction velocity value of less than 0.2 m/s and a zeta value of greater than 1. Friction velocity is a measure of mechanical turbulence in the atmosphere and is calculated according to equation 4.2.

$$u_* = [(\overline{u'w'})^2 + (\overline{v'w'})^2]^{1/4} \qquad 4.2$$

Here, u is the northerly wind component, v is the easterly wind component and w is the vertical wind component. Low friction velocity values can indicate insufficient turbulence to measure eddy covariance fluxes. Zeta is a non-dimensional stability parameter generated by dividing observation altitude by the calculated Obukhov length (L) which is presented in Equation 4.3.

$$L = \frac{-\overline{\theta_v} u_*^3}{k \cdot g \cdot (\overline{w' \theta_v'})} \quad 4.3$$

Here, is θ_v virtual potential temperature, u_* is friction velocity, k is the dimensionless von Karman constant estimated as 0.4 and g is the gravitational acceleration constant 9.8 m s^{-1}. Virtual potential temperature is calculated according to equation 4.4.

$$\theta_v = \theta(1 + 0.61 r_{sat} - r_L) \quad 4.4$$

Here, r_{sat} is the water vapor saturation value and r_L is the liquid water mixing ratio (used if the air parcel is supersaturated). Negative zeta values indicate neutral to unstable conditions that generate turbulence sufficient for eddy covariance flux measurements while positive zeta values indicate stable conditions that may not be suitable for flux observations (Stull, 1988). All flagged data were not used for subsequent analysis or calculations. Additionally, as data quality is also dependent on a suitable number of observations through the boundary layer to characterize the flux gradient, experiments where less than two observations at each altitude were available were discarded. Of the 296 observations, 18 were flagged and of the 37 experiments, up to 5, 7 and 8 were discarded using these criteria for sensible heat, latent heat and CO_2 flux, respectively.

4.3.2 Error Analysis

An important part of any analytical measurement is uncertainty analysis. Errors affecting measurements may be random or systematic (biases). Though methods have been published to calculate both random and bias error, here only random error was calculated (Mann and Lenschow, 1994; Rannik and Vesala, 2012; Salesky et al., 2012; Wang et al., 2014). The experimental design and applied corrections are made so as to minimize any bias in the measurement technique due to lag in the data or spectral under-sampling. Other bias in the flux calculation shown in Equation 4.1 may come from bias in the scalar measurement, wind measurement, or groundspeed measurement. An important feature of the calculation is that perturbations from the mean are used, not absolute concentration. Therefore any biases in the absolute measurements should cancel out. For instance, the vertical wind component is corrected for variability in lift-induced upwash, however a constant ~2 m/s upwash bias is left over in the data. From calibrations with NOAA/ESRL standards described in Chapter 2, uncertainty in the scalar concentrations are 0.3 ppm and 30 ppm for CO_2 and H_2O, respectively, while the error in the vertical winds is 0.06 m/s and in the groundspeed is 0.4 m/s (Garman et al., 2006; Garman et al., 2008). Importantly, wind and scalars do not deviate from expected relationship (-5/3 slope) in the inertial subrange indicating there is not inherent bias in the instrument set-up for the parameters. Power spectral density plots of vertical winds, potential temperature, CO_2 and H_2O are shown in Figure 4.9. Propagating the instrument uncertainties through Equation 4.1 gives an expected uncertainty of ~3 % which is small compared to extrapolation errors that will be discussed. As there may be unknown

systematic errors, the aircraft data will be compared to tower measurement at all three sites to observe any residual biases after data processing.

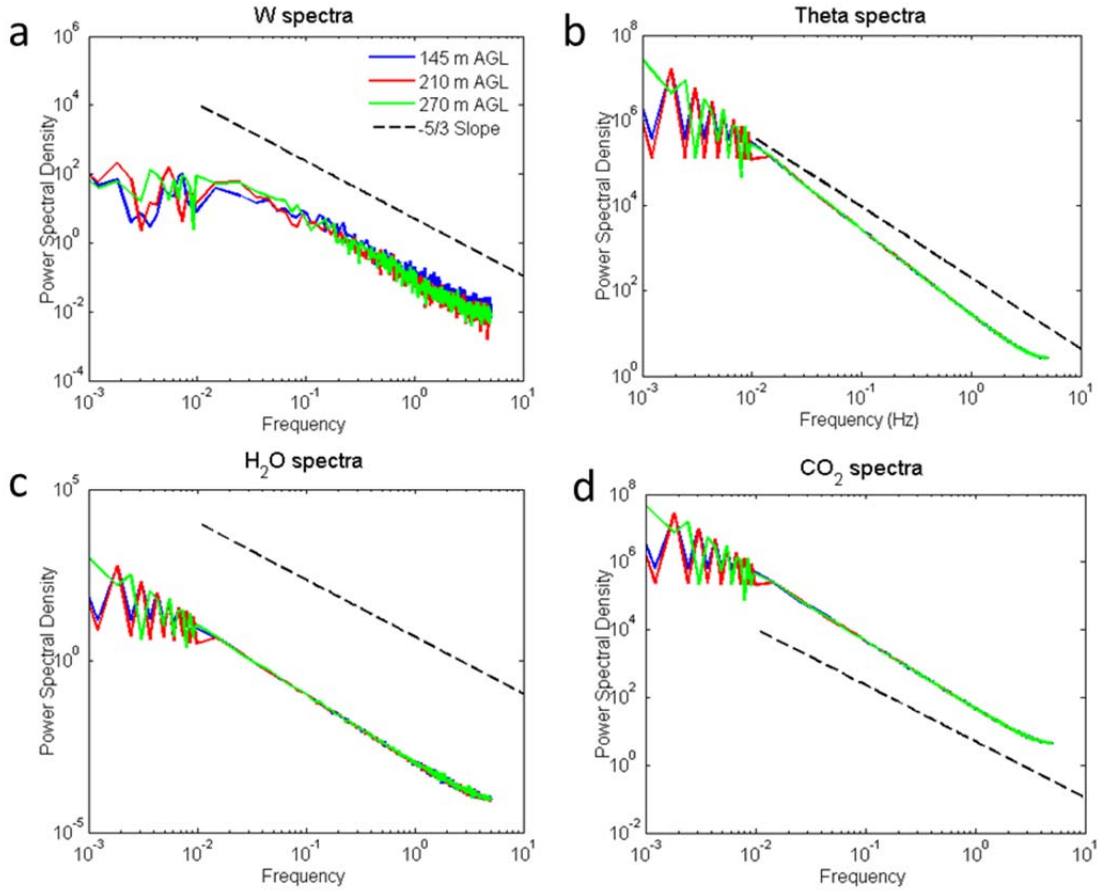

Figure 4.9 Power spectral density plots for three altitudes during Flight 7/7/2012 over Harvard Forest. Shown are spectra for (a) vertical wind, (b) potential temperature, (c) H_2O and (d) CO_2 with the expected -5/3 relationship as a dashed black line.

Random errors for individual observations (σ_F) are calculated according to Mann and Lenschow (1994), shown in Equation 4.5.

$$\sigma_F = 0.57 z_*^{\frac{1}{6}} \left(\frac{1+r_{ws}^2}{r_{ws}^2}\right)^{\frac{1}{2}} (1-\gamma \cdot z_* - z_*) \left(\frac{L}{z_i}\right)^{-\frac{1}{2}} (F_i - m \cdot z_i) \quad 4.5$$

Here, z_* is the observation altitude in m (z_i) scaled by boundary layer depth in m, L is the length of the transect (m) and F_i is the observation flux. The slope,m, is derived from the gradient of the fluxes averaged at each altitude for each experiment. The variables $r_{ws}^2$and γ are defined in Equations 4.6 and 4.7, respectively.

$$r_{ws} = \frac{(1+(\gamma-1)z_*)0.75{z_*}^{-\frac{1}{3}}}{(1-0.8z_*)\left[z_*^{-0.9}+3.1\gamma^2(1-z_*)^{-\frac{3}{2}}+3\gamma\right]^{\frac{1}{2}}} \quad 4.6$$

$$\gamma = \frac{F_i}{F_i - m \cdot z_i} \quad 4.7$$

These equations have been rearranged slightly from the original published form that included the extrapolated surface flux (F_0) in the calculations. The reason for this is to approximate the observed gradient, which is an important variable that affects the uncertainty estimate. However, due to the experimental design, the gradient can be measured directly. To obtain error estimates that rely solely on measured variables, and not extrapolations that have their own errors, F_0 has been substituted with $F_i - m \cdot z_i$. Additionally, the error on the extrapolated flux was calculated according to Equation 4.8, also from Mann and Lenschow (1994).

$$\sigma_{F_0}^2 = \frac{\overline{\sigma_F^2} \cdot \overline{z_i^2}}{N \cdot \sigma_z^2} \quad 4.8$$

Median individual observation errors for sensible, latent and CO_2 flux were 11%, 10% and 12%, respectively. These values are about a factor of 2 less than the relative standard deviations of fluxes collected at similar altitudes, 26% for sensible heat, 25% for latent heat and 27% for CO_2 flux. Given that fluxes at different altitudes were collected at different times, during which key parameters may change, it is not surprising that the standard deviation at altitudes are higher than the observational error. Median errors for

the extrapolated surface flux were 12%, 12% and 13% for sensible heat, latent heat and CO_2 flux, respectively.

To obtain a representative total error estimate, the calculated errors described above were combined in quadrature with the other pertinent source of error, the standard deviation of the spectral corrections. Median total errors for sensible heat, latent heat and CO_2 flux are reported in Table 4.2.

Table 4.2 Median errors and corrections for each flux

Flux	Spectral Correction Error (%)	Flux Error (%)		Total Error (%)	
		Observation	Regression	Observation	Regression
H	9	11	12	15	15
LE	8	10	12	13	15
CO_2	8	12	13	14	15

4.4 Flux Footprint Calculations

The surface area contributing to the measured flux, known as the footprint, was calculated according to the Kljun et al. (2004) parameterization of the Kljun et al (2002) analytical footprint model. This model is applicable for conditions where friction velocity is greater than 0.2 m/s and zeta is less than 1. Accordingly, the few observations observed that were not under these conditions were not used. This model uses various parameters such as friction velocity and surface roughness to calculate a non-dimensional footprint function. Here surface roughness is synonymous with aerodynamic roughness length, a measure of where wind speed goes to zero that is specific to different surface types (e.g.

forest, barren, hilly, flat) (Stull, 1988). The non-dimensional function is then scaled appropriately to produce real values that can be applied to the surface. Surface roughness values used were 2.5 m for Harvard Forest (hilly terrain), 1.3 m for Howland Forest (~20 m conifer forest) and 1.05 m for Duke Forest (mixed forest) (De Bruin and Moore, 1985; Hansen, 1993). The extent of the footprint is particularly affected by the flight altitude. Figure 4.10 shows an example footprint model output for three altitudes over Howland Forest on 7/11/12.

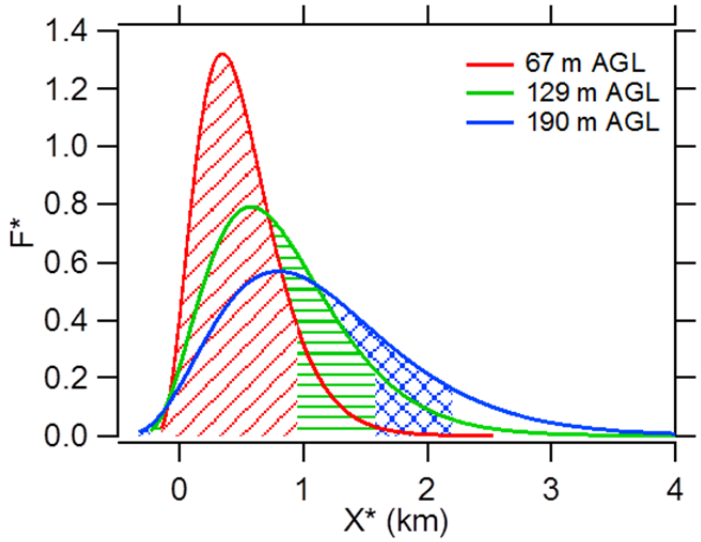

Figure 4.10 Normalized footprint function outputs for three altitudes on 7/11/2012. The shaded regions represent the area up to the 90% threshold.

The model output is a continuous non dimensional footprint contribution (F*) function that includes extends slightly downwind (-X* values) and primarily upwind (+X* values), as shown in Figure 4.10. For practicality, the footprint function is usually truncated at some percent of the whole footprint. For this analysis the footprint up to 90%

of the total is used. The 90% footprint is then projected along the entire flight path to produce transect footprints. Figure 4.11 shows an example footprint projected onto a United States Geological Survey (USGS) topographic map for a flight on 7/7/2012.

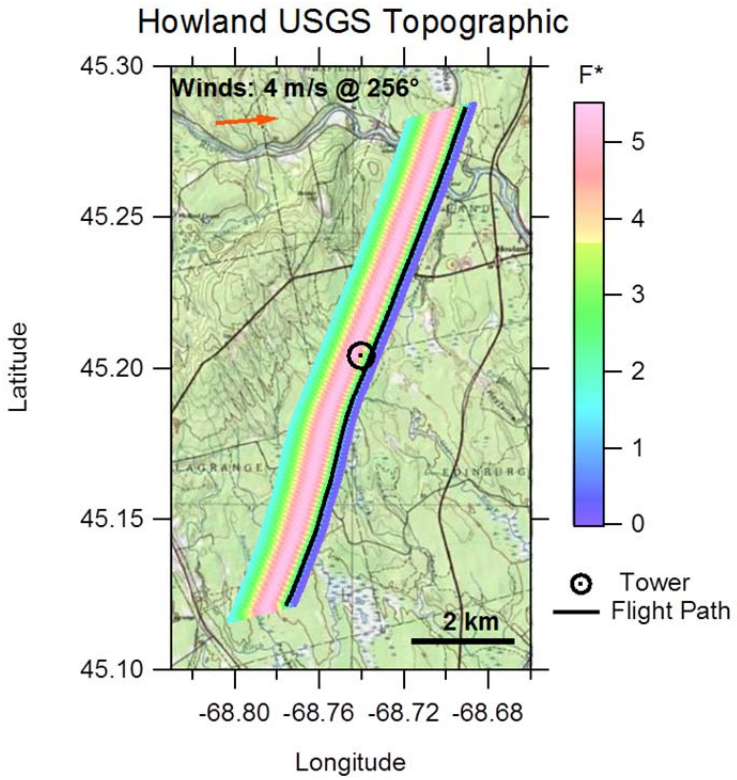

Figure 4.11 Projected footprint function for 7/11/2012 at 190 m AGL. The solid black line indicates the original flight track, while the shading of the footprint indicates the magnitude of contribution at that point.

4.5 Results

4.5.1 Footprint Analysis

Median, minimum and maximum 90% footprint distances were 1.79 km, 0.31 km and 6.74 km, respectively. The median, minimum and maximum footprint areas were 30.0 km^2, 5. 6 km^2 and 81.5 km^2. As shown in Figure 4.12, flight altitude most significantly affected the footprint 90% distance.

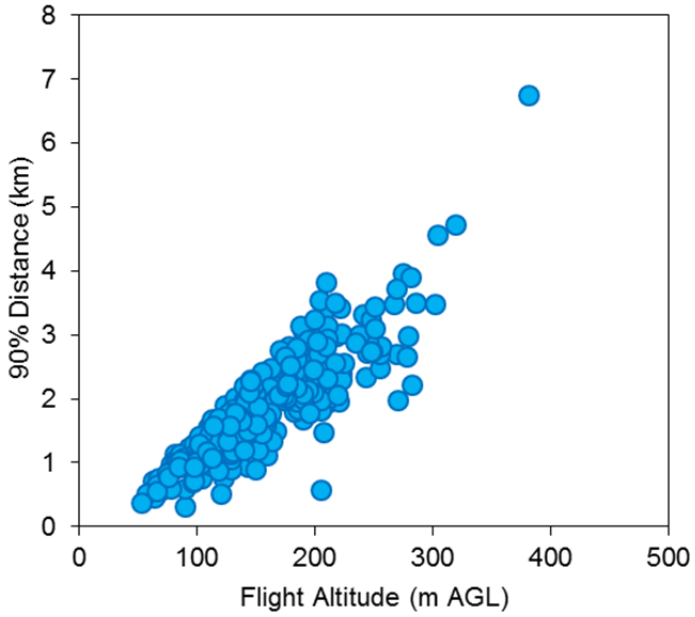

Figure 4.12 Aircraft footprint 90% length perpendicular to the flight track as a function of flight altitude.

The footprint function allows footprint weighted variables to be calculated for the entire transect. Footprint weighted average landcover distributions were calculated for all

days and footprint average surface soil moisture and RZSM were calculated for days with coincident soil moisture data. The most prominent landcover type was deciduous forest and was the main landcover component in 51% of the experiments. Figures 4.13 and 4.14 show landcover distributions with a deciduous landcover majority for Harvard Forest and Duke Forest, respectively. Evergreen forest was the next most prominent landcover type and was the main landcover component for 27% of the experiments. Figure 4.15 shows landcover distributions with a majority of evergreen landcover for Harvard Forest and Howland Forest. The remaining 7% of experiments had other major landcover types, or a relatively equal distribution between several landcover types. The landcover distributions for these sites are shown in Figure 4.16.

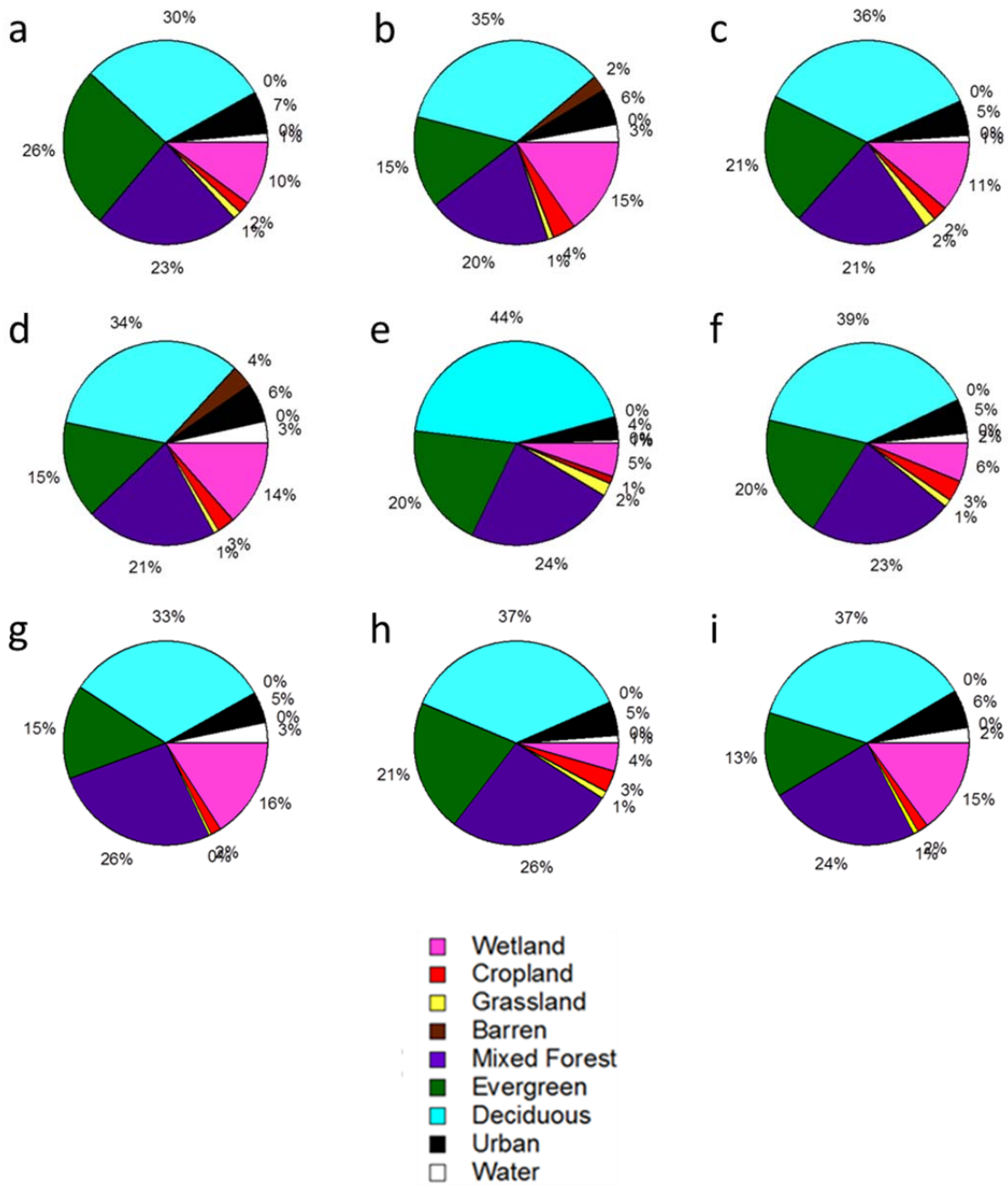

Figure 4.13 Average footprint-weighted landcover distributions of Harvard Forest sites with a majority of deciduous landcover. Sites shown were sampled on (a) 7/7/2012, (b) 7/7/2012, (c) 7/8/2012, (d) 7/8/2012, (e) 7/9/2012, (f) 7/9/2012, (g) 5/30/2013, (h) 5/31/2013 and (i) 8/21/2013.

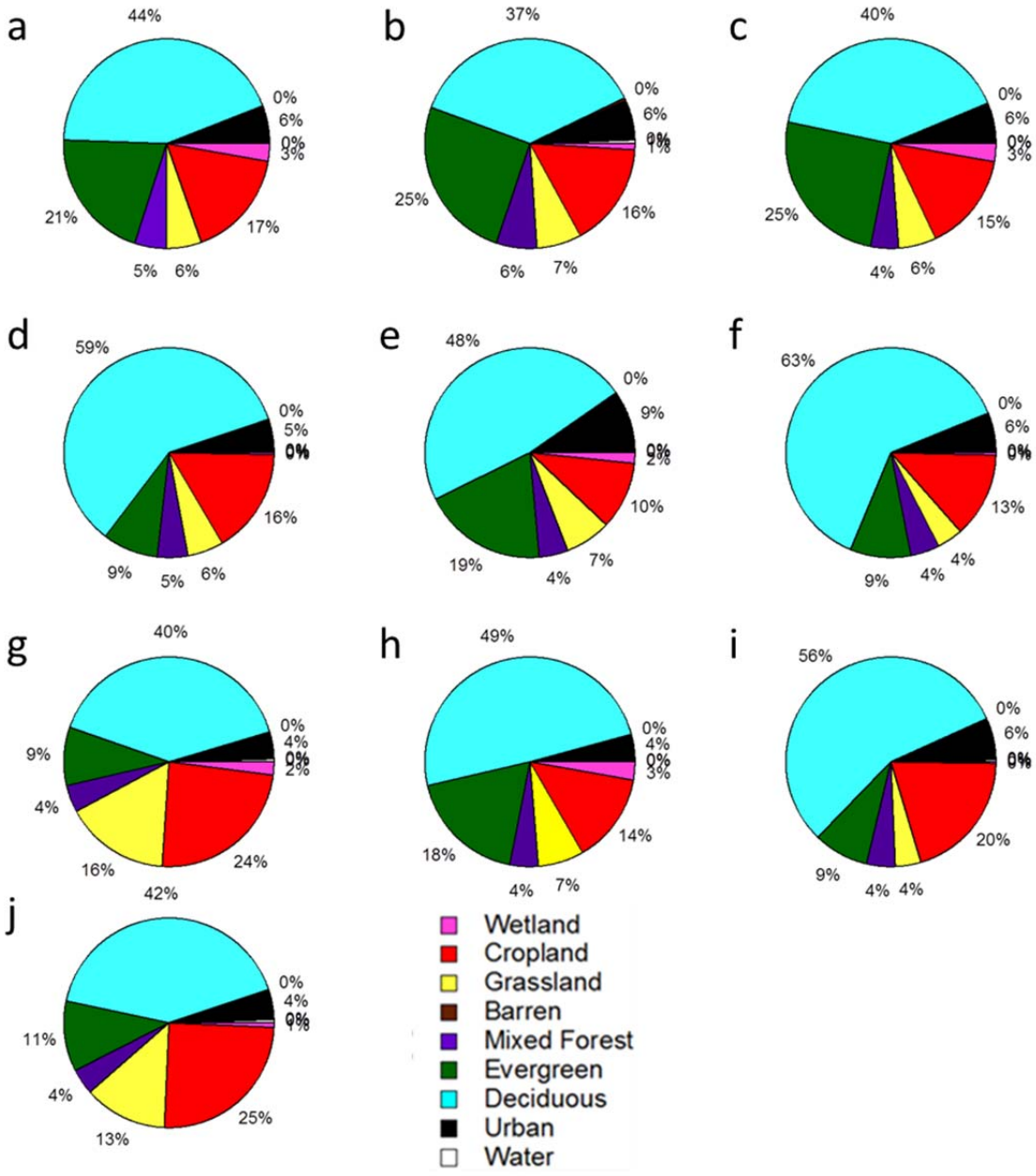

Figure 4.14 Average footprint-weighted landcover distributions of Duke Forest sites with a majority of deciduous landcover. Sites shown were sampled on (a) 6/4/2013, (b) 7/7/2013, (c) 7/8/2013, (d) 7/8/2013, (e) 7/9/2013, (f) 7/9/2013, (g) 7/10/2013, (h) 8/23/2013, (i) 8/24/2013 and (j) 8/24/2013.

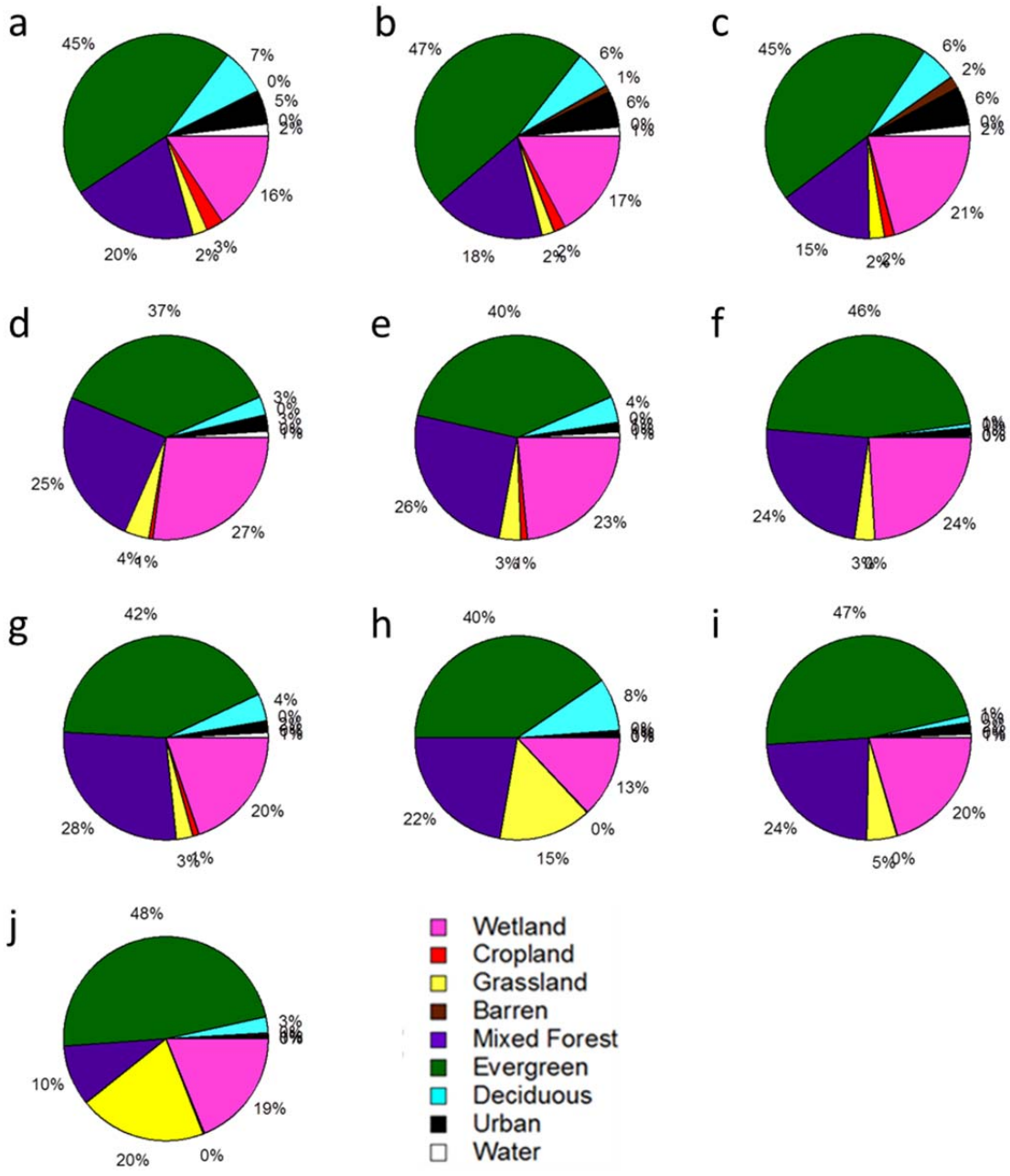

Figure 4.15Average footprint-weighted landcover distribution of Harvard and Howland Forest sites with a majority of evergreen landcover. Sites shown were sampled over Harvard Forest on (a) 7/8/2012, (b) 5/30/2013 and (c) 8/22/2013. Howland Forest sites were sampled on (d) 7/10/2012, (e) 7/11/2012, (f) 6/1/2013, (g) 6/1/2013, (h) 6/2/2013, (i) 8/19/2013 and (j) 8/20/2013.

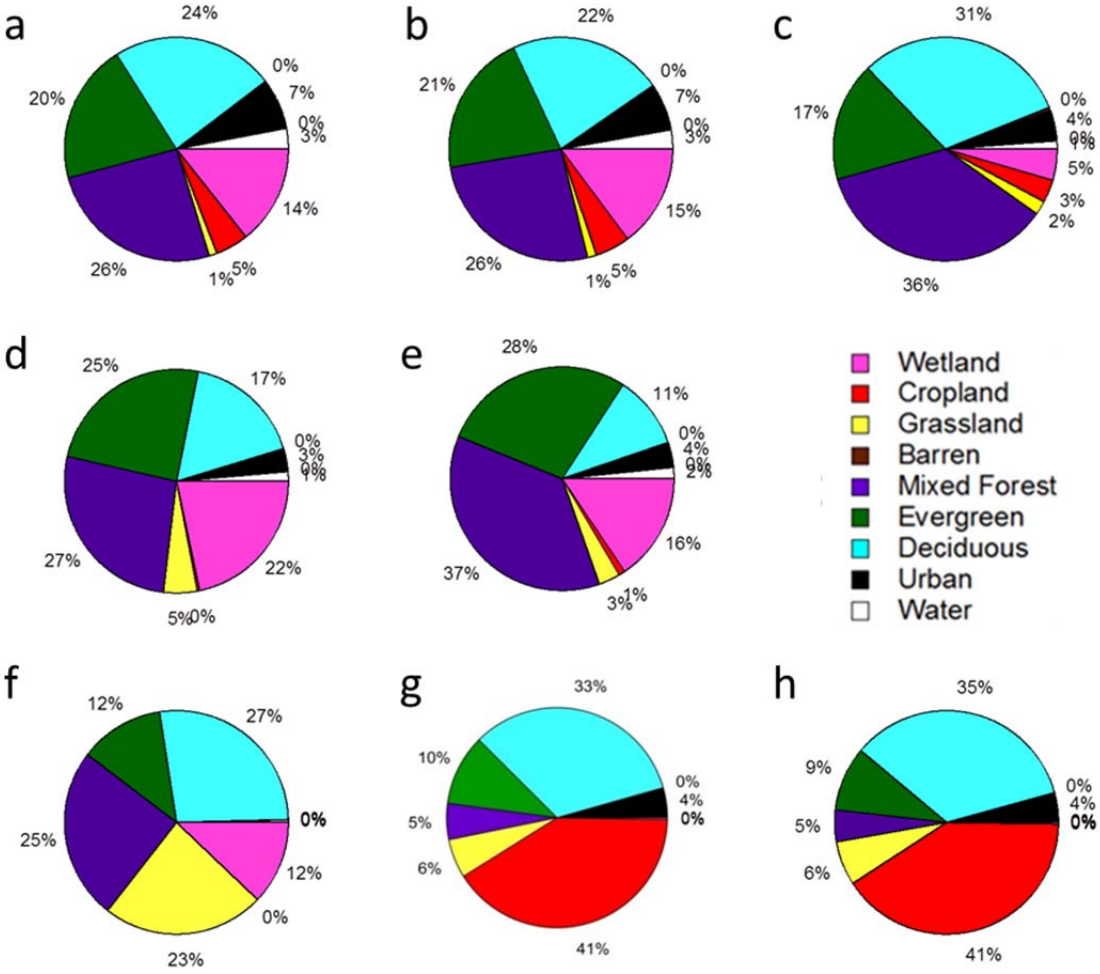

Figure 4.16 Average footprint-weighted landcover distributions of Harvard, Howland and Duke Forest sites with a majority of other landcover types or no clear majority. Sites shown were sampled over Harvard Forest on (a) 5/31/2013, (b) 8/21/2013 and (c) 8/22/2013. Howland Forest sites were sampled on (d) 7/10/2012, (e) 8/19/2013 and (f) 6/2/2013. Duke Forest sites were sampled on (g) 6/4/2013 and (h) 7/10/2013.

Footprint averaged soil moisture values are presented in Table 4.3. An important consideration for extrapolated fluxes is the effect of changing surface variables that may influence the extrapolation. As altitude increases, more upwind area is contributing to the observed flux. In non-homogeneous areas this could lead to observable differences in landcover type or soil moisture at different altitudes. However, after examining

individual landcover and soil moisture data at different altitudes for all sites, no discernable difference was found between altitudes indicating the sites were homogeneous enough for the flux extrapolation technique to be suitable. Figure 4.17 shows an example flight on 7/7/2012 with minimally changing landcover distributions as a function of altitude.

Table 4.3 Average surface and root zone soil moisture for each available experiment. Soil moisture is reported as column averaged fractional percent by volume.

Flight Date	Time	Site	Surface SM	RZSM
5/30/2013	13:45	Harvard	0.366 ± 0.014	0.465 ± 0.009
5/30/2013	15:52	Harvard	0.319 ± 0.009	0.428 ± 0.008
6/2/2013	12:19	Howland	0.324 ± 0.027	0.467 ± 0.011
6/2/2013	13:35	Howland	0.312 ± 0.010	0.494 ± 0.011
6/4/2013	1237	Duke	0.239 ± 0.013	0.349 ± 0.013
6/4/2013	14:01	Duke	0.217 ± 0.010	0.304 ± 0.008
7/9/2013	12:39	Duke	0.469 ± 0.019	0.557 ± 0.022
7/9/2013	14:37	Duke	0.493 ± 0.013	0.576 ± 0.014
8/19/2013	12:47	Howland	0.402 ± 0.015	0.492 ± 0.012
8/19/2013	14:17	Howland	0.479 ± 0.016	0.549 ± 0.013
8/22/2013	12:20	Harvard	0.268 ± 0.009	0.377 ± 0.008
8/22/2013	13:58	Harvard	0.354 ± 0.004	0.459 ± 0.004
8/24/2013	12:20	Duke	0.262 ± 0.005	0.371 ± 0.009

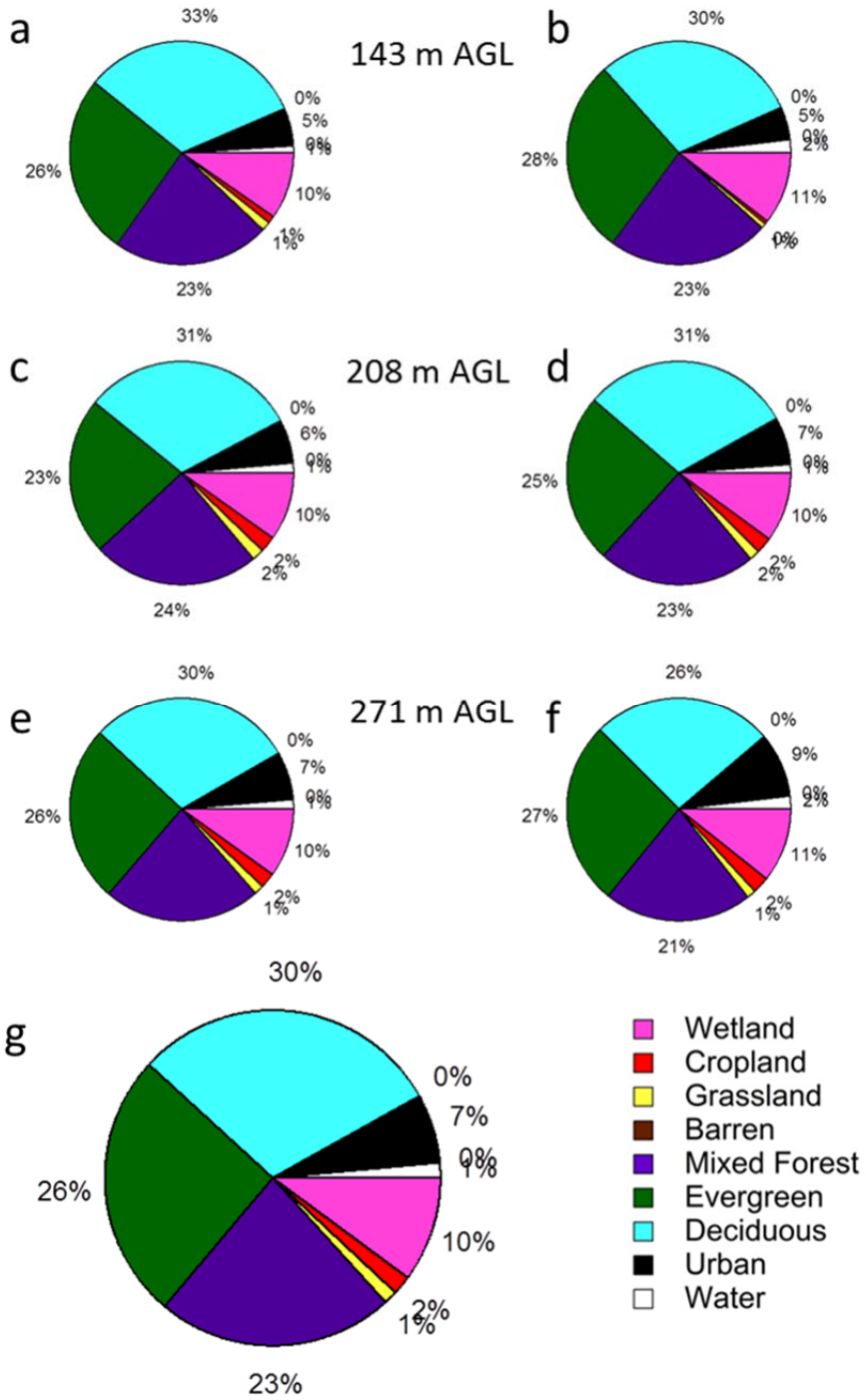

Figure 4.17 Example of the change in landcover distributions of transects at different heights. Shown here are distributions for 7/7/2012 at (a-b) 143 m AGL, (c-d) 208 m AGL, (e-f) 271 m AGL and (g) the Site 2 average for all transects.

4.5.2 Transect Length Analysis

An important variable in the flux error calculation shown in equation 4.5 is the transect length. Transect length is also the main contributor to the experiment length duration of ~90 min. The average transect length for all experiments was ~17 km. In order to quantify the effect of using smaller transect lengths, the original error calculation was made for transect lengths ranging from 1 to 25 km for all observations. The results are shown in Figure 4.18. Noticeably, error starts to rapidly increase below about 5 km for all fluxes. However, there is very little change in error between 25 and 5 km.

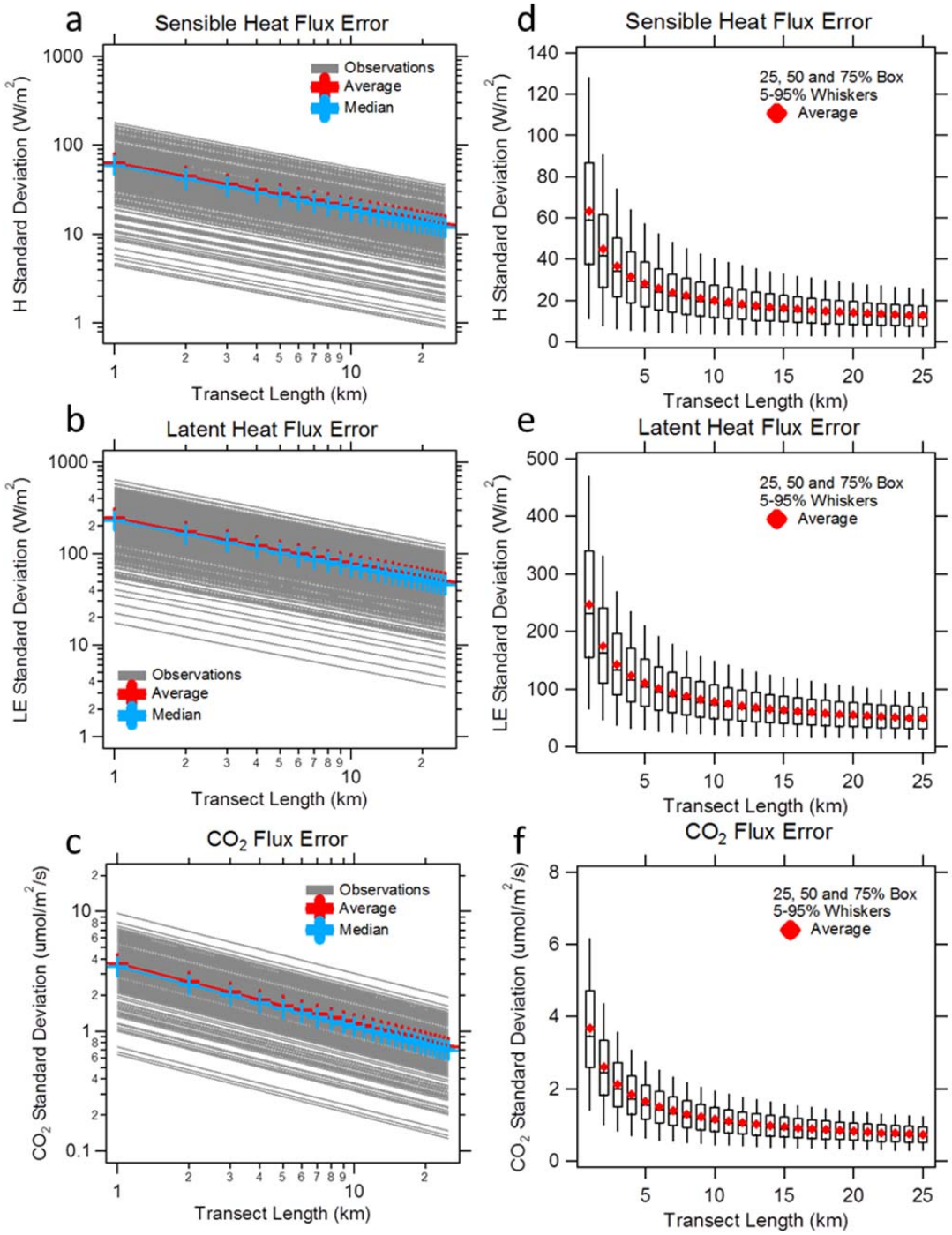

Figure 4.18 Log-log plots of the flux standard deviations as a function of transect length for (a) sensible heat, (b) latent heat and (c) CO_2 flux. Also shown are box and whisker plots where the whiskers extend to the 5-95% range of the data for (d) sensible heat, (e) latent heat and (f) CO_2 flux.

While the error analysis indicates that transects as low as 5 km may be viable, these physical distances may not be long enough to sample all important eddy sizes. It is important to also consider the cospectrum between vertical wind and the flux scalar. Smaller transects may not allow larger eddies to be characterized. Underestimation of the portion of the flux carried by larger eddies may cause underestimation of fluxes as well. One way to potentially circumvent this problem is to segment longer transects, but use the mean of the whole transect when calculating perturbations from the mean in equation 4.1. This may allow smaller segments to keep large eddy information that would otherwise be removed using a local segment mean. These two scenarios, using a transect mean (TM) or local mean (LM) for smaller segment flux calculations, were investigated for Site 1 on Flight 7/8/2012. This flight had average transect lengths of 20 km, one of the longest in this data set. The transects were divided into 10 km, 5 km and 2 km segments. Figure 4.19 shows log-log plots of the sensible heat cospectra for both the TM and LM scenarios.

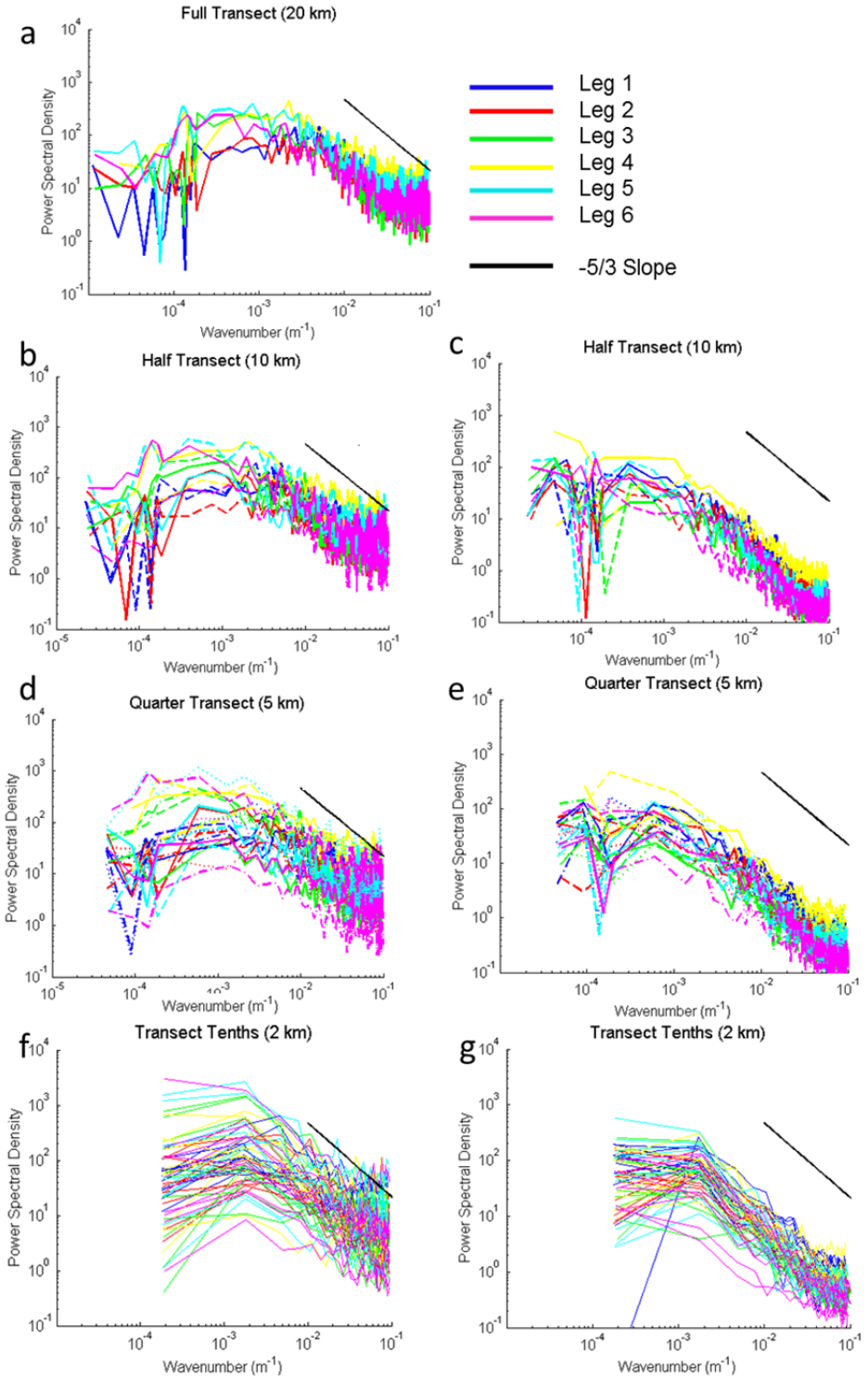

Figure 4.19 Log-log sensible heat cospectra for the (a) original 20 km transect, (b) 10 km TM, (c) 10 km LM, (d) 5 km TM, (e) 5 km LM, (f) 2 km TM and (g) 2 km LM scenarios. Also shown in black is the expected -5/3 slope in the inertial sub-range.

The cospectra show noticeable loss of large eddy information starting at transect lengths of 5 km. Also evident is the larger scatter in the TM scenario cospectra than the LM cospectra. This is also evident in the computed fluxes as standard deviations of the 5 and 2 km TM fluxes were higher than standard deviations of the 5 and 2 km LM fluxes. The segmented fluxes were also corrected for high frequency spectral loss. The median high frequency loss value did not change with decreasing transect length, though again, the standard deviation increased at transect lengths starting at 5 km. This is expected as high frequency spectral characterization should be possible even at 2 km given that this region typically encompasses eddy sizes of less than ~100 m (Stull, 1988). The expected -5/3 slope in the inertial subrange is also plotted and all spectra show a similar slope (Stull, 1988). The loss of information at low frequencies, however, may result in underestimation of the total flux. To examine this possibility, segments were averaged and compared to the original transect flux. The results from this analysis are shown in Figure 4.20.

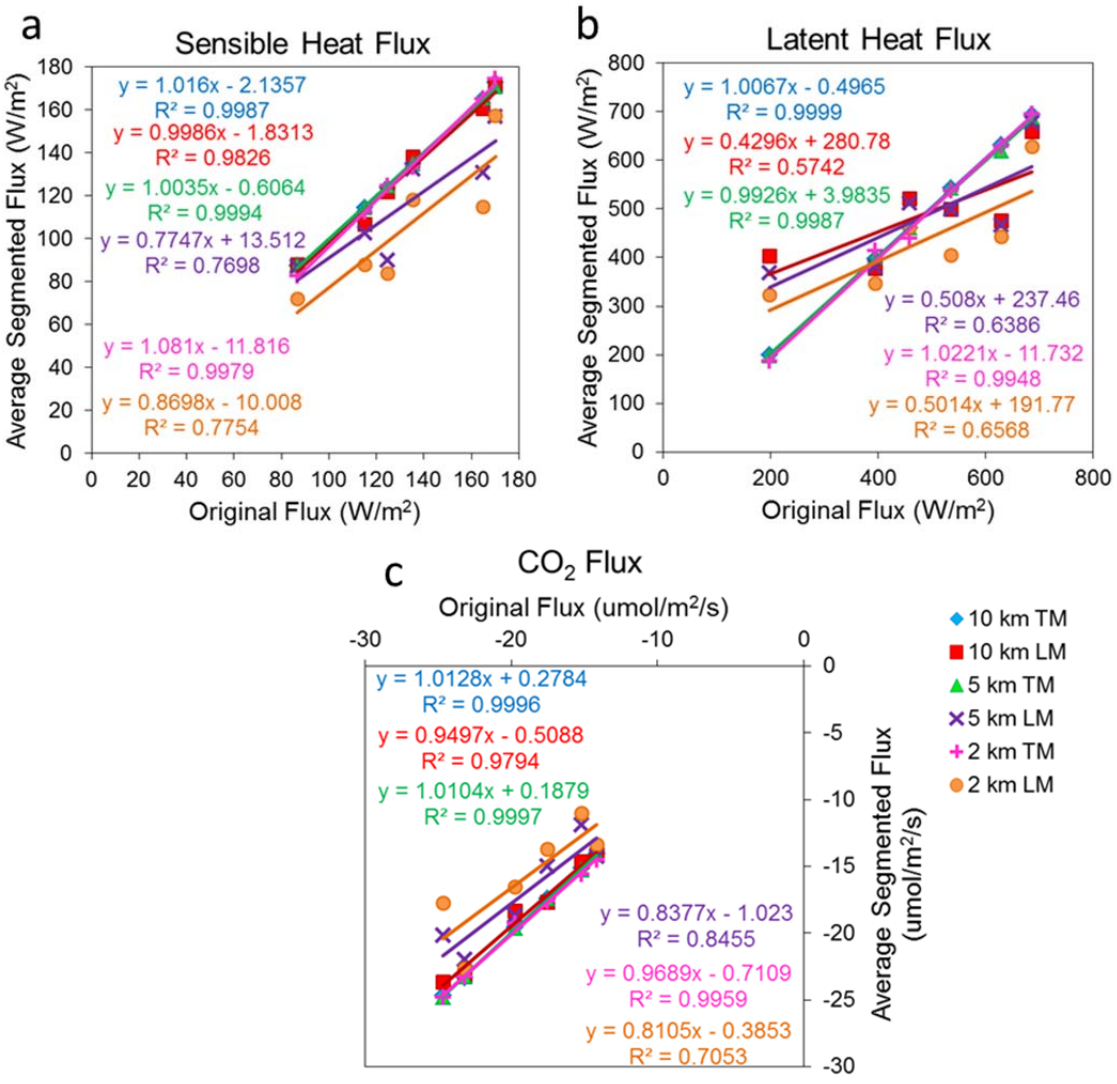

Figure 4.20 The effect of using smaller transect lengths and either the original transect mean (TM) or the segment local mean (LM) on the averaged flux for (a) sensible heat, (b) latent heat and (c) CO_2 flux.

Both sensible heat and CO_2 flux show good agreement between the original flux and the averaged TM fluxes at all transect lengths. However, both show decreased fluxes starting at 5 km. Latent heat is an interesting case as differences in averaged fluxes for the LM approach are seen at 10 km and the effect does not produce a uniform decrease in the latent heat fluxes. Instead, the spread in the flux values is decreased. This has the effect of changing and generally reducing the magnitude of the slope of the flux extrapolation. The results of an extrapolation using the averaged LM segments are shown in Figure 4.21. The magnitude of the slope decreases with decreasing transect length and the extrapolation flux result decreases. Overall the optimal transect length appears to be between 10 and 5 km.

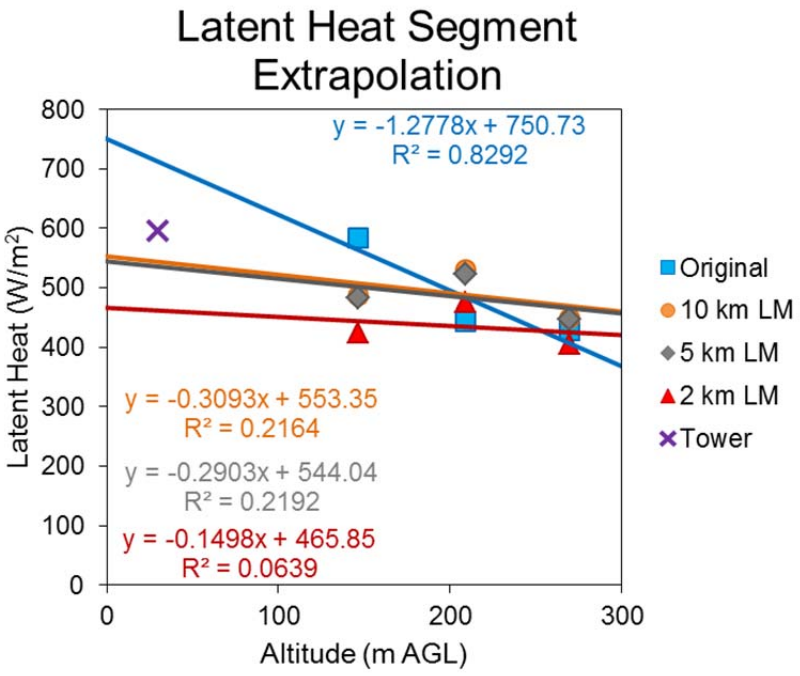

Figure 4.21 The effect of the LM transect segmenting on an example LE extrapolation.

4.5.3 Environmental Variables Influencing Fluxes

To determine the identity of the main meteorological and environmental variables responsible for the observed variability in the flux, regression plots were made for all pertinent variables and least-squares regressions were plotted. High correlation coefficients of regression plot may indicate variables of interest that should be measured accurately, and which may be interrogated through aircraft flux measurements. Likewise, regressions with large magnitude slopes may indicate variables that fluxes are particularly sensitive to. In order to directly compare slopes from regression of different variables with different units and data spread, all variables were first median centered and normalized by the median parameter variable. This produces a variable′ series represented as a percent deviation from the average value. The median value was used as some variables showed skewed distributions or outliers. In some cases (as for landcover and soil moisture) variables are already calculated in percent form and are therefore only median centered.

Important variables included in this analysis were altitude, scaled altitude, wind direction (WD), wind speed (WS), pressure, CO_2, H_2O, air temperature, incoming radiation, psi (the angle between the aircraft heading and oncoming wind), landcover fraction, surface soil moisture and RZSM. Radiation data from NOAA archives (downward shortwave radiation), which is applicable to regions far from the towers, and net radiation available from the tower was used. Net radiation is the sum of all downwelling radiation (shortwave + longwave) minus the sum of all upwelling radiation (shortwave + longwave). Regression plots for selected variables are shown in Figures 4.22.

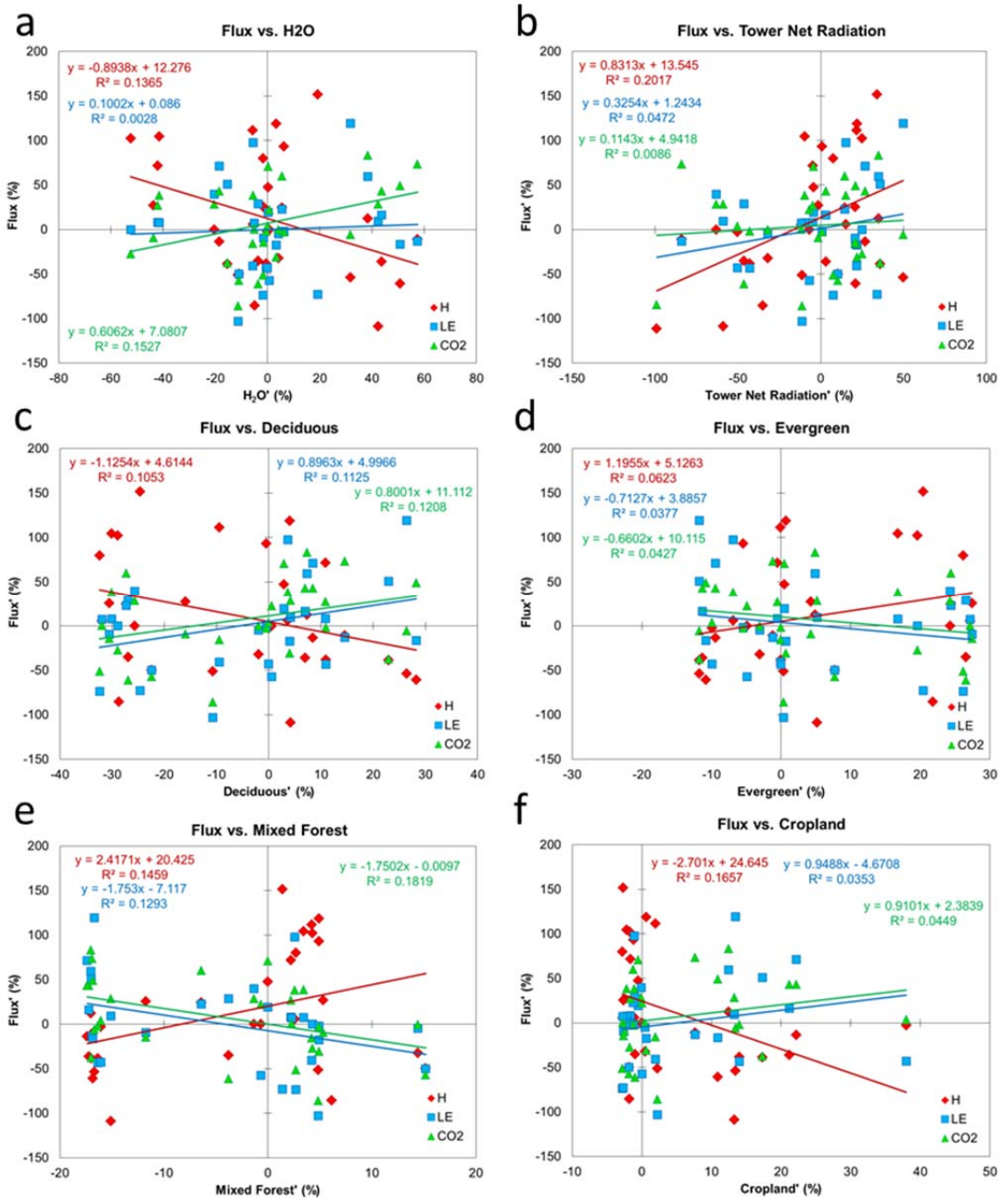

Figure 4.22 Selected regression plots for (a) air H_2O fraction, (b) tower net radiation, (c) deciduous landcover fraction, (d) evergreen landcover fraction, (e) mixed forest landcover fraction and (f) cropland landcover fraction.

Though some slopes were large in magnitude, most were not statistically different from zero due to the large scatter in the data. Latent heat slopes were never statistically different from zero. Sensible heat showed statistically significant slopes for air H_2O fraction mixed forest, cropland and wetland landcover fraction and tower net radiation. CO_2 flux shoed statistically significant slopes for air H_2O fraction and mixed forest landcover fraction.

In addition, landcover and soil moisture were analyzed for patterns that might correspond to different surface fluxes. Due to the observed sensitivity to evergreen and deciduous landcover fraction, sites with a deciduous to evergreen transition where either landcover was sustained over at least 5 km were identified. Three Harvard Forest experiments with a transition along the flight path from deciduous to evergreen were segmented along the observed transition. Resulting transect lengths were ~10 km. Landcover analysis, shown in Figure 4.23, showed that though there was a distinct shift along the transect, isolating only deciduous or evergreen sites was impossible due to the heterogeneous nature of the landcover. Calculated surface fluxes for the deciduous and evergreen transects of all three experiments are reported in Table 4.4 and were not statistically different.

Table 4.4 Evergreen and deciduous transect surface fluxes

Date	CO_2 Flux ($\mu mol/m^2/s$)		
	Original	Evergreen	Deciduous
7/7/2012	-16.0 ± 2.4	-20.2 ± 4.6	-22.8 ± 4.4
7/8/2012	-31.6 ± 4.0	-28.0 ± 5.4	-30.2 ± 6.2
7/9/2012	-23.5 ± 2.8	-19.9 ± 4.1	-22.5 ± 4.0

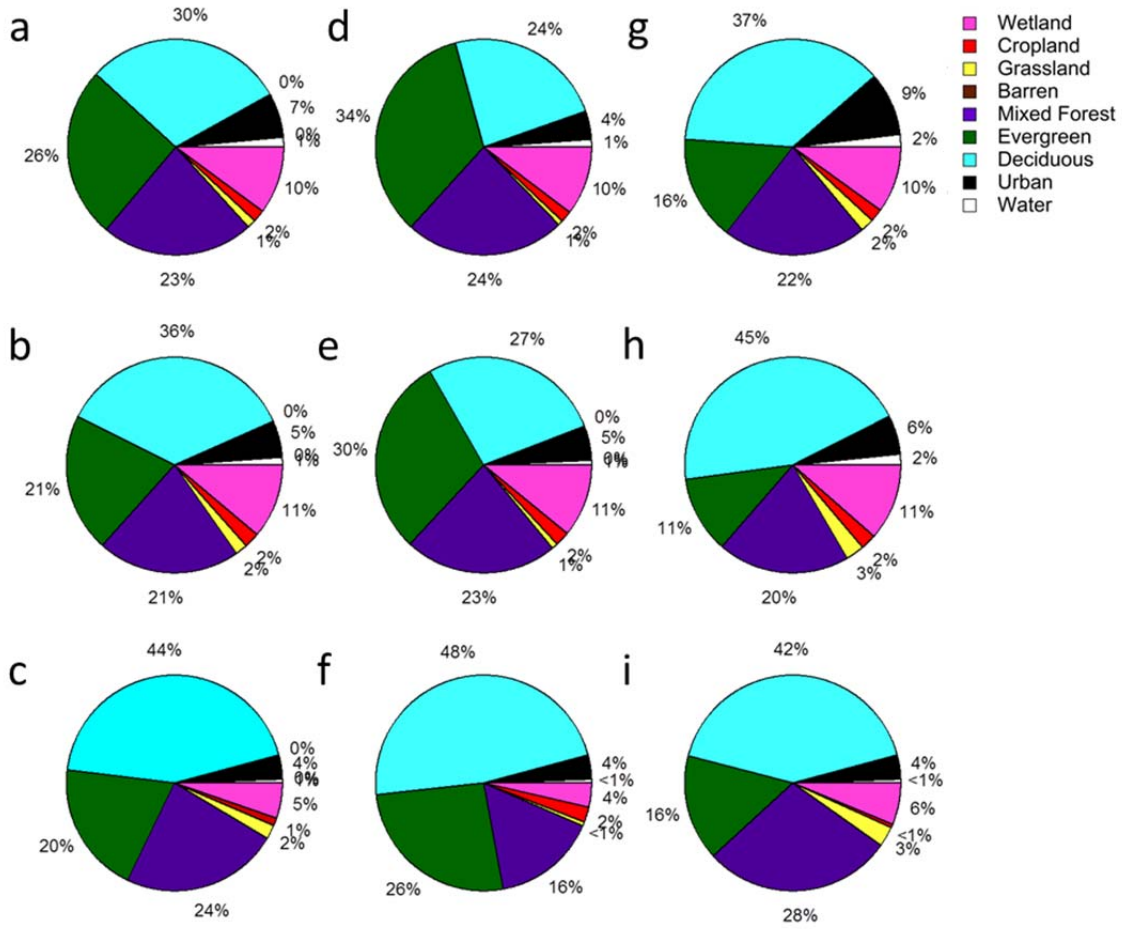

Figure 4.23 Landcover pie charts for original Harvard Forest experiments on (a) 7/7/2012, (b) 7/8/2012 and (c) 7/9/2012. Pie charts for corresponding (d-f) evergreen and (g-i) deciduous ~10 km segments are also shown.

Additionally, one site during the 6/4/2913 experiment over Duke Forest showed a transition from a relatively wetter, to drier RZSM. The transect was bisected along the transition resulting in ~10 km transects. Calculated footprint averaged RZSM for the 'wet' site was 0.29 ± 0.01 cm^3/cm^3 and 0.27 ± 0.03 cm^3/cm^3 for the 'dry' site thus the RZSM values were not significantly different. The calculated CO_2 fluxes for the wet and

dry sites, -19.9 ± 2.3 μmol/m^2/s and -17.8 ± 2.1 μmol/m^2/s, respectively, were also not significantly different.

4.5.4 Aircraft-Tower Comparison

The results of the aircraft-tower comparisons are reported in Table 4.5. As both aircraft and tower results can have comparable errors, an orthogonal distance regression (ODR) was used to fit the data. ODR analysis minimizes both the x and y residuals allowing the calculated fit to account for uncertainty in the x-axis measurement (Boggs and Rogers, 1990). Several regression scenarios are reported to examine differences between sites close to and far from towers, regressions for experiments at specific forest sites and regressions for all experiments of similar landcover distribution as determined by footprint analysis results. Because perfect agreement between the aircraft and tower data is not necessarily expected since the footprints for all experiments are not the same experiments were separated into sites near and away from tower. Near tower sites showed similar landcover distribution as the tower and contained the tower location within their footprint. Sites near towers should have the most similar landcover and environmental variables and should be the most similar. Results for sites close to and far from towers are shown in Figure 4.24.

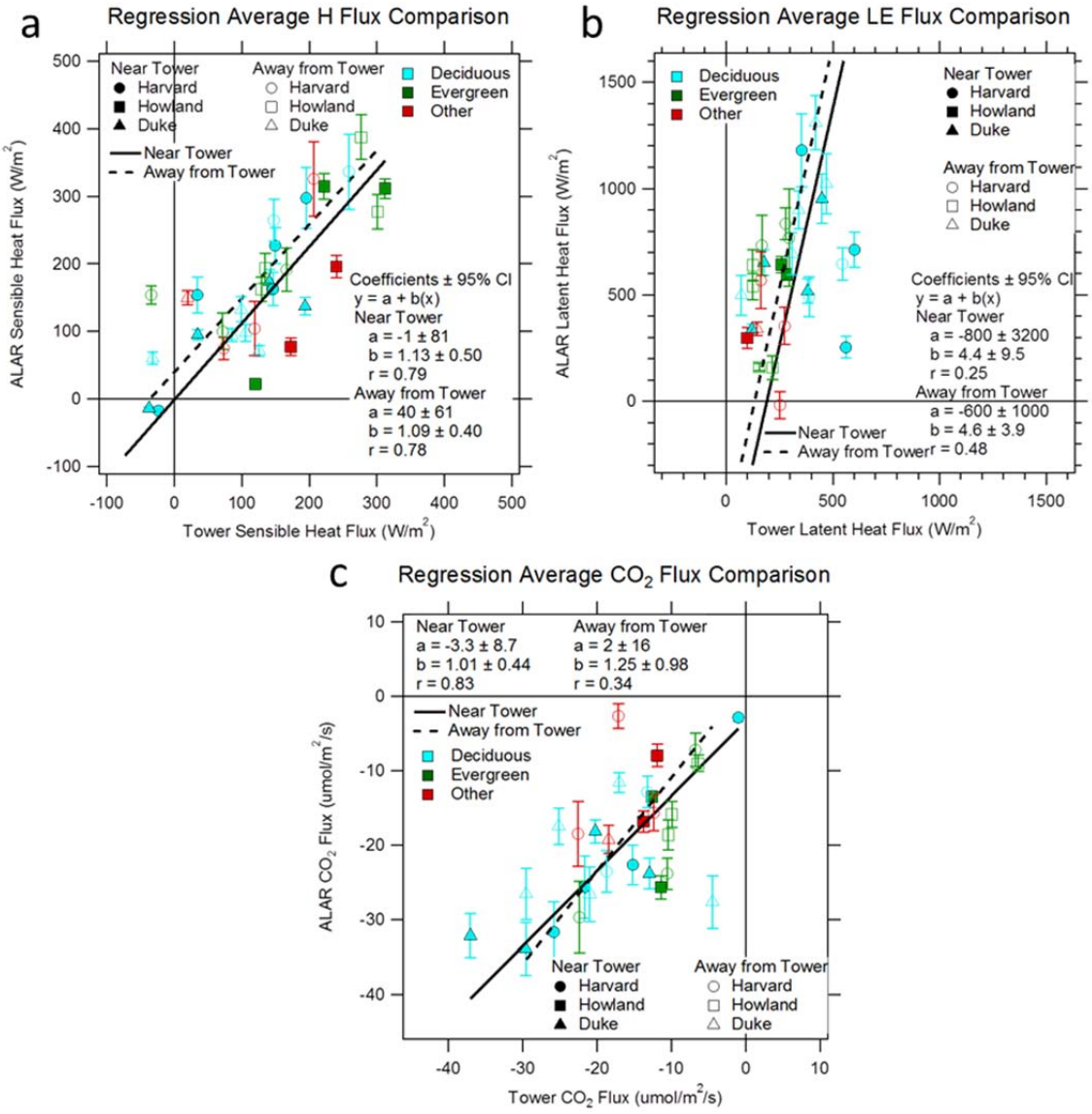

Figure 4.24 Scatter plots of the aircraft and tower data for (a) sensible heat, (b) latent heat and (c) CO_2 flux. Orthogonal distance regression results for all sites and 95% confidence intervals are shown in black along with the Pearson product-moment correlation constant. Solid and dashed lines show ODR results for experiments close to towers and away from towers, respectively.

Both sensible heat and CO_2 flux show good agreement with tower data for sites close to and far from the tower exhibiting ODR slopes that are not statistically different

from 1 and intercepts that are not statistically different from 0 and the 95% confidence interval. Additionally, the slopes and intercepts for the near and away from tower scenarios are not statistically different from each other or results from the ODR of all experiments. The Pearson product-moment correlation coefficients (r) using all data points for sensible heat and CO_2 flux were 0.77 and 0.61, respectively, indicating a moderately strong correlation between these data. Latent heat, as originally calculated, was routinely much higher than tower latent heat values, and higher that incident radiation in some cases, indicating a systemic overestimation of latent heat flux. This is likely due to the inclusion of advective water vapor sources that are present over large areas and the inherently different sampling of eddies by time and spatially averaged flux methods (Lothon et al., 2007; Alfieri et al., 2012; Metzger et al., 2012; Higgins et al., 2013; Eder et al., 2014). These discrepancies might be enhanced by conditions that suppress turbulent transport and thus promote advective transport, such as low friction velocity. To exclude larger eddies, the latent heat transects were reduced to an average of ~10, and ~5 km, based on the previous results that suggest calculated error rapidly increased after 5 km. The actual averages for the segmented transect lengths were 8.4 and 4.25 km. This method acts as an effective high pass filter that retains the flux from smaller eddies, but removes larger flux information from larger eddies as shown previously in Figure 4.19. Results of the segmented latent heat transects are shown in Figure 4.25.

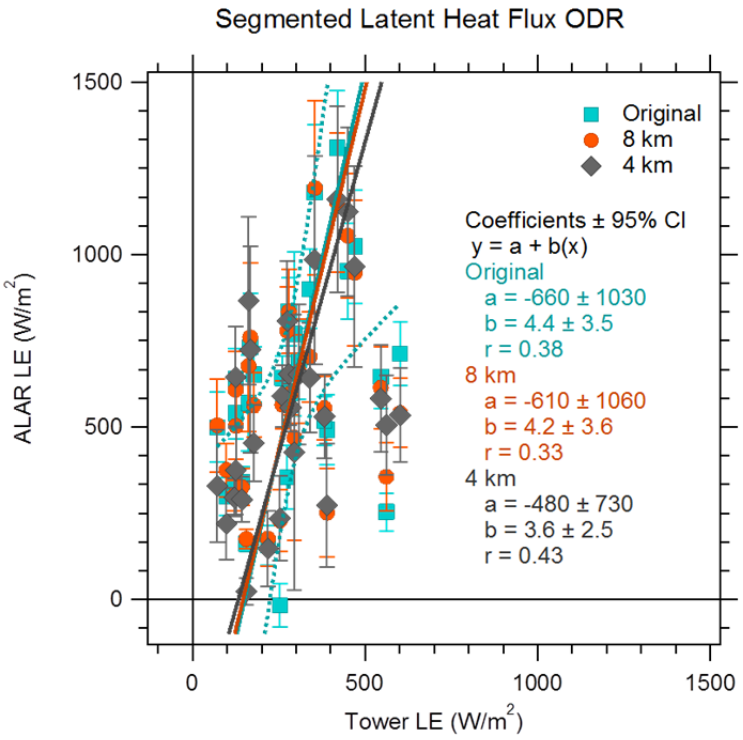

Figure 4.25 Regression results from the averaged segments of LE.

Agreement between the tower and ALAR increased slightly, but an overall overestimation by ALAR was still observed. Using the same techniques described in section 4.5.3, variables influencing the LE discrepancy were examined. As suggested by previous works, variables linked to more stable conditions that promote advection (low friction velocity, high pressure) showed relationships with increasing LE discrepancy (Lothon et al., 2007; Alfieri et al., 2012; Metzger et al., 2012; Higgins et al., 2013; Eder et al., 2014). Decreasing friction velocity is correlated to increasing LE discrepancy and increasing pressure and recorded air H_2O fraction are correlated to increasing LE discrepancy. The discrepancy was also biggest in cases where there was low downward shortwave radiation. Correlation plots for selected variables are presented in Figure 4.26.

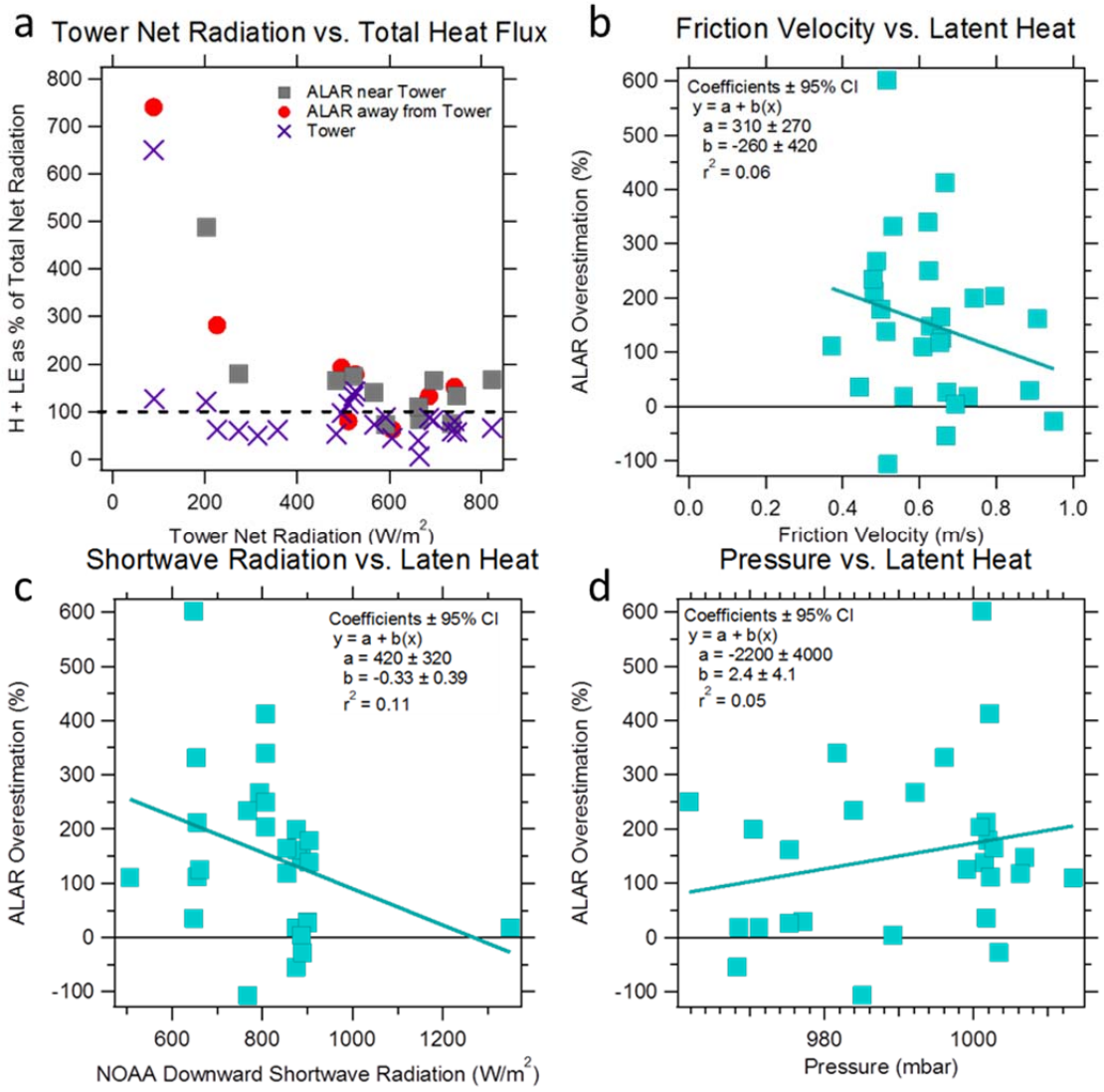

Figure 4.26 (a) H + LE as a fraction of net radiation recorded by the tower, and ALAR overestimation of tower LE as a function of (b) friction velocity, (e) NOAA downward shortwave radiation and (d) pressure.

Figure 4.27 shows individual experiment results colored by the major landcover component of the average experiment footprint as identified by the footprint landcover analysis in section 4.5.1. There is no observable clustering of specific landcover types and ODR slopes and intercepts of particular landcover types are not statistically different

from each other or from 1 and 0, respectively. However, the correlation coefficient of the deciduous and evergreen landcover regressions increased for CO_2 flux relative to the correlation coefficient for all data points. Regression statistics including 95% confidence intervals are calculated parameters and the Pearson's product-moment correlation coefficient are presented in Table 4.5.

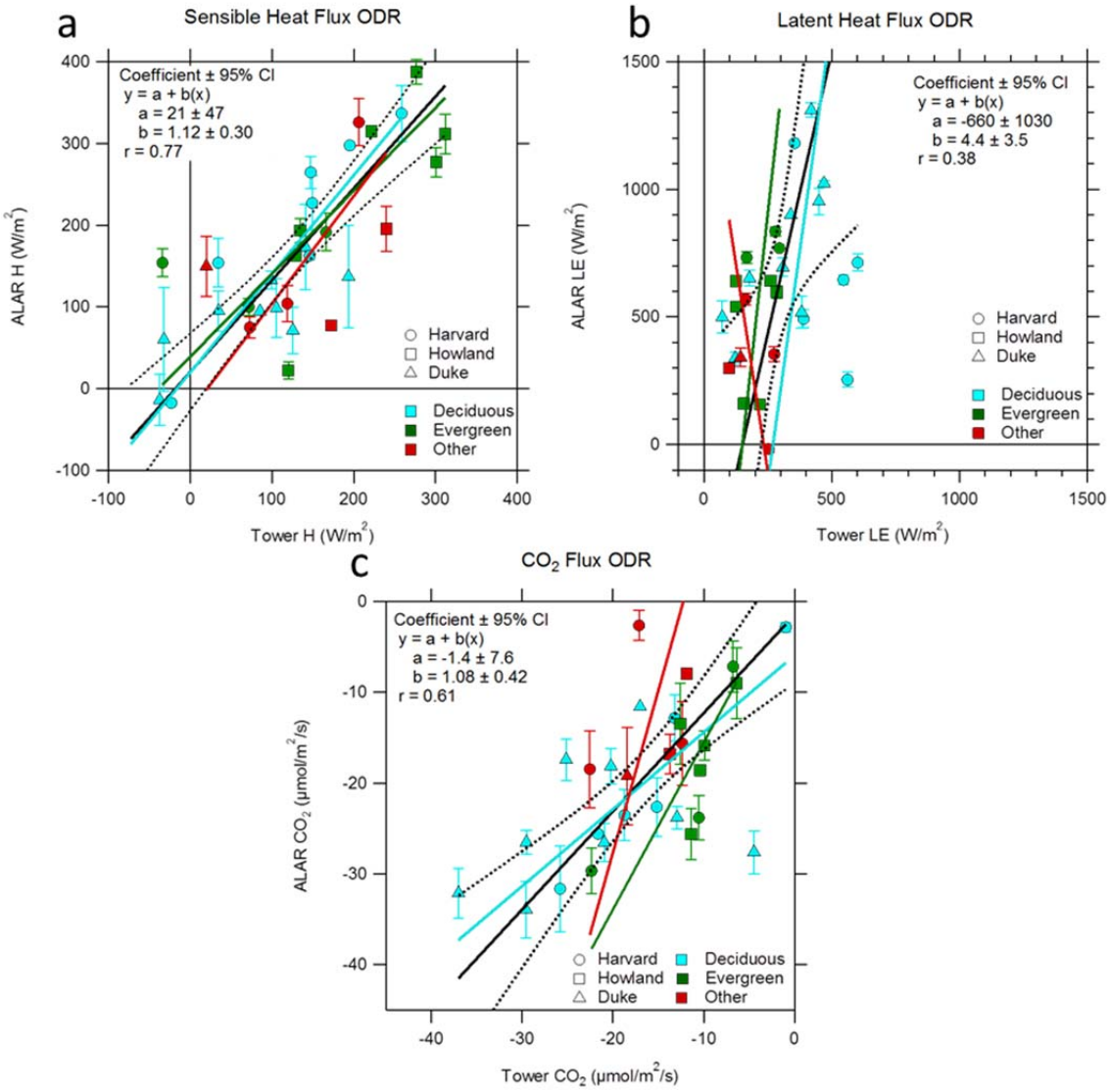

Figure 4.27 Scatter plots of the aircraft and tower data for (a) sensible heat, (b) latent heat and (c) CO_2 flux. Orthogonal distance regression results for all sites and 95% confidence intervals are shown in black along with the Pearson product-moment correlation constant. Blue, green and red lines show ODR results for landcover classes, deciduous, evergreen and other, respectively.

Table 4.5 ODR Statistics for ALAR-tower comparisons.

Flux		All Data Points	Near Tower	Away from Tower	Deciduous	Evergreen	Other	Harvard	Howland	Duke
H	a	21 ± 47	-1 ± 81	40 ± 61	20 ± 53	40 ± 120	-30 ± 330	38 ± 74	-160 ± 250	57 ± 48
	b	1.12 ± 0.3	1.13 ± 0.50	1.09 ± 0.40	1.20 ± 0.41	1.01 ± 0.63	1.3 ± 2.2	1.25 ± 0.53	1.8 ± 1.1	0.59 ± 0.48
	r	0.77	0.79	0.78	0.84	0.75	0.50	0.82	0.78	0.63
LE	a	-660 ± 1030	-800 ± 3200	-600 ± 1000	-2000 ± 6200	-1400 ± 4200	1500 ± 4800	2 E4 ± 4.3 E5	-1600 ± 8100	-10 ± 470
	b	4.4 ± 3.5	4.4 ± 9.5	4.6 ±3.9	7 ± 17	9 ± 20	-7 ± 26	-100 ± 1200	11 ± 47	2.5 ± 1.5
	r	0.38	0.25	0.48	0.20	0.36	-0.39	-0.01	0.25	0.79
CO_2	a	-1.4 ± 7.6	-3.3 ± 8.7	2 ± 16	-6 ± 10	3 ± 16	40 ± 170	6 ± 15	70 ± 260	-13 ± 14
	b	1.08 ± 0.42	1.01 ± 0.44	1.25 ± 0.98	0.85 ± 0.48	1.8 ± 1.4	4 ± 11	1.53 ± 0.90	7 ± 24	0.50 ± 0.63
	r	0.61	0.83	0.34	0.64	0.77	0.30	0.72	0.3	0.37

Here, a is the y-intercept, b is the slope and r is the Pearson product-moment correlation.

4.6 Discussion and Conclusions

Analysis of the transect length on both flux error and flux magnitude revealed that optimum transect length appears to be around 5-10 km. Decreased transect length will allow flux experiments to be completed with a better chance that environmental variables are constant. Currently, the optimal flux experiment set up of 3 altitudes repeated 3 times takes ~90 minutes to conclude. The same experiment set up for 10 km transect repetitions could be expected to take 45 min and would allow for more sites to be sampled or for additional altitudes to be samples. A 5 point extrapolation, for example, would reduce error in the extrapolation. However, at the sites studied here, shorter transects were not able to distinguish between surface fluxes that might be affected by different surface landcover and RZSM, likely due to the heterogeneous nature of these variables even at shorter transect lengths. This may be overcome by more selective targeting of sites that experience a transition from one landcover to another, or areas with a persistent RZSM gradient. Additionally, other data processing techniques, discussed later, could be used.

Analysis of environmental variables through regression plots showed low correlation for all fluxes, though particularly low correlation was observed for LE. Importantly, very low correlation was observed for wind direction, wind speed and psi (aircraft heading relative to wind direction) indicating that aircraft set up does not affect either calculated fluxes or uncertainty. The investigation of aircraft specific sources of error are important for evaluating the quality of aircraft flux data because calculated fluxes have been shown to be sensitive to some aircraft specific parameters, most notably those affecting pressure and vertical winds (Vellinga et al., 2013). Overall, most calculated slopes were not statistically different from zero, even for parameters such as

temperature which have a known effect on CO_2 flux, likely due to the complex interactions of multiple parameters (Berry and Bjorkman, 1980; Monson et al., 1982; Long et al., 1991). Weak correlation and statistically significant sensitivity to air H_2O fraction was observed for H and CO_2 flux, as reported by Metzger et al. 2013. Increasing deciduous fraction and decreasing evergreen fraction was associated with higher CO_2 uptake, though CO_2 flux only showed statistically significant sensitivity to mixed forest landcover fraction. Previous studies have also reported lower CO_2 uptake at predominantly evergreen sites relative to deciduous sites during the growing season (Waring and Franklin, 1979; Buchmann and Schulze 1999; Hollinger et al., 1999; Miglietta et al., 2007).

One limitation of the environmental analysis is the availability of soil moisture data for only 13 of the total 37 experiments. Low correlation and sensitivity for both surface soil moisture and RZSM were observed. As part of the AirMOSS project, modeled soil moisture will be available at hourly resolution for all 2013 flights. The Penn State Integrated Hydrological Model (PIHM) is used to model soil moisture in watersheds near towers (Qu and Duffy, 2007). This data, shown by way of example in Figure 4.28 may allow for improved environmental analysis.

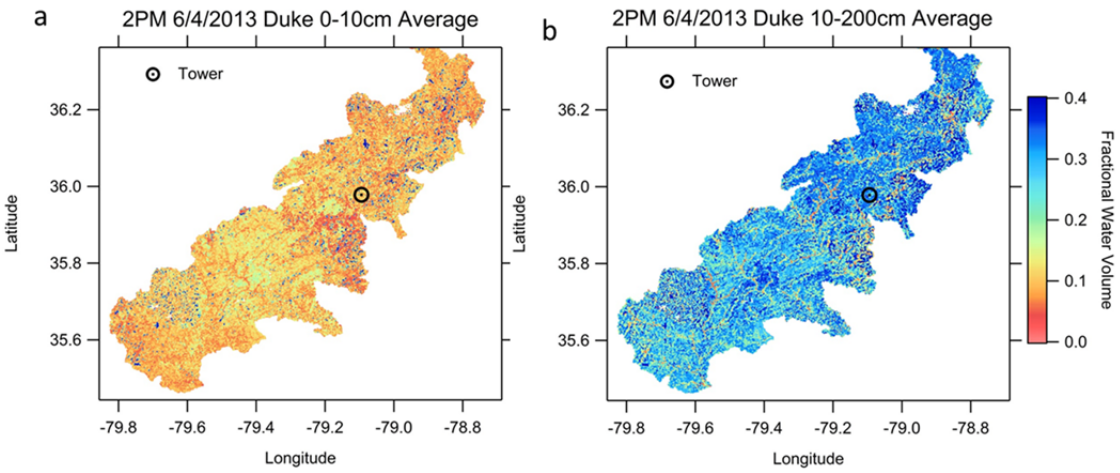

Figure 4.28Average modeled soil moisture for Duke Forest on 6/4/2013 at depths of (a) 0-10 cm and (b) 10-200 cm.

The aircraft-tower comparison showed good agreement for sensible heat and CO_2 flux. The average landcover of the ALAR experiment sites at each location is quite similar to the overall distribution of the forest as shown in Figure 4.29 (total forest landcover pie charts are shown in Figure 4.2). Contrastingly, the tower sites (shown in Figure 4.3) used in this analysis predominantly cover deciduous forest at Harvard and evergreen forest in Howland and Duke.

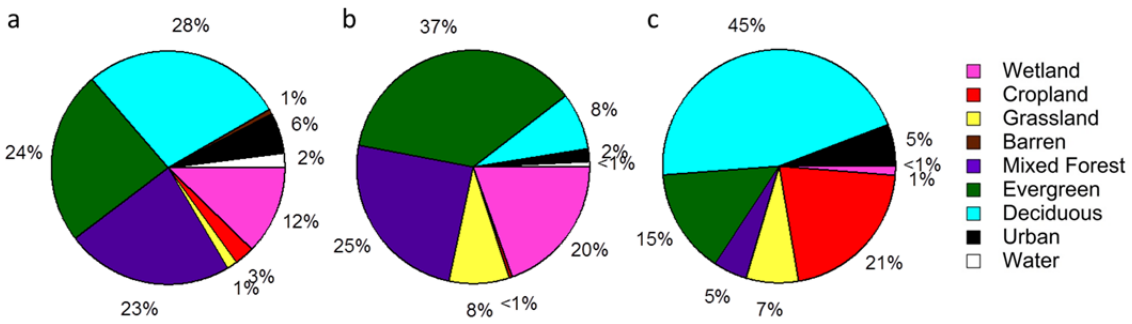

Figure 4.29 ALAR average landcover distributions for all experiments at (a) Harvard, (b) Howland and (c) Duke Forest.

This work presents the first use of aircraft data to investigate spatial representativeness of tower sites to much broader regions. Previous aircraft studies have either been limited to regions within ~15 km of towers (Desjardins et al., 1989; Desjardins et al., 1995; Desjardins et al., 1997; Gioli et al., 2004; Kirby et al., 2008; Metzger et al., 2012), or cover large regions where towers are not available for comparison (Gioli et al., 2006; Miglietta et al., 2007; Hutjes et al., 2010; Maselli et al., 2010; Vellinga et al., 2010; Metzger et al., 2013). While the analysis presented here is specific to the sampled sites, the sampling strategy is broadly applicable to other sites. This method is attractive as it uses entirely independent data and error analysis is straightforward. Overall, due to the varied nature of the sampling and slopes statistically not different than 1 produced by the ODR, it appears the tower sites do not sample significantly different sensible heat and CO_2 flux measurements than the broader heterogeneous ecosystem they are expected to represent for modeling purposes. However, some trends based on landcover may be present. ALAR fluxes at evergreen sites were generally lower than ALAR experimental sites with deciduous landcover. If

more data were available, ALAR-tower regression for these landcovers may have statistically different slopes. Moderate strength Pearson product-moment correlations for all flux comparisons indicate that there is still much variability that is not explained solely by landcover type.

Despite good agreement between aircraft and tower CO_2 and sensible heat flux, there was significant overestimation of latent heat by the aircraft fluxes. Other aircraft campaigns have also observed higher LE values compared to tower sites (Desjardins, et al., 1997; Metzger et al., 2012). It is well known that tower sites do not close the energy budget. This means that the measured energy (heat) fluxes do not account for the total incoming energy (radiation) (Wilson et al., 2002; Kidston et al., 2010). At these tower sites on these measurement days, typically only 80% of the energy budget was explained. It is also know that the energy budget is more easily closed at larger spatial scales (Foken, 2008). This may be due to the presence on non-propagating waves that transfer energy, but are not measured at tower sites due to the time-averaging strategy used. In aircraft, where distance averaging is used, these sources are more easily measured. More work is needed to understand the aircraft-tower latent heat discrepancy. In particular it is necessary to understand if the ALAR fluxes are reasonable or over-predict the available energy budget in the atmosphere. Since this study ALAR has been equipped with a Net Radiometer that will allow coincident measurements of available energy in the form of incoming radiation. This data should be able to address whether the ALAR fluxes are reasonable and if they close the energy budget.

The contribution of large non-propagating eddies causing inflation to the latent heat flux could also be identified using a wavelet analysis, as described by Torrence and

Compo (1998). Briefly, wavelet analysis allows flux measurements to be decomposed in the space and time regimes by calculating fluxes using a moving window approach. The moving window used is a wavelet function applied to the data. The output of a wavelet analysis provides information as to the size of eddies contributing to the flux and their location along the transect. This analysis has been shown to be useful for aircraft fluxes by Metzger et al. (2013) and Karl et al. (2009). This approach could also be used to provide fluxes at very fine spatial scales (~90 m) that may be useful for isolating surface heterogeneity. This type of information may be useful for investigating relationships between variables, such as landcover and RZSM, which are not easily analyzed by aircraft over larger regions due to their small scale heterogeneity.

Though the tower-aircraft intercomparison is useful to provide a sense of the regional scale variability in fluxes, it is reasonable to estimate that a 1:1 relationship may not be expected due to regional scale landcover, soil moisture and other variable changes. More towers for use in modeling efforts would inevitably be valuable. However, comparison of the aircraft fluxes with a model designed to predict fluxes over the same area that the aircraft measured would also be very useful in evaluating the ability of the model to reproduce regionally accurate carbon fluxes. As part of the AirMOSS project the Ecosystem Demography 2 (ED-2) model will be used to compute hourly NEE fluxes at 1 km resolution for each of the 9 AirMOSS biomes as well as 50 km scale NEE for the entire North American continent (Medvigy et al., 2009). This model will use the measured RZSM to improve water interactions in the model. This work is ongoing as part of the AirMOSS project and will eventually enable comparison of the model and aircraft measurements. A sample NEE output for Harvard Forest is shown in Figure 4.30.

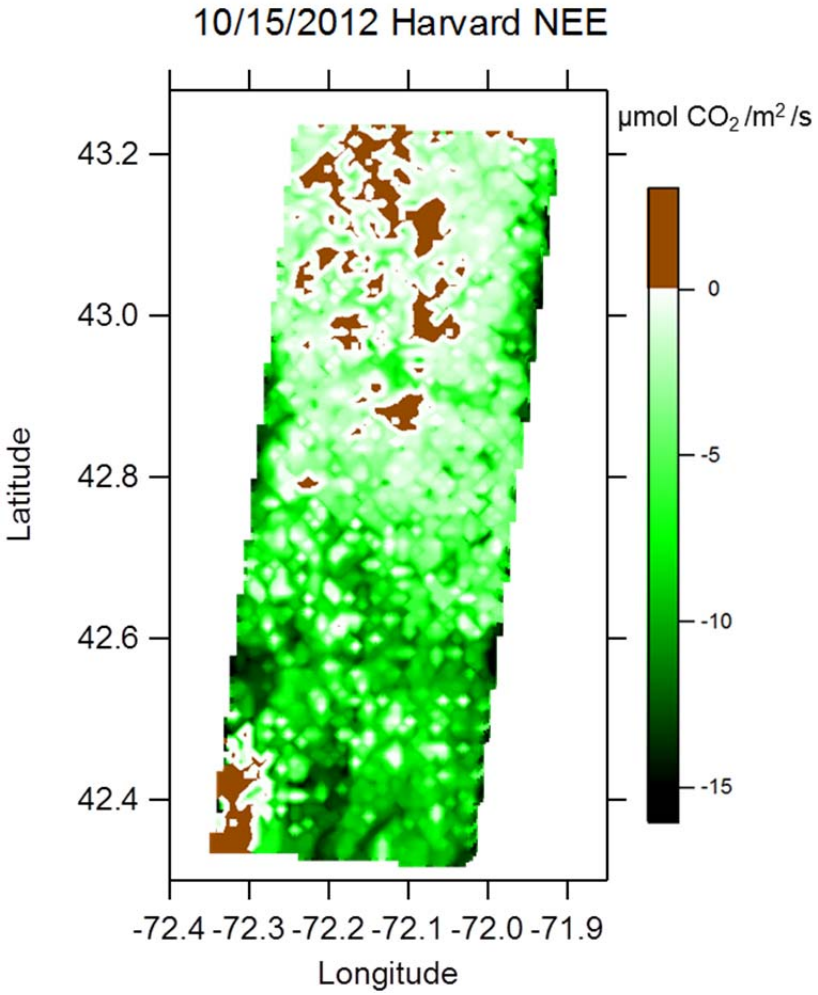

Figure 4.30 ED-2 modeled net ecosystem exchange for Harvard forest on 10/15/2012.

CHAPTER 5. CONCLUSIONS AND FUTURE WORK

The research presented in this dissertation focuses on the improved identification and quantification of greenhouse gas sources and sinks using an aircraft platform. The aircraft platform offers a clear advantage when targets are inaccessible and transient, such as fossil fuel sources, or wide spread regions, such as forests. In addition, high-precision instrumentation and improved experimental design and uncertainty analysis allow for relatively low calculated uncertainty that in some situations may allow real variability to be observed and quantified.

This research is the first to measure mass-balance CH_4 emissions from natural gas drilling operations in the Marcellus Shale of Pennsylvania. The magnitude of the emission rate was 2-3 orders of magnitude higher than EPA estimates for wells in the drilling phase. The source of the high CH_4 emission is most likely the surrounding shallow coal seams that emit low-hydrocarbon CH_4. The underbalanced-drilling method that appeared to be employed at these sites allowed the coal seam CH_4 to be vented and contributed to the suppressed hydrocarbon to CH_4 ratios observed in the region. In addition, the drilling emissions from 8 well pads contributed an outsized proportion of a large regional flux supporting the hypothesis of an asymmetric distribution of emitters (Brandt et al., 2013) as shown in Figure 5.1.

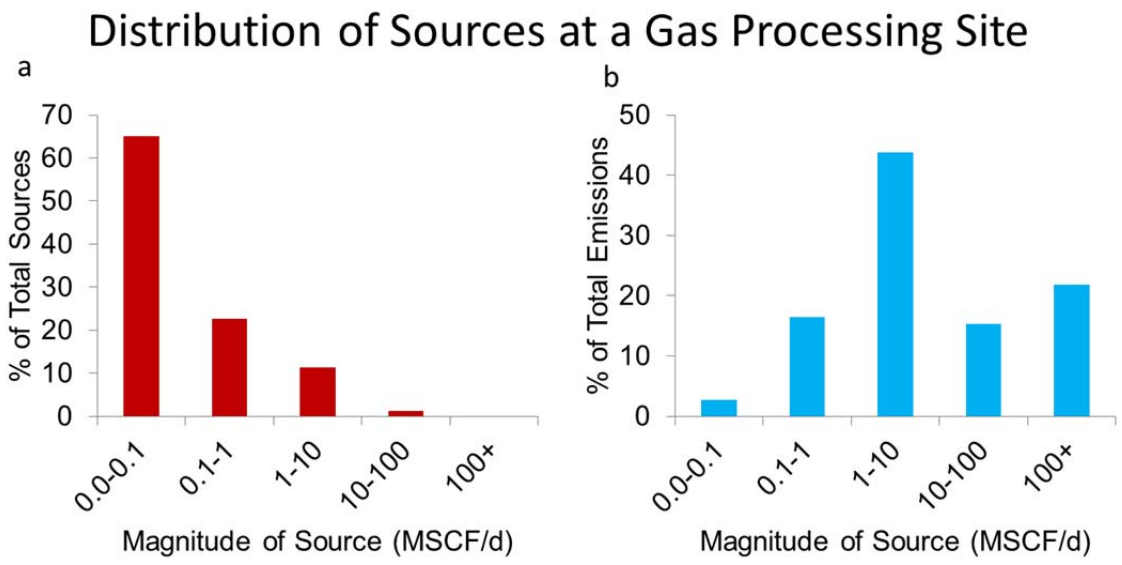

Figure 5.1 Natural gas leaks at a gas processing site for a total of ~18,000 measurements. Shown are the distributions of (a) the source strength and (b) the contribution to the total emissions. Data from Brandt et al. (2013).

More work is needed to identify and understand the cause of super-emitters. This requires long-term and intensive field studies to obtain representative samples of the entire distribution of emitters. Though the aircraft platform can usefully sample isolated super-emitters and regional emissions, it is not suited to measuring low (<40 g CH_4/s) emission rates or quantify hundreds of single well pads (Lavoie et al., in prep). For instance, well pads north of Washington, Pennsylvania in the production stage sampled during this analysis showed no observable downwind enhancement. Ground mobile sampling or unmanned aerial vehicles equipped with CH_4 monitoring equipment will be necessary to quantify emissions from the majority of the range of emitters (Katzenstein et al., 2003; Petron et al., 2012; Karion et al., 2013; Petron et al., 2014; Dunbabin and Marques, 2012; Leifer et al., 2014).

The first in-situ collection of flare data used to calculate CH_4 destruction efficiency was also made using the aircraft platform over the Bakken Formation in North Dakota. Though laboratory-scale and full-scale measurements of flare efficiency have been made, these results are the first to measure DRE from field configurations, which may be substantially different from experimental set-ups. The CH_4 DREs calculated were higher than the EPA reported 98% for all flares sampled and indicate that even flares in impermanent set-ups can almost completely remove CH_4 that would have otherwise been vented to the atmosphere. Though precise operational conditions leading to the high observed DREs could not be obtained, flares were notably observed to be continuously lit and not sputtering or going out. Analysis presented here of limited measurements of sputtering flares in Texas showed DREs close to the reported 98% value. Additionally, crosswind speed did not appear to have a significant detrimental effect on DRE.

Though natural gas flares may not be a significant source of CH_4, they may emit other important GHGs such as black carbon, or toxic chemicals from incomplete combustion. Insufficient assist technology or accelerants may mean larger hydrocarbons are not broken down fully into CO_2 but instead form toxic byproducts such as CO and benzene (Huffman and Staley, 1987). Instrumentation to measure black carbon, CO, particulate matter and VOCs would be extremely useful to identify and quantify non-CO_2 products of flaring. In addition, a key limitation of the work presented here was the inability to employ a mass-balance technique to quantify individual flare or regional fluxes. Representative flux samples could be used to independently scale up flare emissions to the regional level. Currently, EFs must be used in conjunction with state

data of flare volume, which is not always available in a timely manner and difficult to independently verify.

Airborne fluxes of heat and CO_2 were measured over three east-coast temperate forests in Massachusetts, Maine and North Carolina. These data allowed for characterization of regional scale fluxes and covered landcover distributions that were more representative of the region of interest than the tower sites. Despite this, agreement between tower and aircraft fluxes is good for CO_2 and sensible heat flux. Latent heat flux shows regular overestimation with the current experimental design. Analysis of transect length showed ideal transect lengths could be reduced to 10 km and still retain experimental integrity while slightly reducing the latent heat overestimation. However, latent heat discrepancy is still evident at this transect length and should be investigated. Linear regressions between fluxes and variables of interest show low correlation with all parameters and illustrate the complex relationship between forest productivity and corresponding environmental variables, e.g. temperature, soil moisture, soil type and nutrient availability. However, some variables showed high sensitivities (slopes). These include air H_2O fraction and mixed forest landcover fraction. Deciduous sites were observed to correspond to larger uptake of CO_2 relative to evergreen sites, as previously reported (Buchmann and Schulze 1999; Hollinger et al., 1999; Miglietta et al., 2007).

This analysis shows a new approach to characterizing tower representativeness of fluxes of heterogeneous landscapes over larger regions. Though towers are critical for long-term monitoring and ecosystem characterization, they are often used to represent ecosystem types across complex landscapes. Aircraft fluxes can be a useful supplement to other long-term measurement techniques in improving regional NEE modeling.

Programs like NEON that aim to characterize larger regions around their core tower sites with aircraft data may help supplement tower data and estimate regional scale surface flux heterogeneity (Keller et al., 2008).

The advancement of aircraft flux measurement techniques has a wide range of applications including source identification and environmental response functions (Karl et al, 2009; Metzger et al., 2013). To garner more data from resource-intensive aircraft field campaigns, wavelet analysis can be employed. Wavelet analysis, described in Section 4.6, can produce fluxes at very fine spatial resolution that can be used to investigate surface heterogeneity and covariance among suspected important environmental variables. Additionally, it may identify anomalously high contributions among eddies. For instance, instead of choosing an arbitrary high-pass filter to reduce the latent heat fluxes, the flux contributions can be examined and only suspect wavelengths can be excluded. This may provide important independent heat flux and energy balance data to large regions where it is well known that tower sites do not close the available energy budget.

While experimental design can improve some aspects of GHG quantification, advancements in instrumentation can provide further improvement. Differential Absorption LIDAR (DIAL) is a technique that allows column concentrations to be measured. This technique uses light detecting and ranging (LIDAR) light pulses to determine total aerosol concentration as a function of altitude (Browell, 1983). Additionally, a wavelength that corresponds to a specific trace gas spectral feature in the IR range (called the on-line wavelength) and a wavelength away from the spectral feature (called the off-line wavelength) are monitored (Browell, 1983). These ‘on-line’ and ‘off-

line' measurements can be used to extract the proportional amount of a trace species relative to the total aerosol concentration as a function of altitude (Browell, 1983). When installed on an aircraft, DIAL can be used to measure the concentrations in the column below the aircraft. When flown at the boundary layer height, measurements of a plume downwind of a source could be collected more quickly than the mass-balance technique used here with no need to use an interpolation technique. Replicate measurements of small point sources could be performed quickly and large area sources could be quantified within a time-frame during which meteorological conditions do not change greatly (<1 hr). Currently this technology has been developed as a ground-based technique for many gases including CO_2, hydrocarbons, CH_4, O_3, H_2O and SO_2 (Chambers et al., 2006). Ground-based LIDAR can be used to quantify emissions downwind of fossil fuel production activities where signals may be too small to see from an aircraft (Chambers et al., 2006). The LIDAR technique has also been used to measure the wind field (including vertical winds) as a function of altitude (Bilbro et al. 1984). Airborne DIAL instruments have been developed for O_3, H_2O, aerosol and CO_2 (Browell et al., 1998; Abshire et al., 2010). An example data output of the vertical profile of aerosol and O_3 are presented in Figure 5.2 from an airborne DIAL flying downwind of Mount Pinatubo in 1994 when low volcanic activity was present and show the structure of the tropopause at ~8-9 km (Browell et al., 1998). There are significant power consumption and space requirements that currently require larger aircraft than ALAR (Abshire et al., 2010). Data has been recorded for CO_2 at ~1 Hz with precision estimated at 1 ppm, however, if advancements are made and fast (≥10 Hz) measurements can be made this technique may also be used to calculate eddy-covariance flux profiles of the

atmosphere (Abshire et al., 2010). This would allow instantaneous evaluation of the flux gradient.

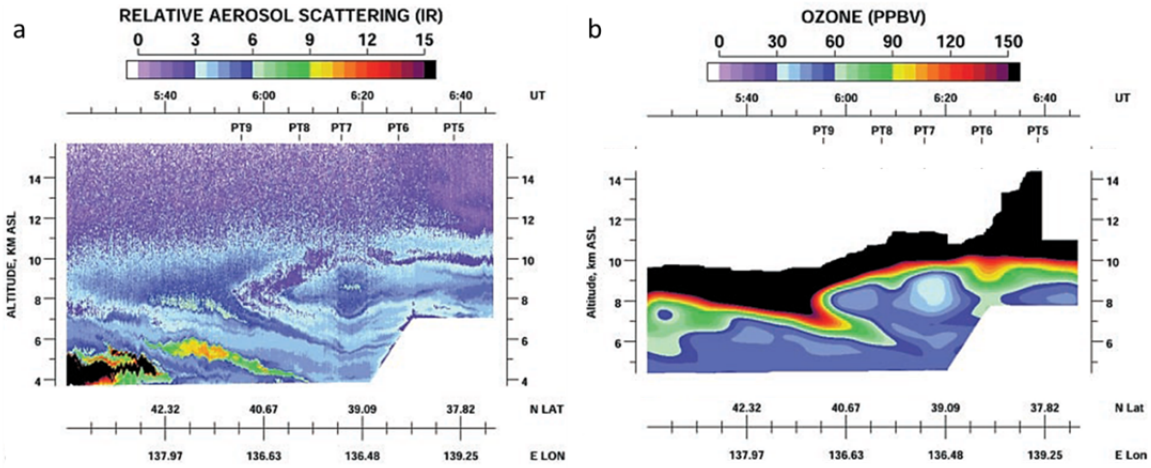

Figure 5.2 (a) a vertical aerosol distribution from LIDAR measurements and (b) a vertical O3 distribution from DIAL measurements (from Browell et al., 1998).

Finally, though the improvement of GHG source and sink quantification is in itself useful, there is expedient opportunity to investigate their interactions. For instance, in determining the lifecycle GHG emissions of ethanol produced from marginal crop biomass (biomass leftover after harvesting), increased CO_2 emissions from removal of soil organic carbon (SOC) in fallow corn fields was not originally included in the lifecycle emission calculation. Under traditional farming practices SOC is oxidized slowly and can remain in place for decades while organics removed from fields for ethanol production are quickly oxidized to CO_2 and cause a net removal of SOC (Liska et al., 2014). The inclusion of this emission in ethanol lifecycle emissions analysis shows very little to no GHG reduction using marginal corn biomass derived ethanol (Liska et

al., 2014). With respect to fossil fuel production GHG lifecycle analysis, no literature has quantified the effect of development of the fragmentation and removal of forest CO_2 uptake. Drohan et al. (2012) found that about half of the newly permitted natural gas wells in Pennsylvania in 2005 corresponded to land that was forested at the time. Natural gas production associated land development in the form of well pads, roads and pipelines can reduce and fragment forest area. Fragmented forests can affect wildlife, plant distribution and have a wide range of effects on important parameters that affect CO_2 uptake (Matlack, 1993; Malcolm, 1994; Gehlhausen et al., 2000; Fahrig, 2003). Globally, natural gas production and use is expected to increase and the impact of natural gas production on forest productivity should be investigated and incorporated into future natural gas lifecycle analyses (McJeon et al., 2014).

LIST OF REFERENCES

LIST OF REFERNCES

Abshire, J. B., Riris, H., Allan, G. R., Weaver, C. J., Mao, J., Sun, X., Hasselbrack, W. E.,Kawa, R., Biraud, S. Pulsed airborne lidar measurements of atmospheric CO_2 column absorption. *Tellus,* 62B, 770-783, 2010.

Akeredolu, F. A., Sonibare, J. A. A review of the usefulness of gas flares in air pollution control. *Management of Environmental Quality.*15 (6)*,* 574-583, 2004.

Alfieri, J. G., Kustas, W. P., Prueger, J. H., Hipps, L. E., Evett, S. R., Bassara, J. B., Neale, C. M. U., French, A. N., Colaizzi, P., Agam, N., Cosh, M. H., Chaves, J. L., Howell, T. A. On the discrepancy between eddy covariance and lysimetry-based surface flux measurements under strongly advective conditions. *Adv. Wat. Res.,* 50, 62-78, 2012.

Allen, D. T., Torres, V. M., Thomas, J., Sullivan, D. W., Harrison, M., Hendler, A., Herndon, S. C., Kolb, C. E., Fraser, M. P., Hill, A. D., Lamb, B. K., Miskimins, J., Sawyer, R. F., Seinfeld, J. H.. Measurements of methane emissions at natural gas production sites in the United States. *Proc. Natl. Acad. Sci. U.S.A.,* 110, 17768-17773, 2013.

Alvarez, R. A., Pacala, S. W., Winebrake, J. J., Chameides, W. L., Hamburg, S. P. Greater focus needed on methane leakage from natural gas infrastructure. *Proc. Natl. Acad. Sci. U.S.A.,* 109, 6435-6440, 2012.

API. *Compendium of Greenhouse Gas Emissions Methodologies for the Oil and Natural Gas Industry* (American Petroleum Institute, Washington DC, 2009, Prepared by T. M. Shires et al. of the URS Coproration).

Arrhenius, S. On the influence of carbonic acid in the air upon the temperature on the ground. *Philos. Mag. J. Sci.,* S15(41), 237-276, 1896.

Arrigo, K. R., van Dijken, G., Long, M. Coast Southern Ocean: A strong anthropogenic CO_2 sink. *Geophys. Res. Lett.,* 35(21), L21602, 2008.

ASME. Drilling Fluids Processing Handbook. American Society of Mechanical Engineers Shale Shaker Committee: Amsterdam, NY, 2005.

Baldocchi, D. D., Hicks, B. B., Meyers, T. P. Measuring biosphere-atmosphere exchanges of biologically related gases with micrometeorological methods. *Ecology,* 69(5), 1331-1340, 1988.

Baldocchi, D. B., Falge, E., Gu, L., Olson, R., Hollinger, D., Running, S., Anthoni, P., Bernhofer, C., Davis, K., Evans, R., Fuentes, J., Goldstein, A., Katul, G., Law, B., Lee, X., Malhi, Y., Meyers, T., Munger, W., Oechel, W., Paw U, K. T., Pilegaard, K., Schmid, H. P., Valentini, R., Verma, S., Vesala, T., Wilson, K., Wofsy, S. FLUXNET: A New Tool to Study the Temporal and Spatial Variability of Ecosystem-Scale Carbon Dioxide, Water Vapor, and Evergy Flux Densities. *Bull. Am. Meteorol. Soc.,* 82(11), 2415-2434, 2001.

Ballantyne, A. P., Alden, C. B., Miller, J. B., Tans, P. P., White, J. W. C. Increase in observed net carbon dioxide uptake by land and oceans during the past 50 years. *Nature,* 488(7409), 70-73, 2012.

Barcza, Z., Kern, A., Haszpra, L., Kljun, N. Spatial representativeness of tall tower eddy covariance measurements using remote sensing and footprint analysis. *Agr. Forest Meteorol.,*149, 798-807, 2009.

Barford, C. C., Wofsy, S. C., Goulden, M. L., Munger, J. W., Pyle, E. H., Urbanski, S. P., Hutyra, L., Saleska, S. R., Fitzjarrald, D., Moore, K. Factors Controlling Long and Short-Term Sequestration of Atmospheric CO_2 in a Mid-latitude Forest. *Science,* 294(5547), 1688-1691, 2001.

Bell, M. L., Dominici, F., Samet, J. M. A Meta-Analysis of Time-Series Studies of Ozone Mortality with Comparison to the National Morbidity, Mortality and Air Pollution Study. *Epidemiology,* 16(4), 436-446, 2005.

Berden, G., Peeters, R., Meijer, G. Cavity ring-down spectroscopy: Experimental schemes and application. *Int. Rev. Phys. Chem.,* 19(4), 565-607, 2000.

Berner, R. A. The long-term carbon cycle, fossil fuels and atmospheric composition. *Nature,* 426, 323-326, 2003.

Berry, J., Bjorkman, O., Photosynthetic temperature response and adaptation to temperature in higher plants. *Annu. Rev. Plant Physiol.,* 31, 491-543, 1980.

Bertoldi, G., Kustas, W. P., Albertson, J. D. Evaluating Source Area Contributions from Aircraft Flux Measurements Over Heterogeneous Land Using Large-Eddy Simulation. *Bound.-Lay. Meterol.,* 147, 261-279, 2013.

Boggs, P. T., Rogers, J. E. Orthogonal distance regression. *Cont. Math.,* 112, 183-194, 1990.

Brandt, A. R., Heath, G. A., Kort, E. A., O'Sullivan, F., Petron, G., Jordan, S. M., Tans, P., Wilcox, J., Gopstein, A. M., Arent, D., Wofsy, S., Brown, N. J., Bradley, R., Stucky, G. D., Eardley, D., Harriss, R. Methane Leaks from North American Natural Gas Systems. *Science,* 343, 733-735, 2014.

Braziel, E.R. Infrastructure Projects Connect Marcellus Shale to Ethane, NGL Markets, *Amer. Oil Gas Reporter,* March, 2011. (Available at http://www.aogr.com/index.php/magazine/coverstory/infrastructure-projects-connect-marcellus-shale-to-ethane-ngl-markets).

Browell, E. V., Ismail, S., Grant, W. B. Differential absorption lidar (DIAL) measurements from air and space. *Appl.Phys. B,* 67, 399-410, 1998.

Browell, E. V. Remote Sensing of Tropospheric Gases and Aerosols with an Airborne DIAL system. *Opt. Laser Rem. Sens.,* 39, 138-147, 1983.

Buchmann, N., Schulze, E. D. Net CO_2 and H_2O fluxes of terrestrial ecosystems. *Glob. Biogeo. Cyc.,* 13(3), 751-760, 1999.

Burba, G. Eddy Covariance Method. LI-COR Biosciences, Lincoln, Nebraska, 2005.

Burnham, A., Han, J., Clark, C. E., Wang, M., Dunn, J. B., Palou-Rivera, I. Life-Cycle Greenhouse Gas Emissions of Shale Gas, Natural Gas, Coal, and Petroleum. *Environ. Sci. Technol.,* 46,619-627, 2012.

Businger, J.A., Wyngaard, J.C., Izumi, Y., Bradley, E.F. Flux-Profile Relationships in the Atmospheric Surface Layer. *J. Atmos. Sci.,* 28, 181-189, 1971.

Cambaliza, M. O., Shepson, P. B., Caulton, D. R., Stirm, B. H., Samarov, D., Gurney, K. R., Turnbull, J., Davis, K. J., Possolo, A., Karion, A., Sweeney, C., Moser, B., Hendricks, A., Lauvaux, T., Mays, K., Whetstone, J., Huang, J., Razlivanov, Miles, N. L., Richardson, S. J. Assessment of uncertainties of an aircraft-based mass-balance approach for quantifying urban greenhouse gas emissions. *Atmos. Chem. Phys.,* 14, 9029-9050, 2014.

Campbell, G. S., Norman, J. M. An Introduction to Environmental Biophysics. Springer, New York, 1998.

Caspersen, J. P., Pacala, S. W., Jenkins, J. C., Hurtt, G. C., Moorcroft, P. R., Birdsey, R. A. Contributions of Land-Use History to Carbon Accumulation in U.S. Forests. *Science,* 290(5494), 1148-1151, 2000.

Chambers, A. K., Strosher, M., Wootton, T., Moncrieff, J., McCready, P. DIAL Measurements of Fugitive Emissions from Natural Gas Plants and the Comparison with Emission Factor Estimates. *15th Annual Emissions Inventory Conference*, US Environmental Protection Agency, New Orleans. 2006.

Chen, H., Winderlich, J., Gerbig, C., Hoefer, A., Rella, C. W., Crosson, E. R., Van Pelt, A. D., Steinback, J., Kolle, O., Beck, V., Daube, B. C., Gottlieb, E. W., Chow, V. Y., Santoni, G. W., Wofsy, S. C. High-accuracy continuous airborne measurements of greenhouse gases (CO_2 and CH_4) using the cavity ring-down spectroscopy (CRDS) technique. *Atmos. Meas. Tech.,* 3, 375-386, 2010.

Chen, B., Coops, N. C., Fu, D., Margolis, H. A., Amiro, B. D., Black, T. A., Arain, M. A., Barr, A. G., Bourque, C. P. A., Flanagan, L. B., Lafleur, P. M., McCaughey, J. H., Wofsy, S. C. Characterizing spatial representativeness of flux tower eddy-covariance measurements across the Canadian Carbon Program Network using remote sensing and footprint analysis. *Rem. Sens. Environ.,* 124, 742-755, 2012.

Chu, D. The GLOBEC kriging software package – EasyKrig3.0, The Woods Hole Oceanographic Institution, 2004. Available at http://globec.whoi.edu/software/kriging/easy_krig/easy_krig.html, (accessed January 2011).

Ciais, P., Peylin, P., Bousquet, P. Regional biospheric carbon fluxes as inferred from atmospheric measurements. *Ecol. Appl.,* 10(6), 1574-1589, 2000.

Clark, V. R., Herzog, H. J. Assessment of the US EPA's Determination of the role for CO_2 Capture and storage in new fossil fuel-fired power plants. *Environ. Sci. Technol.,* 40, 7723-7729, 2014.

Cornic, G., Ghashghaie, J. Effect of temperature on net CO_2 assimilation and photsystem II quantum yield of electron transfer of French bean (Phaseolus vulgaris L.) leaves during drought stress. *Planta,* 185, 255-260, 1991.

Crawford, T. L., Dobosy, R. J. A sensitive fast-response probe to measure turbulence and heat flux from any airplane. *Boud. Lay. Meteor.,* 59, 257-278, 1992.

Crawford, T. L., McMillen, R. T., Dobosy, R. J. MacPherson, I. Correcting airborne flux measurements for aircraft speed variation. *Bound. Layer Meteor.,* 66(3), 237-245, 1993.

Crawford, M. "Hydraulic Fracturing: Mature Technology, Modern Marvel." American Society of Mechanical Engineers., 2013. Available at www.asme.org/engineering-topics/articles/fossil-power/hydraulic-fracturing-mature-technology-modern.

Crosson, E. R., Tan, S., Fidric, B., Paldus, B. Wavelength control for cavity ringdown spectrometer. US7106763 B2, September 12, 2006.

Crosson, E. R. A cavity ring-down analyzer for measuring atmospheric levels of methane, carbon dioxide, and water vapor. *Appl. Phys. B,* 92, 403-408, 2008.

Dakos, V., Scheffer, M., van Nes, E. H., Petoukhov, V., Held, H. Slowing down as an early warning signal for abrupt climate change. *Proc. Natl. Acad. Sci. USA,* 105(38), 14308-14312, 2008.

Davis, S. J., Shearer, C. Climate change: A crack in the natural-gas bridge. *Nature,* 514, 436-437, 2014.

De Bruin, H. A. R., Moore, C. J. Zero-Plane displacement and roughness length for tall vegetation, derived from a simple mass conservation hypothesis. *Bound.-Lay. Meteorol.,* 31, 39-49, 1985.

Desjardins, R. L., Lemon, E. R. Limitation of an eddy-correlation technique for the determination of the carbon dioxide and sensible heat fluxes. *Bound. Layer Meteor.,* 5(4), 475-488, 1974.

Desjardins, R. L., MacPherson, J. I., Schuepp, P . H., Karanja, F. K. An Evaluation of Aircraft Flux Measurements of CO_2, Water Vapor and Sensible Heat. *Bound.-Lay. Meteorol.,* 47, 55-69, 1989.

Desjardins, R. L., MacPherson, J. I., Neumann, H., Den Hartog, D., Schuepp, P. H. Flux Estimates of Latent and Sensible Heat, Carbon Dioxide, and Ozone using an Aircraft-Tower combination. *Atmos. Environ.,* 29(21), 3147-3158, 1995.

Desjardins, R. L., MacPherson, J. I., Mahrt, L., Schuepp, P., Pattey, E., Neumann, H., Baldocchi, D., Wofsy, S., Fitzjarald, D., McCaughey, H., Joiner, D. W. Scaling up flux measurements for the boral forest using aircraft-tower combinations. *J. gGeophys. Res.,* 102(D31), 29125-29133, 1997.

Dlugokencky, E. J., Nisbet, E. G., Fisher, R., Lowry, D. Global atmospheric methane: budget, changes and dangers. *Phil. Trans. R. Soc. A,* 369(1943), 2058-2072, 2011.

Dobosy, R. J., Crawford, T. L., MacPherson, J. I., Desjardins, R. L., Kelley, R. D., Oncley, S. P., Lenschow, D. H. Intercomparison among four flux aircraft at BOREAS in 1994. *J. Geophys. Res.,* 102(D24), 29101-29111, 1997.

Dolman, A. J., Gerbig, C., Noilhan, J., Sarrat, C., Miglietta, F. Detecting regional variability in sources and sinks of carbon dioxide: a synthesis. *Biogeosci.,* 6, 1015-1026, 2009.

Drohan, P. J., Brittingham, M., Bishop, J., Yoder, K. Early Trends in Landcover Change and Forest Fragmentation Due to Shale-Gas Development in Pennsylvania: A Potential Outcome for the Northcentral Appalachians. *Envrion, Manage.,* 49, 1061-1075, 2012.

Dunbain, M., Marques, L. Robotics for Environmental Monitoring.*IEEE Robotics & Automation Mag.,* 19(1), 24- 39, 2012.

Dung, E. J.; Bombom, L. S.; Agusomu, T. D. The effects of gas flaring on crops in the Niger Delta, Nigeria. *GeoJournal*. 73 (4), 297-305, 2008.

Entekhabi, D., Njoku, E. G., O'Neill, P. E., Kellog, K. H., Crow, W. T., Edelstein, W. N., Entin, J. K., Goodman, S. D., Jackson, T. J., Johnson, J., Kimball, J., Piepmeier, J. R., Koster, R. D., Martin, N., McDonald, K. C., Moghaddam, M., Moran, S., Riechle, R., Shi, J. C., Spencer, M. W., Thurman, S. W., Tsang, L., Van Zyl, J.The Soil Moisture Active Passive (SMAP) Mission. *Proc. IEEE,* 98(5), 704-716, 2010.

Eby, M., Zickfeld, K., Montenegro, A., Archer, D., Meissner, K. J., Weaver, A. J. Lifetime of Anthropogenic Climate Change: Millennial Time Scales of Potential CO_2 and Surface Temperature Perturbations. *J. Climate.,* 22, 2501-2511, 2009.

ECCP. Investigation of Flare Gas Emissions in Alberta. Environment Canada Conservation and Protection, Alberta Energy and Utilities Board and the Canadian Association of Petroleum Producers: Calgary, Alberta, 1996. (available at: www.ags.gov.ab.ca/publications/SPE/PDF/SPE_005.pdf).

Eder, F., Schmidt, M., Damian, T., Traumner, K., Mauder, M. Meso-scale eddies affect near-surface turbulent exchange: evidence from lidar and tower measurements. *J. Appl. Meterol. Clim.,* doi: http://dx.doi.org/10.1175/JAMC-D-14-0140.1, 2014.

EIA. Natural Gas: Transportation Process and Flow. U.S. Energy Information Administration: Washington, DC, 2008.

EIA. International Energy Outlook 2013. U.S. Energy Information Administration: Washington, DC, 2013a.

EIA. U.S. Energy-Related Carbon Dioxide Emissions, 2012. Energy Information Administration: Washington, DC, 2013b.

EIA. 2014 Annual Energy Outlook. U.S. Energy Information Administration: Washington, DC, 2014a.

EIA. Natural Gas Gross Withdrawals and Production. U.S. Energy Information Administration. http://www.eia.gov/dnav/ng/ng_prod_sum_a_EPG0_FGW_mmcf_a.htm (Accessed June 18, 2014b).

EIA. Number of Producing Gas Wells. U.S. Energy Information Administartion. http://www.eia.gov/dnav/ng/ng_prod_wells_s1_a.htm. (Accessed Nov. 5, 2014c).

EPA. Methane Emissions from the Natural Gas Industry: Vented and Combustion Source Summary; U.S. Environmental Protection Agency and Gas Research Institute: Washington, DC, 1996; www.epa.gov/gasstar/documents/emissions_report/6_vented.pdf.

EPA. Greenhouse Gas Reporting Program 2010 Summary. U.S. Environmental Protection Agency: Washington, DC, 2010a. (available at: http://www.epa.gov/ghgreporting/ghgdata/2010data.html).

EPA. Greenhouse Gas Emissions Reporting from the Petroleum and Natural Gas Industry: Background Technical Support Document. U.S. Environmental Protection Agency: Washington, DC, 2010, 2010b. (available at: www.epa.gov/ghgreporting/documents/pdf/2010/Subpart-W_TSD.pdf).

EPA. ANNEX 3: Methodological Descriptions for Additional Source or Sink Categories. U.S. Environmental Protection Agency: Washington , DC, 2012a, available at http://www.epa.gov/climatechange/ghgemissions/usinventoryreport.html).

EPA. Approval and Promulgation of Federal Implementation Plan for Oil and Natural Gas Well Production Facilities. U.S. Environmental Protection Agency, Fort Berthold Indian Reservation (Mandan, Hidatsa, and Arikara Nations), ND, *Federal Register*. 77 (158), 48,878-48,898, 2012b.

EPA. Inventory of U.S. Greenhouse Gas Emissions and Sink: 1990-2011. U.S. Environmental Protection Agency: Washington, DC, 2013.

Fahrig, L. Effects of Habitat Fragmentation on Biodiversity. *Ann. Rev. Ecol. Evol. Sys.,* 34, 487-515, 2003.

Fan, S., Gloor, M., Mahlman, J., Pacala, S., Sarmiento, J. Takahashi, Tans, P. A Large Terrestrial Carbon Sink in North America Implied by Atmospheric and Oceanic Carbon Dioxide Data and Models. *Science,* 282(5388), 442-446, 1998.

Fann, N., Lamson, A. D., Anenberg, S. C., Wesson, K., Risley, D., Hubbell, B. J. Estimating the National Public Health Burden Associated with Exposure to Ambient $PM_{2.5}$ and Ozone. *Risk Anal.,* 32(1), 81-95, 2012.

Feely, R. A., Coney, S. C., Cooley, S. R. Ocean Acidification: Present Conditions and Future Changes in a High-CO_2 World. *Oceanography,* 22(4), 36-47, 2009.

Fidric, B. G., Provencal, R. A., Tan, S. M., Crosson, E. R., Kachanov, A. A., Paldus, B. A. "Bananas, Explosives and the Future of Cavity Ring-Down Spectroscopy". *Optics & Photonics News,* July, 25-29, 2003.

Flückiger, J., Monnin, E., Stauffer, B., Schwander, J., Stocker, T. F. High-resolution N_2O ice core record and its relationship with CH_4 and CO_2. *Glob. Biogeo. Cyc.,* 16(1), 1010, 2002.

Foken, T. The Energy Balance Closure Problem: An Overview. *Ecol. Appl.,* 18(6), 1351-1367, 2008.

Fowlie, M., Goulder, L., Kotchen, M., Borenstein, S., Bushnell, J., Davis, L., Greenstone, J., Kolstad, C., Knittel, C., Stavins, R., Wara, M., Wolak, F., Wolfram, C. An economic perspective on the EPA's Clean Power Plan. *Science,* 346(6211), 815-816, 2014.

Frank, J. M., Massman, W. J., Ewers, B. E. Underestimates of sensible heat flux due to vertical velocity measurements errors in non-orthogonal sonic anemometers. *Agr. For. Meteorol.,* 171-172, 72-81, 2013.

Friedl, M. A., McIver, D. K., Hodges, J. C. F., Zhang, X. Y., Muchoney, D., Strahler, A. H., Woodcock, C. E., Gopal, S., Schneider, A., Cooper, A., Baccini, A., Gao, F., Schaaf, C. Global land cover mapping from MODIS: algorithms and early results. *Rem. Sens. Environ.,* 83, 287-302, 2002.

Friedlingstein, P., Fung, I., Holland, E., John, J., Brasseur, G., Erickson, D., Schimel, D. On the contribution of CO_2 fertilization to the missing biospheric sink. *Global Biogeochem. Cycles,* 9(4), 541-556, 1995.

Friedlingstein, P., Cox, P., Betts, R., Bopp, L., von Bloh, W., Brovkin, V., Cadule, P., Doney, S., Eby, M., Fung, I., Bala, G., John, J., Jones, C., Joos, F., Kato, T., Kawamiya, M., Knorr, W., Lindsay, K., Matthews, H. D., Raddats, T., Rayner, P., Reick, C., Roeckner, E., Schnitzler, K. G., Schnur, R., Strassmann, K., Weaver, A. J., Yoshikawa, C., Zeng, N. Climate-Carbon Cycle Feedback Analysis: Results from the C^4MIP Model Intercomparison. *J. Climate,* 19(14), 3337-3353, 2006.

Friedlingstein, P., Houghton, R. A., Marland, G., Hackler, J., Boden, T. A., Conway, T. J., Canadell, J. G., Raupach, M. R., Ciais, P., Le Quéré, C. Update on CO_2 emissions. *Nature Geosci.,* 3, 811-812, 2010.

Friedlingstein, P., Meinshausen, M., Arora, V. K., Jones, C. D., Anav, A., Liddicoat, S. K., Knutti, R. Uncertainties in CMIP5 Climate Projections due to Carbon Cycle Feedbacks. *J. Clim.,* 27(2), 511-526, 2014.

Fu, D., Chen, B., Zhang, H., Wang, J., Black, T. A., Amiro, B. D., Bohrer, G., Bolstad, P., Coulter, R., Rahman, A. F., Dunn, A., McCaughey, J. H., Meyers, T., Verma, S. Estimating landscape net ecosystem exchange at high spatial-temporal resolution based on Landsat data, an improved upscaling model framework, and eddy covariance flux measurements. *Rem. Sens. Environ.,* 141, 90-104, 2014.

Garman, K.E., Hill, K.A., Wyss, P., Carlsen, M., Zimmerman, J.R., Stirm, B.H., Carney, T.Q., Santini, R., Shepson, P.B. An airborne and wind tunnel evaluation of a wind turbulence measurement system for aircraft-based flux measurements. *J. Atmos. Oceanic Tech*., 23, 1696-1708, 2006.

Garman, K.E., Wyss, P., Carlsen, M., Zimmerman, J.R., Stirm, B.H., Carney, T.Q., Santini, R., Shepson, P.B. The contribution of variability of lift-induced upwash to the uncertainty in vertical winds determined from an aircraft platform. *Boundary-Layer Meteorol*., 126, 461-476, 2008.

Gehlhausen, S. M., Schwarts, M. W., Augspurger, C. K. Vegetation and microclimatic edge effects in two mixed-mesophytic forest fragments. *Plant Ecol.,* 147, 21-35, 2000.

Gioli, B., Miglietta, F., De Martino, B., Hutjes, R. W. A., Dolman, H. A. J., Lindroth, A., Schumacker, M., Sanz, M. J., Manca, G., Peressotti, A., Dumas, E. J. Comparison between tower and aircraft-based eddy covariance fluxes in five European regions. *Agr. Forest Meteorol.,*127, 1-16, 2004.

Gioli, B., Miglietta, F., Vaccari, F. P., Zaldei, A., De Martino, B. The Sky Arrow ERA, an innovative airborne platform to monitor mass, momentum and energy exchange of ecosystems. *Ann. Geophys.,* 49, 109-116, 2006.

Goulden, M. L., Munger, J. W., Fan, S. M., Daube, B. C., Wofsy, S. C. Measurements of carbon sequestration by long-term eddy covariance: methods and a critical evaluation of accuracy. *Glob. Change Biol.,* 2, 169-182, 1996.

Grace, J., Mitchard, E., Gloor, E. Perturbations in the carbon budget of the tropics. *Glob. Change Biol.,* 20(10), 3238-3255, 2014.

Griffis, T. J. Black, T. A., Gaumont-Guay, D., Drewitt, G. B., Nesic, Z., Barr, A. G., Morgenstern, K., Kljun, N. Seasonal variation and partitioning of ecosystem respiration in a southern boreal aspen forest. *Agr. Forest Meteorol.,*125, 207-223, 2004.

Gurney, K. R., Law, R. M., Denning, A. S., Rayner, P. J., Baker, D., Bousquet, P., Bruhwiler, L., Chen, Y. H., Ciais, P., Fan, S., Fung, I. Y., Gloor, M., Heimann, M., Higushi, K., John, J., Maki, T., Maksyutov, S., Masarie, K., Peylin, P., Prather, M., Pak, B. C., Randerson, J., Sarmiento, J., Taguchi, S., Takahashi, T., Yuen, C. W. Towards robust regional estimates of CO_2 sources and sinks using atmospheric transport models. *Nature,* 415, 626-630, 2002.

Gurney, K. R., Law, R. M., Denning, A. S., Rayner, P. J., Pak, B. C., Baker, D., Bousquet, P., Bruhwiler, L., Chen, Y. H., Ciais, P., Fung, I. Y., Heimann, M., John, J., Maki, T., Maksyutov, S., Peyling, P. Prather, Taguchi. Transcom 3 inversion Intercomparison: Model mean results for the estimation of seasonal carbon sources and sinks. *Global Biogeochem*. *Cycles,* 18(1), GB1010, 2004.

Hamilton, J.G., E.H. DeLucia, K. George, S.L. Naidu, A.C. Finzi, and W.H. Schlesinger. Forest carbon balance under elevated CO_2. *Oecologia* 131(2): 250-260, 2002.

Hansen, F. V. Surface Roughness Lengths.Army Research Laboratory, ARL-TR-61, 1993.

Hansen, J., Sato, M., Kharecha, P., Beerling, D., Berner, R., Masson-Delmotte, V., Pagani, M., Raymo, M., Royer, D. L., Zachos, J. C., Target atmospheric CO_2: Where should humanity aim? *Open Atmos. Sci. J.,* 2, 217-231, 2008.

Hartman, D. L. Global Physical Climatology. Academic Press, San Diego, 1994.

Hatcher, P. G., Clifford, D. J. The organic geochemistry of coal: from plant materials to coal. *Org. Geochem.,* 27(5-6), 251-257, 1997.

Hayes, D. J., D. W. Kicklighter, A. D. McGuire, M. Chen, Q. Zhuang, F. Yuan, J. M. Melillo and S. D. Wullschleger, The impacts of recent permafrost thaw on land–atmosphere greenhouse gas exchange *Environ. Res. Let.,*. 9, 045005, 2014.

Herrick, J. D., Thomas, R. B. Effects of CO_2 enrichment on the photosynthetic light response of sun and shade leaves of canopy sweetgum trees (*Liquidambar styraciflua*) in a forest ecosystem. *Tree Phys.,* 19, 779-786, 1999.

Higgins, C. W., Pardyjak, E., Froidevaux, M., Simeonov, V., Parlange, M. B. Measured and Estimated Water Vapor Advection in the Atmospheric Surface Layer. *J. Hydrometeorol.,* 14, 1966-1972, 2013.

Hollinger, D. Y., Goltz, S. M., Davidson, E. A., Lee, J. T., Tu, K., Valentine, H. T. Seasonal patterns and environmental control of carbon dioxide and water vapour exchange in an ecotonal boreal forest. *Glob. Change Biol.,* 5, 891-902, 1999.

Hollinger, D. Y., Aber, J., Dail, B., Davidson, E. A., Goltz, S. M., Hughes, H., Leclerc, M. Y., Lee, J. T., Richardson, A. D., Rodrigues, C., Scotts, N. A., Achuatavaries, D., Walsh, J. Spatial and temporal variability in forest-atmosphere CO_2 exchange. *Glob. Change Biol.,* 10, 1689-1706, 2004.

Hong, B., Swaney, D. P., Howarth, R. W. A toolbox for calculating net anthropogenic nitrogen inputs (NANI). *Environ. Model. Softw.* 26, 623-633, 2011.

Horst, T. W., Doran, J. C. Nocturnal drainage flow on simple slopes. *Bound. Lay. Meteor.,* 34(3), 263-286, 1986.

Howarth, R., Santoro, R., Ingraffea, A. Methane and the greenhouse-gas footprint of natural gas from shale formations. *Clim. Change,* 106, 679-690, 2011.

Huffman, G. L., Staley, L. J. The Formation of Products of Incomplete Combustion in Research Combustors. *Nuc. Chem. Waste Manag.,* 7, 29-32, 1987.

Hutjes, R. W. A., Vellinga, O. S., Gioli, B., Miglietta, F. Dis-aggregation of airborne flux measurements using footprint analysis. *Agr. Forest Meteorol.,*150, 966-983, 2010.

Hultman, N., Rebois, D., Scholten, M., Ramig, C. The greenhouse impact of unconventional gas for electricity generation. *Environ. Res. Lett.,* 6, 1-9, 2011.

IPCC, Climate Change 2013: The Physical Science Basis. Working Group I Contribution to the Fifth Assessment Report of the Intergovernmental Panel on Climate Change. Cambridge University Press: New York, 2013.

Isaksen, I. S. A., Gauss, M., Myhre, H., Anthony, K. M. W., Ruppel, C. Strong atmospheric chemistry feedback to climate warming from Arctic methane emissions. *Global Biogeochem. Cycles*, 25(2), GB2002, 2011.

Jacob, D. J. “Lectures on Invers Modeling”, Harvard University: January, 2007.

Jain, A. K., Briegleb, B. P., Minschwaner, K., Wuebbles, D. J. Radiative forcings and global warming potentials of 39 greenhouse gases. *J. Geophys. Res.,* 105(D16), 20773-20790, 2000.

Jiang, M., Griffin, W. M., Hendrickson, C., Jaramillo, P., VanBriesen, J., Venkatesh, A. Life Cycle Greenhouse Gas Emissions of Marcellus Shale Gas. *Environ. Res. Lett.,*6, 034014, 2011.

Johnson, M. R., Kostiuk, L .W. Efficiencies of Low-Momentum Jet Diffusion Flames in Crosswinds. *Combust. Flame*. 123(1-2), 189-200, 2000.

Johnson, M. R., Devillers, R. W., Thomas, K. A. Quantitative Field Measurement of Soot Emission from a Large Gas Flare Using Sky-LOSA. *Environ. Sci. Technol.* 45 (1)*,* 345-350, 2011.

Joos, F., Roth, R., Fuglestvedt, J. S., Peters, G. P., Enting, I. G., von Bloh, W., Brovkin, V., Burke, E. J., Eby, M., Edwards, N. R., Friedrich, T., Frolicher, T. L., Halloran, P. R., Holden, P. B., Jones, C., Kleinen, T., Mackenzie, F. T., Matsumoto, K., Meinshausen, M., Plattner, G.-K., Reisinger, A., Segschneider, J., Shaffer, G., Steinacher, M., Strassmann, K., Tanaka, K., Timmermann, A., Weaver, A. J. Carbon dioxide and climate impulse response fucntions for the computation of greenhouse gas metrics: a multi-model analysis. *Atmos. Chem. Phys.,* 13(5), 2793-2825, 2013.

Jorgensen, H. Methane emission by growing pigs and adult sows as influenced by fermentation. *Livest. Sci.* 109, 216-219, 2007.

Justice, C. O., Townshend, J. R. G., Vermote, E. G., Masuoka, E., Wolfe, R. W., Saleous, N., Roy, D. P., Morisette, J. T. An overview of MODIS Land data processing and product status. *Rem. Sens. Environ.,* 83, 3-15, 2002.

Kaimal, J. C. Measurment of Momentum and Heat Flux Variation in the Surface Boundary Layer. *Radio Sci.,* 4(12), 1147-1153, 1969.

Kaimal, J. C., Wyngaard, J. C., Izumi, Y., Cote, O. R. Spectral characteristics of surface-layer turbulence. *Quart. J. R. Met. Soc.,* 98, 563-589, 1972.

Kaimal, J. C., Wyngaard, J. C. The Kansas and Minnesota Experiments. *Bound. Layer Meteor.,* 50(1-4), 31-47, 1990.

Karion, A., Sweeney, C., Petron, G., Frost, G., Hardesty, R. M., Kofler, J., Miller, B. R., Newberger, T., Wolter, S., Banta, R., Brewer, Al, Dlugokencky, E., Lang, P., Montzka, S. A., Schnell, R., Tans, P., Trainer, M., Zamora, R., Conley, S. Methane emissions estimate from airborne measurements over a western United States natural gas field. *Geophys. Res. Lett.,* 40, 4393-4397, 2013.

Karl, T., Apel, E., Hodzic, A., Riemer, D. D., Blake, D. R., Wiedinmyer, C. Emissions of volatile organic compounds inferred from airborne flux measurements over a megacity. *Atmos. Chem. Phys.,* 9, 271-285, 2009.

Katzenstein, A. S., Doezema, L. A., Simpson, I. J., Blake, D. R., Rowland, F. S. Extensive regional atmospheric hydrocarbon pollution in the southwestern United States. *Proc. Natl. Acad. Sci. U.S.A.,* 100, 11975-11979, 2003.

Keeling, C. D., Bacastow, R. B., Bainbridge, A. E., Ekdahl, C. A., Gunther, P R., Waterman, L. S. Atmospheric carbon dioxide variations at Mauna Loa Observatory, Hawaii. *Tellus,* 28(6), 538-551, 1976.

Keller, M., Schimel, D. S., Hargrove, W. W., Hoffman, F. M. A continental strategy for the National Ecological Observatory Network. *Front. Ecol. Environ.,* 6(5), 282-284, 2008.

Kerr, Y. H., Waldtuefel, P., Wigneron, J. P., Martinuzzi, J. M., Font, J., Berger, M. Soil Moisture Retreival from Space: The Soil Moisture and Ocean Salinity (SMOS) Mission. *IEEE Trans. Geosci. Rem. Sens.,* 39(8), 1729-1735, 2001.

Kidston, J., Brummer, C., Black, T. A., Morgenstern, K., Nesic, Z., McCaughey, J. H., Barr, A. G. Energy Balance Closure Using Eddy Covariance Above Two Different Land Surfaces and Implications for CO_2 Flux Measurements. *Bound.-Lay. Meteorol.,* 136, 193-218, 2010.

Kim, S. W., McKeen, S. A., Frost, G. J., Lee, S. H., Trainer, M., Richter, A., Angevine, W. M., Atlas, E., Bianco, L., Boersma, K. F., Brioude, J., Burrows, J. P., de Gouw, J., Fried, A., Gleason, J., Hilboll, A., Mellqvist, J., Peischl, J., Richter, D., Rivera, C., Ryerson, T., te Lintel Hekkert, S., Walega, J., Warneke, C., Weibring, P., Williams, E. Evaluations of NO_x and highly reactive VOC emission inventories in Texas and their implications for ozone plume simulations during the Texas Air Quality Study 2006. *Atmos. Chem. Phys.,* 11, 11361-11386, 2011.

Kirby, S., Dobosy, R., Williamson, D., Dumas, E. An aircraft-based data analysis method for discerning individual fluxes in a heterogeneous agricultural landscape. *Agr. For. Meteorol.,* 148, 481-489, 2008.

Kirschke, S., Bousquet, P., Ciais, P., Saunois, M., Canadell, J. G., Dlugokencky, E. J., Bergamaschi, P., Bergmann, D., Blake, D. R., Bruhwiler, L., Cameron-Smith, P., Castaldi, S., Chevallier, F., Feng, L., Fraser, A., Heimann, M., Hodson, E. L., Houweling, S., Josse, B., Fraser, P. J., Krummel, P. B., Lamarque, J.-F., Langenfelds, R. L., Le Quéré, C., Naik, V., O'Doherty, S., Palmer, P. I., Pison, I., Plummer, D., Poulter, B., Prinn, R. G., Rigby, M., Ringeval, B., Santini, M., Schmidt, M., Shindell, D. T., Simpson, I. J., Spahni, R., Steele, L. P., Strode, S. A., Sudo, K., Szopa, S., van der Werf, G. R., Voulgarakis, A., van Weele, M., Weiss, R. F., Williams, J. E., Zeng, G. Three decades of global methane sources and sinks. *Nature Geosci.,* 6(10), 813-823, 2013.

Kljun, N., Rotach, M. W., Schmid, H. P. A Three-Dimensional Backward Lagrangian Footprint Model for a Wide Range of Boundary-Layer Stratifications. *Bound.-Lay. Meteorol.,* 103, 205-226, 2002.

Kljun, N., Calanca, P., Rotach, M. W., Schmid, H. P. A Simple Parameterisation for Flux Footprint Predictions. *Bound.-Lay. Meteorol.,* 112, 503-523, 2004.

Knighton, W. B., Herndon, S. C., Franklin, J. F., Wood, E. C., Wormhout, J., Brooks, W., Fortner, E. C., Allen, D. T. Direct measurement of volatile organic compound emissions from industrial flares using real-time online techniques: Proton Transfer Reaction Mass Spectrometry and Tunable Infrared Laser Differential Absorption Spectroscopy. *Ind. Eng. Chem. Res.* 51 (39), 12674-126684, 2012.

Knutti, R., Sedlacek, J. Robustness and uncertainties in the new CMIP5 climate model projections. *Nature Clim. Change,* 3(4), 369-373, 2013.

Kort, E. A., Wofsy, S. C., Daube, B. C., Diao, M., Elkings, J. W., Gao, R. S., Hintsa, E. J., Hurst, D. F., Jimenez, R., Moore, F. L., Spackman, J. R., Zondlo, M. A. *Nature Geosci.,* 5, 318-321, 2012.

Kostiuk, L. W., Majeski, A. J., Poudens, M. B., Johnson, M. R., Wilson, D. J. Scaling of wake-stabilized jet diffusion flames in a transverse air stream. *Proc. Combust. Inst.* 28 (1), 553-559, 2000.

Kotarba, M. J. Composition and origin of coalbed gases in the Upper Silesian and Lublin basins, Poland. *Org. Geochem.* 32, 163-180, 2001.

Krishnan, P. Black, T. A., Grant, N. J., Barr, A. G., Hogg, E. H., Jassal, R. S., Morgenstern, K. Impact of changing soil moisture distribution on net ecosystem productivity of a boreal aspen forest during and following drought. *Agr. Forest Meteorol.,* 139, 208-223, 2006.

Kustas, W. P., Anderson, M. C., French, A. N., Vickers, D. Using a remote sensing field experiment to investigate flux-footprint relations and flux sampling distributions for tower and aircraft-based observations. *Adv. Water Res.,* 29, 355-368, 2006.

Lee, X., Neumann, H. H., Hartog, G., Mickle, R. E., Fuentes, J. D., Black, T. A., Yang, P. C., Blanken, P. D. Observation of gravity waves in a boreal forest. *Bound. Lay. Meteor.,* 84(3), 383-398, 1997.

Leifer, I., Melton, C., Gupta, M., Leen, B. Mobile Monitoring of Methane Leakage. *Gases & Instrumentation,* July/August, 20-24, 2014.

LeMone, M. A., Grossman, R. L., Chan, F., Ikeda, K., Yates, D. Choosing the Averaging Interval for Comparison of Observed and Modeled Fluxes along Aircraft Transects over a Heterogeneous Surface. *J. Hydrometeorol.,* 4, 179-195, 2003.

Lenschow, D. H., Mann, J., Kristensen, L. How Long is Long Enough When Measuring Fluxes and Other Turbulence Statistics? *J. Atmos. Ocean. Technol.,* 11(3), 661-673,1994.

Le Quéré, C., Andres, R. J., Boden, T., Conway, T., Houghton, R. A., House, J. I., Marland, G., Peters, G. P., van der Werf, G. R., Ahlstrom, A., Andrew, R. M., Bopp, L., Canadell, J. G., Ciais, P., Doney, S. C., Enright, C., Friedlingstein, P., Huntingford, C., Jain, A. K., Jourdain, C., Kato, E., Keeling, R. F., Goldewijk, K. K., Levis, S., Levy, P., Lomas, M., Poulter, B., Raupach, M. R., Schwinger, J., Sitch, S., Stocker, B. D., Viovy, N., Zaehle, S., Zeng, N. The global carbon budget 1959-2011. *Earth Syst. Sci. Data,* 5(1), 165-185, 2013.

Le Quéré, C., Peters, G. P., Andres, R. J., Andrew, R. M., Boden, T. A., Ciais, P., Friedlingstein, P., Houghton, R. A., Marland, G., Moriarty, R., Sitch, S., Tans, P., Arneth, A., Arvantis, A., Bakker, D. C. E., Bopp, L., Canadell, J. G., Chini, L. P., Doney, S. C., Harper, A., Harris, I., House, J. I., Jain, A. K., Jones, S. D., Kato, E., Keeling, R. F., Goldewijk, K. K., Kortzinger, A., Kove, C., Lefevre, N., Maignan, F., Omar, A., Ono, T., Park, G. H., Pfeil, B., Poulter, B., Raupach, M. R., Regnier, P., Rodenbeck, C., Saito, S., Schwinger, J., Segschneider, J., Stocker, B. D., Takahashi, T., Tilbrook, B., van Heuven S., Viovy, N., Wanninkhof, R., Wiltshire, A., Zaehle, S. The global carbon budget 2013. *Earth Syst. Sci. Data,* 6(1), 235-263, 2014.

Leuning, R., Moncrieff, J. Eddy-Covariance CO_2 Flux Measurements Using Open- and Closed-Path CO_2 Analysers: Corrections for Analysser Water Vapour Sensitivity and Damping of Fluctuation in Air Sampling Tubes. *Bound.-Lay. Meteorol.,* 53, 63-76, 1990.

Long, S. P. Modification of the response of photosynthetic productivity to rising temperature by atmospheric CO2 concentrations: Has its importance been underestimated? *Plant Cell Environ.,* 14, 729-739, 1991.

Lothon, M. Couvreux, F., Donier, S., Guichard, F., Lacarrere, P., Lenschow, D. H., Noilhan, J., Said, F. Impact of coherent eddies on airborne measurements of vertical turbulent fluxes. *Bound.-Lay. Meteorol.,* 124, 425-447, 2007.

Luo, Y., B. Medlyn, D. Hui, D. Ellsworth, J. Reynolds, and G. Katul. Gross primary productivity in Duke Forest: Modeling synthesis of CO_2 experiment and eddy-flux data. *Ecological Applications* 11(1): 239-252, 2001.

MacRae, M. "Fracking: A Look Back." American Society of Mechanical Engineers, Dec. 2012. Available at www.asme.org/engineering-topics/articles/fossil-power/fracking-a-look-back.

Magnani, F., Mencuccini, M., Borghetti, M., Berbigier, P., Berninger, F., Delzon, S., Grelle, A., Hari, P., Jarvis, P. G., Kolari, P., Kowalski, A. S., Lankreijer, H., Law, B. E., Lindrtoh, A., Loustau, D., Manca, G., Moncrieff, J. B., Rayment, M., Tedeschi, V., Valentini, R., Grace, J. The human footprint in the carbon cycle of temperate and boreal forests.

Malcolm, J. R. Edge Effects in Central Amazonian Forest Fragments. *Ecol. Soc. Amer.,* 75(8), 2438-2445, 1994.

Mann, J., Lenschow, D. H. Errors in airborne flux measurements. *J. Geophys. Res.,* 99(D7), 14519-14526, 1994.

Maselli, F., Gioli, B., Chiesi, M., Vaccari, F., Zaldei, A., Fibbi, L., Bindi, M., Miglietta, F. Validating an integrated strategy to model net land carbon exchange against aircraft flux measurements. *Remote Sen. Environ.,* 114, 1108-1116, 2010.

Massman, W. J. A simple method for estimating frequency response corrections for eddy covariance systems. *Agr. Forest Meteorol.,*104, 185-198, 2000.

Matlack, G. R. Microenvironment variation within and among forest edge sites in the eastern United States. *Biol. Cons.,* 66, 185-194, 1993.

Mays, K. L., Shepson, P. B., Stirm, B. H., Karion, A. K., Sweeney, C., Gurney, K. R. Aircraft-Based Measurements of the Carbon Footprint of Indianapolis. *Environ. Sci. Technol.,* 43(20), 7816-7823, 2009.

McCarthy, H.R., R. Oren, A.C. Finzi, D.S. Ellsworth, H.S. Kim, K.H. Johnsen, and B. Millar. Temporal dynamics and spatial variability in the enhancement of canopy leaf area under elevated atmospheric CO_2**.** *Global Change Biology* 13(12): 2479-2497, 2007.

McJeon, H., Edmonds, J., Bauer, N., Clarke, L., Fisher, B., Flannery, B. P., Hilaire, J., Krey, V., Marangoni, G., Mi, R., Riahi, K., Rogner, H., Tavoni, M. Limited impact on decadal-scale climate change from increased use of natural gas. *Nature,* 514, 482-485, 2014.

McNaughton, K. G., Lauback, J. Power Spectra and Cospectra for Wind and Scalars in a Disturbed Surface Layer at the Base of an Advective Inversion. *Bound. Lay. Meteor.,* 96(1-2), 143-185, 2000.

Medvigy, D., Wofsy, S. C., Munger, J. W., Hollinger, D. Y., Moorcroft, P. R. Mechanistic scaling of ecosystem function and dynamics in space and time: Ecosystem Demography model version 2. *J. Geophys. Res.,* 114(G1), G01002, 2009.

Medvigy, D., Wofsy, S. C., Munger, J. W., Moorcroft, P. R. Responses of terrestrial ecosystems and carbon budgets to current and future environmental variability. *Proc. Nat. Acad. Sci. U.S.A.,* 107(18), 8275-8280, 2010.

Metzger, S., Junkermann, W., Mauder, M., Beyrich, F., Butterback-Bahl, K., Schmid, H. P., Foken T. Eddy Covariance flux measurements with a weight-shift microlight aircraft. *Atmos. Meas. Tech.,* 5, 1699-1717, 2012.

Metzger, S., Junkermann, W., Mauder, M., Butterback-Bahl, K., Trancon y Widemann, B., Neidl, F., Schager, K., Wieneke, S., Zheng, X. H., Schmid, H. P., Foken, T. Spatially explicit regionalization of airborne flux measurements using environmental response functions. *Biogeosci.,* 10, 2193-2217, 2013.

Miglietta, F., Gioli, B., Hutjes, R. W. A., Reichstein, M. Net regional ecosystem CO_2 exchange from airborne and ground-based eddy covariance, land-use maps and weather observations. *Glob. Change Biol.,* 13, 548-560, 2007.

Miller, J. C., Miller J. N. *Statistics for Analytical Chemistry,* 3rd ed.; Ellis Horwood Ltd.: Chichester, 1993.

Miller, S. M., Wofsy, S. C., Michalak, A. M., Kort, E. A., Andrews, A. E., Biraud, S. C., Dlugokencky, E. J., Eluszkiewicz, J., Fischer, M. L., Janssens-Maenhout, G., Miller, B. R., Miller, J. B., Montzka, S. A., Nehrkorn, T., Sweeney, C. Anthropogenic emissions of methane in the United States. *Proc. Natl. Acad. Sci. U.S.A.,* 110, 20018-20022, 2013.

Moghaddam, M., Saatchi, S., Cuenca, R. H. Estimating Subcanopy soil moisture with radar. *J. Geophys. Res.,*105(D11), 14899-14911, 2000.

Monson, R. K., Stidham, M. A., Williams, G. J., Edwards, G. E., Uribe, E. G. Temperature Dependence of Photosynthesis in *Agropyron smithii* Rydb. *Plant Physiol.,* 69, 921-928, 1982.

Moorcroft, P. R. How close are we to a predictive science of the biosphere? *TRENDS Ecol. Evol.,* 21(7), 400-407, 2006.

Moore, C. J. Frequency response corrections for eddy correlation systems. *Bound.-Lay. Meteor.,* 37, 17-35, 1986.

NETL. Life Cycle Greenhouse Gas Inventory of Natural Gas Extraction, Delivery and Electricity Production. National Energy Technology Laboratory: 10/24/2011, 2011.

Nieuwstadt, F. T. M., de Valk, J. P. J. M. M. A large eddy simulation of buoyant and non-buoyant plume dispersion in the atmospheric boundary layer. *Atmos. Environ.*, 21 (12), 2573-2587, 1987.

O'Connor, F. M., Boucher, O., Gedney, N., Jones, C. D., Folberth, G. A., Coppell, R., Friedlingstein, P., Collins, W. J., Chappellaz, J., Ridley, J., Johnson, C. E. Possible Role of Wetlands, Permafrost, and Methane Hydrates in the Methane Cycle Under Future Climate Change: A Review. *Rev. Geophys.,* 48(4), RG4005, 2010.

Office of the Federal Register. Standards of Performance for Greenhouse Gas Emissions From New Stationary Sources: Electric Utility Generating Units. A Propos. Rule by EPA 01/08/2014.

Olivier, J. G. I., Janssens-Maenhout, G ., Peters, J. A. H. W. Trends in Global CO_2 Emissions. PBL Netherland Environmental Assessment Agency: Paris, 2013. p.16-17.

Oltmans, S., Schnell, R., Johnson, B., Petron, G., Mefford, T., Neely III, R. Anatomy of wintertime ozone associated with oil and natural gas extraction activity in Wyoming and Utah. *Elementa,* 2, 000024, 2014.

Oren, R., D.S. Ellsworth, K.H. Johnsen, N. Phillips, B.E. Ewers, C. Maier, K.V.R. Schafer, H. McCarthy, G. Hendrey, S.G. McNulty, and G.G. Katul. Soil fertility limits carbon sequestration by forest ecosystems in a CO_2-enriched atmosphere. *Nature,* 411(6836): 469-472, 2001.

Orimoogunje, O. O., Ayanlade, A., Akinkuolie, T. A., Odiong, A. U. Perception on Effect of Gas Flaring on the Environment. *Res. J. Environ. Earth Sci*. 2 (4), 188-193, 2010.

Osborne, S. G., McIntosh, J. C. Chemical and isotopic tracers of the contribution of microbial gas in Devonian organic-rich shales and reservoir sandstones, northern Appalachian Basin. *Appl. Geochem.,* 24, 456-471, 2010.

Osborne, S. G., Vengosh, A., Warner, N. R., Jackson, R. B. Methane contamination of drinking water accompanying gas-well drilling and hydraulic fracturing. *Proc. Natl. Acad. Sci. U.S.A.,* 108, 8172-8176, 2011.

Otto-Bliesner, B. L., Marshall, S. J., Overpeck, J. T., Miller, G. J., Hu, A., CAPE Last Interglacial Project members. Simulating Arctic Climate Warmth and Icefield Retreat in the Last Interglaciation. *Science,* 311(5768), 1751-1753, 2006.

Ouyang, Z., Chen, J., Becker, R., Chu, H., Xie, J., Shao, C., John, R. Disentangling the confounding effects of PAR and air temperature on net ecosystem exchange at multiple time scales. *Ecological Complexity,* 19, 46-58, 2014.

Pacala, S. W., Hurtt, G. C., Baker, D., Peylin, P., Houghton, R. A., Birdsey, R. A., Heath, L., Sundquist, E. T., Stallard, R. F., Ciais, P., Moorcroft, P., Caspersen, J. P., Shevliakova, E., Moore, B., Kohlmaier, G., Holland, E., Gloor, M., Harmon, M. E., Fan, S. M., Sarmiento, J. L., Goodale, C. L., Schimel, D., Field, C.B. Consistent Land and Atmosphere-Based U. S. Carbon Sink Estimates. *Science,* 292(5525), 2316-2320, 2001.

PADEP. "Internal File Review: Permitted Wells: 12524400-02, 12524425, 125124516, 12524517, 12524529-41, 12524552, 12524553, 1252455-58, 12524563, 12524564, 12524589, 12524600, 12524617, 12524618, 12524627, 12524628, 12524696, 12524713, 12524714, 12524762." 14 Aug 2012. Pennsylvania Department of Environmental Protection (PADEP), Southwest Regional Office, Pittsburgh PA.

PADEP. Comparison of Air Emission Standards for the Oil & Gas Industry. Pennsylvania Department of Environmental Protection (PADEP), Bureau of Air Quality, Pittsburgh PA. 2014.

Pan, Y., Birdsey, R. A., Fang, Jingyun, F., Houghton, R., Kauppi, P. E., Kurz, W. A., Phillips, O. L., Shvidenko, A., Lewis, S. L., Canadell, J. G., Ciais, P., Jackson, R. B., Pacala, S. W., McGuire, A. D., Piao, S., Rautiainen, A., Sitch, S., Hayes, D. A Large and Persistent Carbon Sink in the World's Forests. *Science,* 333(6045), 988-993, 2011.

Parazoo, N. C., Bowman, K., Fisher, J. B., Frankenberg, C., Jones, D. B. A., Cescatti, A., Perez-Priego, O., Wohlfahrt, G., Montagnani, L. Terrestrial Gross Primary Production Inferred From Satellite Fluorescence and Vegetation Models. *Glob. Change Biol.,* 20(10), 3103-3121, 2014.

Parks, P. J., Hardie, I. W., Tedder, C. A., Wear, D. N. Using Resource Economics to Anticipate Forest Land Use Change in the U.S. Mid-Atlantic Region. *Environ. Mon. Assess.,* 63(1), 175-185, 2000.

Peischl, J., Ryerson, T. B., Brioude, J., Aikin, K. C., Andres, A. E., Atlas, E., Blaek, D., Daube, B. C., de Gouw, J. A., Dlugokencky, E., Frost, G. J., Gentner, D. R., Gilman, J. B., Goldstein, A. H., Harley, R. A., Holloway, J. S., Kofler, J., Kuster, W. C., Lang, P. M., Novelli, P. C., Santoni, G. W., Trainer, M., Wofsy, S. C., Parrish, D. D. Quantifying sources of methane using light alkanes in the Los Angeles basin, California. *J. Geophys. Res. Atmos.,* 118, 4974-4990, 2013.

Peters, W., Jacobson, A., Sweeney, C., Andrews, A., Conway, T., Masarie, K., Miller, J., Bruhwiler, L., Pétron, G., Hirsch, A., Worthy, D., van der Werf, G., Randerson, J., Wennberg, P., Krol, M.m Tans, P. An atmospheric perspective on North American carbon dioxide exchange: CarbonTracker. *Proc. Natl. Acad. Sci. USA,* 104 (48), 18925-18930, 2007.

Petron, G., Frost, G., Miller, B. R., Hirsch, A. I., Montzka, S. A., Karion, A., Trainer, M., Sweeney, C., Andrews, A. E., Miller, L., Kofler, J., Bar-Ilan, A., Dlugokencky, E. J., Patrick, L., Moore, C. T., Ryerson, T. B., Siso, C., Kolodzey, W., Lang, P. M., Conway, R., Novelli, P., Masarie, K., Hall, B., Guenther, D., Kitzis, D., Miller, J., Welsh, D., Wolfe, D., Neff, W., Tans, P. Hydrocarbon emissions characterization in the Colorado Front Range: A pilot study. *J. Geophys. Res.,* 117, D04304, 2012.

Petron, G., Karion, A., Sweeney, C., Miller, B. R., Montzka, S. A., Frost, G., Trainer, M., Tans, P., Andrews, A. E., Kofler, J., Detlev, H., Guenther, D., Dlugokencky, E. J., Lang, P. M., Newberger, T., Wolter, S., Hall, B., Novelli, P., Brewer, A., Conley, S., Hardesty, M., Banta, R., White, A., Noone, D., Wolfe, D., Schnell, R. A new look at methane and non-methane hydrocarbon emissions from oil and natural gas operations in the Colorado Denver-Julesburg Basin. *J. Geophys. Res. Atmos.,* 11, 6836-6852, 2014.

Peylin, P., Baker, D., Sarmiento, J., Ciais, P., Bousquet, P. Influence of transport uncertainty on annual mean and seasonal inversions of atmospheric CO_2 data. *J. Geophys. Res*., 107(D19), 4385, 2002.

Qu, Y., Duffy, C. J. A semidiscrete finite volume formulation for multiprocess watershed simulation. *Water Resour. Res.,* 43, W08419, 2007.

Prandtl, L. Uber Flussigkeits bewegung bei sehr kleiner Reibung. *Verhaldlg III Int. Math. Kong,* 484–491, 1904. Translation available: Motion of fluids with very little viscosity.

Rannik, U., Vesala, T. Autoregressive filtering versus linear detrending in estimation of fluxes by the eddy covariance method. *Bound.-Lay. Meteor.,* 91, 259-280, 1999.

Raupach, M. R., Rayner, P. J., Barrett, D. J., Defries, R. S., Heimann, M., Ojima, D. S., Quegan, S., Schmullius, C. C. Model-data synthesis in terrestrial carbon observation: methods, data requirements and data uncertainty specifications. *Glob. Change Biol.,* 11(3), 378-397, 2005.

Raupach, M. R., Gloor, M., Sarmiento, J. L., Canadell, J. G., Frölicher, T. L., Gasser, T., Houghton, R. A., Le Quéré, C., Trudinger, C. M. The declining uptake rate of atmospheric CO_2 by land and ocean sinks. *Biogeosciences Discuss.,* 10(11), 18407-18454, 2013.

Reigber, A., Moreira, A. First Demonstration of Airborne SAR Tomography Using Multibaseline L-Band Data. *IEEE Trans. Geosci. Rem. Sens.,* 38(5), 2142-2152, 2000.

Retcofsky, H. L. Investifation of the Chemical Structure of Coal by Nuclear Magnetic Resonance and Infrared Spectrometry. *Appl. Spec.,* 31(2), 116-121, 1977.

Reuter, M., Buchwitz, M., Hilboll, A., Richter, A., Schneising, O., Hilker, M., Heymann, J., Bovensmann, H., Burrows, J. P. Decreasing emissions of NO_x relative to CO_2 in East Asia inferred from satellite observations. *Nature Geosci.,* 7, 792-795, 2014.

Rogner, H. H. An Assessment of World Hydrocarbon Resources. *Annu. Rev. Energy Environ.* 22, 217-262,1997.

Rojey, A., Jaffret, C., Cornot-Gandolphe, S., Durand, B., Jullian, S., Valais, M. Natural Gas: Production, Processing, Transport. Rojey, A., Ed.; Imprimerie Nouvelle: Paris, 1997. p.17.

Ryerson, T. B., Trainer, M., Angevine, W. M., Brock, C. A., Dissly, R. W., Fehsenfeld, F. C., Frost, G. J., Goldan, P. D., Holloway, J. S., Hubler, G., Jakoubek, R. O., Kuster, W. C., Neuman, J. A., Nicks Jr., D. K., Parrish, D. D., Roberts, J. M., Sueper, D. T. Effect of petrochemical industrial emissions of reactive alkenes and NO_x on tropospheric ozone formation in Houston, Texas. *J. Geophys. Res.,* 108(D8), 4249, 2003.

Sage, R. F., Way, D. A., Kubien, D. S. Rubisco, Rubisco activase and global climate change. *J. Exp. Bot.*, 59(7), 1581-1595, 2008.

Salesky, S. T.,Chamecki, M., Dias, N. L. Estimating the Random Error in Eddy-Covariance Based Fluxes and Other Turbulence Statistics: The Filtering Method. *Bound.-Lay. Meteor.,* 144, 113-135, 2012.

Schafer, K.V.R., R. Oren, D.S. Ellsworth, C.T. Lai, J.D. Herrick, A.C. Finzi, D.D. Richter, and G.G. Katul. Exposure to an enriched CO_2 atmosphere alters carbon assimilation and allocation in a pine forest ecosystem. *Global Change Biology,* 9(10): 1378-1400, 2003.

Schimel, D., Melillo, J., Tian, H., McGuir, A. D., Kicklighter, D., Kittel, T., Rosenbloom, N., Running, S., Thornton, P., Ojima, D., Parton, W., Kelly, R., Sykes, M., Neilson, R., Rizzo, B. Contribution of Increasing CO_2 and Climate to Carbon Storage by Ecosystems in the United States. *Science,* 287(5460), 2004-2006, 2000.

Schlesinger, W. H., Bernhardt, E. S., DeLucia, E. H., Ellsworth, A. C., Finzi, A. C., Hendrey, G. R., Hofmockel, K. S., Lichter, J., Matamala, R., Moore, D., Oren, R., Pippen, J. S., Thomas, R. B. The Duke Forest FACE Experiment: CO2 Enrichment of a Loblolly Pine Forest. *Ecol. Stud.,* 187, 197-212, 2006.

Schobert, H. H. Chemistry of Fossil Fuels and Biofuels. Cambridge University Press: Cambridge, NY, 2013.

Schwietzke, S., Griffin, W. M., Matthews, H. S., Bruhwiler, L. M. P. Natural Gas Fugitive Emissions Rates Constrained by Global Atmospheric Methane and Ethane. *Environ. Sci. Technol.,* 48, 7714-7722, 2014.

Seneviratne, S. I., Corti, T., Davin, E. L., Hirschi, M., Jaeger, E. B., Lehner, I., Orlowsky, B., Teuling, A. J. Investigatin soil moisture-climate interactions in a changing climate: A review. *Earth Science Reviews,* 99, 125-161, 2010.

Shakhova, N., Semiletov, I., Salyuk, A., Yusupov, D. K., Gustafsson, O. Extensive Methane Venting to the Atmosphere from Sediments of the East Siberian Arctic Shelf. *Science,* 327(5970), 1246-1250, 2010.

Shindell, D., Kuylenstierna, J. C. I., Vignati, E., van Dingenen, R., Amann, M., Klimont, Z., Anenberg, S. C., Muller, N., Janssens-Maenhout, G., Raes, F., Schwarts, J., Faluvegi, G., Pozzoli, L., Kupiainen, K., Hoglund-Isaksson, L., Emberson, L., Streets, D., Ramanathan, V., Hicks, K., Oanh, N. T. K., Milly, G., Williams, M., Demkine, V., Fowler, D. Simultaneously Mitigating Near-Term Climate Change and Improving Human Health and Food Security. *Science,* 335(6065), 183-189, 2012.

Smetacek, V. Diatoms and the Ocean Carbon Cycle. *Protist,* 150, 25-32, 1999.

Stephens, B. B., Gurney, K. R., Tans, P. P., Sweeney, C., Peters, W., Bruhwiler, L., Ciais, P., Ramonet, M., Bousquet, P., Nakazawa, T., Aoki, S., Machida, T., Inoue, G., Vinnichenko, N., Lloyd, J., Jordan, A., Heimann, M., Shibistova, O., Langenfelds, R. L., Steele, L. P., Francey, R. J., Denning, A. S. Weak Northern and Strong Tropical Land Carbon Uptake from Vertical Profiles of Atmospheric CO_2. *Science,* 316(5832), 1732-1735, 2007.

Stephenson, E., Doukas, A., Shaw, K. Greenwashing gas: Might a 'transition fuel' label legitimize carbon-intensive natural gas development? *Energy Policy,* 46, 452-459, 2012.

Stephenson, T., Valle, J. E., Riera-Palou, X. Modeling the Relative GHG Emissions of Conventional and Shale Gas Production. *Environ. Sci. Technol.,* 45, 10757-10764, 2011.

Stohl, A., Klimont, Z., Eckhardt, S., Kupianinen, K., Schevchenko, V. P., Kopeikin, V. M., Novigatsky, A. N. Black carbon in the Arctic: the underestimated role of gas flaring and residential combustion emissions. *Atmos. Chem. Phys.,* 12, 8833-8855, 2013.

Stull, R. B. An Introduction to Boundary Layer Meteorology. Kluwer Academic Publishers, Dordrecht, 1988.

Skoog, D. A., West, D. M., Holler, F. J. Analytical Chemistry An Introduction. Saunder College Publishers, Philadelphia, 1994.

Tans, P. P., Fung, I. Y., Takahashi, T. Observational Constraints of the Global Atmospheric CO_2 Budget. *Science,* 247(4949), 1431-1438, 1990.

Tans, P. P., Bakwin, P. S. Climate Change and Carbon Dioxide Forever. *Ambio,* 24(6), 376-378, 1995.

Torrence, C. Compo, G. P. A Practical Guide to Wavelet Analysis. *Bull. Amer. Meteor. Soc.,* 79(1), 61-78, 1997.

Torres, V. M., Herndon, S., Kodesh, Z., Allen, D. T. Industrial Flare Performance at Low Flow Conditions. 1. Study Overview. *Ind. Eng. Chem. Res.* 51 (39), 12559-12568, 2012a.

Torres, V. M., Herndon, S., Allen, D. T. Industrial Flare Performance at Low Flow Conditions. 2. Steam- and Air-Assisted Flares. *Ind. Eng. Chem. Res.* 51 (39), 12569-12576, 2012b.

Torres, V. M., Herndon, S., Wood, E., Al-Fadhli, F. M., Allen, D. T. Emissions of Nitrogen Oxides from Flares Operating at Low Flow Conditions. *Ind. Eng. Chem. Res.,* 51(39), 12600-12605, 2012c.

Trainer, M., Ridley, B. A., Buhr, M. P., Kok, G., Walega, J., Hubler, G., Parrish, D. D., Fehsenfeld, F. C. Regional ozone and urban plumes in the southeastern United States: Birmingham, a case study. *J. Geophys. Res.,* 100(D9), 18823-18834, 1995.

Tulapurkara, E. G. Hundred years of the boundary layer – Some aspects. *Sadhana,* 30(4), 499-512, 2005.

Turnbull, J. C., Karion, A., Fisher, M. L., Faloona, I., Guilderson, T., Lehman, S. J., Miller, B. R., Montzka, S., Sherwood, T., Saripalli, S., Sweeney, C., Tans, P. P. Assessment of fossil fuel carbon dioxide and other anthropogenic trace gas emissions from airborne measurements over Sactamento, California in spring 2009. *Atmos. Chem. Phys.,* 11(2), 705-721, 2011.

Ulaby, F. T., Dubois, P. C., van Zyl, J. Radar mapping of surface soil moisture. *J. Hydrol.,* 184, 57-84, 1996.

Urbanski, S., Barford, C., Wofsy, S., Kucharik, C., Pyle, E., Budney, J., McKain, K., Fitzjarrald, D., Czikowsky, M., Munger, J. W. Factors controlling CO_2 exchange on timescales from hourly to decadal at Harvard Forest. *J. Geophys. Res.,* 112, G02020, 2007.

Van der Hoven, I. Power spectrum of horizontal wind speed in the frequency range from 0.0007 to 900 cycles per hour. *J. Meteor.,* 14(2), 160-164, 1957.

Vellinga, O. S., Gioli, B., Elbers, J. A., Holtslag, A. A. M., Kabat, P., Hutjes, R. W. A. Regional carbon dioxide and energy fluxes from airborne observations using flight-path segmentation based on landscape characteristics. *Biogeosci.,* 7, 1307-1321, 2010.

Vellinga, O. S., Dobosy, R. J., Dumas, E. J., Gioli, B., Elbers, J. A., Hutjes, R. W. A. Calibration and Quality Assurance of Flux Observations from a Small Research Aircraft. *J. Atmos. Oceanic Technol.,* 30, 161-181, 2013.

Venkatesh, A., Jaramillo, P., Griffin, W. M., Matthews, H. S. Uncertainty in Life Cycle Greenhouse Gas Emissions from United States Natural Gas End-Uses and its Effects on Policy. *Environ. Sci. Technol.,* 45, 8182-8189, 2011.

Vesala, T., Kljun, N., Rannik, U., Rinne, J., Sogachev, A., Markkanen, T., Sabelfeld, K., Foken, T., Leclerc, M. Y. Flux and concentration footprint modelling: State of the art. *Environ. Poll.,* 152, 653-666, 2008.

Villasenor, R. et al. An air quality emission inventory of offshore operations for the exploration and production of petroleum by the Mexican oil industry. *Atmos. Environ*., 37 (26), 3713-3729, 2003.

Wang, J., Zhuang, J., Wang, W., Liu, S., Xu, Z. Assessment of Uncertainties in Eddy Covariance Flux Measurement Based on Intensive Flux Matrix of HiWATER-MUSOEXE. *IEEE Geosci. Rem. Sens. Lett.,* 12(2), 259-263, 2014.

Waring, R. H., Franklin, J. F. Evergreen Coniferous Forests of the Pacific Northwest. *Science,* 204(4400), 1380-1386, 1979.

Webb, E. K., Pearman, G. I., Leuning, R. Correction of flux measurements for density effects due to heat and water vapour transfer. *Quart. J. R. Met. Soc.,* 106, 85-100, 1980.

Weber, C. L., Clavin, C. Life Cycle Carbon Footprint of Shale Gas: Review of Evidence and Implications. *Environ. Sci. Technol.,* 46, 5688-5695, 2012.

Wilczak, J. M., Oncley, S. P., Stage, S. A. Sonic Anemometer Tilt Correction Algorithms. *Bound.-Lay. Meteor.,* 99, 127-150, 2001.

Wilson, K., Goldstein, A., Falge, E., Aubinet, M., Baldocchi, D., Berbigier, P., Bernhofer, C., Ceulemans, R., Dolman, H., Field, C., Grelle, A., Ibrom, A., Law, B. E., Kowalski, A., Meyers, T., Moncrieff, J., Monson, R., Oechel, W., Tenhunen, J., Valentini, R., Verma, S. Energy balance closure at FLUXNET sites. *Agr. Forest Meteorol.,* 113, 223-243, 2002.

Wofsy, S. C., Goulden, M. L., Munger, J. W., Fan, S. M., Bakwin, P. S., Daube, B. C., Bassow, S. L., Bazzaz, F. A. Net Exchange of CO_2 in a Mid-Latitude Forest. *Science,* 260(5112), 1314-1317, 1993.

Wuebbles, D. J., Jain, A., Edmonds, J., Harvey, D., Hayhoe, K. Global change: state of the science. *Environ. Poll.,* 100, 57-86, 1999.

Wyngaard, J. C., Cote, O. R., Izumi, Y. Local Free Convection, Similarity and the Budgets of Shear Stress and Heat Flux. *J. Atmos. Sci.,* 28, 1171-1182, 1971a.

Wyngaard, J. C., Izumi, Y., Collins, S. A. Behavior of the Refractive Index Structure Parameter Near the Ground. *J. Opt. Soc. Am.,* 61, 1646-1650, 1971b.

Wyngaard, J. C., Cote, O. R. The Budgets of Turbulent Kinetic Energy and Temperature Variance in the Atmospheric Surface Layer. *J. Atmos. Sci.,* 28, 190-201, 1971.

Wyngaard, J. C., Cote, O. R. Cospectral similarity in the atmospheric surface layer. *Quart. J. R. Met. Soc.,* 98, 590-603, 1972.

Zhou, J. B., Jiang, M. M., Chen, G. Q. Estimation of methane and nitrous oxide emission from livestock and poultry in China during 1949-2003. *Energ. Policy* 35, 3759-3767, 2007.

VITA

VITA

Dana Rae Caulton was born on April 29, 1988 to John and Lorraine Caulton. She grew up in Woodridge, IL with two older brothers. When she turned 8, her parents gave her a toy microscope which sparked a life-long interest in science. She attended Downers Grove North High School and graduated in 2006. She went on to attend Indiana University where her great-uncle, Ken Caulton, is a professor of Chemistry. There she learned about atmospheric chemistry and other environmental sciences in her classes and the research lab of Prof. Phil Stevens. She graduated from Indiana University with a Bachelor's of Science in Chemistry and a minor in Political Science in 2010. Later in 2010 she started her graduate career in analytical chemistry in the atmospheric chemistry lab of Prof. Paul Shepson and studied the quantification of greenhouse gases including from fossil fuel production activities. Her graduate research has allowed her to travel and gain valuable field experience. In addition, these opportunities led to the publication of an article that allowed her to win the Peter B. Wagner Memorial Award for Women in Atmospheric Sciences in 2014. She plans to pursue a career in atmospheric chemistry with a focus on greenhouse gas quantification.

PUBLICATIONS

Toward a better understanding and quantification of methane emissions from shale gas development

Dana R. Caulton[a,1], Paul B. Shepson[a,b], Renee L. Santoro[c], Jed P. Sparks[d], Robert W. Howarth[d], Anthony R. Ingraffea[c,e], Maria O. L. Cambaliza[a], Colm Sweeney[f,g], Anna Karion[f,g], Kenneth J. Davis[h], Brian H. Stirm[i], Stephen A. Montzka[f], and Ben R. Miller[f,g]

Departments of [a]Chemistry, [b]Earth, Atmospheric and Planetary Science, and [i]Aviation Technology, Purdue University, West Lafayette, IN 47907; [c]Physicians, Scientists and Engineers for Healthy Energy, Ithaca, NY 14851; Departments of [d]Ecology and Evolutionary Biology and [e]Civil and Environmental Engineering, Cornell University, Ithaca, NY 14853; [f]National Oceanic and Atmospheric Administration, Boulder, CO 80305; [g]Cooperative Institute for Research in Environmental Sciences, University of Colorado, Boulder, CO 80309; and [h]Department of Meteorology, The Pennsylvania State University, University Park, PA 16802

Edited* by Barbara J. Finlayson-Pitts, University of California, Irvine, Irvine, CA, and approved March 12, 2014 (received for review September 4, 2013)

The identification and quantification of methane emissions from natural gas production has become increasingly important owing to the increase in the natural gas component of the energy sector. An instrumented aircraft platform was used to identify large sources of methane and quantify emission rates in southwestern PA in June 2012. A large regional flux, 2.0–14 g CH_4 s^{-1} km^{-2}, was quantified for a ∼2,800-km^2 area, which did not differ statistically from a bottom-up inventory, 2.3–4.6 g CH_4 s^{-1} km^{-2}. Large emissions averaging 34 g CH_4/s per well were observed from seven well pads determined to be in the drilling phase, 2 to 3 orders of magnitude greater than US Environmental Protection Agency estimates for this operational phase. The emissions from these well pads, representing ∼1% of the total number of wells, account for 4–30% of the observed regional flux. More work is needed to determine all of the sources of methane emissions from natural gas production, to ascertain why these emissions occur and to evaluate their climate and atmospheric chemistry impacts.

unconventional gas | greenhouse gas | hydraulic fracturing

Methane is a very important component of the Earth's atmosphere: it represents a significant component of the natural and anthropogenically forced greenhouse effect, with a global warming potential 28–34 times greater than CO_2 using a 100-y horizon and even greater on shorter time scales (1, 2). It also is an important sink for the hydroxyl radical, the dominant agent that defines the atmosphere's cleansing capacity (3), has a significant impact on tropospheric ozone, and is one of the important sources of water vapor in the stratosphere, which in turn impacts stratospheric ozone and climate (4). The recent observation that global methane concentrations have begun increasing (5), after a decade of static or decreasing emissions in the late 1990s to ∼2007, has renewed interest in pinpointing the causes of global methane trends. Recently natural gas has been explored as a potential bridge to renewable energy, owing in part to the reduction in carbon emissions produced from electricity generation by natural gas compared with coal (6–9). Advances in drilling and well stimulation techniques have allowed access to previously locked reservoirs of natural gas, such as the Marcellus shale formation in Pennsylvania, which has led to a boom in natural gas production in the last decade (10). This has led to estimations of the carbon footprint of natural gas to examine the impact of increasing our reliance on natural gas for various energy needs (11–16). An important unresolved issue is the contribution of well-to-burner tip CH_4 emission to the greenhouse gas footprint of natural gas use. Given that CH_4 is a much more potent greenhouse gas than CO_2, quantifying CH_4 emissions has become critical in estimating the long- and short-term environmental and economic impacts of increased natural gas use. According to a recent study, if total CH_4 emissions are greater than approximately 3.2% of production, the immediate net radiative forcing for natural gas use is worse than for coal when used to generate electricity (8).

The first estimates for CH_4 emissions from shale gas development were reported in late 2010 and are based on uncertain emission factors for various steps in obtaining the gas and getting it to market (17, 18). In the short time since these first estimates, many others have published CH_4 emission estimates for unconventional gas (including tight-sand formations in addition to shales), giving a range of 0.6–7.7% of the lifetime production of a well emitted "upstream" at the well site and "midstream" during processing and 0.07–10% emitted during "downstream" transmission, storage, and distribution to consumers (reviewed in refs. 18 and 19). The highest published estimates for combined upstream and midstream methane emissions (2.3–11.7%) are based on actual top-down field-scale measurements at specific regions (20, 21). Whereas a recent shale gas study (22) based on field sites across the United States to which the authors were given access scaled actual measurements up to the national level and found lower emissions than US Environmental Protection Agency (EPA) estimates, an equally recent study (23) used atmospheric measurements of greenhouse gases across the United States to inform a model and found CH_4 emissions, cumulatively and specifically from fossil fuel production activities, to be underestimated by the EPA.

The current range of observed CH_4 emissions from US natural gas systems (2.3–11.7%), if it were representative of the national scale, applied to the reported 2011 unassociated gas production number yields a range of CH_4 emissions between 5.6 and 28.4 Tg

Significance

We identified a significant regional flux of methane over a large area of shale gas wells in southwestern Pennsylvania in the Marcellus formation and further identified several pads with high methane emissions. These shale gas pads were identified as in the drilling process, a preproduction stage not previously associated with high methane emissions. This work emphasizes the need for top-down identification and component level and event driven measurements of methane leaks to properly inventory the combined methane emissions of natural gas extraction and combustion to better define the impacts of our nation's increasing reliance on natural gas to meet our energy needs.

Author contributions: P.B.S., J.P.S., R.W.H., M.O.L.C., and B.H.S. designed research; D.R.C., P.B.S., and R.L.S. performed research; D.R.C., P.B.S., R.L.S., J.P.S., R.W.H., A.R.I., K.J.D., S.A.M., and B.R.M. analyzed data; D.R.C., P.B.S., R.L.S., J.P.S., R.W.H., A.R.I., C.S., A.K., S.A.M., and B.R.M. wrote the paper; and B.H.S. designed and installed aircraft setup.

The authors declare no conflict of interest.

*This Direct Submission article had a prearranged editor.

[1]To whom correspondence should be addressed. E-mail: dcaulton@purdue.edu.

This article contains supporting information online at www.pnas.org/lookup/suppl/doi:10.1073/pnas.1316546111/-/DCSupplemental.

CH_4, whereas the EPA reports 6.7 Tg CH_4 from natural gas systems in 2011 and only 28 Tg CH_4 total anthropogenic emissions (24). Natural gas systems are currently estimated to be the top source of anthropogenic CH_4 emission in the United States, followed closely by enteric fermentation, but the top-down observations suggest that natural gas may play a more substantial role than previously thought (24). Inadequate accounting of greenhouse gas emissions hampers efforts to identify and pursue effective greenhouse gas reduction policies.

Although it is clear that analysis of the effect of natural gas use would benefit from better measurements of emissions from unconventional gas wells, the inaccessible and transient nature of these leaks makes them difficult to identify and quantify, particularly at a scale at which they are useful for bottom-up inventories or mitigation strategies (i.e., leak rates of individual components or activities). Previous techniques have used either bottom-up inventories of the smallest scale of contributions or top-down apportionment of observed large-scale regional enhancements over a complex area to identify the source of the enhancements (11, 17, 20–23, 25). Although the latter suggest that the leak rate may be higher than what bottom-up inventories have allocated, they give little to no information about where in the upstream production process these leaks occur, thus hampering the interpretation of these data for bottom-up inventories or mitigation purposes.

Here we use an aircraft-based approach that enables sampling of methane emissions between the regional and component level scales and can identify plumes from single well pads, groups of well pads, and larger regional scales, giving more information as to the specific CH_4 emission sources. We implemented three types of flights over 2 d in June 2012: investigative (I), mass-balance flux (MB), and regional flux (RF). Details of each flight are presented in Table 1. Our results indicate a large regional CH_4 flux in southwestern PA. We show that the methane emission flux from the drilling phase of operation can be 2 to 3 orders of magnitude greater than inventory estimates, providing an example and improved understanding of the differences between observed data and bottom-up inventories.

Results and Discussion

We conducted measurements in southwestern PA in the Marcellus shale formation region in June 2012. For two morning flights we calculated a regional flux of 2.0–13.0 g CH_4 s^{-1} km^{-2} for RF-1 over a box that approximates the size of our flight path (dashed box in Fig. 1) that we define as the original sampling area (OSA) and 2.0–14.9 g CH_4 s^{-1} km^{-2} for RF-2. These ranges represent our analysis of the combined effect of all sources of uncertainty, which is dominated by the range of accumulation time scales over which the enhancement may have occurred (i.e., a maximum of 18 h commencing with the time of collapse of the boundary layer the day before, to a minimum of 5–6 h for air to flush through the sampling area). These estimates are not statistically different from the range of estimates obtained by summing up bottom-up emissions

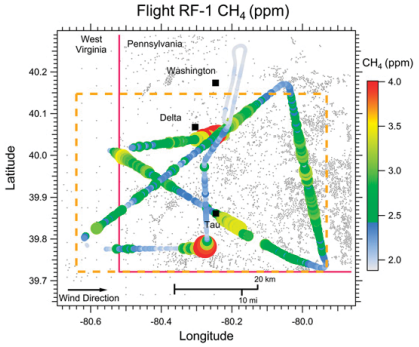

Fig. 1. Regional enhancement of methane at 250 m AGL on the morning of June 20th. The dashed orange box represents the OSA, 2,844 km^2, and the gray dots show well locations.

estimates for oil and gas development, coal mining, and other sources for the OSA depicted by the dashed orange box in Fig. 1 (corresponding to a ~6-h time scale) and for the 18-h upwind accumulation area (UAA) shown in Fig. S1: 2.3–4.6 g CH_4 s^{-1} km^{-2}. Methane emissions from natural gas contribute 22–62% of the estimated bottom-up flux in this region. Using our top-down flux measurements, the assumed range of methane from natural gas contribution (22–62%), and industry reported production rates, we estimate a possible range for the fugitive methane emission rate of 2.8–17.3% of production in this region, which applies only to these two specific study dates.

It is important to note that we could find no evidence from state records or from our analysis of photographs taken during flights of wells in flowback after hydraulic fracturing in the area during the sampling time (discussed in *SI Text*). Flowback is the period after fracturing when a portion of the fracturing fluid used returns up the wellbore, flushing out with it substantial amounts of natural gas. We used data submitted voluntarily by oil and gas operators to FracFocus.org to identify one potential flowback event (for a pad not sampled in this study) and included the emissions in our bottom-up inventory. We would expect the regional emission rate to be greater if more wells were in flowback (11, 17, 18).

Although our top-down and bottom-up flux estimates are not statistically different, the top-down flux estimate encompasses a range of larger magnitude fluxes compared with the bottom-up method, and the upper limit for the fraction of production emitted is large enough to provide ample motivation to pursue investigation of possible significant methane emission processes not included in the bottom-up inventory. To quantify emission rates from significant sources of CH_4 emissions in this shale gas

Table 1. Meteorological conditions and time duration of each aircraft flight experiment

Flight type	Flight no.	Date	Start time (EDT)	Duration, min	Wind speed, m/s	Wind direction
RF	1	6/20/2012	10:00	96	3.0	276
RF	2	6/21/2012	8:55	89	3.7	270
MB	1	6/20/2012	11:55	30	3.1	236
MB	2	6/20/2012	15:15	56	3.3	239
MB	3	6/21/2012	16:00	60	5.5	252
MB	4	6/21/2012	14:05	73	4.7	226
I	1	6/20/2012	12:25	5	3.0	258
I	2	6/21/2012	15:22	6	4.7	227
I	3	6/21/2012	9:14	15	4.2	257

Flights are classified into three flight types: RF, MB, and I (defined in text). Investigative flights were short and occurred between and during the longer RF and MB flights. Flights are identified by their flight type and flight number (e.g., RF-1, MB-3, etc.). Note that flights MB-1 through MB-3 are near pad Delta and flight MB-4 is near pad Tau.

drilling region we conducted mass-balance flights (MB-1–MB-4) for well pads with observed enhancements large enough to use the aircraft-based mass-balance technique, as described in ref. 26. In the region between Washington, PA and south to the border of WV we observed multiple high concentration methane plumes and investigated two areas where initial observations revealed well pads with potentially high methane emission rates. The high density of pads in this region and the prevailing wind direction (SW) during the time of measurement combined to make plume attribution to single pads difficult. In cases in which fluxes from individual pads could not be isolated, we averaged the calculated flux from a wider region over the number of pads that could have possibly contributed. Fig. 2 shows the downwind methane concentrations in a vertical plane perpendicular to the mean wind direction from an isolated pad designated "Delta" (shown in Fig. 1 near the northern hotspot). Attribution of the flux to that (or any specific) source involved maneuvering in a circular pattern around the prospective source, with observed enhanced methane concentrations only on the downwind side, as shown in Fig. S2. Fig. 3 shows the downwind methane concentrations that include signal enhancement from a pad "Tau" (shown in Fig. 1 near the southern hotspot), as well as from other upwind pads, coal-bed methane wells, and a significant plume from an adjacent coal mine. The high density of potential upwind sources around Tau made attribution to specific sources impossible, although it is probable that some of this flux comes from at least one pad in the drilling stage (Tau). Combining results of MB-1 thru MB-3 yielded an average of 236 g CH_4 s^{-1} per pad for seven high emitting pads, corresponding to 34 g CH_4 s^{-1} per well. Individual MB flight results are presented in Table 2. Note that these seven pads, with ∼40 wells, representing approximately 1% of the wells in the 2,844-km^2 OSA region, contributed a combined emission flux of 1.7 kg CH_4 s^{-1}, equal to 4.3–30% of our top-down measured flux.

The methane emissions from the gas wells reported in Table 2 are surprisingly high considering that all of these wells were still being drilled, had not yet been hydraulically fractured, and were not yet in production. The Pennsylvania Department of Environmental Protection (27) confirmed that total vertical depth had not yet been reached in these wells at the time of the sampling, and our photographic evidence recorded equipment typical during the drilling phase, as shown in Fig. S3. Because of the large number of wells in our study region we were not able to review all well files to determine the total number of wells being drilled during the time of study. EPA greenhouse gas inventories report a total of 51.3 kg CH_4 per well from the entire drilling period that typically lasts 2 wk (24). Using, as limits, a 2-wk and a 2-d (the duration of our observations) drilling phase time scale, this leads to an estimated flux of 0.04–0.30 g CH_4 s^{-1} per well, 2 to 3 orders of magnitude lower than our observed average flux per well (for the high emitters we studied) of 34 g CH_4 s^{-1}. Although we only quantitatively sampled pads where we saw significant enhancement above the background, it is important to note

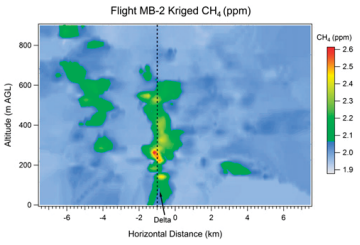

Fig. 2. Interpolated methane concentration ∼1 km downwind of pad Delta, showing isolated methane plume near the center of the transect.

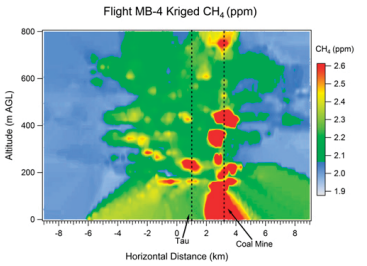

Fig. 3. Interpolated methane concentration from several pads near pad Tau. A distinct methane plume from a nearby coal mine occurs around 3 km.

that we could detect little to no emission from many other pads, particularly in the region north of the OSA, from Washington north to Pittsburgh. Thus, we do not intend for our regional flux estimate to be taken as necessarily representative of the Marcellus as a whole but only for the region defined as the OSA for these days. We also note that some sources were too intermittent to determine a flux via the aircraft mass-balance method. At a compressor station north of Washington we observed methane concentrations up to 45 ppm, but there was no consistent plume between consecutive passes downwind of the station.

Bottom-up emission factor studies usually assume no emission from gas wells during this prehydraulic fracturing period (11–16). Release from gas kicks—gas entry into the wellbore during vertical drilling despite efforts to keep the wellbore at a higher pressure than surrounding rock, a technique known as overbalanced drilling—is one possible explanation. However, it is generally assumed that gas kicks are not significant emission sources and are transient (28), although we observed comparable emissions on consecutive days. Alternatively, underbalanced drilling methods may have been used on these wells, where lower pressure in the wellbore allows fluids and gas from the various geological formations (i.e., coal deposits) being drilled through to seep into the wellbore and up to the surface, resulting in emission of hydrocarbons, including methane, during the drilling phase if the emissions are not contained or flared (28). Note that although these well pads were not permitted as coal bed methane wells the entire southwest region of Pennsylvania contains underlying coal deposits. The underbalanced drilling hypothesis is supported by aerial pictures that show a lack of a shale shaker or mud pits at these sites that are typically used in overbalanced drilling. Whatever the source of high emissions from the pads we identified as in the drilling stage, these emissions, equaling 0.6g CH_4 s^{-1} km^{-2}, are not included in our bottom-up estimate (or any other bottom-up estimate). The addition of this emission to our bottom-up inventory would shift the estimates slightly higher, but because our original results were not statistically different owing to the large range of estimates from our top-down approach, our conclusions are no different.

During the morning RF-2 flight we acquired whole-air samples using the National Oceanic and Atmospheric Administration (NOAA) programmable flask package, which were analyzed for hydrocarbons and CH_4. We found that relative to other studies of shale-well natural gas, the air samples in this region exhibited much lower mole ratios of propane and n-butane to methane, at 0.007 ± 0.001 and 0.0018 ± 0.0003, respectively. Previous reports indicate molar ratios of ∼0.05 for propane (28, 29) and ∼0.01 for n-butane (30). However, the observed n-butane to propane ratio, 0.27 ± 0.01, is very similar to values reported in previous work, which average 0.24 (31). These findings suggest that the shale natural gas signal is being diluted by an essentially pure CH_4 source. Although this is not the only possibility, these results support the hypothesis that the methane plumes derive from underbalanced drilling methods as wells are drilled through

Table 2. Results from four MB experiments and the number of pads and wells contributing to the flux

Flight	Flight MB-1	Flight MB-2*	Flight MB-3	Flight MB-4	Average ± σ
Total flux (g CH_4/s)	380	248	1,880	1,490	—
Total pads contributing	2	1	7	—	—
Flux (g CH_4/s) per pad	190	248	269	—	236 ± 41
Total permitted wells	15	8	41	—	—
Flux (g CH_4/s) per well	25	31	46	—	34 ± 11

Flights 1–3 were conducted near pad Delta and flight 4 near pad Tau. Flux per pad and per well is obtained by dividing the total flux by either the total number of pads or total number of wells.
*Isolated pad Delta.

formations such as shallow coal pockets producing coal-bed methane during the drilling phase. Coal-bed methane is typically composed of very high percentages of CH_4 (~98%), with trace heavier hydrocarbons (32).

Conclusions

This work shows that it is possible to interrogate and quantify emissions from individual pads and pad clusters at scales relevant to bottom-up inventories and mitigation strategies and to estimate the emission rate for a region encompassing a large number of well pads using the aircraft measurement approach. The range of regional leak rates found here for the OSA (3–17%) is similar to leak rates found by recent studies across the United States in the CO Denver-Julesburg Basin (20) and the UT Uintah Basin (21). Additionally, although a leakage rate was not calculated, a study over large areas of TX, OK, and KS (25) found surprisingly high methane emissions, indicating that high fugitive emission rates are likely to be a national-scale issue, although the mechanisms of these fugitive leaks may be different at each site. Although a recent study (22) found production sites, to which they were given access, to be emitting less CH_4 than EPA inventories suggest, these regional scale findings and a recent national study (23) indicate that overall sites leak rates can be higher than current inventory estimates. Additionally, a recent comprehensive study of measured natural gas emission rates versus "official" inventory estimates found that the inventories consistently underestimated measured emissions and hypothesized that one explanation for this discrepancy could be a small number of high-emitting wells or components (33).

These high leak rates illustrate the urgent need to identify and mitigate these leaks as shale gas production continues to increase nationally (10). The identification presented here of emissions during the drilling stage 2 to 3 orders of magnitude larger than inventory estimates indicates the need to examine all aspects of natural gas production activity to improve inventory estimates and identify potential opportunities for mitigation strategies and that top-down measurements provide an important complement to bottom-up inventory determinations. Shale gas production is expected to increase globally as many shale gas plays are starting to be explored (34). If a midrange value of the reported fraction of production that is emitted, 7%, is applied to the projected global peak shale gas production rate, 23 trillion ft^3 per year (34), it would correspond to 24 Tg CH_4 emitted per year, or ~4% of the current global total (natural and anthropogenic) CH_4 emission rate (35). Further studies are needed to enable better understanding of the operational details that lead to the largest emissions, how they might be better controlled, and to provide a more detailed picture of the expected life cycle-integrated emissions from unconventional gas wells.

Table 3. Total expected emissions from all sources and percent contribution to the total emission for the OSA and the UAA using Howarth et al. (11) emission factors and for the OSA using NETL (16) emission factors

Area	Source	Expected emissions, g CH_4 s^{-1} km^{-2}	Contribution, %
OSA (Howarth EFs)	Natural gas	0.85 (low)–2.23 (high)	21.9–42.0
	Oil	0	0
	Coal	2.96	55.7–76.3
	Flowback	0.05–0.10	1.3–1.9
	AFO	0.015	0.3–0.4
	Other	0	0
	Total (average)	3.88–5.31 (4.60)	
UAA (Howarth et al. EFs)	Natural gas	0.76 (low)–1.70 (high)	42.0–61.6
	Oil	0	0
	Coal	1.01	36.6–55.8
	Flowback	0.01–0.02	0.6–0.7
	AFO	0.015	0.5–0.8
	Other	0.019	0.7–1.0
	Total (average)	1.81–2.76 (2.29)	
OSA (NETL EFs)	Natural gas	1.41	31.4–31.8
	Oil	0	0
	Coal	2.96	65.9–66.7
	Flowback	0.05–0.10	1.1–2.3
	AFO	0.015	0.3
	Other	0	0
	Total (average)	4.42–4.49 (4.46)	

AFO, animal feeding operation; EFs, emission factors; NETL, National Energy Technology Laboratory.

Table 4. Natural gas portion of the top-down flux as a percentage of the unassociated natural gas production rate

	18-h Estimate		5 to 6-h Estimate	
Parameter	Low	High	Low	High
Top-down flux, g CH_4 s^{-1} km^{-2}	2.0	4.2	6.6	14.0
CH_4 from natural gas, %	22	62	22	62
Natural gas production rate, g CH_4 s^{-1} km^{-2}	15.9		50.1	
Natural gas flux/ production rate, %	2.8	16.4	2.9	17.3

Methods

Measurements were conducted between June 18, 2012 and June 21, 2012 over southwestern PA using Purdue's Airborne Laboratory for Atmospheric Research, a modified Beechcraft Duchess aircraft. This aircraft is equipped with a 50-Hz Best Air Turbulence probe, described by ref. 36, that measures wind vectors and pressure, a 50-Hz microbead thermistor that measures temperature, a 50-Hz global positioning system/inertial navigation system, and a 0.5-Hz high precision Picarro $CO_2/CH_4/H_2O$ cavity ring down spectrometer (CRDS). The CRDS has ~0.05% (1 ppb) precision for methane determined during in-flight calibration, and comparable accuracy, using three NOAA Earth System Research Laboratory tanks with CH_4 concentrations of 1.8030, 2.2222, and 2.5995 ppm. A programmable flask package (PFP) provided by NOAA for whole-air sampling was also installed on the aircraft. The PFP consists of 12 flasks that hold air pressurized to 2.7 atm in 0.7-L bottles. Flasks are analyzed for 55 species, including CH_4, and hydrocarbons, by NOAA.

We calculated a regional flux on two mornings by integrating the enhancement in CH_4 above the background in the OSA (enhancement area of 2,844 km^2). The height of the box was defined as the boundary layer height, which was determined from the earliest [~10:00 AM Eastern Daylight Time (EDT)] vertical profiles of potential temperature, H_2O, CH_4, and CO_2. Boundary layer heights were observed to be 370 m above ground level (AGL) for flight RF-1 and 500 m AGL for flight RF-2 and assumed to be constant during the data collection period for each flight. The raw CH_4 data from flight at a constant altitude (~250 m AGL) around the area of interest was interpolated using the EasyKrig3.0 program (37). For RF-1 the observed concentrations are presented in Fig. 1, and the flight data for RF-2 are shown in Fig. S4. The 2D interpolation output was turned into a 3D matrix of CH_4 values by assuming the CH_4 concentration decreased linearly with height up to the boundary layer top, with background concentrations of 1.89 ppm CH_4. This assumption was based on the observed vertical profiles that depict an approximately linear decrease of the CH_4 mole ratio with altitude. We compared integration of CH_4 under the actual vertical profile and a linear regression of the vertical profile, shown in Fig. S5, and found less than a 7% difference, which supports use of the linear approximation for the whole study region. Fig. S5 shows a vertical profile obtained during flight RF-1 at ~10:00 AM EDT. The profile extends into the residual layer above the stable boundary layer. The residual layer represents well mixed (i.e., clean, air from the previous day as the boundary layer collapsed and is used to estimate the CH_4 background concentration, 1.89 ppm on both days). The CH_4 enhancement was then calculated by removing the background value and converting to $mol \cdot m^{-3}$. Multiplying the enhancement by the pixel volume, 29,386.5 m^3 (171.6 m longitudinal•171.25 m latitudinal•1 m vertical), and integrating over all pixels in the sample area produces the total enhancement in moles, which can be converted to units of g or kg. To obtain a flux, the enhancement was then divided by a chosen time scale, discussed below, and divided by the total area of the OSA, 2,844 km^2, to obtain the flux in g $s^{-1}km^{-2}$.

Uncertainty was assessed by examining the range of reasonable assumptions to calculate the CH_4 enhancement and the time scale of the accumulation. A simpler CH_4 enhancement estimate was done by assuming a spatially uniform CH_4 enhancement in the box taken from the observed CH_4 vertical profile after it had been smoothed. The CH_4 enhancement differed by approximately ±30% using this technique. In addition, the effect of background CH_4 estimate was quantified by using reasonable upper limits in background concentration from background air observed in the southwest and west of the OSA during both flights, which was generally higher than the concentrations observed in the residual layer. We estimate the upper limit to the background concentration to be 2.00 ppm. In this scenario a 20% difference in the calculated CH_4 enhancement is observed. The time scale was changed to reflect different possibilities for accumulation. The lower limit to the accumulation time scale used (6 h for RF-1, 5 h for RF-2) was the time for the observed winds to flush the box. The flush time of the box represents the physical minimum time for enhanced air to be replaced with assumed cleaner upwind air, at the observed wind speeds. This assumption is supported by the observation that both RF-1 and RF-2 show cleaner air in the upwind area at the time of flight (W corner of the OSA box; Fig. 1 and Fig. S4), consistent with much smaller density of wells, as can be seen in Fig. 1 and Fig. S4. The longest time scale used (18 h) represents the time from the collapse of the boundary layer the day before (~6:00 PM) to the time observations were made. These component uncertainties are then propagated to produce the total range of the flux estimate.

A complicating factor affecting our ability to directly compare the top-down flux estimate with the bottom-up inventory is the influence of advective transport. At night, surface winds are typically low and unsustained, leading to very slow transport of air masses, and winds on the morning of our flights were low (2–3 m/s). However, for an 18-h accumulation, it is likely that these observations include mixing with air containing emissions (and/or cleaner air) from a region upwind (SW) of the measurement region. To investigate the potential impact of the upwind area we used the NOAA Hybrid Single Particle Lagrangian Integrated Trajectory Model (HYSPLIT) to predict the maximum size of the upwind area (ready.arl.noaa.gov/HYSPLIT.php). Starting at the time of observations (10:00 AM EDT) we ran an 18-h matrix back trajectory encompassing the area of observations. The 18-h time scale was chosen because it presents the largest estimate of potential upwind influence. We chose the isobaric mode with an effective altitude that is constant at 50 m to represent transport within the stable surface layer. The resulting area of influence, which we call the UAA, covers 14,597 km^2 and is shown in Fig. S1. This area is five times larger than the original sample area. An appropriate comparison with a bottom-up inventory will, therefore, have to include an estimate for an area encompassing the entire 18-h back trajectory region (UAA) and an estimate for the OSA. The average emissions over the UAA corresponds to a lower limit for the bottom-up flux, because the top-down measurements likely did not sample completely mixed air, and in this case the upwind area contains cleaner air, which dilutes the emissions. Likewise, the OSA represents an upper limit for comparison with the bottom-up flux because the top-down measurements similarly did not sample air exclusively influenced by the OSA (which has a higher density of emission sources), and accumulation may have effectively occurred over a time scale greater than the estimated 5–6 h.

Bottom-up inventories including energy sector, agriculture, landfill, and other miscellaneous emissions were produced for both the OSA and the UAA and are described in *SI Text*. Energy sector emissions were computed using the following national and state databases: Pennsylvania Department of Environment databases of oil, gas, and coal production and locations; West Virginia Department of Environment databases of oil, gas, and coal production and locations; Ohio Department of Natural Resources databases of oil, gas, and coal production; Energy Information Administration databases of state to state pipeline transmission and location; Department of Labor database of Employment and Production; and the Pipeline and Hazardous Material Safety Administration database of pipeline transmission. Default gas compositions were used (38), and all conversions between volume and mass assume standard gas conditions: 15 °C and 1 atm. Emission factors from ref. 11 are used to calculate routine fugitive emissions from natural gas production and processing and for life cycle fugitive emissions from coal and oil energy sectors. Emissions from natural gas transmission and distribution and well flowback events are calculated from emission factors provided in refs. 16 and 17, respectively. For comparison, a bottom-up inventory of natural gas sector emissions using only ref. 16 emission factors was also completed for the OSA. Methane emissions from the agriculture sector were calculated from total animal counts in the counties of interest (39) multiplied by methane emission factors from refs. 40 and 41. Other methane emissions were included from EPA-reported greenhouse gas emissions from landfills and other miscellaneous sources (42). Table 3 shows the total emissions from the bottom-up inventory for the OSA and UAA, as well as the comparison inventory for the OSA. More detailed emissions are presented for the OSA in Table S1 and the UAA in Table S2.

The comparison of uncaptured natural gas emissions as a percentage of total natural gas produced has been used as a standard of comparison between studies. We used the bottom-up inventories to compute the proportion of our observed top-down flux that would be expected to come from the natural gas sector. As shown in Table 3, the total contribution of methane emissions from the natural gas sector is assumed to be between 22% and 62% in this region. This range was used to calculate the contributing portion of natural gas emissions from the extrema in the top-down flux to be divided by the local unassociated production rates of 50.1 g CH_4 s^{-1} km^{-2} for the OSA and 15.9 g CH_4 s^{-1} km^{-2} for the UAA, as shown in Table 4. We report emission rates in Table 4 and estimate a fugitive emission rate between 2.8% and 17.3% of natural gas production for this region on these particular days. This estimate should be compared with other estimates with caution because these estimates generally use more comprehensive temporal data (16, 17, 19, 20).

Nevertheless, the upper range of this emission rate is surprisingly high, particularly because there were no major or widespread activities such as flowback events or well workovers of which we are aware that are typically associated with higher methane emission rates.

The mass-balance technique used here is described in ref. 26. Briefly, CH_4 concentration data are collected at varying altitudes downwind of a source approximately perpendicular to the prevailing wind direction. Downwind transects were flown to the top of the boundary layer, determined from vertical profiles of potential temperature, H_2O, CH_4, and CO_2, or more commonly, until the signal reached background levels. The observation of plumes that did not extend all of the way to the boundary layer top is attributed to the fact that downwind transects were typically flown 2–5 km downwind of a source, corresponding to too short a transport time scale for complete vertical mixing but necessary to isolate sources in a landscape with a dense distribution of potential sources. Fig. S6 shows raw CH_4 transect data 1.1 km downwind of pad Delta during flight MB-2. Interpolation of the raw transect data to create a 2D matrix of CH_4 values was done using EasyKrig3.0 (37). Fig. 2 shows the output from the interpolation of the raw data in Fig. S6. After the interpolated CH_4 and horizontal wind matrices are obtained, the flux is calculated according to Eq. **1**.

$$F = \int_0^{z_i} \int_{-x}^{x} \Delta[CH_4]_{ij} \times M_{\perp_{ij}} dx dz \qquad [1]$$

Here the limit z_i is the top of the boundary layer, or the height at which the plume stops, and the limits x and $-x$ are the horizontal limits determined from an arbitrary reference point in the middle of the transects. ΔCH_4 is obtained by converting CH_4 concentrations from ppm to mol·m^{-3} using measured temperature and pressure, then subtracting an average background CH_4 value, calculated by averaging the edges of the interpolated matrix, from each point in the interpolated CH_4 matrix, denoted by the subscripts ij. $M_\perp$ is the component of the mean wind that is perpendicular to the plane downwind of the source, which has also been interpolated from observations. Integrating across x and z and multiplying by dx, 110 m, and dz, 20 m, gives the flux in mol/s per cell, which can then be converted to units of g/s or kg/s. In cases in which there were multiple well pads contributing, the number of potential upwind pads was determined from visually inspecting the CH_4 data and spatial distribution of pads in the upwind direction.

Hydrocarbon concentration values were obtained from flask samples taken during flight RF-2. Of the 12 flasks, 2 were sampled in the free troposphere and excluded from hydrocarbon ratio calculations. The lowest hydrocarbon mole ratios in a single flask within the boundary layer were used as an estimate of background values and subtracted from the remaining nine flasks to obtain delta hydrocarbon values. The least-squares regression, forced through zero, between delta values of hydrocarbons, was used to find the hydrocarbon ratio. The uncertainty in the ratio reported is the uncertainty in the least-squares regression slope.

ACKNOWLEDGMENTS. We thank Karen Edelstein and Bongghi Hong for their help in compiling the bottom-up inventory and Carolina Siso for flask VOC analysis. The data presented here can be made available by the authors, by contacting pshepson@purdue.edu. Funding was provided by the David R. Atkinson Center for a Sustainable Future at Cornell University.

1. Stocker T, et al. (2013) in *Climate Change 2013: The Physical Science Basis: Technical Summary*, eds Joussaume S, Penner J, Fredolin T (Cambridge University Press, New York), Table 8.7.
2. Shindell DT, et al. (2009) Improved attribution of climate forcing to emissions. *Science* 326(5953):716–718.
3. Thompson AM (1992) The oxidizing capacity of the Earth's atmosphere: Probable past and future changes. *Science* 356(5060):1157–1165.
4. Solomon S, et al. (2010) Contributions of stratospheric water vapor to decadal changes in the rate of global warming. *Science* 327(5970):1219–1223.
5. Frankenberg C, et al. (2011) Global column-averaged methane mixing ratios from 2003 to 2009 as derived from SCIAMACHY: Trends and variability. *J Geophys Res* 116(D4):D04302.
6. Pacala S, Socolow R (2004) Stabilization wedges: Solving the climate problem for the next 50 years with current technologies. *Science* 305(5686):968–972.
7. Myhrvold NP, Caldeira K (2012) Greenhouse gases, climate change and the transition from coal to low-carbon electricity. *Environ Res Lett*, 10.1088/1748-9326/7/1/014019.
8. Alvarez RA, Pacala SW, Winebrake JJ, Chameides WL, Hamburg SP (2012) Greater focus needed on methane leakage from natural gas infrastructure. *Proc Natl Acad Sci USA* 109(17):6435–6440.
9. Venkatesh A, Jaramillo P, Griffin WM, Matthews HS (2011) Uncertainty in life cycle greenhouse gas emissions from United States natural gas end-uses and its effects on policy. *Environ Sci Technol* 45(19):8182–8189.
10. US Energy Information Administration (2013) EIA annual energy outlook 2013. Available at www.eia.gov/forecasts/aeo/pdf.0383(2013).pdf. Accessed August 7, 2013.
11. Howarth RW, Santoro RL, Ingraffea A (2011) Methane and the greenhouse-gas footprint of natural gas from shale formations. *Clim Change* 106(4):679–690.
12. Hultman N, Rebois D, Scholten M, Ramig C (2011) The greenhouse impact of unconventional gas for electricity generation. *Environ Res Lett*, 10.1088/1748-9326/6/4/044008.
13. Jiang M, et al. (2011) Life cycle greenhouse gas emissions of Marcellus shale gas. *Environ Res Lett*, 10.1088/1748-9326/6/3/034014.
14. Stephenson T, Valle JE, Riera-Palou X (2011) Modeling the relative GHG emissions of conventional and shale gas production. *Environ Sci Technol* 45(24):10757–10764.
15. Burnham A, et al. (2012) Life-cycle greenhouse gas emissions of shale gas, natural gas, coal, and petroleum. *Environ Sci Technol* 46(2):619–627.
16. National Energy Technology Laboratory (2011) *Life Cycle Greenhouse Gas Inventory of Natural Gas Extraction, Delivery and Electricity Production* (DOE/NETL Publication 2011/1522). Available at www.netl.doe.gov/File%20Library/Research/Energy%20Analysis/Life%20Cycle%20Analysis/NG-GHG-LCI.pdf. Accessed December 11, 2012.
17. US Environmental Protection Agency (2010) Greenhouse gas emissions reporting from the petroleum and natural gas industry: Background technical support document. Available at www.epa.gov/ghgreporting/documents/pdf/2010/Subpart-W_TSD.pdf. Accessed December 15, 2011.
18. Howarth RW, Shindell D, Santoro RL, Ingraffea A, Phillips N, Townsend-Small A (2011) *Methane Emissions from Natural Gas Systems*. National Climate Assessment, Feb. Report No. 2011-003 (Office of Science and Technology Policy, Washington, DC).
19. Weber CL, Clavin C (2012) Life cycle carbon footprint of shale gas: Review of evidence and implications. *Environ Sci Technol* 46(11):5688–5695.
20. Pétron G, et al. (2012) Hydrocarbon emissions characterization in the Colorado Front Range: A pilot study. *J Geophys Res*, 10.1029/2011JD016360.
21. Karion A, et al. (2013) Methane emissions estimate from airborne measurements over a western United States natural gas field. *Geophys Res Lett*, 10.1002/grl.50811.
22. Allen DT, et al. (2013) Measurements of methane emissions at natural gas production sites in the United States. *Proc Natl Acad Sci USA* 110(44):17768–17773.
23. Miller SM, et al. (2013) Anthropogenic emissions of methane in the United States. *Proc Natl Acad Sci USA* 110(50):20018–20022.
24. US Environmental Protection Agency (2013) *Inventory of US Greenhouse Gas Emissions and Sinks: 1990-2011*. EPA Publication 430-R-13-001 (US Environmental Protection Agency, Washington, DC).
25. Katzenstein AS, Doezema LA, Simpson IJ, Blake DR, Rowland FS (2003) Extensive regional atmospheric hydrocarbon pollution in the southwestern United States. *Proc Natl Acad Sci USA* 100(21):11975–11979.
26. Mays KL, et al. (2009) Aircraft-based measurements of the carbon footprint of Indianapolis. *Environ Sci Technol* 43(20):7816–7823.
27. Pennsylvania Department of Environmental Protection (2012) Internal File Review: Permitted Wells: 12524400-02, 12524425, 125124516, 12524517, 12524529-41, 12524552, 12524553, 1252455-58, 12524563, 12524564, 12524589, 12524600, 12524617, 12524618, 12524627, 12524628, 12524696, 12524713, 12524714, 12524762 (Pennsylvania Department of Environmental Protection, Southwest Regional Office, Pittsburgh).
28. American Society of Mechanical Engineers Shale Shaker Committee (2005) *Drilling Fluids Processing Handbook* (American Society of Mechanical Engineers Shale Shaker Committee, Amsterdam, NY).
29. US Environmental Protection Agency (2012) ANNEX 3: Methodological descriptions for additional source or sink categories. Available at www.epa.gov/climatechange/ghgemissions/usinventoryreport.html. Accessed February 19, 2013.
30. Braziel ER (2011) Infrastructure projects connect Marcellus shale to ethane, NGL markets. Available at www.aogr.com/index.php/magazine/cover-story/infrastructure-projects-connect-marcellus-shale-to-ethane-ngl-markets. Accessed November 26, 2012.
31. Osborn SG, McIntosh JC (2010) Chemical and isotopic tracers of the contribution of microbial gas in Devonian organic-rich shales and reservoir sandstones, northern Appalachian Basin. *Appl Geochem* 25(3):456–471.
32. Kotarba MJ (2001) Composition and origin of coalbed gases in the Upper Silesian and Lublin basins, Poland. *Org Geochem* 32(1):163–180.
33. Brandt AR, et al. (2014) Energy and environment. Methane leaks from North American natural gas systems. *Science* 343(6172):733–735.
34. Mohr SH, Evans GM (2011) Long term forecasting of natural gas production. *Energy Policy* 39(9):5550–5560.
35. Dlugokencky EJ, Nisbet EG, Fisher R, Lowery D (2011) Global atmospheric methane: budget, changes and dangers. *Phil Trans R Soc A* 369(1943):2058–2072.
36. Garman KE, et al. (2006) An airborne and wind tunnel evaluation of a wind turbulence measurement system for aircraft-based flux measurements. *J Atmos Ocean Technol* 23(12):1696–1708.
37. Chu D (2004) The GLOBEC kriging software package–EasyKrig3.0. Available at http://globec.whoi.edu/software/kriging/easy_krig/easy_krig.html. Accessed January 7, 2011.
38. American Petroleum Institute (2009) Compendium of greenhouse gas emissions methodologies for the oil and natural gas industry. Available at www.api.org/ehs/climate/new/upload/2009_ghg_compendium.pdf. Accessed December 14, 2012.
39. Hong B, Swaney DP, Howarth RW (2011) A toolbox for calculating net anthropogenic nitrogen inputs (NANI). *Environ Model Softw* 26(5):623–633.
40. Jorgensen H (2007) Methane emission by growing pigs and adult sows as influenced by fermentation. *Livest Sci* 109(1-3):216–219.
41. Zhou JB, Jiang MM, Chen GQ (2007) Estimation of methane and nitrous oxide emission from livestock and poultry in China during 1949-2003. *Energy Policy* 35(7):3759–3767.
42. US Environmental Protection Agency (2010) EPA greenhouse gas reporting program 2010 summary. Available at www.epa.gov/ghgreporting/ghgdata/2010data.html. Accessed May 8, 2013.

Environmental Science & Technology

Article

pubs.acs.org/est

Methane Destruction Efficiency of Natural Gas Flares Associated with Shale Formation Wells

Dana R. Caulton,*[,†] Paul B. Shepson,[†,‡] Maria O. L. Cambaliza,[†] David McCabe,[§] Ellen Baum,[§,⊥] and Brian H. Stirm[#]

[†]Department of Chemistry and [‡]Department of Earth, Atmospheric and Planetary Sciences, Purdue University, 560 Oval Drive, West Lafayette, Indiana 47907, United States

[§]Clean Air Task Force, 18 Tremont Street, Suite 530, Boston, Massachusetts 02108, United States

[#]Department of Aviation Technology, Purdue University, 1581 Aviation Drive, West Lafayette, Indiana 47907, United States

Supporting Information

ABSTRACT: Flaring to dispose of natural gas has increased in the United States and is typically assumed to be 98% efficient, accounting for both incomplete combustion and venting during unintentional flame termination. However, no in situ measurements of flare emissions have been reported. We used an aircraft platform to sample 10 flares in North Dakota and 1 flare in Pennsylvania, measuring CO_2, CH_4, and meteorological data. Destruction removal efficiency (DRE) was calculated by assuming a flare natural gas input composition of 60−100% CH_4. In all cases flares were >99.80 efficient at the 25% quartile. Crosswinds up to 15 m/s were observed, but did not significantly adversely affect efficiency. During analysis unidentified peaks of CH_4, most likely from unknown venting practices, appeared much larger in magnitude than emissions from flaring practices. Our analysis suggests 98% efficiency for nonsputtering flares is a conservative estimate for incomplete combustion and that the unidentified venting is a greater contributor to CH_4 emissions.

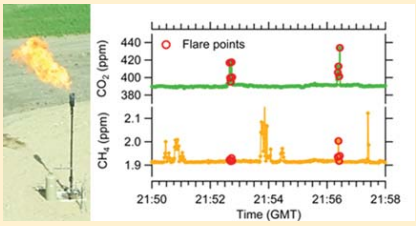

INTRODUCTION

Worldwide, gas flaring is a large source of greenhouse gases (GHG) and other pollutants.[1] Flaring is common at hydrocarbon production sites where natural gas is not captured for sale or utilized on site. This allows production sites to dispose of natural gas relatively safely and also converts the more potent GHG CH_4, along with other polluting components such as volatile organic compounds and aromatics, into CO_2. Hydraulic fracturing and horizontal drilling have recently allowed access to reserves of oil in shale and other "tight" low-porosity formations such as the Bakken Formation in North Dakota. Since 2005, flaring has increased in the United States after declining for many years with a factor of 2 increase in flaring between 2004 and 2012, due to flaring in areas producing oil from tight formations that generally produce significant quantities of natural gas in addition to oil.[1−3] The rapid expansion of oil production in the Bakken, for example, has outpaced the deployment of natural gas pipelines and ancillary systems to transport associated gas from oil wells to market, leading to an increase in flaring.[4] Currently, about one-third of the natural gas produced in North Dakota is not marketed, meaning it is either flared or vented to the atmosphere.[3] The amount of natural gas vented or flared in North Dakota has increased by a factor of 30 since 2004, when flaring rates had been relatively steady for several years.[3]

As horizontal drilling and hydraulic fracturing have increased domestic production of both oil and natural gas,[5] there has been interest in GHG emissions from production of these fuels. A number of studies have focused on natural gas production, with a focus on methane life-cycle emissions from leaks and venting of gas.[6−10] Additionally, some recent studies yielded leak rates for some parts of the production process for oil and natural gas.[11−15] On a 100-year time horizon fossil CH_4 is a 30−36 times more potent GHG than CO_2, making it particularly important to determine methane emissions in actual operating conditions.[16] There has been less focus on upstream GHG emissions from oil production. With the large quantity of flaring occurring in the Bakken, accurate quantification of emissions from flares is essential, including emissions of methane due to incomplete combustion. Typically, inventories of oil and gas methane emissions and life-cycle assessment use an estimate of 98% destruction removal efficiency (DRE) for flaring, citing the 1996 study by the EPA and the Gas Research Institute (GRI) or inventories that rely on that study.[17,18] As presented by the EPA/GRI study,

Received: January 29, 2014
Revised: July 17, 2014
Accepted: July 22, 2014
Published: July 22, 2014

   dx.doi.org/10.1021/es500511w | Environ. Sci. Technol. 2014, 48, 9548−9554

this figure accounts for both imperfect combustion, investigated in this study, and time periods when the flame goes out (due to fuel flow interruptions or other operational problems). The EPA/GRI study reviewed earlier studies but noted that only two of them used natural gas. None, to our knowledge, used a hydrocarbon mix representative of associated gas from an oil well, which may have significant amounts of noncombustible gases such as water and carbon dioxide and higher concentrations of propane and heavier alkanes than processed natural gas.

Although there have been studies investigating the efficiencies of flares in laboratory settings, which usually involve scaled down simulations of a flare and predict very high efficiencies, we are aware of no peer-reviewed publications regarding in situ measurements of flare efficiency.[19,20] As field flaring techniques may differ significantly from the laboratory scale, there is potential for flaring to be much less efficient. One technical report from two field flare sites in Canada reported efficiencies as low as 66−84% for natural gas flares despite small-scale and full-scale laboratory tests that yielded much higher efficiencies (98−99%).[21]

Recently there has been more work done to understand flare efficiency, combustion products, and particulate matter emissions.[22−25] However, these studies focused on an industrial chemical process flare at a test facility, representing a permanent flare subject to regulations on emissions. These studies (and previous studies of industrial flares) typically used mixtures with significant amounts of propylene, which is not present in associated gas, and most of the tests were of steam-assisted flares, technology predominantly found at refineries and chemical plants.[26] Flares from natural gas or oil fields are often temporary, simple, and may not be subject to emissions reporting or permitting requirements. Depending on the volume of associated gas expected and its heat content, an operator may choose an air-assisted setup to ensure a smokeless flare.[26] To obtain methane emission factors for associated gas flares representative of conditions typical of flaring, we used an aircraft platform, capable of repeatedly sampling in situ flare plumes across a wide range of wells. This work was done in the Williston Basin in North Dakota, sampling wells producing oil from the Bakken Shale Formation. In addition, we sampled a single flare in southwestern Pennsylvania, at a Marcellus Shale gas well. Here we report the methane destruction efficiency of these flares.

EXPERIMENTAL PROCEDURES

Site Description. Ten flares in western North Dakota were identified visually, and their plumes were sampled by repeated passes on May 14, 2012, and June 12−14, 2012. In addition, one flare in southwestern Pennsylvania was sampled on June 18, 2012. Flare locations and sampling dates are reported in Table S1 and shown in Figure S1 of the Supporting Information. Flaring was prevalent in North Dakota across the entire Bakken Formation, whereas in southwestern Pennsylvania at the time of this study we observed only one large flare. Flares were selected randomly on the basis of their visible detection and covered a variety of different sites and operators. This was done in an attempt to sample a range of common flare configurations (flare stack height, gas exit velocity, etc.) actually used in the field, as these parameters can affect efficiency. However, as large flares were the most easily identified and sampled, our sampling approach may be biased toward the largest, and potentially most efficient, flares. It is important to note that all flares identified and sampled were continuously operating over the sampling period, that is, not sputtering or showing periods of intermittency or temporary extinguishment. In addition, the small number of flares sampled may miss so-called "superemitters", that is, relatively anomalous sources that emit an outsized portion of the total emissions of interest. This may also bias our results toward more efficient flares.[27] However, a variety of flares, under a variety of wind conditions, were sampled, and it is not clear that the superemitter phenomenon would be relevant to destruction efficiency in a flare flame. A range of wind speeds was observed, allowing for an analysis of the effect of crosswind speed on flare efficiency. Flare configurations varied from very small stacks burning in small dugout pits, which we managed to successfully sample only once, to flares with stacks several meters high. Typical flare stack heights for elevated flares are 9−30 m above ground level (AGL), and our observations suggest in this region elevated flares were ∼9 m AGL.[26] Flame heights varied between sites and meteorological conditions.

Instrumentation. Purdue's Airborne Laboratory for Atmospheric Research (ALAR), a modified Beechcraft Duchess aircraft, was used to sample flare plumes. The aircraft is equipped with a best air turbulence (BAT) probe as described by Garman et al.,[28] which measures 50 Hz wind vectors and pressure and is equipped with a microbead thermistor. Air is sampled at ∼1800 L min^{-1} through a pair of inlets connected to a 5 cm diameter Teflon sample manifold with a residence time of ∼0.1 s. Fifty Hz GPS/INS data are recorded to enable calculation of the wind vectors. Also onboard is a 0.5 Hz CO_2/CH_4/H_2O high-precision Picarro cavity ring-down spectrometer (CRDS) that measures and records species nearly simultaneously (within 0.2 s).[29] An in-flight calibration system allows the CRDS to sample three NOAA/ESRL calibration standards containing CH_4 concentrations of 1803.05 ± 0.40, 2222.2 ± 0.3, and 2599.5 ± 1.2 ppb and CO_2 concentrations of 378.491 ± 0.013, 408.826 ± 0.021, and 438.288 ± 0.019 ppm, respectively. Conversion to concentration is thus based on three-point calibration curves conducted for each flight. Composite calibration plots for the whole experiment (May 14−June 14, 2012) are presented in Figure S2 of the Supporting Information and show the excellent linearity and stability of the instrument.[30] The in-flight precisions (1σ) for CO_2 and CH_4 were 0.07 ppm and 1 ppb, respectively, from 30 s averages of sampling the standard gases.

Flare Plume Isolation. The structure of flare plumes has been examined, largely at laboratory scale, and is expected to produce a distinct combustion (i.e., buoyant) plume and unburned fuel (i.e., nonbuoyant) plume.[20,31] At the local scale this will result in inhomogeneous plume profiles.[31] However, in convective boundary layers near the surface, both buoyant and nonbuoyant plumes have similar dispersion rates due to the influence of updrafts and atmospheric turbulence, which quickly mixes heat and pollutants.[32,33] Thus, we assume that the CO_2 and CH_4 plumes are correlated and relatively well-mixed at our sampling height and distance and will evaluate that assumption under Results and Discussion. To sample flare plumes, we flew directly into the flare plume from the downwind side, parallel to the wind direction, and completed the sampling transect by flying directly over the flare to maximize data collected in the plume. Sampling transects were flown at low altitudes prior to reaching a flare. A sample flight path over a sampled flare showing observed CO_2 concentrations is presented in Figure 1. To identify flare plume data,

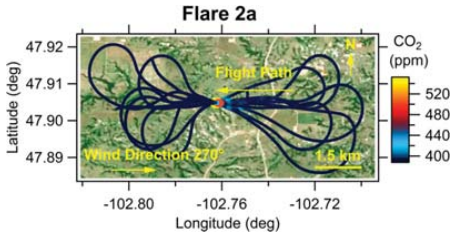

Figure 1. Plot of the flight path to sample flare 2a colored by observed CO_2 concentration.

the mean and standard deviation of background concentrations of CO_2 and CH_4 were first calculated from flight legs where no flare or methane emission plumes were present. In many cases flare sites were far from the initial background sample area, and the background concentration changed slightly. For these sites background values were calculated as the mean excluding outliers (plumes) in the area of study. The standard deviation of CO_2 near the flare was assumed to be the same as the background area, which ranged from 0.27 to 0.44 ppm in North Dakota and was 0.61 ppm in Pennsylvania. The mean background concentrations ranged from 385.37 to 393.25 ppm and from 1874.4 to 1919.8 ppb for CO_2 and CH_4, respectively. Background concentrations were subtracted from observations to produce ΔCO_2 and ΔCH_4 time series for each flare. Flare plumes were identified from flight transects in the plume of each flare where ΔCO_2 was at least 7σ above the background and within 4 s of the maximum CO_2 peak, to exclude weak CO_2 plumes that may have been produced by combustion-driven equipment on or near the pads. The standard deviations (1σ) of the background for CH_4 ranged from 1.1 to 3.6 ppb. Figure 2a shows an example time series of CO_2 and CH_4 with points identified as flare plumes (in red) for one of the flares sampled.

Efficiency Calculations. To calculate flare efficiency, emission factors (EF) were calculated using two methods. First, a standard regression of ΔCO_2 versus ΔCH_4 was performed for all plume points from a single flare during one sampling flight. Regressions were forced through zero, and the slope of such a regression is equal to the EF for that particular flare. This allows the calculation of EFs for each flare. A sample regression is shown in Figure 2b.

Second, an aggregate analysis was performed. EFs were calculated as the ratio of ΔCH_4 (in ppm) to ΔCO_2 (in ppm) for all data points within flare plumes. This was done by directly calculating the ΔCH_4 to ΔCO_2 ratio (in ppm/ppm) for all simultaneous data points identified as flare plumes (n = 355) in the entire data set. For this analysis, flare plume points were screened for ΔCH_4 values that were not significantly different from zero. All flare plume points with ΔCH_4 values within 3σ of the background, a standard limit of detection threshold, were considered indistinguishable from the background.[34] The effective limit of quantification (LOQ) we observed for EFs due to the combined effect of distinguishing CO_2 plumes indicative of flares and CH_4 values above the background is 9.0×10^{-5} ppm/ppm and is indicated in Table 1. An ogive (cumulative frequency) plot was made for EFs and is shown in Figure 3 for EFs up to the 95th percentile EF. Ogive plots present the cumulative integral of the frequency of each measurement versus the value of each measurement, in this case EFs, and give information about the density of measurements around a given value.[34] This technique is similar to a histogram plot showing normalized frequency, but is more useful for data that spans many orders of magnitude where the use of histogram "classes" may separate data too coarsely to provide relevant detailed information. Sequentially increasing histogram "class" width may give a false impression of uniform frequency of events or greater measurement variability than actually observed. The full ogive is given in the Supporting Information in Figure S3.

Traditional definitions of efficiency refer to combustion efficiency (CE), which is a measure of how well the flare converts carbon in the fuel gas to CO_2 ($carbon_{CO_2}/carbon_{fuel}$), or destruction removal efficiency (DRE), which is a measure of how well a flare destroys a particular fuel component regardless of the product (species X_{flare}/species X_{fuel}). Without the instrumentation to measure all of the products of CH_4 combustion or information on the actual flow rate and composition of the flare fuel at the time of study, we cannot truly measure CE or DRE. However, CH_4 emission was the primary concern of this study as the most potent greenhouse gas emitted and the most difficult to oxidize in the atmosphere with a lifetime of 12.4 years.[16] To estimate DRE we assume that CH_4 combusts fully to CO_2 and that production of CO and other non-CO_2 products is negligible. We assume the amount

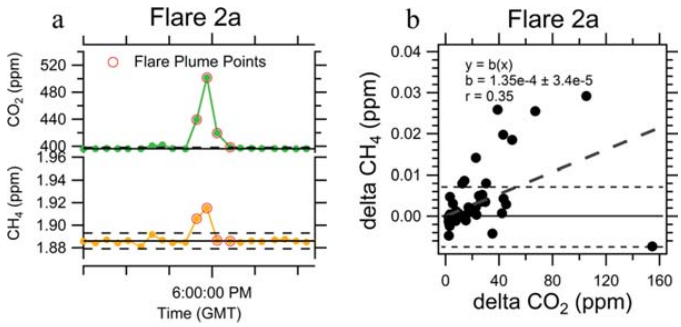

Figure 2. (a) Time series of CO_2 and CH_4 showing flare plume measurements in red above the 7σ CO_2 threshold (dashed black line) and within 4σ of the maximum CO_2 plume value. Background values are shown as solid black lines. The 3σ CH_4 background is shown as dashed black lines. (b) Regression of identified flare plume points. The regression has been forced through zero, and error on the slope is reported as 1σ. Dashed lines show the 3σ threshold around 0 for CH_4.

Table 1. EF and DRE Statistics Including the Median, Minimum, Maximum, Mean, and 25 and 75% Quartile Values[a]

				DRE		
statistics		EF ppm/ppm	statistics	100% CH_4	80% CH_4	60% CH_4
	min	$<9.0 \times 10^{-5}$	max	>99.99	>99.98	>99.97
quartiles	25%	$<9.0 \times 10^{-5}$	75%	>99.99	>99.98	>99.97
	med	$<9.0 \times 10^{-5}$	med	>99.99	>99.98	>99.97
	75%	7.1×10^{-4}	25%	99.93	99.88	99.80
	max	3.5×10^{-2}	min	96.61	94.33	90.91
	mean	1.11×10^{-3}	mean	99.89	99.81	99.69
	LOQ	9.0×10^{-5}	LOQ	99.99	99.98	99.97

[a]Also shown is the limit of quantification (LOQ) for the EF and the corresponding highest quantifiable DRE for each scenario.

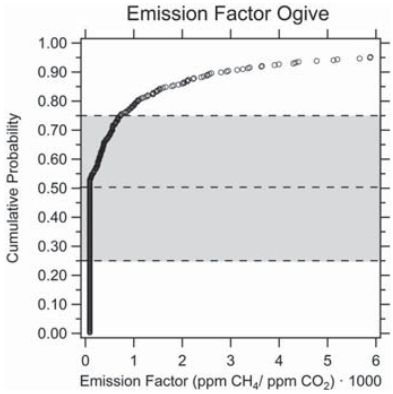

Figure 3. EF ogive up to 95% cumulative probability. The shaded area represents the 25–75% quartiles. The EF LOQ is 9.0×10^{-5}.

of CH_4 in the original flare gas is equal to the unburnt CH_4 we observed in the flare plus some fraction of the amount of CO_2 we observed based on commonly assumed CH_4 compositions of raw natural gas, which range from 60 to 100%, with the most commonly used composition being 80%.[35] The fractions of CH_4 in the total gas were converted to molar carbon ratios by assuming the other major constituents were C_2H_6, C_3H_8, C_4H_{10}, and C_5H_{12} as given in ref 36. Table S2 in the Supporting Information presents assumed CH_4 mole percent and the resulting carbon mole percent for three cases. The expression used for DRE is shown in eq 1.

$$\text{DRE}\ (\%) = \left(\frac{\mu CH_4}{((X) \times \mu CO_2) + \mu CH_4}\right) \times 100 \quad (1)$$

Here μCH_4 and μCO_2 are molar ratios and X is the fractional carbon composition attributed to CH_4 in the preignited flare gas (1–0.35).

RESULTS AND DISCUSSION

Our regression analysis revealed several very low correlation coefficients and corresponding high uncertainty in the calculated EFs. Full regression results, error, and correlation coefficients are reported in Table S3 in the Supporting Information. Regression EFs range from 1.0×10^{-4} to 1.7×10^{-3} ppm/ppm with a median value of 2.7×10^{-4} ppm/ppm. The 25–75% quartile range for the regression analysis is from 2.0×10^{-4} to 6.5×10^{-4} ppm/ppm. We chose to aggregate the data in our second EF analysis approach, described under Experimental Procedures, in an attempt to verify our regression findings and provide results with more robust statistics. We obtained 355 data points satisfying the sampling criteria from 10 flares that were successfully sampled. EF and DRE quartiles are reported in Table 1. We observed large overall variability in the EFs most likely attributable to the small size of the plume and the difficulty in obtaining this measurement as well as actual variability in, and small quantity of, the unburnt CH_4 and possible inhomogeneity within the flare plume. It may be that scatter caused by inhomogeneous plumes could be minimized by integrating plumes for each transect through the plume. Because the flare plumes are quite small and were sampled over a time period of a few seconds (i.e., from an aircraft traveling at ~50 m/s), it was quite difficult to obtain data above our criteria threshold at our sampling frequency. For one case, flare 8, we were unable to detect any CO_2 plumes, even after multiple passes. In a similar case we attempted to resample flare 3, which had already been successfully sampled, but were unable to identify any CO_2 plumes during analysis. Typically we were able to obtain three to four data points that satisfied our criteria per plume per pass; multiple passes were made for each flare to obtain the number of samples (n = 355). This then creates difficulties in attempting integration of the plume transect, as the small number of samples per pass renders the peaks not smooth. Nevertheless, we performed regression analysis of the integrated transects for each, including transects with at least three plume points for all flares, to assess whether there was any bias in our single-point analysis from plume inhomogeneity. The results of these regressions are reported in Table S4 and are not statistically different from the original regression (Table S3), indicating that our original point-by-point approach, which has the advantage of preserving more data points, is not significantly biased. However, in most cases the correlation of the integration results significantly improved, indicating random spatial variability in the flare plume may account for much of the scatter in our data and plume homogeneity should not be assumed. Even with improved correlation coefficients, the integration regression slope error generally increased due to the decreased number of data points.

Of the 355 flare plume points identified, 168 had ΔCH_4 values above the 3σ background criteria; thus, 53% of our collected EFs are reported as $<9.0 \times 10^{-5}$ ppm/ppm, our effective LOQ. EF quartile values are reported in Table 1 along with the mean value, which is above the 75% quartile value, as the mean is greatly affected by extreme values. Other factors affecting our EF range could be direct venting or leaking

sources close to the flares that we could not visually identify. Mixing of plumes from venting or leaking into the flare plumes may explain the few very high EFs we observed that were nearly 2 orders of magnitude greater than our 75% quartile value. However, our LOQ–75% quartile range, from 9.0×10^{-5} to 7.1×10^{-4} ppm/ppm, spans only a factor of 8, indicating that EFs do not vary greatly among the sites sampled or over time at the same sites, even as flare gas flow rates and flare stack structures vary from site to site and over time. The range of EFs produced by both the regression technique and aggregate analysis are consistent.

For the aggregate analysis we observed very high DRE quartiles for all gas composition cases with no 25% quartile value <99.80%. The 25% quartile values represent the best estimate of the lower limit of the DRE for the observed flares. In contrast, the mean DRE is strongly affected by extreme low values of the DRE, which may be due to contamination of the flare plume with methane emissions from a vent or leak. Highest quantifiable DREs were 99.99, 99.98, and 99.97% for the 100, 80, and 60% CH_4 scenarios, respectively. DRE values for the aggregate analysis are reported in Table 1 with individual flare DRE values reported in Table S5 in the Supporting Information. Calculated DRE ogives for each of the assumed CH_4 compositions of the flare gas are plotted in Figure 4. Full ogives are given in Figure S4. As previously

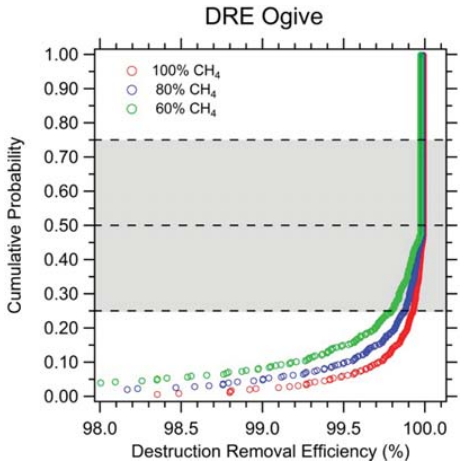

Figure 4. DRE ogives showing DREs >98% efficient. The shaded area represents the 25–75% quartiles.

mentioned, the flares sampled may be biased toward larger flares that are more efficient because these were the easiest to identify and sample. Even so, very high efficiency was observed for all flares sampled. Flares with smaller flames, which could be caused by slower flowing natural gas or gas with a low fraction of combustible material, may be less efficient, but could not be easily sampled using this approach. Thus, these observations apply to flares under conditions that do not produce sputtering or periodically extinguished flames (i.e., substantial and continuous gas flow), as we observed no such sputtering flares during our sampling. This indicates that emissions of methane from lit flares calculated using the default estimate for destruction efficiency of 98% may be too high. However, it is important to emphasize that the default 98% DRE, at least as originally recommended, also accounts for periods when the flame is out (i.e., DRE = 0), and this study does not address that flare condition. Thus, whereas our study indicates that large continuous flares such as those sampled in the Bakken and Marcellus shale deposits are very efficient in CH_4 removal, flares with significant flame sputtering may be better represented by the original 98% DRE value as it represents an integrated average DRE including intermittent venting.

We also examined the relationship between crosswind speed and emission factor, shown in Figure 5. Our wind data were

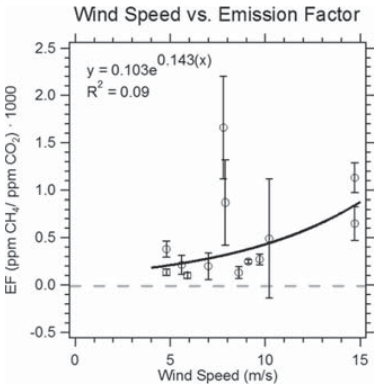

Figure 5. EF regression values for each flare plotted against crosswind speed. Error bars represent the 1σ error of the slope.

measured at our flight altitude (~150 m AGL on average), whereas the flare stacks experience wind at a height around 9 m AGL. This small difference in height should have a negligible effect on actual wind speed for this analysis, particularly as the terrain was relatively flat and the atmosphere unstable during the flights, with wind speeds of 5 m/s or greater and a factor of 3 in wind speed range.[33] Previous laboratory work has indicated a nonlinear relationship between crosswind speed and inefficiency, with inefficiency reaching ~10%.[19,20] To address this we used the regression data as we could directly compare the regression EF and the observed wind speed at each flare site. A weak relationship between crosswind speed and inefficiency appears in our data, with EFs increasing with wind speed and a coefficient of determination (R^2) value of 0.09 for an exponential fit, the fit that most closely resembles the expected relationship from previous studies.[19,20] However, the highest crosswind speeds (~15 m/s) did not significantly adversely affect efficiency as these flares have >99.68% efficiency in all CH_4 composition scenarios. Several reasons for this discrepancy may exist, the most likely being the effect of higher gas exit velocities and larger inside stack diameters that correspond to lower sensitivity of the efficiency to crosswind speeds.[19,20] We have no data regarding the actual gas exit velocity, inside diameter, or the nature of any assist technology (e.g., air-assisted) the flares used, but it is possible that these variables are present in configurations such that they decrease the adverse effect of the crosswind. Overall, the emitted CH_4 is very small, indicating that although in situ flaring efficiencies are sensitive to crosswind speed, the overall adverse effect is small.

During our flights over the Bakken field we observed CH_4 plumes that were uncorrelated to CO_2 plumes and thus unrelated to lit flares. A sample data sequence, shown in Figure 6, shows that these plumes were often much larger in magnitude than the flare CH_4 signals. Also, these plumes

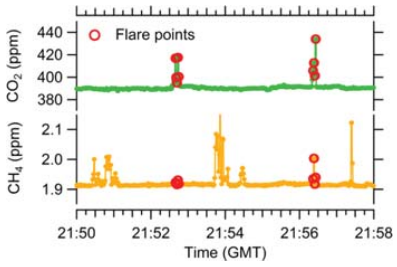

Figure 6. Time series of CO_2 and CH_4 showing flare signals circled in red. Several large CH_4 peaks are uncorrelated with flare signals.

were sampled at altitudes 2−3 times higher than those at which the flare signals were sampled and were observed at greater distances from sources, further indicating a considerably larger source strength. These plumes most likely correspond to intentional vents or unintentional leaks from oil or natural gas facilities as other common sources of methane (landfills, wetlands, dairy farms, wastewater treatment plants, etc.) were scarce, with the majority of the land being cropland or undeveloped and extensively dotted with oil well pads. However, in one case, we identified the source as a dairy farm by circling the potential source and seeing a CH_4 plume only on its downwind side. The processes leading to the observed venting events are uncertain, but they appear to be more important CH_4 emitters than flares. More work is needed to identify the nature of these sources and how they might be mitigated.

This work demonstrates that existing shale gas well flares can be very efficient in converting CH_4 to CO_2 and, if the CH_4 would have otherwise been vented, may result in a beneficial climate impact. No substantial negative impact on flare efficiency from crosswind was identified in this study. Future EF studies may benefit from the use of high-frequency instruments to allow plume data to be integrated, thus reducing the potential for scatter during data analysis. However, emissions of other compounds that can affect air quality or contribute to climate change from flaring are relatively little studied in the United States and should be pursued.[37−39]

■ ASSOCIATED CONTENT

Supporting Information

All supplemental tables and figures referenced in the text. This material is available free of charge via the Internet at http://pubs.acs.org.

■ AUTHOR INFORMATION

Corresponding Author

*(D.R.C.) E-mail: dcaulton@purdue.edu. Phone: (765) 496-2404. Fax: (765) 494-0239.

Present Address

⊥(E.B.) Climate and Health Research Network, 269 White Road, Bowdoinham, ME 04008, USA.

Author Contributions

The manuscript was written through contributions of all authors. All authors have given approval to the final version of the manuscript. D.R.C., P.B.S, and D.M. contributed equally.

Notes

The authors declare no competing financial interest.

■ ACKNOWLEDGMENTS

Funding was provided by the Clean Air Task Force for work in North Dakota and by the David R. Atkinson Center for a Sustainable Future at Cornell University for work in Pennsylvania.

■ ABBREVIATIONS

GHG	green house gas
BAT	best air turbulence
ALAR	Airborne Laboratory for Atmospheric Research
CRDS	cavity ring-down spectrometer
EF	emission factor
CE	combustion efficiency
DRE	destruction removal efficiency
LOQ	limit of quantification
AGL	above ground level

■ REFERENCES

(1) Olivier, J. G. I.; Janssens-Maenhout, G.; Peters, J. A. H. W. *Trends in Global CO_2 Emissions*; PBL Netherland Environmental Assessment Agency: Paris, France, 2013; pp 16−17.

(2) Rogner, H. H. An assessment of world hydrocarbon resources. *Annu. Rev. Energy Environ.* **1997**, *22*, 217−262, DOI: 10.1146/annurev.energy.22.1.217.

(3) U.S. Energy Information Administration. *Natural Gas Gross Withdrawals and Production*; http://www.eia.gov/dnav/ng/ng_prod_sum_a_EPG0_FGW_mmcf_a.htm (accessed June 18, 2014).

(4) U.S. EPA. Approval and promulgation of federal implementation plan for oil and natural gas well production facilities; Fort Berthold Indian Reservation (Mandan, Hidatsa, and Arikara Nations), ND. *Fed. Regist.* **2012**, *77* (158), 48878−48898.

(5) Annual Energy Outlook 2013, DOE/EIA-0383(2013); U.S. Energy Information Administration: Washington, DC, USA, 2013; www.eia.gov/forecasts/aeo/pdf/0383(2013).pdf.

(6) Howarth, R. W.; Santoro, R.; Ingraffea, A. Methane and the greenhouse-gas footprint of natural gas from shale formations. *Climatic Change* **2011**, *106* (4), 679−690, DOI: 10.1007/s10584-011-0061-5.

(7) Hultman, N.; Rebois, D.; Scholten, M.; Ramig, C. The greenhouse impact of unconventional gas for electricity generation. *Environ. Res. Lett.* **2011**, *6* (4), 1−9, DOI: 10.1088/1748-9326/6/4/044008.

(8) NETL. *Life Cycle Greenhouse Gas Inventory of Natural Gas Extraction, Delivery and Electricity Production*; National Energy Technology Laboratory: Pittsburgh, PA, USA, 2011.

(9) Stephenson, T.; Valle, J. E.; Riera-Palou, X. Modeling the relative GHG emissions of conventional and shale gas production. *Environ. Sci. Technol.* **2011**, *45* (24), 100757−10764, DOI: 10.1021/es2024115.

(10) Burnham, A.; Han, J.; Clark, C.; Wang, M.; Dunn, J. B.; Palou-Rivera, I. Life-cycle greenhouse gas emissions of shale gas, natural gas, coal and petroleum. *Environ. Sci. Technol.* **2012**, *46* (2), 619−627, DOI: 10.1021/es201942m.

(11) Petron, G.; et al. Hydrocarbon emissions characterization in the Colorado Front Range: a pilot study. *J. Geophys. Res.* **2012**, *117* (D4), D04304 DOI: 10.1029/2011JD016360.

(12) Peischl, J.; et al. Quantifying sources of methane using light alkanes in the Los Angeles basin, California. *J. Geophys. Res. Atmos.* **2013**, *118* (10), 4974−4990, DOI: 10.1002/jgrd.50413.

(13) Karion, A.; et al. Methane emissions estimate from airborne measurements over a western United States natural gas field. *Geophys. Res. Lett.* **2013**, *40* (16), 4393−4397, DOI: 10.1002/grl.50811.

(14) Miller, S. M.; et al. Anthropogenic emissions of methane in the United States. *Proc. Natl. Acad. Sci. U.S.A.* **2013**, *110* (50), 20018−20022, DOI: 10.1073/pnas.1314392110.

(15) Caulton, D. R.; et al. Toward a better understanding and quantification of methane emissions from shale gas development. *Proc. Natl. Acad. Sci. U.S.A.* **2014**, *111* (17), 6237−6242, DOI: 10.1073/pnas.1316546111.

(16) Stocker, T., et al. *Climate Change 2013: The Physical Science Basis: Technical Summary*; Joussaume, S., Penner, J., Fredolin, T., Eds.; Cambridge University Press: New York, 2014; Table 8.7.
(17) *Methane Emissions from the Natural Gas Industry: Vented and Combustion Source Summary*; U.S. Environmental Protection Agency and Gas Research Institute: Washington, DC, USA, 1996; www.epa.gov/gasstar/documents/emissions_report/6_vented.pdf.
(18) *Greenhouse Gas Emissions Reporting from the Petroleum and Natural Gas Industry: Background Technical Support Document*; U.S. Environmental Protection Agency: Washington, DC, USA, 2010; www.epa.gov/ghgreporting/documents/pdf/2010/Subpart-W_TSD.pdf.
(19) Johnson, M. R.; Kostiuk, L.W. Efficiencies of low-momentum jet diffusion flames in crosswinds. *Combust. Flame* **2000**, *123* (1−2), 189−200, DOI: 10.1016/S0010-2180(00)00151-6.
(20) Kostiuk, L. W.; Majeski, A. J.; Poudens, M. B.; Johnson, M. R.; Wilson, D. J. Scaling of wake-stabilized jet diffusion flames in a transverse air stream. *Proc. Combust. Inst.* **2000**, *28* (1), 553−559, DOI: 10.1016/S0082-0784(00)80255-6.
(21) *Investigation of Flare Gas Emissions in Alberta*; Environment Canada Conservation and Protection, Alberta Energy and Utilities Board and the Canadian Association of Petroleum Producers: Calgary, Alberta, Canada, 1996; www.ags.gov.ab.ca/publications/SPE/PDF/SPE_005.pdf.
(22) Torres, V. M.; Herndon, S.; Kodesh, Z.; Allen, D. T. Industrial flare performance at low flow conditions. 1. Study overview. *Ind. Eng. Chem. Res.* **2012**, *51* (39), 12559−12568, DOI: 10.1021/ie202674t.
(23) Torres, V. M.; Herndon, S.; Allen, D. T. Industrial flare performance at low flow conditions. 2. Steam- and air-assisted flares. *Ind. Eng. Chem. Res.* **2012**, *51* (39), 12569−12576, DOI: 10.1021/ie202675f.
(24) Knighton, W. B.; Herndon, S. C.; Franklin, J. F.; Wood, E. C.; Wormhout, J.; Brooks, W.; Fortner, E. C.; Allen, D. T. Direct measurement of volatile organic compound emissions from industrial flares using real-time online techniques: proton transfer reaction mass spectrometry and tunable infrared laser differential absorption spectroscopy. *Ind. Eng. Chem. Res.* **2012**, *51* (39), 12674−126684, DOI: 10.1021/ie202695v.
(25) Johnson, M. R.; Devillers, R. W.; Thomas, K. A. Quantitative field measurement of soot emission from a large gas flare using Sky-LOSA. *Environ. Sci. Technol.* **2011**, *45* (1), 345−350, DOI: 10.1021/es102230y.
(26) Akeredolu, F. A.; Sonibare, J. A. A review of the usefulness of gas flares in air pollution control. *Manage. Environ. Qual.* **2004**, *15* (6), 574−583, DOI: 10.1108/14777830410560674.
(27) Brandt, A. R.; et al. Methane leaks from North Americal natural gas systems. *Science* **2014**, *343* (6172), 733−735, DOI: 10.1126/science.1247045.
(28) Garman, K. E.; Hill, K. A.; Wyss, P.; Carlsen, M.; Zimmerman, J. R.; Stirm, B. H.; Carney, T. Q.; Santini, R.; Shepson, P. B. An airborne and wind tunnel evaluation of a wind turbulence measurement system for aircraft-based flux measurements. *J. Atmos. Oceanic Technol.* **2006**, *23* (12), 1696−1708, DOI: 10.1175/JTECH1940.1.
(29) Crosson, E. R. A cavity ring-down analyzer for measuring atmospheric levels of methane, carbon dioxide, and water vapor. *Appl. Phys. B: Laser Opt.* **2008**, *92* (3), 403−408, DOI: 10.1007/s00340-008-3135-y.
(30) Chen, H.; et al. High-accuracy continuous airborne measurements of greenhouse gases (CO_2 and CH_4) using the cavity ring-down spectroscopy (CRDS) technique. *Atmos. Meas. Technol.* **2010**, *3* (2), 375−386, DOI: 10.5194/amt-3-375-2010.
(31) Gollahalli, S. R.; Nanjundappa, B. Burner wake stabilized gas jet flames in cross-flow. *Combust. Sci. Technol.* **1995**, *109* (1−6), 327−346, DOI: 10.1080/00102209508951908.
(32) Nieuwstadt, F. T. M.; de Valk, J. P. J. M. M. A large eddy simulation of buoyant and non-buoyant plume dispersion in the atmospheric boundary layer. *Atmos. Environ.* **1987**, *21* (12), 2573−2587, DOI: 10.1016/0004-6981(87)90189-2.
(33) Stull, R. B. *An Introduction to Boundary Layer Meterorology*. Kluwer Academic Publishers: Dordecht, The Netherlands, 1988.
(34) Miller, J. C.; Miller, J. N. *Statistics for Analytical Chemistry*, 3rd ed.; Ellis Horwood: Chichester, UK, 1993.
(35) Weber, C. L.; Clavin, C. Life cycle carbon footprint of shale gas: review of evidence and implications. *Environ. Sci. Technol.* **2012**, *46*, 5688−5696, DOI: 10.1021/es300375n.
(36) Rojey, A.; Jaffret, C.; Cornot-Gandolphe, S.; Durand, B.; Jullian, S.; Valais, M. *Natural Gas: Production, Processing, Transport*; Rojey, A., Ed.; Imprimerie Nouvelle: Paris, France, 1997; p 17.
(37) Orimoogunje, O. O.; Ayanlade, A.; Akinkuolie, T. A.; Odiong, A. U. Perception on effect of gas flaring on the environment. *Res. J. Environ. Earth Sci.* **2010**, *2* (4), 188−193.
(38) Dung, E. J.; Bombom, L. S.; Agusomu, T. D. The effects of gas flaring on crops in the Niger Delta, Nigeria. *GeoJournal* **2008**, *73* (4), 297−305, DOI: 10.1007/s10708-008-9207-z.
(39) Villasenor, R.; et al. An air quality emission inventory of offshore operations for the exploration and production of petroleum by the Mexican oil industry. *Atmos. Environ.* **2003**, *37* (26), 3713−3729, DOI: 10.1016/S1352-2310(03)00445-X.